RESISTANCE HEATING OF STEEL CONDUCTORS OF CIRCULAR CROSS-SECTION

PHILIP TSAPPI

Doctor of Philosophy

THE UNIVERSITY OF ASTON IN BIRMINGHAM

March, 1987

The University of Aston in Birmingham

Resistance Heating of Steel Conductors of Circular Cross-section

Philip Tsappi. Doctor of Philosophy 1987

SUMMARY

The object of this thesis is to develop a method for calculating the losses developed in steel conductors of circular cross-section and at temperatures below 100^0C, by the direct passage of a sinusoidally alternating current. Three cases are considered.

1. Isolated solid or tubular conductor.
2. Concentric arrangement of tube and solid return conductor.
3. Concentric arrangement of two tubes.

These cases find applications in process temperature maintenance of pipelines, resistance heating of bars and design of bus-bars.

The problems associated with the non-linearity of steel are examined. Resistance heating of bars and methods of surface heating of pipelines are briefly described. Magnetic-linear solutions based on Maxwell's equations are critically examined and conditions under which various formulae apply investigated. The conditions under which a tube is electrically equivalent to a solid conductor and to a semi-infinite plate are derived. Existing solutions for the calculation of losses in isolated steel conductors of circular cross-section are reviewed, evaluated and compared. Two methods of solution are developed for the three cases considered. The first is based on the magnetic-linear solutions and offers an alternative to the available methods which are not universal. The second solution extends the existing B/H step-function approximation method to small diameter conductors and to tubes in isolation or in a concentric arrangement. A comprehensive experimental investigation is presented for cases 1 and 2 above which confirms the validity of the proposed methods of solution. These are further supported by experimental results reported in the literature. Good agreement is obtained between measured and calculated loss values for surface field strengths beyond the linear part of the d.c. magnetisation characteristic.

It is also shown that there is a difference in the electrical behaviour of a small diameter conductor or thin tube under resistance or induction heating conditions.

Steel, resistance heating, surface heating, losses, tubes.

ACKNOWLEDGMENTS

I would like to thank Professor R.D.Langman for his guidance and supervision and Mr.R.A.Savill, Head of Electrical and Electronic Engineering Department at the North East London Polytechnic, for his encouragement and provision of facilities.

Grateful thanks are also due to the Electricity Council and to my employers for their financial and material support.

The valuable assistance of Mark Archer and Don Reynolds, of the Technician Staff of the Polytechnic's Electrical Engineering Department, in carrying out the experimental work, is gratefully acknowledged, as well as the assistance received from the Electricity Council Research Centre, which provided the chemical analysis of two steel tubes and from the Royal Naval Engineering College, which provided the respective photomicrographs.

Finally, I would like to thank Pauline Archer for the unenviable task of typing the thesis.

CONTENTS

LIST OF SYMBOLS

The symbols used by the authors of the papers to which reference is made, have been changed in some cases to avoid duplication.

a_1', b_1' = constants in B/H characteristic representation

a_1, b_1 = constants in Frohlich curve

a, b = internal and external radius of tube, m

c_1 = constant in B/H characteristic representation

c_1', c_2' = constants in the harmonic representation of B

d = bar diameter, m

d_o = external diameter of tube, m

d_i = internal diameter of tube, m

f = frequency, Hz

h = multiplying factor

h_o = dimensionless parameter, [ref. 9]

i = instantaneous current, A

k_b = function of b_1' [ref. 14]

k_b, k_x = functions of b/δ_s [ref. 57]

r, θ, z = cylindrical polar co-ordinates

m = $\sqrt{\mu\omega\sigma}$

$p(t)$ = instantaneous active power, W m^{-1}

$q(t)$ = instantaneous reactive power, VA

s = distance between centres of parallel conductors, m

t_s = depth beyond which the current density is zero, m

t = time, tube wall thickness, s, m

v = surface velocity of separating surface (Agarwal), m s^{-1}

x = $\sqrt{2}\ b/\delta_s$

x' = $\sqrt{2}\ mt$

y = distance into conductor, m

z = dimensionless parameter, $2\pi f \mu t^2 \sigma$

$\alpha(z), b(z)$ = functions of z

A, B, C, D = constants

B, B_A, B_s, B_1 = magnetic flux density equivalent step-function flux density, saturation flux density, fundamental component of B, T

$\bar{B}$ = flux density vector

C' = $2\pi f \mu_r \mu_o \sigma$

C'' = $\sqrt{C'/2}$

$\bar{E}$ = electric field vector

$|E(t)|$ = electric field at surface of conductor, V m^{-1}

E, F = constants

H, H_s = magnetic field strength, surface magnetic field strength, A m^{-1}

H_r = magnetic field at distance r, A m^{-1}

H_{s1} = fundamental component of H_s, A m^{-1}

H_{si} = magnetic field strength at the inner surface of a tube, A m^{-1}

$\mathcal{J}$ = imaginary part of complex quantity

I = rms current, A

$\hat{I}$ = peak current, A

I_1, I_0 = modified Bessel function of the first kind of order one and zero

$\bar{J}$ = current density vector,

J_z = component of $\bar{J}$ in z direction, A m^{-1}

J_r = component of $\bar{J}$ in z direction at distance r, A m^{-1}

J_s = surface current density, A m^{-1}

K, K_o' = Rac/Rdc isolated conductor, concentric arrangement

K_1, K_o = modified Bessel functions of the second kind of order one and zero

L_{ac} = inductance due to internal flux linkages, H m^{-1}

M = Rdc/Zac

P_e = eddy-current loss per unit surface area, W m^{-2}

P_{e+h} = eddy-current and hysteresis loss per unit surface area, W m^{-2}

P = average power, W m^{-1}

P_{cl} = calculated loss (linear theory), W m^{-1}

$P_{c\infty}$ = calculated loss based on semi-infinite slab, W m^{-1}

P_m = measured power, W m^{-1}

P_n = dimensionless power loss, [ref. 9]

P_s = surface power density, W m^{-2}

P_{sc} = calculated surface power density, W m^{-2}

P_y = average power up to depth y, W

P_{sm} = measured surface power density, W m^{-2}

P_{smi} = measured surface power density on internal surface of tube, W m^{-2}

P_c = calculated power loss, W m^{-1}

P_r = perimeter of conductor, m

Q = average reactive power, VA

R_1, R_2 = resistances, Ω

R_{dc} = d.c. resistance of conductor, $\Omega\ m^{-1}$

R_{ac} = a.c. resistance of conductor, $\Omega\ m^{-1}$

S = conductor cross-section area, m^2

X_{ac} = reactance of conductor, Ω

Z_{ac} = complex impedance of conductor

α = temperature coefficient of resistance, per $^{\circ}C$

α_t = temperature coefficient of resistivity at temperature t , per $^{\circ}C$

α_i' = constant in the harmonic representation of B

β = non-dimensional parameter, $2t/d_o$

β_o = non-dimensional parameter for outer tube of concentric arrangement

δ = classical skin depth, $\sqrt{2\rho/\mu\omega}$, m

δ_F = penetration depth based on Frohlich curve, m

δ_s = depth of penetration (Agarwal), m

η = dimensionless parameter, [ref. 9]

Θ = hysteresis angle, rad, degrees

θ_p = conductor temperature, $^{\circ}C$

λ = $2\pi t^2 \sigma \mu_{veff} \mu_o$

μ_v = relative permeability

μ_{veff} = effective relative permeability

ξ = Frohlich curve shape factor, a_1/b_1

ξ_1 = used in derivation of B_1/H_1 curve, [ref. 14]

$\pi_{1,\ldots,N}$ = Buckingham's π factors

ρ = resistivity, Ω m

ρ_2, ρ_1 = resistivity at temperature t_2 and t_1, Ω m

σ = conductivity, S m^{-1}

τ = time for separation surface to reach a certain distance, s

Φ = magnetic flux, Wb

$\psi(t)$ = distance penetrated by separating surface as a function of time, m

$|\psi(t)|$ = distance penetrated by separation surface in time t , m

w = angular frequency, rad s^{-1}

LIST OF FIGURES

LIST OF TABLES

CHAPTER 1

INTRODUCTION

The prediction of losses in magnetic materials is of fundamental importance. It is relevant to electrical machines and transformers, where the aim is to minimise the losses and to eddy-current brakes, induction and resistance heating, where the losses are systematically utilised. This thesis is concerned with the last application in general, but with surface heating in particular. However the analyses developed are also applicable to steel bus-bars and steel wires.

The rigidity of steel pipes is the principle reason for their occasional use, as bus-bars. The pipe size must be specified to ensure that the maximum allowable temperature rise is not exceeded for a given current. Because steel has a larger resistivity than copper, the cross-sectional area of a steel bus-bar needs to be larger than a comparable copper one.

In resistance process heating [1], which is a high temperature application and where an alternating current is passed through the bar, the power to achieve a temperature rise in a given time, with a desirable surface to centre temperature differential has to be specified.

To ensure effective transportation of a highly viscous fluid through a pipe line, a suitable heating system must be provided to keep the fluid temperature at some optimum value. This is a low temperature application of resistance heating and the

surface heating systems which are suitable for long pipelines are reviewed in Chapter 3. These systems exploit the phenomenon of skin effect in steel conductors and a number of variations exist [2].

Two systems are considered in this thesis. The first which is sometimes known by the trade name of SECT*(otherwise referred to as the saddle-tube system), utilises the heat generated by a current flowing through a small-bore tube, electrically in series with a concentric copper conductor and intermittently welded to the transport pipe line [3,4,5].

In the second, which is referred to as the coaxial system [6], the steel transport pipeline is coaxial with a surrounding steel pipe and electrically in series with it.

For both systems, the power required to compensate for heat losses through the pipe insulation has to be specified. However, whereas in the saddle-tube system there is a choice in the radial dimensions of the heating tube beyond a minimum value, in the coaxial system, the transport pipeline's radial dimensions are fixed by the volumetric rate of the fluid and mechanical considerations. These in turn fix the diameter of the surrounding pipe, but the wall thickness is decided by safety considerations as for the case of the saddle-tube system.

The use of steel conductors for these applications. makes analytical solutions difficult, mainly due to the B/H characteristic of steel and in some cases drastic changes in the material's properties. These factors are considered in Chapter 2.

* Skin Effect Current Tracing

Many solutions have been proposed [7-14] which attempt to overcome the difficulties arising from the non-linearity of steel. These solutions relate to the calculation of losses developed by induction in thin and thick steel plates. The analyses for thick plates are also applicable to the resistance heating of a bar or tube, provided the diameter (in the case of a bar) and in addition the wall thickness (in the case of a tube) are large compared to the penetration depth.

By comparison, the problem of resistance process and surface heating (where the heat is generated in a tube or pipe) has not received the same attention.

The work of Koyanagi et al [6], Gillot and Calvert [7], Burke and Lavers [15], Crepaz and Lupi [16], Thornton [17] and Rajagopalan and Murty [18], refers to steel tubes or solid bars. A literature survey and critical review is given in Chapter 5, where it is shown that a method which can predict the losses in steel bars of any diameter and steel tubes of any wall thickness in the absence of proximity effect, or in a concentric configuration, has yet to be fully developed or tested experimentally.

The aim of this thesis is therefore to devise a method for calculating the power loss for the systems under investigation and at the same time make a contribution to the understanding of some associated pheonomena such as depth of penetration and the effect of geometrical boundaries.

Two methods of solution are developed in Chapter 6. The first is based on the step-function B/H characteristic

approximation, which has not hitherto been applied to the cases of a small diameter bar, an isolated tube, or a concentric series arrangement of a tube and solid conductor. It is known that this method over-estimates the losses at low field strengths and under-estimates them at high values. Furthermore, it is only applicable to field strengths beyond the knee of the B/H curve. Some uncertainty exists as to the appropriate value of saturation flux density to substitute into the relevant equations [8,9,14,15]. However it is shown in the thesis, that this method can be used to investigate analytically, the influence of the geometrical dimensions of conductors on the generation of losses.

The second method of solution, is characterised by its simplicity and is based on existing linear solutions for cylindrical conductors. The permeability is replaced by an experimentally derived effective permeability which encompasses all the effects of non-linearity. Beyond the knee of the B/H curve it is found to be a simple function of the surface magnetic field strength and can be obtained by the application of dimensional analysis.

In resistance process heating, the cross-section of a conductor is heated non-uniformly during the short heating cycle. with the result that resistivity and permeability will change considerably.

The assumptions made in the derivation of linear solutions, do not permit these changes to be taken into account. The same limitation applies to the step-function method and in addition

neither method can predict correctly the electric field within the conductor. However, given the surface power density, the technique developed [19] for induction heating of cylindrical bars, can be used to establish approximately, the heating time required for a surface-to-centre temperature differential.

Such high temperature effects, are outside the scope of the thesis and the experimental work reported in Chapter 7 is limited to near ambient temperatures and encompasses the conductor configurations stated previously with the exception of the coaxial system.

This thesis makes the following contributions to the state of the art.

1. A new method is developed for calculating losses in steel conductors of circular cross-section which gives a better prediction of losses than available methods. The method can also be applied to losses produced on a thick plate by induction.
2. The step-function theory is applied to the analysis of thin tubes, small diameter bars and to the concentric arrangement of tube and conductor. Such an analysis has not been reported in the literature.
3. A mechanism is established for predicting universal loss and penetration depth curves for solid bars or thick tubes which cannot be readily approximated to a semi-infinite plate.
4. A new method for establishing the limit of applicability of semi-infinite plate solutions to

finite diameter conductors and the condition under which a tube appears electrically solid is produced.

CHAPTER 2

RESISTANCE HEATING OF STEEL CONDUCTORS

Chapter Summary

The difficulties in obtaining analytical solutions to problems associated with steel conductors are introduced and linear and non-linear solutions defined. Changes in resistivity and permeability are considered and the order of magnitude of hysteresis loss is estimated. The influence of resistivity and permeability on the generation of loss is considered. Direct resistance heating of steel billets is briefly described.

Chapter Contents

2.1 Introduction

When an electric current is passed through a conductor, heat is generated by the Joule effect. Under a.c. conditions ohmic losses in addition to I^2R_{dc} can be experienced by the conductor due to skin and proximity effects. The term skin effect is given to the tendency for current to flow predominantly in the outer layers of the conductor. The term proximity effect is used to describe the tendency for current to flow along one side of a conductor, due to the interaction of the magnetic field of the current in the conductor considered and the currents in adjacent conductors.

Under a.c. conditions the loss in the conductor is given by I^2R_{ac}, where R_{ac} is its resistance corrected for operating temperature, skin and proximity effects and is referred to as effective resistance. In addition, losses may be caused by hysteresis.

For normal current carrying duties, the aim of the designer is to minimise the above losses which are functions of frequency, material properties and conductor geometry. In addition, for steel conductors R_{ac} is a function of current.

For a tubular conductor, skin effect can be reduced by reducing the thickness of the tube wall and increasing its diameter, whilst proximity effect can only be reduced by increasing the distance between conductors.

For heating applications, the designer is looking for a maximum heating effect and therefore skin and proximity effects

are not detrimental.

Irrespective of the application, a method for calculating losses is required, in order to ensure that the temperature rise of the conductor will be within specified limits and to specify the current for a given conductor configuration and required power output.

Although the analysis in the case of non-magnetic conductors is by no means simple, experimentally verified formulae for calculating losses are available for a number of conductor configurations. These formulae are derived from the solution of Maxwell's equations, on the basis of constant permeability given by the slope of a linear B/H characteristic, material homogeity and sinusoidal excitation. In the above case the solutions are referred to as linear and are considered in Chapter 4. The skin depth gives an indication of the extent of diffusion of electromagnetic energy into the conductor from its surface and is associated with the linear theory. It is only a function of material parameters and independent of current or conductor geometry.

In the case of steel conductors, due to the non-linear B/H characteristic, the permeability is not constant over a range of current. In this case, solutions can be obtained, by assigning a value to the permeability corresponding to a given surface magnetic field strength on the B/H curve. These solutions are referred to as "magnetically linear" solutions and predict losses considerably smaller than the measured values (Chapter 5).

For a realistic solution, the mathematical model must take into account two effects which result from the non-linear B/H characteristic.

Firstly, as a result of the attenuation of the magnetic field strength with depth into the conductor, different layers are at a different state of magnetisation during a current cycle. Since a change in the amplitude of the magnetic field strength results in a change of permeability as derived from the d.c. magnetisation curve, an analysis based on values of permeability corresponding to surface values of magnetic field strength will not predict the loss accurately.

Secondly, saturation harmonics must be considered, since a sinusoidal magnetic field strength will produce a non-sinusoidal flux density. A solution therefore which takes into account changes in permeability with depth into the conductor and the distortion of the flux density waveform, will give a more accurate prediction of losses and is referred to as a magnetically non-linear solution.

Further complications arise (which are not explored in this study), with high temperature applications such as resistance billet heating, where during the heating cycle, each layer of a billet can experience different values of resistivity and permeability. Only numerical solutions are appropriate in such cases, but these have not been widely explored in the case of magnetic materials.

Permeability and resistivity are important parameters in resistance and surface heating and these are examined in the

following sections. In addition, hysteresis can contribute to the heat generated in a conductor and its contribution must be evaluated.

2.2 Magnetic Permeability

The magnetisation curve for magnetic materials is obtained by joining the tips of succesive static hysteresis loops obtained for different values of peak flux density. B.S. 5884, 1980, describes the methods for determining the d.c. magnetic properties of magnetic materials. For a bar specimen, the NPL compensated permeameter described in this specification is used.

Different steels have different B/H characteristics depending on their chemical analysis and method of manufacture. Because of the allowed tolerance on the maximum percentage content of the various elements, and, again within permitted tolerances, variations in work history, samples of the same grade of steel can have different magnetisation curves. The chemical composition of some common grades of steels is shown in the extract from B.S. 980, 1950, included in Appendix A.

Because of the magnetic non-linearity of steel, analytical solutions are difficult to obtain and simplifying assumptions have to be made. Some of these solutions are discussed in Chapter 5.

For analytical solutions, a functional representation of the B/H characteristic is required and the Frohlich representation

$$B = \frac{\hat{H}}{a_1 + b_1\hat{H}}$$

is the most extensively used; a_1 determines the initial slope and b_1 the saturation flux density.

Deeley [20] used a modified form given by

$$B = \frac{\hat{H}}{a_1 + b_1\hat{H}} + c_1\hat{H}$$

where the coefficient c_1 controls the slope of the characteristic in the saturation region. Since a B/H curve representation is a curve fitting exercise, no great accuracy is lost by omitting the term in c_1. Widger [21] proposes a rational fraction approximation to the representation of the B/H characteristic and Bowden and Davies [14] observe that the Frohlich representation gives the best fit near the knee of the B/H curve, but a different representation is required in the saturation region.

The simplest form of representation is the step-function with a constant value of flux density for all values of H (see Chapter 5). The Frohlich representation reduces to the step-function if the ratio of $a_1/b_1 = \xi$ is made small compared to H while maintaining the value of b_1 constant [9].

The complexity of an analytical solution depends on the functional representation of the B/H characteristic and the alternative representation $B = a_1' \hat{H}_s^{b_1'}$ can be used in the saturation region to simplify the analysis [14].

An exact representation of the B/H characteristic is not critical for two reasons. Operating conditions for conductive heating of steel conductors differ from the conditions under which magnetisation tests are performed; B/H curves are taken

with a steady longitudinal flux, whereas the magnetising force on the actual conductor varies continuously across its cross-section and produces a circumferential flux in the material. The relation between B/H curves and loss in the case when the magnetic field is parallel to the conductor, may not therefore be the same as when the field is circumferential.

The loss developed for a given current is not typically very sensitive to variations in the B/H characteristic. This is shown in Table 2.1, where the loss for magnetically linear steel, 3 cm diameter, conductor has been calculated using the formulae of Chapter 4. In order to examine the effect of the shape of the B/H characteristic on losses, the values calculated in Table 2.1 have been based on a resistivity of 19 $\times 10^{-8}$ (Ω m). The effect on the loss of the parameter ξ, the shape factor of the B/H characteristic [9], is also shown in the results of Table 2.1.

A factor which influences the permeability of steel is its heating history. Table A2 shows that not only the maximum value of μ_v, but also the corresponding value of H differ if the steel is annealed or normalised.

The conclusion to be drawn is that there is no single B/H curve which can be labelled as correct for a given grade of steel and therefore an accuracy of 10% in the prediction of losses for similar grades of steel has to be acceptable.

Apart from the heating history of steel during manufacture, the value of μ_v is also a function of temperature and reduces to unity at the Curie temperature.

Table 2.1. Influence of Value of Permeability on Power Loss

Reference No.	Steel	μ_r Functional Representation	$\hat{H}$	1000	3000	5000	10000	I	200	600	1000	ξ
			$\hat{H}$	3000	9000	15000						
				μ_r					P_{cL} (Wm^{-1})			
14	ENIA	$525 \times 10^3 \hat{H}^{-0.89}$		1123	422	268	144		56	320	725	-
14	ENIA	$\frac{10^7}{4\pi(288 + 0.51\hat{H})}$		997	437	280	148		57	324	724	565
9	Mild	$\frac{10^7}{4\pi(256 + 0.581\hat{H})}$		950	398	252	131		54.6	307	685	441
9	Mild	$\frac{10^7}{4\pi(270 + 0.577\hat{H})}$		939	398	252	132		54.6	308	687	468
9	Mild	$\frac{10^7}{4\pi(156 + 0.59\hat{H})}$		1067	413	233	131		55.6	308	684	264
8&9	Common Plate	$\frac{10^7}{4\pi(207 + 0.576\hat{H})}$		1016	411	258	133		55	310	690	359
12	0.27%C	$7 \times 10^5 \hat{H}^{-0.94}$		1058	377	233	122		53.3	297	666	-
	0.32-0.4%C	$4.4 \times 10^5 \hat{H}^{-0.9}$		878	327	206	110		49.8	284	643	-
	0.52-0.6%C	$2.9 \times 10^5 \hat{H}^{-0.89}$		817	321	208	115		49.4	289	661	-
	0.62-0.7%C	$2.6 \times 10^5 \hat{H}^{-1.85}$		733	288	186	104		46.9	275	631	-

$2b = 3$ cm $\qquad \rho = 19 \times 10^{-8}\ \Omega \cdot m$

Thornton [17] quotes some values for temperature coefficient of permeability and more recently, King [22], on measurements at $H>10^4$ ($A\ m^{-1}$) on EN3 and EN5 samples, shows that there is a small reduction in permeability between ambient and 200 °C.

For surface heating applications, the selection of steel is important. Excluding other factors, it is apparent from the results of Table 2.1, that the steel with the highest value for a given H, will develop the highest loss. For bar heating this choice does not exist.

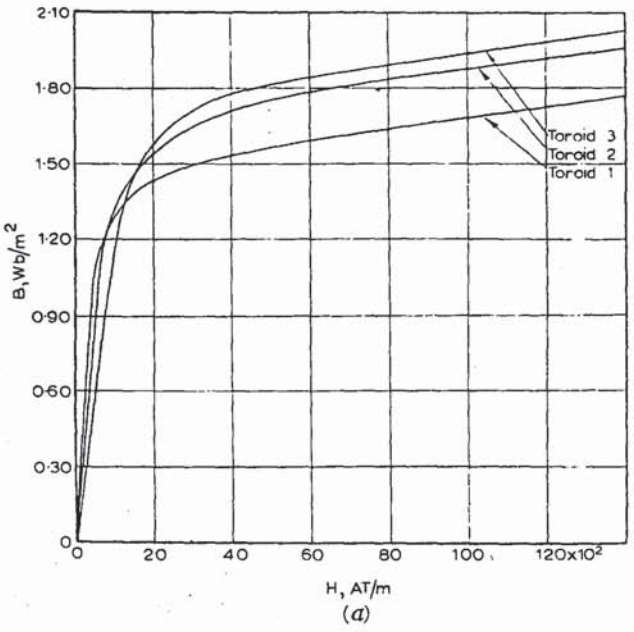

(a)

(σ = hysteresis angle)

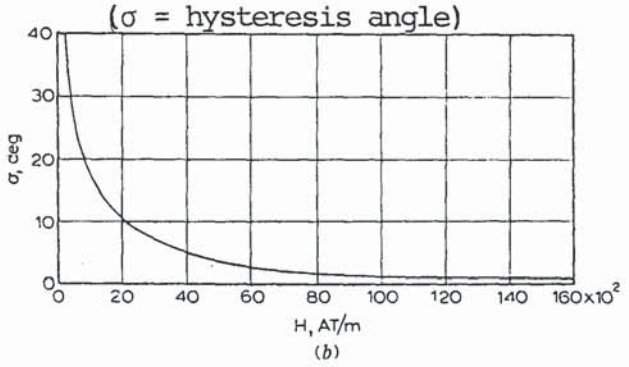

(b)

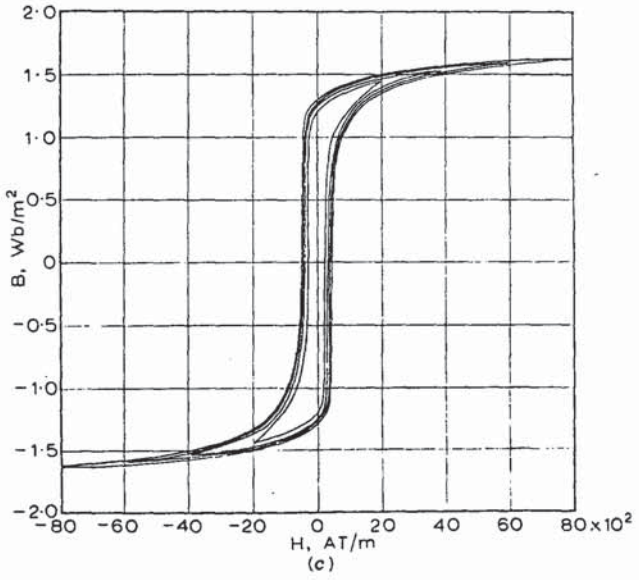

(c)

Fig. 2.1 Magnetic data for toroids 1,2 and 3 (Ref.24)

(a) Mean magnetization characteristics for toroids, 1, 2 and 3
(b) σ/H curves for toroids 1, 2 and 3
(c) Hysteresis loops for toroid 1

2.3 Hysteresis

Referring to Fig. 2.1(c), the area of the hysteresis loop and therefore the energy loss per unit volume of material per cycle, is almost independent of the maximum field strength for values of H exceeding 7,000 ($A\ m^{-1}$). It can therefore be expected that at high levels of saturation, hysteresis loss is insignificant.

Hysteresis effects have been discussed by many authors concerned with losses in laminations or conductors and they either dismiss it as negligible, or attempt to account for it. Lim and Hammond [9] for instance state that magnetic hysteresis reduces the eddy current loss although the total loss is higher than in the absence of hysteresis.

They attribute discrepancies between measured and calculated values for loss to the neglect of hysteresis, although one would expect the level of this discrepancy to decrease with increasing H, which is not the case.

Zakrzewski [10] investigated hysteresis loss on thick and thin steel plates and explains why hysteresis is also present with high values of H.

Agarwal [8] gives a fuller discussion of hysteresis and concludes that except for low values of induction, the reduction in eddy current losses caused by hysteresis is small and it is offset by hysteresis loss.

O'Kelly [23] shows that for thick laminations at a mean H of 5838 ($A\ m^{-1}$), hysteresis constitutes about 7% of the total loss

with a considerably larger percentage at lower values of H.

Thornton [17] discusses hysteresis and on the basis of

$$\hat{B}^{1.6} \times 1 \text{ W/}_{\ell b} \text{ at } 1 \text{ T, equal to } 4.9 \text{ Wkg}^{-1},$$

estimates the hysteresis loss for mild steel tubes at H_s = 1000 (A m^{-1}) to be 4.5% and at about 5000 (A m^{-1}), to be 1.3% of the total loss. Thornton's estimate was based on the mass given by a "skin" thickness which is ill-defined and therefore the percentages quoted above are not very reliable estimates.

Hysteresis loss for various grades of steel are quoted by steel manufacturers but these are only typical values since the magnetic properties of different samples of the same grade can vary by ± 15%. For example, Fig. 2.1(a) shows the saturation curves of three samples all labelled mild steel [24].

It is of interest, particularly for the purpose of experimental verification of loss calculations (Chapter 7), to obtain an alternative estimate of the probable hysteresis loss of mild steel. For this estimation the concept of complex permeability can be used.

For a sinusoidal magnetising force given by

$$H = \alpha_1' \sin wt$$

the corresponding variation in B as a result of the non-linearity and hysteresis will have the form

$$B = c_1' \sin(wt-\theta) + c_3' \sin 3(wt-\theta) + \ldots$$

where α_1', c_1', c_3', are constants. Neglecting the harmonic components of B,

$$H = \mathcal{J}(\alpha_1' e^{jwt}) \text{ and}$$
$$B = \mathcal{J}(c_1' e^{j(wt-\theta)})$$

The ratio $B/H = \mu = \frac{c_1'}{\alpha_1'} e^{-j\theta} = |\mu_1| e^{-j\theta}$

is referred to as complex permeability. As a result of neglecting the harmonics in the flux density waveform, the B/H relationship over one complete period yields a hysteresis loop which is an ellipse [25].

The angle θ is the angle of lag between B and H and is known as the hysteresis angle. Fig. 2.1(b) shows the measured hysteresis angle for three mild steel specimen [24] as a function of the surface field strength.

For values of H in the range 1000 - 5000 Am^{-1}, the corresponding hysteresis angles are in the range of 12° - 5° . These values will of course be somewhat different for different steels.

By replacing μ by the complex permeability in the appropriate Maxwell's equations a magnetic linear solution can be obtained which takes into account hysteresis.

For solid iron Kesavamurty and Rajagopalan [26] show that the losses per unit surface area are given by

$$P_{e+h} = \frac{\cos(\pi/4 - \theta/2)}{\cos \pi/4} P_e$$

Thus for a hysteresis angle of 10°

$$P_{e+h}/P_e = 1.083$$

giving an 8.3% increase in loss due to hysteresis which is within the expected order of magnitude.

The above estimate of hysteresis loss is based on the analysis of thick plates. It is expected that for a finite diameter conductor the results will be somewhat different. Maxwell's equations applied to resistance heating can be solved using complex permeability and thereby take into account the effects of hysteresis. Little, however, will be gained by carrying out this process because of the assumptions which have to be made to obtain a solution and the doubts about the validity of present practice in calculating hysteresis.

The presence or otherwise of hysteresis loss will be sought in the experimental results of Chapter 7.

2.4 Electrical Resistivity

The elements influencing the value of resistivity for a particular grade of steel, are mainly carbon, silicon and nickel. The grain size is also a factor and the resistivity can be influenced by the work history of a sample. Different steels therefore have different values of resistivity and some typical values are shown in Table A1.

Since for steel the resistivity is not a linear function of temperature, its temperature coefficient α , is not constant for all temperature ranges. Over the linear range, the resistivity ρ_2 at temperature t_2 , is related to the resistivity ρ_1 at temperature t_1 by the equation

$$\rho_2 = \rho_1 [1 + \alpha_1 (t_2 - t_1)]$$

where α_1 is the temperature coefficient at temperature t_1 .

The temperatures attained by the steel tube in surface heating applications, are of the order of 100°C and for this temperature range, a 1°C increase in temperature produces a change of about 0.4% in the d.c. resistance. This is significant when measuring losses.

Although the current density through the cross section of a tube is not constant, in the steady state the temperature of the different layers will be almost constant and will attain a value which is dictated by the power dissipated and any thermal insulation surrounding the tube. For the purpose of analysis, the resistivity at a given surface temperature can therefore be considered constant throughout the tube cross section provided

the wall thickness is small.

The temperature gradient between the tube's inner and outer layers will increase with wall thickness and will be greatest for a solid conductor of large diameter.

For high temperature applications as in billet heating, the layers can be at considerably different temperatures at any instant and therefore the single value resistivity cannot be assumed for the analysis. For a constant power input corresponding to ambient temperature and a mean temperature rise, the heating time and the surface to centre temperature difference can be calculated approximately [19].

Since for all other parameters being equal, the power loss increases with an increase in the value of resistivity, for surface heating, tubes of high resistivity are desirable. Steel alloys have a much larger value of resistivity than mild steel but their cost prohibits their use as heating tubes. An examination of resistivity values for mild steel, quoted in the literature, shows that they vary within the range 12.5 to $25 \times 10^{-8} (\Omega\ m)$. Some selection is therefore still possible even if the tube material is limited to mild steel. However the higher resistivity value is normally accompanied by a shift in the knee of the saturation curve to higher values of H and therefore the choice of resistivity is dependent on the value of H required to produce the required loss.

For direct resistance heating applications, there is no choice in parameters since they are dictated by the material to be heated.

2.5 Direct Resistance Heating of Billets [1][14][15][16] [27][28]

The terms resistance and surface heating have already been mentioned and therefore to familiarise the reader, a brief description of resistance heating is given below. Surface heating forms the subject of the next chapter.

Resistance heating is ideal for long lengths of billets, tubes and plates of small regular cross-section. The process can be adapted for rolling, forging, cropping and heat treatment, with the advantages of high thermal efficiency, minimal scale loss and absence of skin decarburisation. By varying the heating time, the efficiency as well as the temperature distribution within the material can be controlled so that it is uniform throughout or differs from surface to core.

A resistance heater consists basically of a single phase transformer connected to the contact clamp heads at each end of the billet, by means of water cooled copper bus-bars and flexible cables.

For rapid heating, large, 50 Hz, currents are required. Power factor correction is required throughout the heating cycle and switchable capacitors are connected on the high voltage side of the heater transformer, whose output voltage can be varied to provide constant current or constant power operation.

In spite of its simplicity, the matching of the heater design to specific requirements is always very difficult due to the fact that the mechanism of non-uniform heat generation in

the billet is created by a set of interdependent variables, which in turn depend not only on the non-linear magnetisation characteristic of the steel but also on the rapid change in temperature during the heating time.

As is often the case in practice, since theoretical analysis can give only an estimate of the expected performance, tests on actual samples have to be performed before the equipment is used on a production line.

However, even approximate analysis can indicate the influence of the various variables on the performance and in this respect serves a useful purpose.

CHAPTER 3

SURFACE HEATING OF PIPES

Chapter Summary

The conditions under which surface heating of pipe-lines is required are examined and the heating systems under investigation described.

Chapter Contents

3.1 The need to trace heat [29][30]

On a traced line, heat can leave the tracer either through the insulation to the surrounding medium or through the pipe wall to the fluid in the pipe (Fig. 3.1.). With the pipe contents in a flowing state, heat can enter and leave the system via the fluid. Two extreme conditions of flow exist "no-flow": and "maximum flow". Under no-flow conditions, the energy required to maintain a given temperature on a pipeline is directly proportional to the line temperature above ambient and the time the temperature is maintained. The amount of heat required is therefore varying as a function of the ambient temperature.

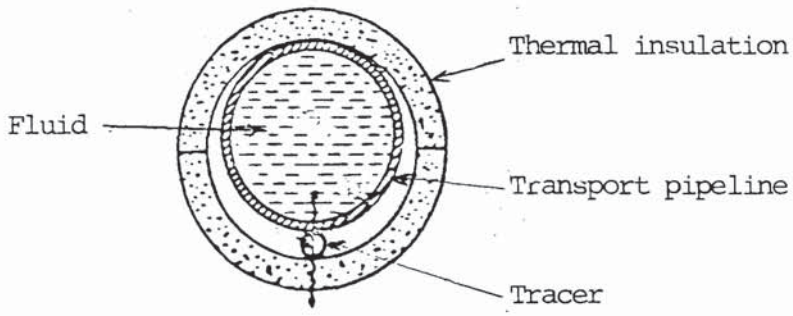

Fig. 3.1 Typical cross section of traced pipe

Under "maximum flow" conditions and with short lengths of pipe, the heat entering a pipe via the fluid flow will maintain the desired temperature, provided the pipe is adequately insulated. There is an economic thickness of insulation which depends on energy and insulation costs. If the pipe is electrically traced and controlled by thermostat or otherwise, the tracer will not be energised. Under reduced flow conditions, in order to maintain the fluid temperature over a long length of line, external heat via the tracer must be provided depending on the ambient temperature. Heating must also be provided under discontinuous flow operation or for heating up the pipeline after a shut down, in which case the power rating of the tracer must satisfy the need to raise the temperature and maintain it.

With the exception of "skin effect" heating and direct pipe line heating, surface heating systems are covered by B.S. 6351: 1983.

3.2 Methods of Surface Heating

3.2.1 Flexible surface heaters [30][31][32][33][34][35]

These include heating tapes of different design and mineral insulated heating cable. The construction and operation of these heaters is well documented in the manufacturers' literature and in the references quoted. Their maximum length is however limited and therefore for long pipelines multiple supplies are required. This disadvantage is overcome by the systems described in section 3.2.2.2 and 3.2.2.3.

3.2.2 Rigid Surface Heaters

3.2.2.1 Direct resistance pipe heating

Since process pipelines are made from steel, such pipelines can act as the heat tracer by passing a 50 Hz current through the pipe. The length of line which can be traced is limited by the permissible voltage drop across the pipeline, which for electrical safety reasons must not exceed 25 V. Thus for most applications multiple feeding must be considered, involving more than one transformer. Prior to the SECT system, (Fig. 3.2) and coaxial pipe heating system, (Fig. 3.6) this method of tracing was considered a possible alternative for medium length pipelines and a pilot study [36] showed a 10% saving in energy costs compared with those of conventional trace heating. A design procedure based on empirical equations has

been proposed by Thornton [17].

3.2.2.2 Saddle-tube (SECT) system [3][4][5]

This heating system makes it possible to heat electrically a pipeline extending up to 40 km from one power source. Details of the two types of the SECT system are shown in Fig. 3.2 and Fig. 3.3, but for pipe tracing only the series circuit is relevant. As can be seen from Fig 3.2, a mains frequency power source 1, is connected to the ends of two conductors, 2 and 4. The other end of conductor 2 is passed through the steel tube 3 (the heat tube) and is connected to one end 6 of the steel tube while the other end of conductor 4 is connected to the other end of the same tube. With the above connections, the alternating current flowing through the steel tube is concentrated along the inner skin of the tube wall due to the proximity effect and therefore there is no electrical potential drop on the outside surface of the steel tube. The heat tube is thus in effect electrically insulated from the transport pipe and therefore intrinsically safe. The mode of connection of the heat tube to the transport pipe and electrical supply is shown in Fig. 3.4 and other details in Fig. 3.5.

The bore of the heat tube varies from 10 mm to 50 mm and its wall thickness from 2.5 mm to 5 mm. The return inner conductor has a cross-section area in the range of 8-60 mm and is insulated with heat resistant polyvinyl, polyethelene, silicon rubber or teflon depending on the operating temperature.

With a supply voltage in the range 300-700 V/km and currents in the range 50-250 A, linear loadings from 15 to 150 W/m can be achieved. Up to about 20% of the linear loading is contributed by the inner conductor.

For pipelines up to 36 cm diameter, one heat tube is used and for larger size pipes the number of heat tubes is increased to improve the temperature distribution on the circumferential surface of the pipeline.

The heat tube is intermittently welded to the pipeline in order to reduce the thermal resistance between them. For this reason the temperature difference in the circumferential direction on the pipeline is in the region of 5-10 ^{o}C and therefore local hot spots cannot be produced.

In order to increase the length of heat tube supplied from a single transformer, the heat tube can be divided into two sections at a feed point which supplies nearly equal currents in each direction along the line (Fig. 3.4).

In order to keep the supply balanced, the transformer is connected in the Scott configuration or in the case of a single phase secondary, phase-balancing equipment is used.

The transport pipe is earthed to prevent static electricity and currents flowing due to induction effects from any nearby transmission lines.

The SECT system becomes economically attractive for pipelines exceeding a length of 1 km.

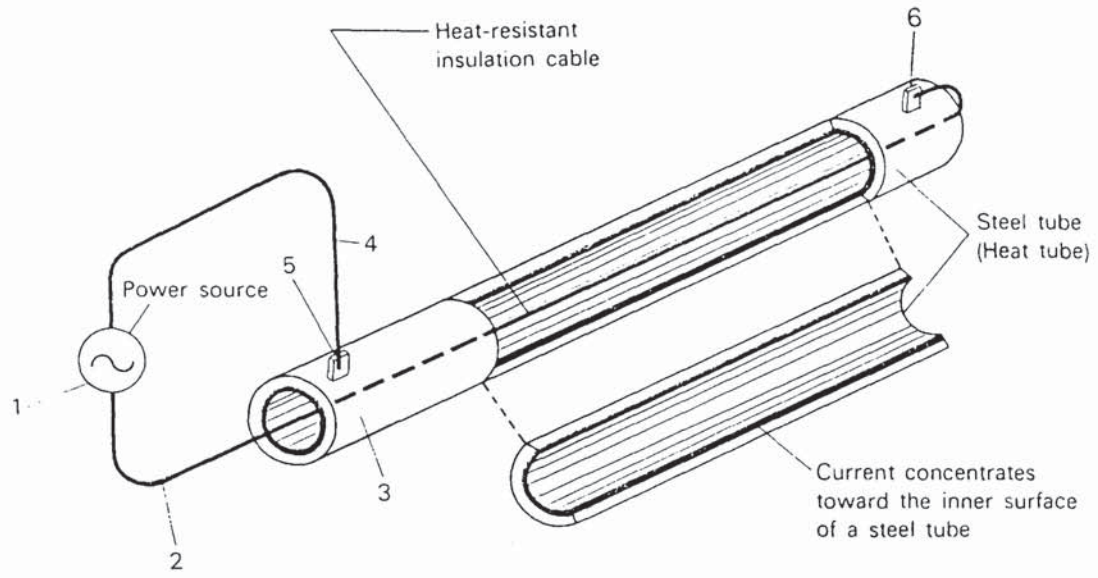

Fig. 3.2 SECT series circuit

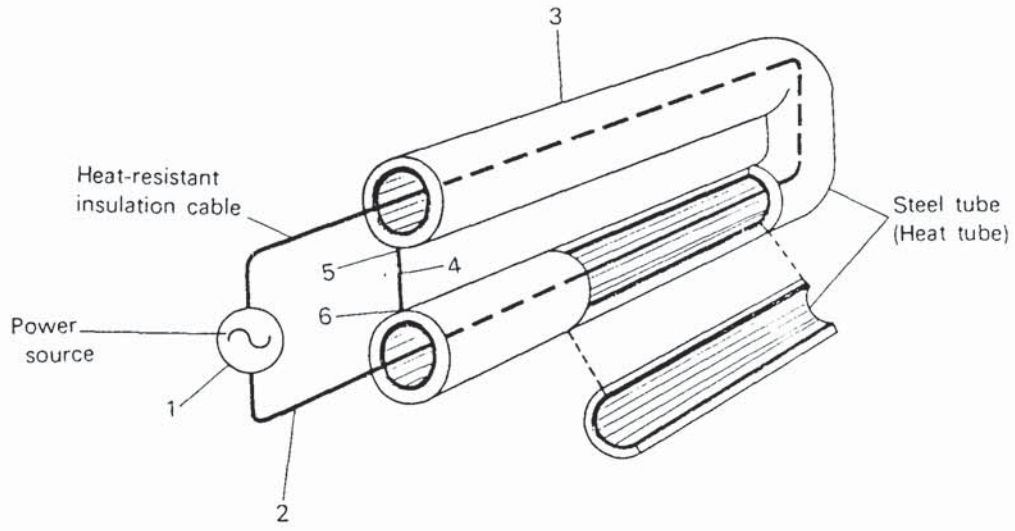

Fig. 3.3 Induction-type SECT circuit

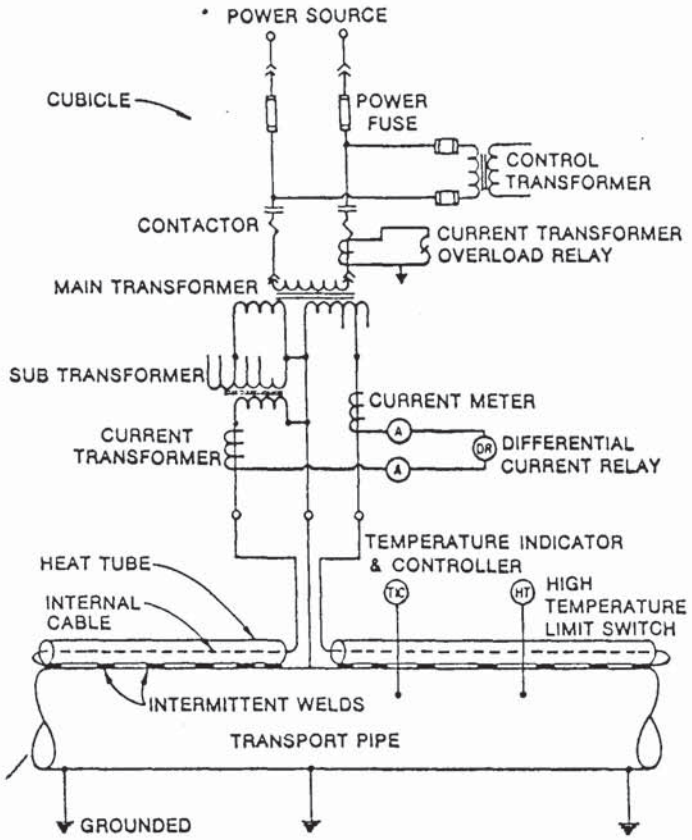

Fig. 3.4 Typical electric circuit of SECT

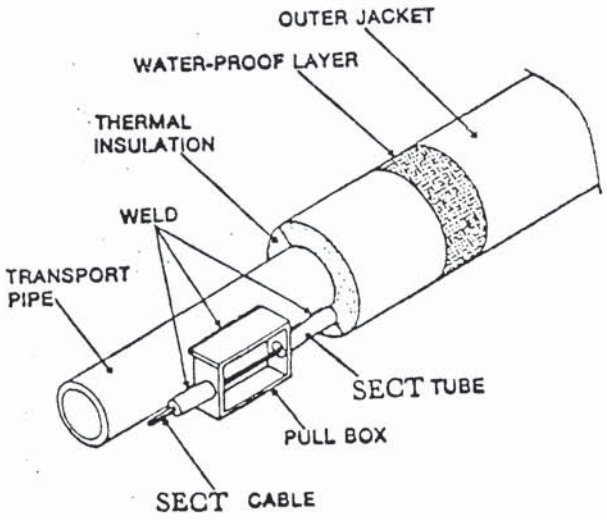

Fig. 3.5 General view of SECT pipe heating above ground

3.2.2.3 Coaxial pipe heating system [6]

Fig. 3.6 shows the basic principle. The heating mechanism is the same as the one described in Section 3.2.2.1 but it also incorporates the safety aspects of the SECT system since the external steel pipe ensures (provided it is sufficiently thick) that a small leakage current to earth exists.

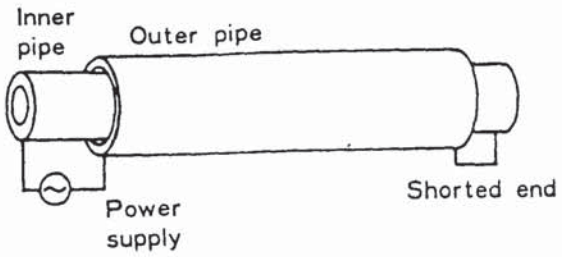

Fig.3.6 Principle of coaxial pipe electric heating system

CHAPTER 4

LINEAR SOLUTIONS

Chapter Summary

Rigorous and approximate formulae are presented for the impedance of an isolated solid or tubular conductor and for a single-phase concentric arrangement.

The limitations of the approximate formulae are specified and the relevance of the linear solutions to the non-linear problem outlined.

Equations are derived for computing the depth required for the full power to be developed for the case of an isolated conductor.

The error in applying the semi-infinite slab solution to the case of a finite diameter conductor is evaluated.

Dimensionless parameters are developed, which form the basis for the derivation of an effective permeability function in Chapter 6.

A numerical solution is presented for the isolated conductor and calculated results based on this solution are compared with values obtained from Arnold's equations.

CHAPTER 4

Chapter Contents PAGE

4. LINEAR SOLUTIONS

4.1 Rigorous Solutions

These solutions involve Bessel functions of the first and second kind, leading to rather complex formulae from which numerical answers can be obtained after lengthy calculations.

For historical interest, Kenelly, Laws and Pierce [37] give a comprehensive bibliography up to 1915. Dwight's work in this field dates back to 1918 with numerous papers added during subsequent years. More recently, Astbury [38] published formal linear solutions for the case of a copper conductor clad in a magnetic sheath and shows that his solution reduces to the case of the isolated tube when the inner layer of the composite conductor is removed. Formulae for the effective resistance and inductance of isolated solid and tubular non-magnetic conductors are also derived by McLachlan [39].

The concentric arrangement of conductors is treated by Dwight [40] and Arnold [41] and the eccentric by Tegopoulos and Kriezis [42]. Formulae for proximity effects due to the return conductor have been collated by Costello [43] and improved formulae have been developed by Arnold [44].

In this Chapter linear solutions are considered for the following reasons:-

1. The information is drawn from many sources and therefore, a collection of relevant formulae with consistent units and symbols is desirable.

2. One solution developed in the thesis, relevant to steel conductors operating under saturation conditions, is based on the linear solutions. It is therefore necessary to investigate these solutions in relation to the physical and electrical parameters applicable to the present investigation, so that the formulae most appropriate to given conditions may be selected.
3. Past workers have been concerned with minimising losses and therefore did not investigate the conditions for increased losses or fully explore available solutions.
4. An examination of the linear solutions for the case of a concentric arrangement of non-magnetic conductors, gives an indication of the expected behaviour of similarly arranged magnetic conductors.

Conductive heating is mainly determined by the effective resistance of the conductor, from which power loss can be calculated. Thus (for the purpose of predicting losses) the means of computing easily the effective resistance of various systems of conductors is required.

To this end computer programmes have been written specifically for the thesis.

4.1.1 Effective impedance of an isolated conductor

The reasons for considering the case of an isolated conductor are three-fold.

Firstly, satisfactory solutions for steel conductors of any diameter are not available and therefore a contribution can be made if a more accurate solution can be developed.

Secondly, independent experimental results on steel conductors have been reported in the literature, thus enabling the method of calculation developed in this thesis to be validated in the first instance.

Thirdly, a successful solution for the case of an isolated steel conductor based on a linear theory, leads to the solution of the single-phase concentric arrangement of steel tube and copper conductor which has not hitherto been investigated analytically or experimentally.

As a result of the non-uniform current density the resistance and internal inductance of a conductor may not be constant. Whilst the change in resistance can be considerable the change in inductance is generally small. These changes are a function of frequency, geometrical dimensions of the conductor and its electrical and magnetic properties.

In the following sections, constant resistivity and permeability are assumed. Thus, the equations apply equally to magnetic conductors above the Curie temperature.

Consider a long cylindrical tube of internal radius a and external radius b having a conductivity σ and permeability μ.

The conductor carries axially a sinusoidally alternating current

$$i = \hat{I}e^{j\omega t}$$

where ω is the angular frequency. The return conductor is at a large distance away from the conductor under consideration, to avoid proximity effects.

Neglecting displacement currents,

$$\text{curl } \bar{E} = \frac{-\partial \bar{B}}{\partial t} = -\mu \frac{\partial \bar{H}}{\partial t} \tag{4.1}$$

where $\mu = \mu_r \mu_o$ for a linear material

$$\bar{J} = \sigma \bar{E} \tag{4.2}$$

$$\text{curl } \bar{H} = \bar{J} \tag{4.3}$$

From (4.1) and (4.2) if we assume constant conductivity,

$$\text{curl } \bar{J} = \sigma \text{curl } \bar{E} = -\mu\sigma \frac{\partial \bar{H}}{\partial t} \tag{4.4}$$

$$\text{curl (curl } \bar{J}) = -\nabla^2 \bar{J} + \nabla(\nabla . \bar{J}) = -\mu\sigma \text{curl} \left(\frac{\partial \bar{H}}{\partial t} \right)$$

since div $\bar{J} = o$

$$\nabla^2 \bar{J} = \mu\sigma \frac{\partial \bar{J}}{\partial t} = j\mu\sigma\omega J$$

If we consider cylindrical polar coordinates r, θ, z, because of symmetry the current density varies in the r direction only.

Expanding $\nabla^2\bar{J}$

$$\frac{\partial^2 J}{\partial r^2} + \frac{1}{r}\frac{\partial J}{\partial r} = j\omega\mu\sigma J \tag{4.5}$$

where J is the z component of $\bar{J}$

setting $m^2 = \mu\omega\sigma$

the solution of equation (4.5) is

$$J_r = (A+jB)(\text{ber}mr+j\text{bei}mr)+(C+jD)(\text{ker}mr+j\text{kei}mr) \tag{4.6}$$

where A, B, C, D are constants to be evaluated from the boundary conditions

since at $r = a$ $\quad \frac{\partial J}{\partial r} = 0$, from (4.6)

$$\frac{C+jD}{A+jB} = \frac{-(\text{ber}'ma+j\text{bei}'ma)}{(\text{ker}'ma+j\text{kei}'ma)} \tag{4.7}$$

The total current is given by $I = \int_a^b 2\pi rJdr$ or

$$I = \frac{2\pi}{m}\left[(A+jB)r(\text{bei}'mr-j\text{ber}'mr) + (C+jD)r(\text{kei}'mr-j\text{ker}'mr)\right]_{r=a}^{r=b} \tag{4.8}$$

for r=a the term in the square brackets of equation (4.8) is zero, hence

$$I = \frac{2\pi b}{m}\left[(A+jB)(\text{bei}'mb-j\text{ber}'mb) + (C+jD)(\text{kei}'mb-j\text{ker}'mb)\right] \tag{4.9}$$

Let Z_{ac} be the effective impedance per metre length of the conductor due to its effective resistance R_{ac} and its inductance L_{ac} due to the flux linkages internal to the conductor

$$E = IZ_{ac} = \rho(J)_{r=b} \text{ or}$$

$$IZ_{ac} = \rho\left[(A+jB)(\text{ber}mb+j\text{bei}mb) + (C+jD)(\text{ker}mb+j\text{kei}mb)\right]$$

$$\text{with } R_{dc} = \frac{\rho}{\pi(b^2-a^2)}$$

$$\frac{Z_{ac}}{R_{dc}} = \frac{jm(b^2-a^2)}{2b} \left[\frac{(bermb+jbeimb) + \frac{C+jD}{A+jB}(kermb+jkeimb)}{(ber'mb+jbei'mb) + \frac{C+jD}{A+jB}(ker'mb+jkei'mb)} \right] \tag{4.10}$$

equation (4.10) is a complex quantity whose real part gives $\frac{R_{ac}}{R_{dc}}$ and the imaginary part $\frac{X_{ac}}{R_{dc}}$

since $mb = \frac{b\sqrt{2}}{\delta}$ where $\delta = \sqrt{\frac{2\rho}{\mu\omega}}$ is the classical skin depth, $\frac{R_{ac}}{R_{dc}}$ and $\frac{X_{ac}}{R_{dc}}$ can be calculated for different ratios of $\frac{b}{\delta}$.

For the case of the solid conductor $\frac{C+jD}{A+jB} = 0$ giving

$$\frac{Z_{ac}}{R_{dc}} = \frac{jmb}{2}\left[\frac{bermb+jbeimb}{ber'mb+jbei'mb}\right] = \frac{bm\sqrt{j}}{2}\,\frac{I_o(mb\sqrt{j})}{I_1(mb\sqrt{j})}$$

$$\text{with } mb = \frac{\sqrt{2}b}{\delta} = x$$

$$\frac{R_{ac}}{R_{dc}} = \frac{x}{2}\left[\frac{berxbei'x-beixber'x}{ber'^2x+bei'^2x}\right]$$

$$\text{and } \frac{X_{ac}}{R_{dc}} = \frac{x}{2}\left[\frac{berxber'x+beixbei'x}{ber'^2x+bei'^2x}\right]$$

For non-magnetic conductors, R_{ac} and X_{ac} are independent of the current and for a given diameter increase with a reduction in δ.

For a tube,

$$\bar{J} = E\, I_o(mrj^{\frac{1}{2}}) + F\, K_o(mrj^{\frac{1}{2}})$$

The constants E and F can be derived from the boundary conditions

$$J = J_s \text{ at } r=b$$

$$\text{and} \left(\frac{\partial J}{\partial r}\right)_{r=a} = 0$$

giving

$$\frac{Z_{ac}}{R_{dc}} = \frac{mj^{\frac{1}{2}}(b^2-a^2)}{2b} \left[\frac{I_o(mbj^{\frac{1}{2}})\ K_1(maj^{\frac{1}{2}}) + K_o(mbj^{\frac{1}{2}})\ I_1(maj^{\frac{1}{2}})}{I_1(mbj^{\frac{1}{2}})\ K_1(maj^{\frac{1}{2}}) - K_1(mbj^{\frac{1}{2}})\ I_1(maj^{\frac{1}{2}})} \right] \qquad (4.11)$$

from which $\frac{R_{ac}}{R_{dc}}$ and $\frac{X_{ac}}{R_{dc}}$ can be obtained by retaining the real and imaginary parts respectively of (4.11) which are expressed in terms of ber, bei, ker, kei and their derivatives, leading to very cumbersome expressions (see McLachlan [39])

4.1.2 Effective impedance of concentric conductors

For a concentric system of conductors, since the inner conductor is not affected by the field of the outer conductor, the equations of section 4.1 apply to the inner conductor. For the outer conductor, the equation for Zac/Rdc is the same equation (4.11) except that a and b are interchanged and the equation is multiplied by -1 giving

$$\frac{Z_{ac}}{R_{dc}} = \frac{m(b^2-a^2)j^{\frac{1}{2}}}{2a} \left[\frac{I_0(maj^{\frac{1}{2}})K_1(mbj^{\frac{1}{2}}) + K_0(maj^{\frac{1}{2}})I_1(mbj^{\frac{1}{2}})}{I_1(maj^{\frac{1}{2}})K_1(mbj^{\frac{1}{2}}) - K_1(maj^{\frac{1}{2}})I_1(mbj^{\frac{1}{2}})} \right] \qquad (4.12)$$

(If the current is defined as positive in the go conductor in the return it is negative. Hence the multiplying factor -1).

Owing to the presence of the inner conductor, the current is carried by the inner surface of the outer tube and the current

density attenuates outwards from the inner surface rather than inwards from the outer surface. Strictly speaking, this redistribution of current density is not a proximity effect, since the current density is uniform around the periphery of the tube and proximity effect implies a non-uniform current density distribution in the circumferential direction.

The outer conductor impedance is unaffected if the inner conductor is a solid or a tube. Provided the current density in the inner conductor of a circular cross-section is a function of the distance from its centre only, the current produced is the same if the whole disturbing current were concentrated at the centre of the conductor i.e. the inner conductor can be replaced for analytical purposes by a current filament. If the inner conductor is eccentric, then due to proximity effects, the finite radius of the inner conductor gives rise to results which differ from those obtained if a filamentary conductor is considered. Thus for experimental purposes, the radius of the inner conductor does not influence results provided eccentricity is avoided.

4.2 Limiting Solutions

4.2.1 Isolated conductors

Because of the complexity of the rigorous formulae, the limitation of published tables of Bessel and Kelvin functions and the slow convergence of these functions, approximate solutions were sought in the past for non-magnetic conductors. The origin of these solutions is difficult to trace, but Dwight [40] has published limiting formulae for low and high frequencies. For the case of low frequencies ($mt<4$), the formula for the resistance ratio of a tube of wall thickness t, consists of a ratio of infinite series of complex numbers whose coefficients are themselves infinite series. For the present purpose this alternative does not offer any advantage over the rigorous formula except that it avoids computing the Bessel and Kelvin functions. It is not considered therefore further and it is sufficient to mention that Dwight [40] has presented the results in this range in a set of graphs.

For the case of a solid conductor, by expanding the Bessel functions in series and keeping the first two terms, at low frequencies ($b < \delta$)

$$R_{ac}/R_{dc} = 1 + \frac{1}{48} \cdot \left(\frac{b}{\delta} \right)^4$$

and

$$X_{ac}/R_{dc} = \frac{1}{4} \left(\frac{b}{\delta} \right)^2 \cdot \left[1 - \frac{1}{96} \cdot \left(\frac{b}{\delta} \right)^4 \right]$$

At high frequencies (this condition is satisfied if $b/\delta > 7$ [45]) for a solid conductor by using the asymptotic representation of the Bessel functions

$$R_{ac}/R_{dc} = mb/_{2\sqrt{2}} + \frac{1}{4} \qquad (4.13)$$

This is the equation of the straight line which is the asymptote of the curve of Rac/Rdc plotted against mb.

The corresponding

$$X_{ac}/R_{dc} = mb/_{2\sqrt{2}} \qquad (4.14)$$

For a tube Dwight [46] gives the equation

$$R_{ac}/R_{dc} = \frac{t(b+a)}{b^2}\left\{ mb/_{2\sqrt{2}} + \frac{1}{4} + \frac{3}{16mb\sqrt{2}} + \ldots\ldots + \right.$$

$$e^{-mt\sqrt{2}}\cos mt\sqrt{2}\left[mb/_{\sqrt{2}} - \frac{3}{4}\,t/_{a} + \frac{3}{32mb\sqrt{2}}\,(7-6b/_{a} + 3b^2/_{a^2})\ldots\right]$$

$$+ e^{-mt\sqrt{2}}\sin mt\sqrt{2}\left[mb/_{\sqrt{2}} - \frac{3}{32mb\sqrt{2}}\,(7-6b/_{a} + 3b^2/_{a^2})\ldots\right]$$

$$\left. + \text{terms in } e^{-2mt\sqrt{2}} \right\} \qquad (4.15)$$

The first two terms of the first line of equation (4.15) is equation (4.13) if the terms in $e^{-mt\sqrt{2}}$ and $e^{-2mt\sqrt{2}}$ are negligible.

Two further formulae are available for the isolated tube at high frequencies. The first is derived on the basis that the

alternating current penetrates at uniform current density to a depth equal to the classical skin depth δ and the a.c. resistance is taken to be equal to the d.c. resistance of a tube consisting of the surface layer of metal of thickness δ . The resulting formula is

$$R_{ac}/R_{dc} = \frac{mt(b+a)}{2b\sqrt{2}\ (1-1/mb\sqrt{2})} \qquad (4.16)$$

which is valid if $\delta/t < 0.3$.

The second formula is obtained by using the asymptotic form of the function [39] yielding

$$R_{ac}/R_{dc} = \frac{m(b^2-a^2)}{2^{3/2}\pi b}\left[\frac{\sinh x + \sin x}{\cosh x - \cos x}\right] \qquad (4.17)$$

For large values of x' [$= mt\sqrt{2}$] equations (4.15) and (4.17) give the same numerical answers.

4.2.2 Single-phase concentric conductors

The equations corresponding to (4.15) and (4.16) are

$$R_{ac}/R_{dc} = \frac{t(b+a)}{a^2}\left\{ ma/2\sqrt{2} - \frac{1}{4} + \frac{3}{16ma\sqrt{2}} + \ldots + \right.$$

$$\left. e^{-mt\sqrt{2}}\cos mt\sqrt{2}\left[ma/\sqrt{2} - \frac{3}{4}\frac{t}{b} + \frac{3}{32ma\sqrt{2}}\left(7-6\frac{a}{b}+3\frac{a^2}{b^2}\right) + \ldots \right] + \right.$$

$$e^{-mt\sqrt{2}}\sin mt\sqrt{2}\left[ma/\sqrt{2} - \frac{3}{32ma\sqrt{2}}\left(7-6\frac{a}{b} + 3\frac{a^2}{b^2}\right) - \ldots\right]$$

$$+ \text{terms in } e^{-2mt\sqrt{2}}\Bigg\} \tag{4.18}$$

and

$$Rac/_{Rdc} = \frac{mt(b+a)}{2\sqrt{2}\,a\left(1 + \frac{1}{ma\sqrt{2}}\right)} \tag{4.19}$$

4.3 Arnold's Approximate Solutions

For the case of isolated and concentric tubular conductors, the approximate formulae of section 4.2 can be used for low and high frequencies. For the intermediate range of frequencies, the rigorous formulae must be used in the absence of an alternative.

Arnold [41] used Dwight's [46] series solutions for the isolated tube to obtain simplified formulae, for values of frequency from zero, to a value beyond which displacement currents cannot be neglected.

He shows that to the first order of β

$$K = 1 + \alpha(z)(1-\beta/2) \qquad (4.20)$$

[Arnold uses $z = 8\pi^2 t^2 f\sigma$ and $\beta = 2t/d_o$ as the two independent variables (in this thesis $z = 2\pi f t^2 \mu\sigma$)]

For a given conductor size and material, z is proportional to the frequency. The range of frequency may be divided into three parts:

Low frequencies corresponding to values of z from 0 to 5, intermediate frequencies corresponding to a value of z from 5 to 25, and high frequencies corresponding to values of z above 25.

In equation (4.20) $\alpha(z)$ is given by

$$0<z<5 \qquad \alpha(z) = \frac{7z^2}{315 + 3z^2} \qquad (4.21)$$

$$z > 30 \qquad \alpha(z) = \sqrt{\frac{z}{2}} - 1 \tag{4.22}$$

Equation (4.20) has an error of less than 1% for all values of β up to 0.2.

Equations (4.21) and (4.22) are not sufficiently accurate for the range $30 < z < 5$ and $\alpha(z)$ is calculated from an infinite series and given in Table 4.1.

By the addition of a term in β^2 in equation (4.20), the maximum error between K and the value obtained from the formal solution occurs when z = 15 and is 0.6% when β is between 0.7 and 0.8.

The improved equation for K is

$$K = 1 + \alpha(z)\left[\, 1 - \beta/_2 - \beta^2 b(z)\right] \tag{4.23}$$

The term in β^2 is chosen so as to make equation (4.23) to agree with the formal solution for the case of the solid conductor. The values of b(z) are given by

$$z < 5 \qquad b(z) = \frac{56}{211 + z^2}$$

$$z > 30 \qquad b(z) = \frac{2}{4\sqrt{2z} - 5}$$

for $30 < z < 5$ values for b(z) are given in Table 4.1.

Arnold tested his formulae for the intermediate range of frequencies and the discrepancy between experimental results and the values given by his formulae were less than 3%. He did not present his results in graphical form and all his measurements were carried out on copper conductors.

At this stage an idea of typical values of z obtained at 50 Hz is instructive. Considering a 4 mm wall thickness,

Table 4.1. Values Of $\alpha(z)$ And $b(z)$ In The Range $5<z<30$

z	$\alpha(z)$	b(z)
5	0.450	0.24
5.5	0.524	
6.	0.599	0.23
6.5	0.675	
7	0.751	0.22
7.5	0.825	
8	0.898	0.21
8.5	0.970	
9	1.040	0.19
9.5	1.108	
10	1.174	0.18
10.5	1.238	
11	1.301	0.17
11.5	1.361	
12	1.420	0.16
12.5	1.477	
13	1.532	0.15
13.5	1.585	
14	1.637	0.14
14.5	1.688	
15	1.737	0.14
15.5	1.786	
16	1.833	0.13
16.5	1.878	
17	1.923	
18	2.010	0.12
19	2.094	
20	2.174	0.11
21	2.252	
22	2.327	0.1
23	2.401	
24	2.473	0.09
25	2.544	
26	2.613	0.09
27	2.680	
28	2.747	0.08
29	2.812	
30	2.876	0.08

(Ref.41)

one made of copper with $\sigma = 0.58 \times 10^8 (S\ m^{-1})$ and one of steel with $\sigma = 0.526 \times 10^7 (S\ m^{-1})$, the z values are

copper $z = 0.367$

steel $z = 13.2$

assuming a relative permeability of 400.

Thus z values in the range $30<z<5$ are obtainable with solid large diameter copper conductors or at high frequencies with thin copper tubes. For steel tubes and for the range of tube wall thickness and currents of interest in the present investigation, the value of z in the range of 5 to 30 is probable and $z>30$ possible for low H and high σ.

For the case of single-phase concentric conductors, for the outer conductor, Arnold gives the equation

$$K_o' = 1 + \alpha(z_o)(1 + \beta_o/_2) \qquad (4.24)$$

Since terms in β^2_o are not included in equation (4.24) it has an inherent error. Arnold did not develop the terms in β_o^2 on the argument that β_o for the outer conductor is likely to be small.

Arnold made measurements on concentric copper tubes with values of β_o up to 0.2141 and he shows that the discrepancy between the theoretical formulae and the experimental results can be considered to be within the limits of experimental error, estimated at 2%.

If the case of a thick-wall outer conductor is to be investigated β_o is not small. In order to assess the error involved by neglecting the term in β^2_o, from equation (4.12)

the value of K_o' can be calculated and then compared with equation (4.24) and the other appropriate approximate formulae.

For this exercise it is convenient to use arguments of Bessel functions which are available in published tables and do not require interpolation.

Example 1

With $\sigma = 0.57 \times 10^8 (S\ m^{-1})$, f = 294 Hz, m = 367.4, ma = 3.7 and mb = 9 from which b = 2.449 and a = 1.007 cm giving a wall thickness of 1.442 cm and $\beta_o = \frac{1.442}{2.449} = 0.5858$ and $z = m^2 t^2 = 28.06$

The following values of K_o' are obtained by the different formulae:

Rigorous formula, equation (4.12)	5.38
High frequency formula, equation (4.18)	5.385
Penetration formula, equation (4.19)	5.398
Arnold's formula, equation (4.24)	4.566

Error in using Arnold's formula = 15%.

To examine the effect of the value of β_o on the resulting error in calculating K_o' the following example can be considered:

Example 2

With b = 5.32 cm, a = 3.193 cm, $\sigma = 4.771 \times 10^7 S\ m^{-1}$, t = 2.127 cm

f = 60 Hz, $\beta_o = 0.4$, mt = 3.2, z = 10.22

Rigorous formula	2.55
High frequency formula	2.55

Penetration formula	2.63
Arnold's formula	2.444

In this example the penetration formula does not give the correct answer because $\delta/_t > 0.3$.

The error using Arnold's formula in this example is 4.1%. Thus for values of β_o larger than 0.3, neglecting the β^2_o term in equation (4.24) results in an error which increases with the value of β_o. Rather than develop terms in β^2_o to add to equation (4.24), in the case of concentric conductors with $\beta_o > 0.3$ equation (4.18) can be used and for $\beta_o < 0.3$ equation (4.24). This last statement needs to be qualified.

For a solid isolated conductor, it was stated that the condition for the high frequency formula to apply was

$$b/_\delta > 7$$

For a tube a limit for mt must also be specified. The criteria $b/_\delta > 7$ does not necessarily apply because of the current density redistribution. The limiting values of $b/_\delta$ and mt, cannot be readily obtained from the relevant equations, but certain conclusions can be drawn from the two examples for which the high frequency formula is known to give correct results.

For Ex. 1 $b/_\delta = 6.29$, $\delta/_t = 0.27$ and $z = 28$

For Ex. 2 $b/_\delta = 5.6$, $\delta/_t = 5.6$ and $z = 10.2$

Ex. 2 gives the more pessimistic limits and therefore $z>9$ and $b/\delta < 5$ can be specified as the approximate conditions for the high frequency formula to apply to the case of the concentric conductors.

The ratio b/δ specifies the depth of penetration as a fraction of the radius of curvature. The radius of curvature applicable in the case of the concentric arrangement is smaller and therefore the ratio of b/δ for which the high frequency formula applies is smaller than in the case of the solid conductor.

For the case of isolated conductors, Arnold's equations give numerical answers in close agreement with the rigorous formula over the complete range of β and f and therefore are adopted subsequently for the computation of losses in steel conductors. Arnold has not published formulae for the calculation of inductance. Formulae could be developed in a manner similar to the case of effective resistance. This is unnecessary since the values of inductance or power factor are not important quantities in conductive surface heating using the concentric configuration. For non-magnetic isolated conductors the numerical solution of Sect. (4.10.1) gives accurate results for resistance, inductance and power factor. For the concentric arrangement, only the rigorous formulae are available and the effort involved in obtaining values of power factor is not justifiable. Since the resistance is increased by the presence of the return inner conductor and the inductance is further

decreased the concentric arrangement has an inherently higher power factor and in practical heating systems using this configuration, measured power factors in excess of 0.9 are quoted.

Figures 4.1 and 4.2 have been produced on the basis of Arnold's equations.

4.4 Magnetic field within a conductor

The depth of penetration of the magnetic field in a conductor is a function of b/δ. At a given frequency, the field decays more rapidly with depth the larger the value of b/δ.

If the field within a tube reduces to zero at a distance less than t, the tube cannot be distinguished from a solid conductor of equal external diameter.

A method of calculating directly the required tube wall thickness for complete penetration is developed in section 4.5. If the field at any depth can be calculated as a fraction of the field at the surface, the depth on which the field reduces to zero can also be established.

An expression for the magnetic field within a conductor will now be developed.

$$\text{from curl } \bar{J} = \frac{-\partial J}{\partial r} \tag{4.25}$$

and from equation (4.4)

$$-\mu\sigma \frac{\partial H}{\partial t} = \frac{-\partial J}{\partial r}$$

with $H = \hat{H} e^{j\omega t}$,

$$-j\mu\omega\sigma H = \frac{-\partial J}{\partial r} \text{ or}$$

$$H = \frac{1}{jm^2} \frac{\partial J}{\partial r} \tag{4.26}$$

at $r = b$ $J = J_s$ the surface current density,

hence from (4.6)

$$J_s = (A+jB)(bermb+jbeimb) + (C+jD)(kermb+jkeimb) \tag{4.27}$$

with

$$bermb + jbeimb = e$$

$$kermb + jkeimb = f$$

$$ber'ma + jbei'ma = c$$

$$ker'ma + jkei'ma = d$$

$$ber'mb + jbei'mb = g$$

$$ker'mb + jkei'mb = h$$

from (4.27)
$$\frac{C+jD}{A+jB} = \frac{-c}{d} \tag{4.28}$$

substituting (4.28) in (4.27)

$$A+jB = \frac{J_s d}{ed-fc} \tag{4.29}$$

hence from (4.28)

$$C+jD = \frac{-J_s c}{ed-fc} \tag{4.30}$$

substituting (4.29) and (4.30) into (4.6)

$$J_r = \frac{J_s}{ed-fc}\left[d(bermr+jbeimr) - c(kermr+jkeimr)\right] \tag{4.31}$$

for a solid cylinder $\frac{c}{d} = 0$ hence

$$\frac{J_r}{J_s} = \frac{bermr+jbeimr}{bermb+jbeimb}$$

from (4.26) and (4.31)

$$H_r = \frac{1}{jm^2}\ \frac{J_s m}{(ed-fc)}\ \left[d(ber'mr+jbei'mr) - c(ker'mr+jkeimr)\right] \tag{4.32}$$

substituting (4.29) and (4.30) in (4.9)

$$H_r = \frac{I}{2\pi b}\left[\frac{d(ber'mr+jbei'mr) - c(ker'mr+jkei'mr)}{dg-ch}\right]$$

since $\frac{I}{2\pi b} = H_s$ the surface magnetic field strength,

$$\frac{H_r}{H_s} = \frac{d(ber'mr+jbei'mr) - c(ker'mr+jkei'mr)}{dg-ch} \tag{4.33}$$

The unexpanded form of equation (4.33) is

$$\frac{H_r}{H_s} = \frac{I_1(mrj^{\frac{1}{2}})\ K_1(maj^{\frac{1}{2}}) - I_1(maj^{\frac{1}{2}})\ K_1(mrj^{\frac{1}{2}})}{K_1(maj^{\frac{1}{2}})\ I_1(mbj^{\frac{1}{2}}) - I_1(maj^{\frac{1}{2}})\ K_1(mbj^{\frac{1}{2}})} \tag{4.34}$$

For a solid

$$\frac{H_r}{H_s} = \frac{ber'mr+jbei'mr}{ber'mb+jbei'mb}$$

or

$$\left|\frac{H_r}{H_s}\right| = \sqrt{\left(\frac{ber'^2mr+bei'^2mr}{ber'^2mb+bei'^2mb}\right)} \tag{4.35}$$

For values of $mr > 25$ equation (4.35) reduces with an accuracy of 1% to

$$\frac{H_r}{H_s} = \sqrt{\frac{b}{b-y}}\ e^{-my/\sqrt{2}}\ e^{-jmy/\sqrt{2}} \tag{4.36}$$

where y is the depth into the conductor from the surface. As b increases $\sqrt{\frac{b}{b-y}}$ tends to 1 and equation (4.36) becomes that of the semiinfinite slab. Thus for large radii or high frequency, the effect of curvature can be neglected.

4.4.1 Penetration of magnetic field within a conductor

Examination of equation (4.35) shows that it also gives the current density distribution into an inductively heated cylinder. Thus the graphs included in Davies and Simpson [19] for the ratio $|J_r/J_s|$ give the ratio $|H_r/H_s|$ of equation (4.35). These graphs show that equation (4.36) is valid for $b/\delta > 6$ and the field attenuates to zero at a distance given by $y/\delta \simeq 5$ when $b/\delta > 6$.

An equation equivalent to (4.34) can be developed for the case of the outer tube of the concentric arrangement from which $|H_r/H_s|$ can be calculated.

Since numerical values cannot be obtained easily, the equation has not been derived. However, for a given current the surface field strength for the outer tube is larger than if it was supplied in isolation. It can be argued therefore that the field will reduce to the same value at a greater depth i.e. the depth for complete penetration is also greater.

4.5 Tube Wall Thickness for Complete Field Penetration

In Section 4.3 it was seen that for values of z in the range of 5 to 30, $\alpha(z)$ and $b(z)$ are calculated by reference to Table 4.1. For the purpose of computing the effective resistance this does not present any difficulty since the series used by Arnold to calculate $\alpha(z)$ and $b(z)$ can be incorporated in the computer programme. For the purpose of calculating the wall thickness, a functional representation of $\alpha(z)$ and $b(z)$ is required. A plot of $\alpha(z)$ and $b(z)$ versus z shows that the curves can be linearised over three ranges of z. Using least squares, the following equations are obtained over the three ranges of z

$5<z<13.5$

$$\alpha(z) = 0.135(z) - 0.194$$
$$b(z) = -0.0117(z) + 0.299 \qquad (4.37)$$

$13.5<z<23$

$$\alpha(z) = 0.085(z) + 0.47$$
$$b(z) = -0.00526(z) + 0.215 \qquad (4.38)$$

$23<z<30$

$$\alpha(z) = 0.067(z) + 0.215$$
$$b(z) = -0.002(z) + 0.137 \qquad (4.39)$$

The loss in accuracy in calculating the power using the above functions is small.

Consider a tube of wall thickness t and external diameter d_o. Beyond a certain value of thickness t_s, the loss calculated for the tube will be equal to the loss calculated for a solid

bar of equal diameter d_o . This condition corresponds to the value of β in Fig. 4.5, when R_{ac} approaches a constant value. This value of β is not clearly defined on the graph.

An increase in wall thickness beyond t_s does not increase the loss and therefore it can be concluded, that the current density and therefore H, below a depth t_s, tends to zero.

Equations will now be developed from which t_s can be calculated.

Consider first the case of $13.5<z<23$

$$Rac/_{Rdc} = 1 + \alpha(z)\ [1 - \beta/_2 - \beta^2 b(z)]$$

For the same current external diameter and frequency, the power is the solid and the tube will be equal if

$$1 + (\sqrt{\frac{z'}{2}} - 1)(0.5 - \frac{2}{8\sqrt{\frac{z'}{2}} - 5}) = [1 + (0.0085(z) + 0.47)(1 - 0.5\beta)]\frac{1}{1 - (d_i/d_o)^2}$$

where d_i is the internal diameter of the tube.

For the tube the term in b(z) has been neglected since $\beta \ll 1$

since $t = \beta d_o/_2$ and $1 - (d_i/d_o)^2 = 2\beta - \beta^2$

with $z' = C'' d_o/_2$ and $z = C' d_o^2 \beta^2/_4$

where $C' = 2\pi f \mu_o \mu_r \sigma$ and $C'' = \sqrt{C'/_2}$

equation (4.36) results in a cubic equation in β given by

$$\left[-\frac{C'' d_o + 4C''^2 d_o^2 - 2}{4\ (4C'' d_o - 5)}\right][2\beta - \beta^2] - 1.47 - 2.125 \times 10^{-2} C' d_o \beta^2 + \qquad (4.40)$$

$$1.06 \times 10^{-2} C' d_o \beta^3 + 0.235\ \beta = 0$$

For the case z>30

$$1 + (\sqrt{z'/_2} - 1)(0.5 - \frac{2}{8\sqrt{z'/_2 - 5}}) = (\sqrt{z/_2} - \sqrt{z/_2}\ \beta/_2 + \beta/_2)\frac{1}{(2\beta - \beta^2)}$$

from which

$$\beta = \frac{3}{2C'd_o - 1} \qquad (4.41)$$

With steel conductors the penetration depth is small and the condition z>30 is not likely to arise.

Since the depth of penetration is proportional to $\frac{1}{\sqrt{f}}$, t_s is also proportional to $\frac{1}{\sqrt{f}}$.

If the curvature of the conductor is neglected i.e. equation (4.36) applies,

$$P_y/_P = e^{-2y/\delta}$$

and therefore negligible loss occurs beyond 2 δ so that

$$t_s \cong 2.5\delta$$

This is not the case under non-linear conditions (see Sections 6.7 and 7.9.3).

4.6 Calculation of Loss Based on the Semi-Infinite Slab Solution

The results of research on losses in thick steel plates, due to a sinusoidal applied magnetic field parallel to the surface of the plate, can be applied to large diameter bars.

In Section 4.4.1 "large" diameter was interpreted as $b/\delta > 6$ and this limit was established by reference to Davies and Simpson's graph (Fig. 12.9, Ref. 19). Referring to the graph, they state that the current density distribution for a cylinder closely approximates to the simple exponential fall-off if $b/\delta > 6$.

In order to test the above criterion for the calculation of power, the case of a steel bar can be considered of resistivity 19×10^{-8} (Ω m) and a surface magnetic field strength of 15,000 (A m^{-1}) peak. For a magnetic linear solution, the value of μ is obtained from the assumed static B/H curve and a value of 100 is representative. At 50 Hz, δ = 3.09 mm and the loss density calculated on the basis of the semi-infinite slab solution is 6915 (W m^{-2}).

For a bar of diameter 5.85 cm, the surface field strength of 15,000 (A m^{-1}) can be obtained by a current of 1949 A. The calculated power loss based on magnetic linear theory is 7487 (W m^{-2}) resulting in an error of 8.2%.

Since for the case above b/δ = 9.63, it appears that the criterion $b/\delta > 6$ is not sufficiently precise for the range of diameters and currents of interest to conductive heating.

A method will now be developed for calculating the bar

diameter for the loss by the semi-infinite slab solution to apply to any desired degree of accuracy.

For $z>30$ and $\beta = 1$, from equation (4.23) and the corresponding values of $\alpha(z)$ and $b(z)$,

$$K = 1 + (\sqrt{\frac{z}{2}} - 1)[0.5 - \frac{2}{(4\sqrt{2z} - 5)}] \tag{4.42}$$

If P_s is the power loss per unit surface area or loss density,

$$P_s = 4\rho H_s^2 K/d \tag{4.43}$$

from (4.42) and (4.43)

$$P_s = \frac{4\rho H_s^2}{d} 0.5\sqrt{\frac{z}{2}} + \frac{4\rho H_s^2}{d} [0.5 - \frac{2}{(4\sqrt{2z} - 5)} (\sqrt{\frac{z}{2}} - 1)] \tag{4.44}$$

since $\sqrt{z} = \frac{d}{2}\sqrt{\frac{\mu w}{\rho}}$ and the loss density for the slab is given by

$$P_s = H_s^2 \sqrt{\mu w \rho}/\sqrt{2} \tag{4.45}$$

the first term of equation, (4.44) reduces to (4.45). The second term therefore represents the error in using equation (4.45) to calculate the loss of a finite diameter bar. Obviously this is zero if d is ∞. For any other diameter, the per unit error will be

$$\frac{4\rho H_s^2}{d} [0.5 - \frac{2}{(4\sqrt{2z} - 5)} (\sqrt{\frac{z}{2}} - 1) \frac{\sqrt{2}}{H_s^2\sqrt{\mu w \sigma}}] \tag{4.46}$$

For a per unit error of 0.04, the equation for d from (4.46) is

$$d^2 - \frac{37d}{\sqrt{\mu w \sigma}} + \frac{25}{\mu w \sigma} = 0 \qquad (4.47)$$

$\frac{37d}{\sqrt{\mu w \sigma}}$ is larger than $\frac{25}{\mu w \sigma}$ by two orders of magnitude and little accuracy is therefore lost by neglecting the last term of equation (4.47) or

$$d = \frac{37}{\sqrt{\mu w \sigma}} \qquad (4.48)$$

For the example considered $\sqrt{\mu w \sigma}$ = 457 and from (4.48)

$$d = 8 \text{ cm}$$

giving a ratio of $b/_{\delta} = 12.9$. For a bar of diameter 8 cm and $\hat{H}$=15,000 ($A\ m^{-1}$) the calculated loss density is 7194 $W\ m^{-2}$ and therefore the error is 4% as specified.

The condition $b/_{\delta} > 6$ gives a diameter of 3.6 cm, which will obviously give an error in excess of 10%.

Since the minimum value of diameter d depends on $\sqrt{\mu w \sigma}$, its value for steel is current dependent. The most pessimistic value of diameter is obtained at the highest working current. Bowden and Davies [14] have used McLachlan's comparison of the solution of the diffusion equation in rectangular and cylindrical co-ordinates, for different values of $b/_{\delta}$, to justify the size of diameter used in their experimental work and in support of their one-dimensional non-linear theory.

The present simple alternative method gives similar results.

In equation (4.45) for magnetically linear steel, if we

assume as previously that μ_r is given by $C\hat{H}_s^{-0.89}$

where C is a constant,

for a slab,

$$P_s = H_s^{1.55}/\sqrt{2}\sqrt{C\mu_0\omega\rho}$$

Thus, for a slab a log/log plot of P_s versus H_s should have a slope of 1.55 or a similar plot for a bar having the same slope indicates that the bar is indistinguishable from a slab.

The 50 Hz loss density has been calculated for various diameters for a conductivity of 0.7×10^7 (S m^{-1}) and the results have been plotted in Fig. 4.3.

The loss calculated for the 8 cm and 10 cm bar is within 2.6% of the loss calculated on the basis of the slab solution and as expected the slope is approximately 1.55.

As the diameter decreases equation (4.45) is no longer applicable and the exponent of H_s varies between 1.55 and 2 depending on the diameter and the value of H .

For Fig. 4.3 plot (b) the slope is 1.65 and changes to almost 2 at a value of H_s approximately equal to 6600 (A m^{-1}). For values of H_s greater than 6600, the loss density under a.c. and d.c. conditions is the same. This happens as a result of the depth of penetration increasing as H_s increases causing the skin effect to become negligible.

For the 0.3 cm diameter bar Fig. 4.3 plot (c) $\delta >> b$ and therefore the d.c. and effective resistances are equal giving a loss which varies as H_s^2 (for H_s = 1000 Rac is slightly greater

than Rdc).

Two important observations have been made which have not been fully appreciated by previous researchers, namely the dependence of the exponent of Hs on the diameter of the bar and on the level of saturation.

The calculated values of loss density do not give experimentally verifiable results since the losses have been calculated on the basis of a linear theory. Nevertheless, the observations made above regarding cylindricity and saturation effects are valid under non-linear conditions considered in a subsequent section.

It is now possible to specify the conditions under which a tube appears as a solid bar and a bar as a semi-infinite slab. Loose statements made in the literature have also been quantified.

4.7 Computed Results

A number of results have been calculated on the basis of equations presented in this Chapter. The calculated results shown in graphical form in Figs. 4.1 - 4.10 have been produced for the purpose of observing the effect of varying the independent variables and are not meant to be used as a means of obtaining numerical answers. The significance of these results to the non-linear problem under investigation is discussed in Section 4.8.

4.7.1 Discussion of computed results

Fig. 4.4 shows the effect of varying the frequency for constant values of β for a copper tube of external diameter 2.54 cm. The case of the solid conductor is that of $\beta = 1$. Since the outer diameter is constant and $z \propto f$ for constant β, the graph of $K \sim f$ is of the same form as the graph of $K \sim z$. Since z is dimensionless, Fig. 4.1 applies to variable conductivity, wall thickness and frequency.

Fig. 4.5 shows the effect of varying β at constant f. It can be observed that for a particular value of β, the tube appears electrically as a solid. For given conditions, this value of β was calculated in Section 4.5 and is a function of frequency, conductivity and conductor diameter.

Fig. 4.6 has been produced to show the increase in Rac as a result of the presence of the return inner conductor. For

$\beta > 0.3$, $mt < 3$ and $b/\delta < 5$ there is an error in establishing Rac. These are the conditions under which the high frequency and Arnold's formulae do not apply. This problem does not arise with steel conductors even at power frequencies and therefore no effort has been made to calculate the values of Rac from the rigorous formula which is the only one giving correct results. In order to avoid these errors, the effect on Rac of varying the external diameter of the tube has been investigated for the case of f = 1000 Hz where the calculated values of Rac are correct for all values of β .

Fig. 4.7 shows the value of Rac for different external diameters. It can be observed that the larger the diameter, the smaller the value of β at which the tube appears as solid and the smaller the value of β for which the presence of the inner return conductor increases Rac.

The percentage increase in Rac due to the return conductor, as a function of the external diameter, for different values of β , is shown in Fig. 4.8. The increase in Rac levels off as the external diameter increases. It appears that, depending on the value of β , little can be gained, if one is seeking to increase the percentage loss, by increasing d_o beyond 4 cm.

The increase in Rac due to the inner conductor, for d_o = 2.54 cm variable and as a function of f is shown in Fig. 4.9. For f = 150 Hz, the values of Rac are underestimated because Arnold's equations give slightly low values under these conditions. The same comment applies to the value of Rac corresponding to β = 0.4 and f = 300 Hz.

Fig. 4.10 has been produced to show the difference in behaviour between keeping the internal rather than the external diameter constant and varying β at constant f. The smaller the internal diameter, the higher is the value of β before there is an increase in Rac due to the return conductor.

Tegopoulos and Kriezis graphs (Fig. 4 of Ref. 42) show this behaviour and the effect of eccentricity on the loss, which increases by as much as 50%, for a ratio of $s/a = 0.8$. For heating applications eccentricity is therefore desirable.

4.8 Relevance of Linear Solutions to the Non-linear Problem

In solving the non-linear problem under investigation the results of the previous section can provide some guidance as to the expected behaviour with steel conductors. For the time being any discussion as to the value to be assigned to the relative permeability for a given conductor current will be deferred and it will be assumed that a value can be determined which correctly predicts the conductor losses.

For a constant current, μ_r is constant and since the parameter z is dimensionless, a given value of z can be obtained by varying any of the constituent variables. Thus for steel and with constant σ and t, a given value of z can be obtained, by increasing f, or decreasing I. Thus the characteristics in Fig. 4.1 are universal. The characteristics in Fig. 4.5 show that for a constant β and frequency, in the case of a steel conductor as the current decreases the effective resistance increases. Fig. 4.6 shows that for constant tube dimensions and frequency, as a result of the presence of the inner conductor the effective resistance increases with a reduction in current, but at a rate which is a function of β . For maximum heating effect, the maximum resistance presented to a given current is required. However, for a given diameter the wall thickness is limited by the space required to accommodate the return conductor.

In Chapter 6 a method will be developed for determining the value of μ_{reff} for different currents and samples.

4.9 Dimensional Analysis

Dimensional analysis is based on the requirement for homogeneous equations to have consistent dimensions, which means that the variables on either side of an equation must have the same dimensions. The requirement for homogeneity is therefore fulfilled, if each term of an equation is dimensionless.

In searching for functional relations in a process represented by the general type of equation $x = F(z,y)$, or in processing experimental data, it is useful, not only to fulfil the requirement of homogeneity but also to provide guidance in determining the functional relation, by combining the variables into dimensionless groups. For this purpose, Buckingham's Pi Theorem gives the minimum number of significant dimensionless groups of the variables involved in any problem. Thus, if n is the number of variables, m the number of primary dimensions and π the number of dimensionless parameters, then, the minimum number of π , is (n-m). πi can be expressed as a function of the other π'_s i.e.

$$\pi_1 = F\ (\pi_2, \pi_3, \pi_4 \ldots . \pi_n\ )$$

There are two advantages in using dimensional analysis. Firstly, the number of experiments required to establish the relationship between the variables is considerably reduced since a number of variables are grouped together. Secondly, it may be possible to carry out the experimental work on a scaled model in terms of the variables grouped in a dimensionless parameter.

4.9.1 Application of dimensional analysis to conductive heating

Assuming that hysteresis loss is negligible, the power loss per unit length P, can be expressed as a function of the variables

$$f,\ H_s,\ t,\ \sigma,\ \mu,\ d_o$$

Since the number of primary constants M (mass), L (length), T (time) and I (current) is four, the number of π factors being sought is three.

The dimensions of the seven variables are listed in Table 4.2.

Table 4.2 Dimensions of Variables

Variable	Dimensions
$t,\ d_o$	$[L]$
H_s	$[L^{-1}I]$
P	$[L^2MT^{-3}]$
f	$[T^{-1}]$
σ	$[L^{-3}M^{-1}T^3I^2]$
μ	$[LMT^{-2}I^{-2}]$

The three π factors are given by

$$\pi_1 = t^{x_1} H_s^{y_1} p^{z_1} f^{v_1}$$

$$\pi_2 = t^{x_2} H_s^{y_2} p^{z_2} f^{v_2} \mu$$

$$\pi_3 = t^{x_3} H_s^{y_3} p^{z_3} f^{v_3} d_o$$

Since each π factor is dimensionless, the indices x_n, y_n ...etc. can be determined by substituting first, for each variable in the π factors its dimensions from Table 4.2 and then equate the indices for each dimension to zero. The resulting factors are

$$\pi_1 = P\sigma / H_s^2 t$$

$$\pi_2 = H_s^2 t^3 f\mu / p$$

$$\pi_3 = d_o / t$$

It is desirable to express the loss in terms of two independent dimensionless parameters and therefore π_2 is unsuitable. However, the product of π_1 and $\pi_2 = \pi_4$ is another dimensionless parameter, $f\sigma\mu t^2$. Hence

$$\pi_1 = F(\pi_3, \pi_4)$$

or

$$P\sigma / H_s^2 t = F(d_o / t, f\sigma\mu t^2)$$

Since 2 and 2π are dimensionless, the above parameters can be written in the alternative form

$$P\sigma / H_s^2 t = F(2t / d_o, 2\pi f\sigma\mu t^2)$$

and the dimensionless parameters β and z in Arnold's equations

can be identified. This functional relation applies equally to solid or tubular conductors. A plot of $P\sigma/_{H_s^2 t}$ versus z for constant values of β will show the effect on losses of all the variables.

However, it must be borne in mind that in conductive heating, Hs and do are not independent but are related through the conductor current. In addition to constant β, constant d_o must therefore be specified for a functional relation between $P\sigma/_{H_s^2 t}$ and z to apply.

Since

$$P\sigma/_{H_s^2 t} = KR_{dc}\pi^2 d_o^2 \sigma/_t$$

for a given β and d_o, the shape of the graphs of $P\sigma/_{H_s^2 t}$ versus z is the same as the K ~ z graphs.

In the absence of an analytical solution for the calculation of conductor losses, experimental results can be used to establish the set of graphs, relating the three dimensionless groups, from which functional relations can be defined by curve fitting techniques. Since for linear conditions well tested analytical solutions are available, the need to obtain the relation between the dimensionless groups empirically, does not arise. However, in seeking non-linear solutions for steel conductors it will be shown (Chapter 6) that consideration of dimensionless analysis in conjunction with experimental results and a linear analysis, leads to a satisfactory semi-empirical solution.

4.9.2 Alternative dimensionless parameters

Lim and Hammond [9] in calculating eddy current losses in

thick steel plates, of half thickness d, used the dimensionless parameters

$$\sigma f B_s d^2/\xi, \quad H/\xi, \quad P_s \sigma d/H^2$$

where in this case P_s is the power per unit surface area and ξ is the ratio of a_1/b_1 in the Frohlich equation $B = \dfrac{\hat{H}}{a_1 + b_1 \hat{H}}$

Since $a_1 \simeq \frac{1}{\mu}$ and $b_1 \simeq \frac{1}{B_s}$, the parameter $\sigma f B_s d^2/\xi$ reduces to

$$z \times \text{constant}.$$

Since ξ and Bs have no significance with non-magnetic materials and μ in z reflects the shape of the B-H curves, the parameters developed in the previous section describe fully the conductive heating problem. In dealing with magnetic materials, there is some advantage in adopting the parameters $\sigma f B_s t^2/\xi$ H/ξ, and β. A discussion is deferred to when steel conductors are considered.

4.10 Numerical Solutions

Analytical solutions have the advantage that the influence of various parameters on the dependent variables can be readily evaluated. These solutions are limited however to homogeneous media and to simple geometric boundaries.

For certain problems, where for example the resistivity and permeability of each segment of a heated bar vary considerably during the heating cycle, or for non-linearities relating to magnetic materials, numerical solutions are the only methods available.

To do justice to numerical techniques within the bounds of a section, or even a chapter, is impossible particularly since numerical techniques are continually evaluated and improved. No attempt therefore is made to review numerical techniques. The books by Stoll [45] and by Silvester [48] offer a good introduction on the application of numerical techniques to the solution of electromagnetic problems.

In spite of the ever increasing number of papers published on numerical solutions, the particular problems of conductive heating has received little attention. Silvester's [49][50][51] method for calculating the a.c. resistance and reactance offers the advantage that it can deal with complicated conductor profiles, but has only been applied to non-magnetic conductors. Lim and Hammond's [52] numerical solution and numerous attempts by others involving finite element or finite difference techniques refer to inductively heated steel plates and

therefore are irrelevant to the present investigation.

The only papers which deal with conductive heating of steel bars are those by Burke and Lavers [15] and by Lavers [53]. Burke and Lavers numerical model is slightly different from Lavers, but since it is based on Lavers technique it is not considered.

4.10.1 Laver's numerical technique

Fig. 4.11 shows a section of a tube of internal radius a and external radius b, divided into N equal annular rings of width Δr.

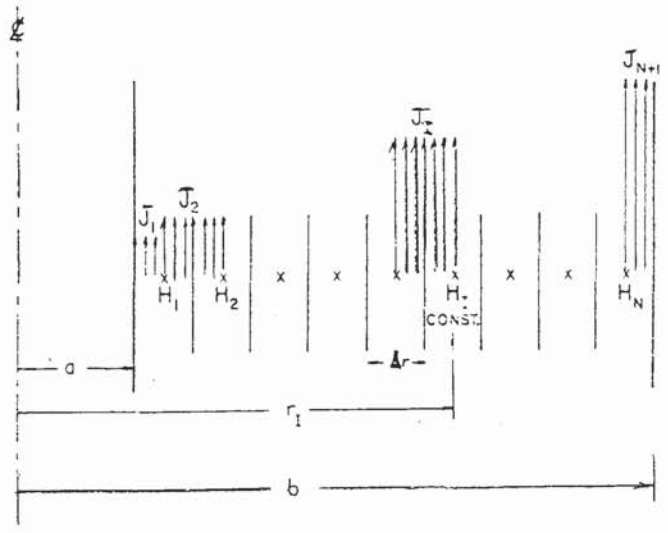

Fig. 4.11 Subdivision of Tube for Numerical Solution [53]

If Δr is sufficiently small,

J_I is constant in the region $r_I - \Delta r \leq r \leq r_I$

and H is constant in the region $r_I - \frac{\Delta r}{2} \leq r \leq r_I + \frac{\Delta r}{2}$

A value is assumed for J_1 in order to start the solution.

The total current flowing in the ring $a \leq r \leq r_1$ is

$$I_1 = \pi \Delta r J_1 \left(a + \frac{\Delta r}{4}\right)$$

The magnetic field H_1 at r_1 is

$$H_1 = \frac{I_1}{2\pi r_1}$$

H_1 is now known so μ_1 can be calculated from the B/H curve and the solution advanced.

Since $$\frac{\partial}{\partial r}(\rho J) = j\omega\mu H$$

$$\rho_1 (J_2 - J_1) = j\omega\mu_1 H_1 \Delta r$$

or $$J_2 = J_1 + j\frac{\omega}{\rho_1}\mu_1 \Delta r H_1 \qquad (4.49)$$

after I - 1 steps in the solution J_I is known.

For the Ith step,

$$r_I = r_{I-1} + \Delta r$$

$$I_I = \pi J_I \Delta r (2r_I - \Delta r)$$

and $$H_s = \frac{1}{2\pi r_I} \sum_{i=1}^{I} I_i$$

from (4.49)

$$J_{I+1} = J_I + j\frac{\mu_I}{\rho_I}\omega \Delta r H_I$$

when J_{N+1} is known.

$$I_{N+1} = \pi J_{N+1} \Delta r \left(r_N + \frac{\Delta r}{4}\right)$$

and the total current I is given by

$$I_T = \sum_{i=1}^{N+1} I_i$$

No information is given by Laver as to the method of computing the various quantities of interest. However he includes in his paper a programme for the HP25 for the case of a non-magnetic solid cylinder. Although the steps are tabled, the programme cannot be easily interpreted. A programme in BASIC for the SHARP personal computer has been written instead, for use with the present investigation.

At the end of the programme execution the following quantities are displayed: current, surface current density, surface magnetic field strength, Rac, Xac, K, p.f. and power density.

For non-magnetic conductors the results are obtained in one pass. Two current densities are assumed which give an improved current density resulting in the equalisation of the impressed current and the sum of the individual rings.

For magnetic conductors an iterative process is required but the current density J_1 converges to the value which gives the supplied current after a few iterations.

One hundred steps proved to give sufficiently accurate results. For magnetic conductors, in order to make the results more accurate as an alternative to a very large number of steps or grading, it was found that the iteration could start with the inner ring at about 3 skin depths, from the surface of the conductor. This is justified by the knowledge that there is no

appreciable field below this depth.

Table 4.3 compares the results obtained using Arnold's equation and the numerical method of this section. They are in complete agreement to three significant figures. The case of steel conductors is considered in a later section.

Table 4.3. Calculated Values of Effective Resistance by Two Methods

External Radius cm	Internal Radius cm	Numerical Method 100 Steps		Arnold's Equation
		$R_{ac} \times 10^{-3}\ \Omega \cdot m^{-1}$	Power Factor	$R_{ac} \times 10^{-3}\ \Omega \cdot m^{-1}$
1.27	1.14	0.177	0.972	0.177
↓	1.08	0.129	0.903	0.129
	1.02	0.11	0.815	0.11
	0.89	0.105	0.724	0.105
	0.76	0.111	0.729	0.111
	0.64	0.112	0.737	0.112
	0.51	↓	0.739	↓
	0.25		0.738	
	0		0.738	

Copper tube of external diameter 2.54 cm and variable β
Resistivity $1.72 \times 10^{-8}\ \Omega \cdot m$
Frequency 1000 Hz

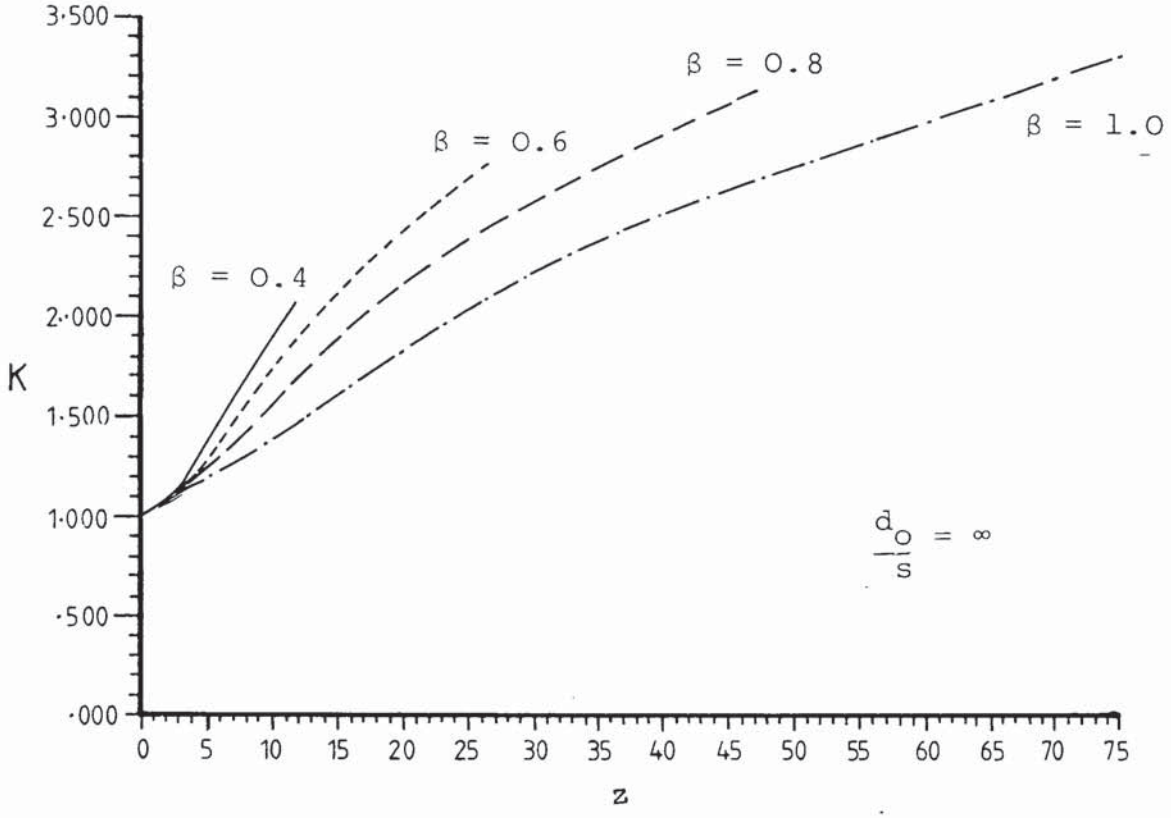

Fig. 4.1 Resistance ratio of isolated non-magnetic conductors as a function of z

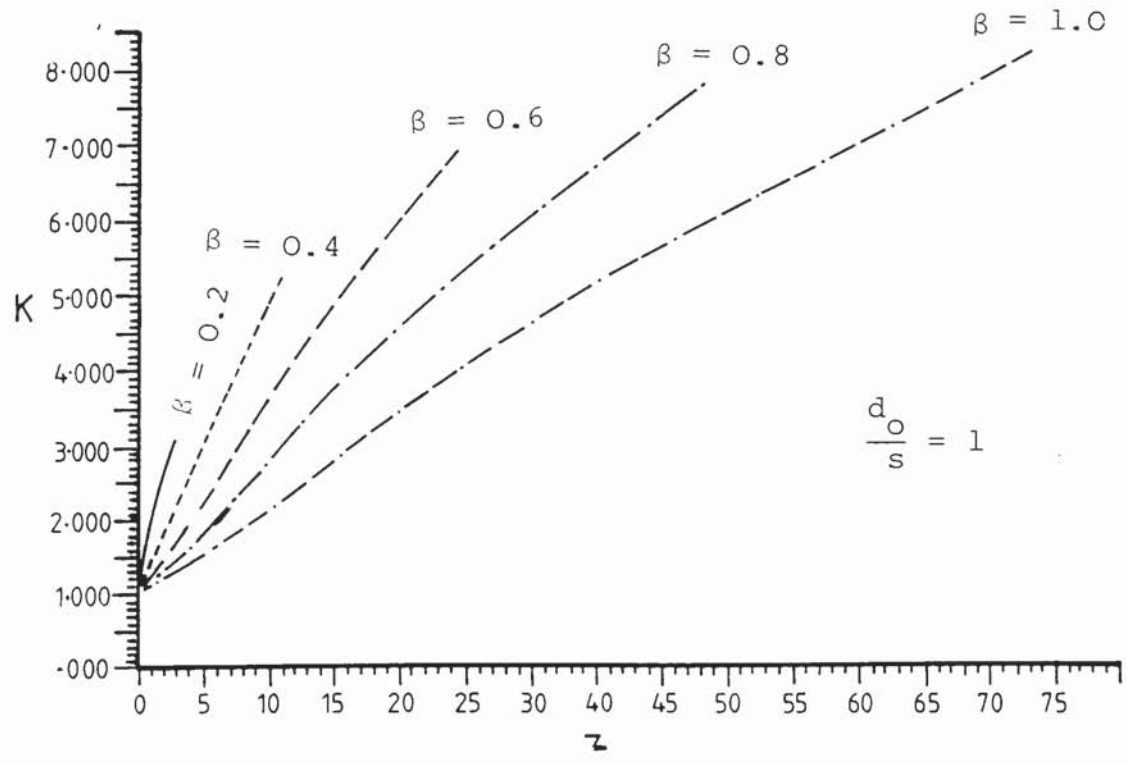

Fig 4 2 Proximity effect of non-magnetic conductors

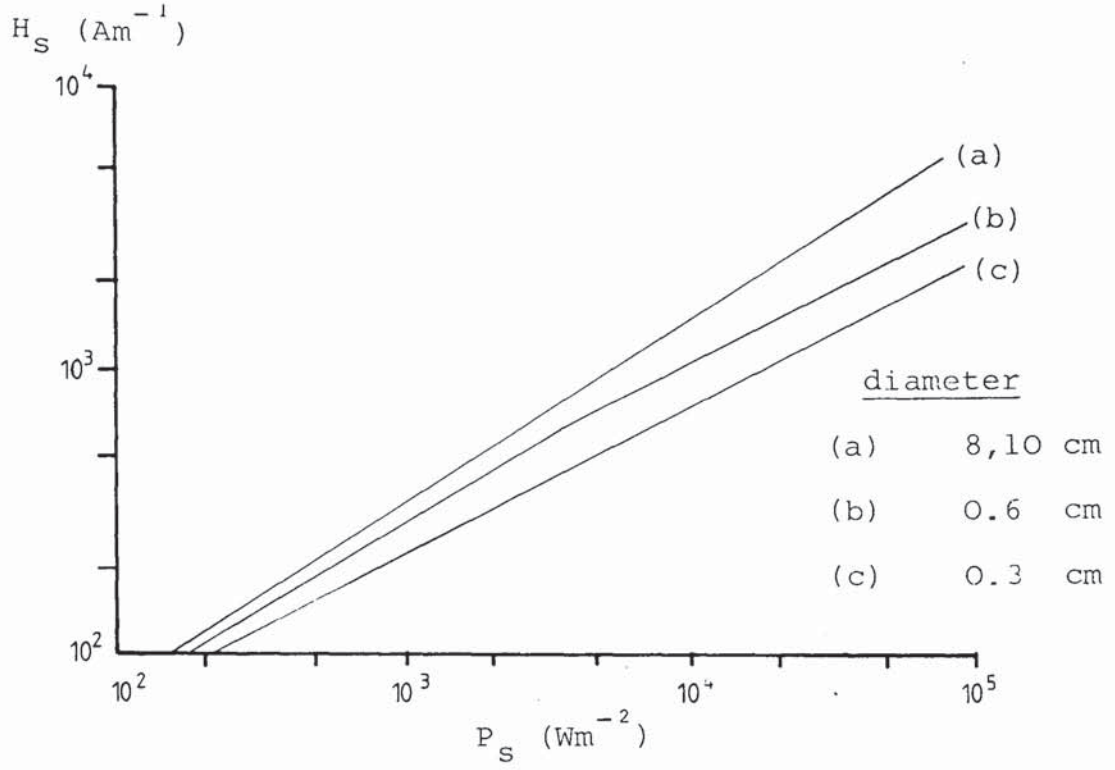

Fig. 4.3 Calculated surface power densities for magnetic - linear steel as a function of surface field strength

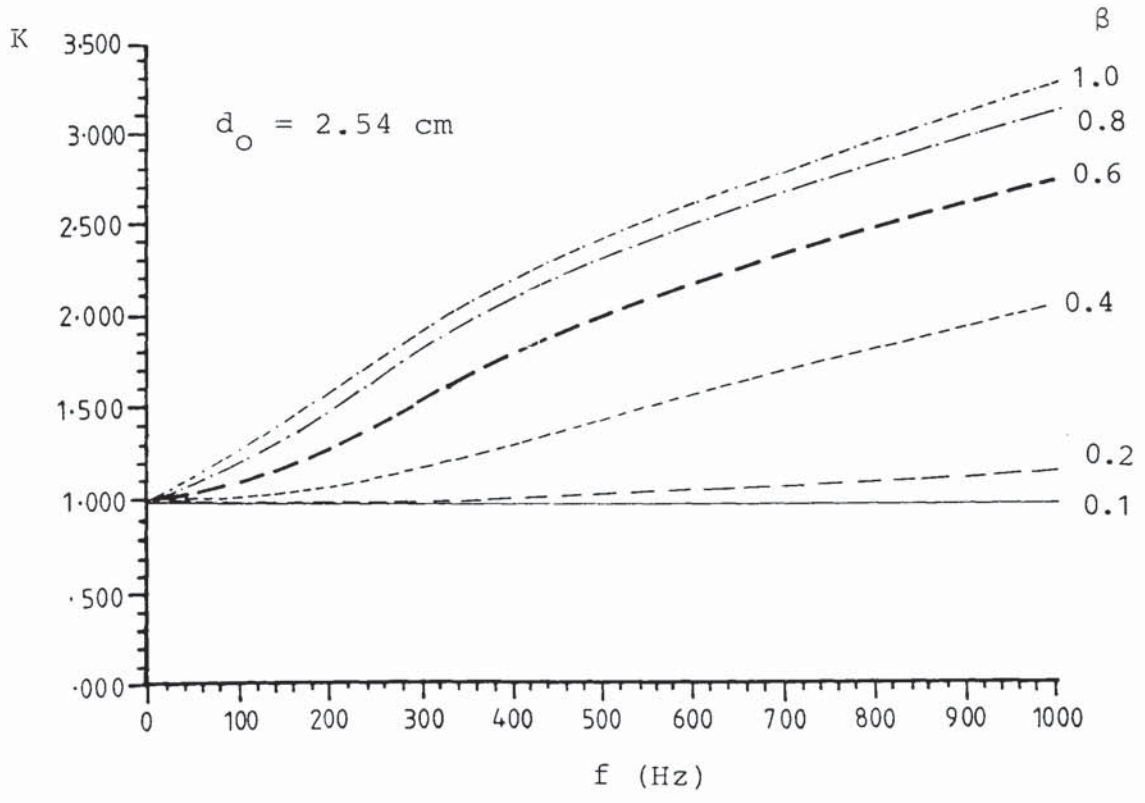

Fig. 4.4 Resistance ratio of isolated copper conductors as a function of frequency

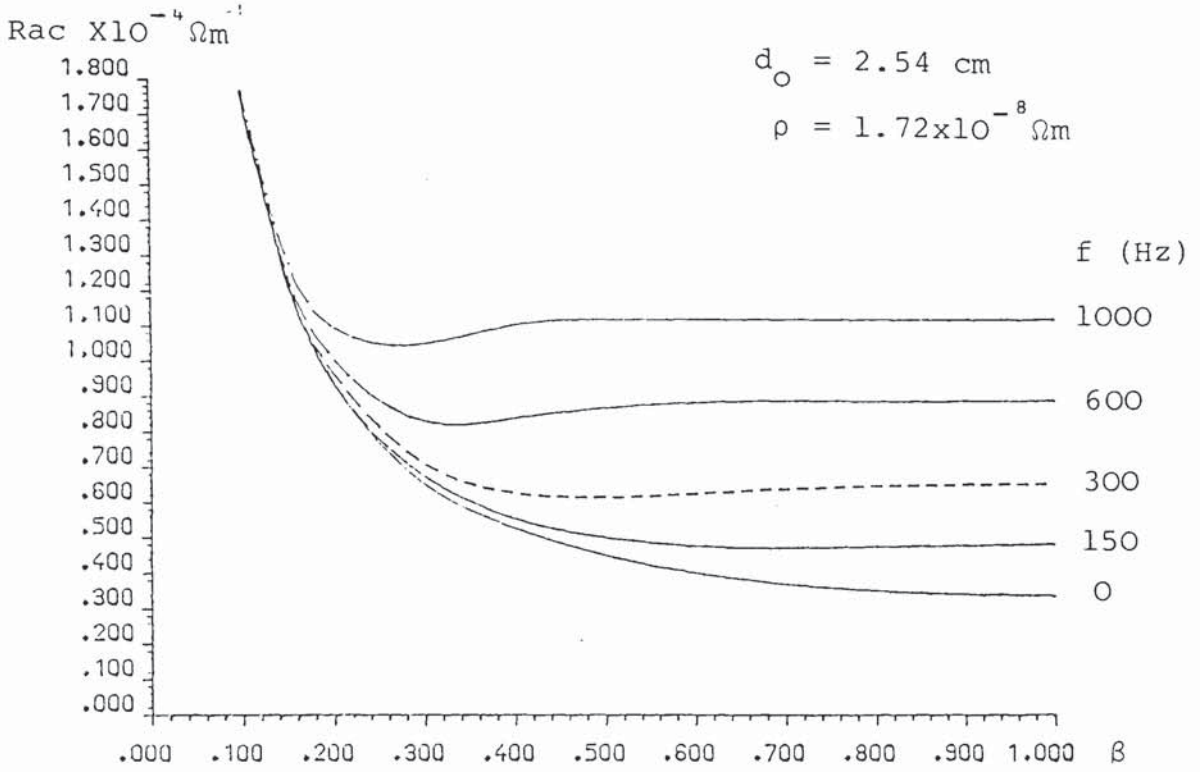

Fig. 4.5 Effective resistance of isolated copper conductors as a function of β

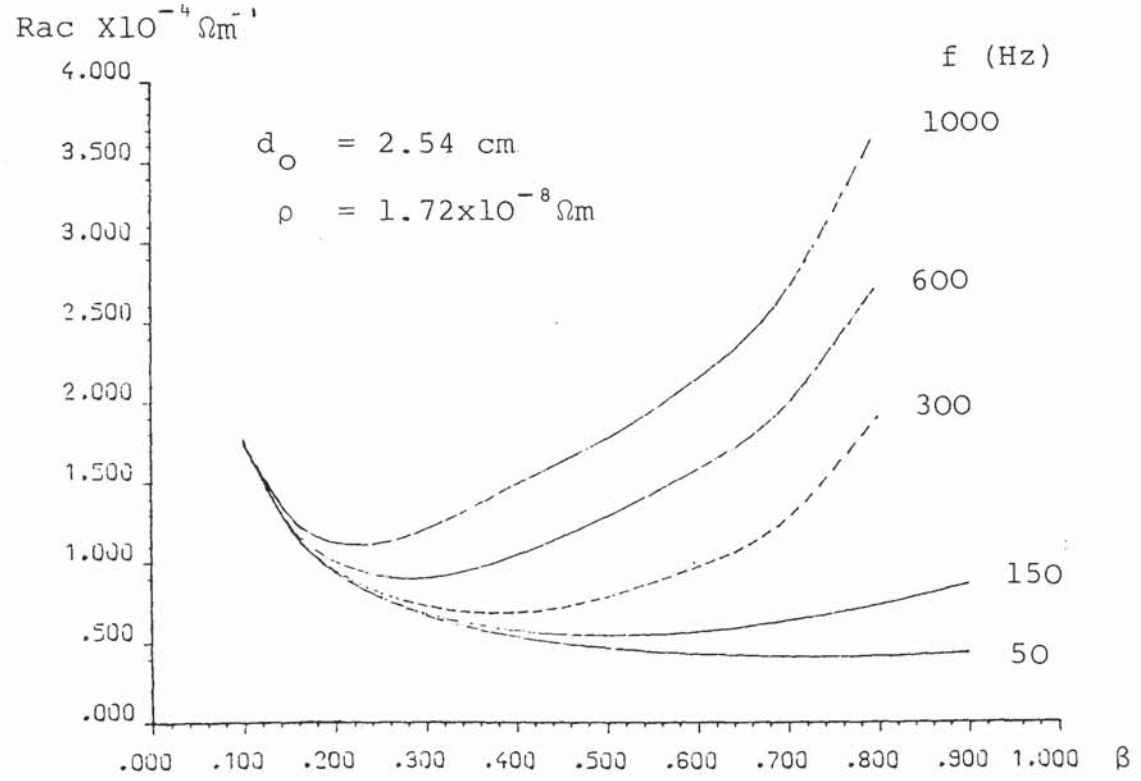

Fig. 4.6 Effective resistance of outer copper tube in concentric arrangement

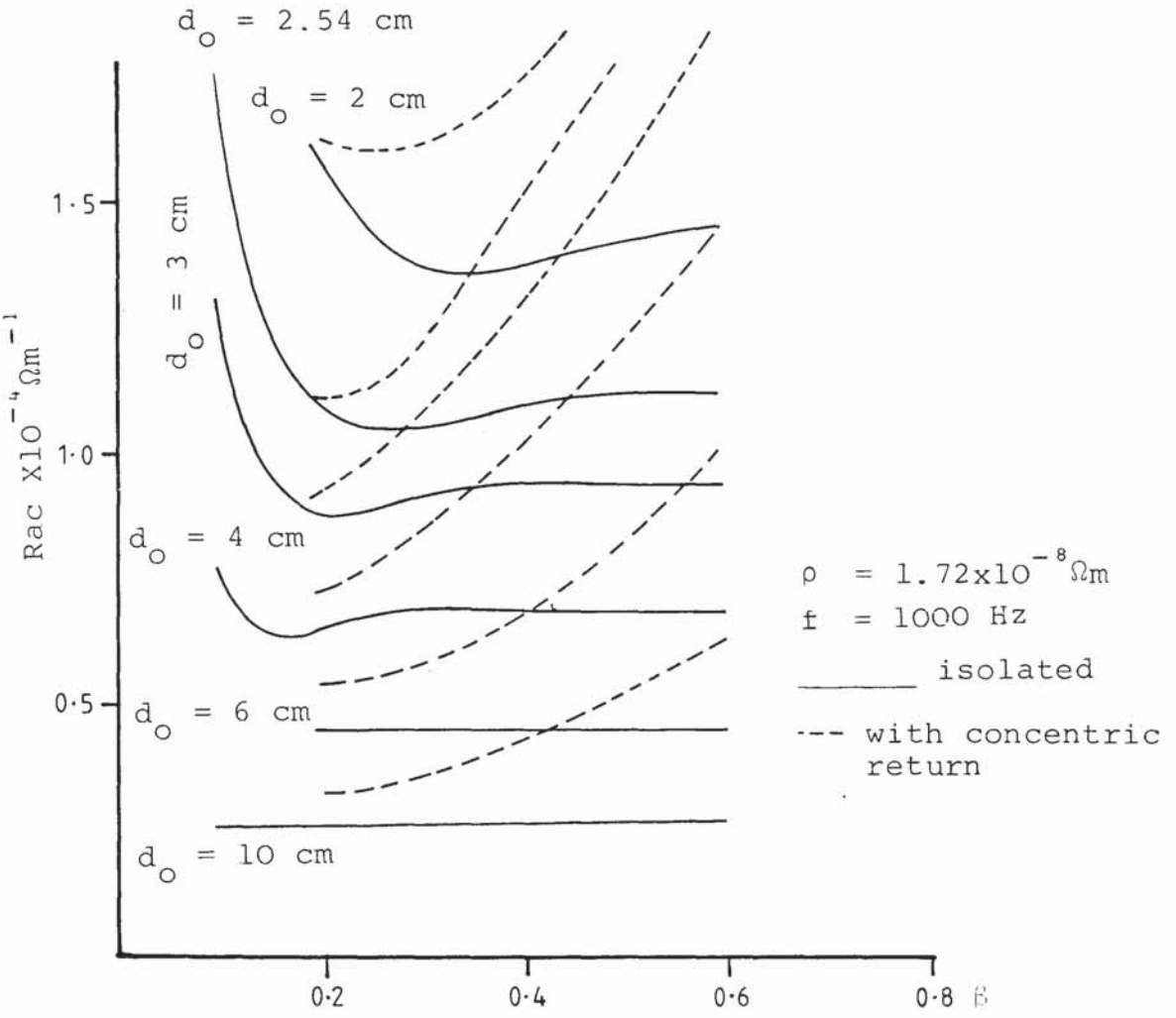

Fig. 4.7 Effect of external diameter on calculated effective resistances as a function of β

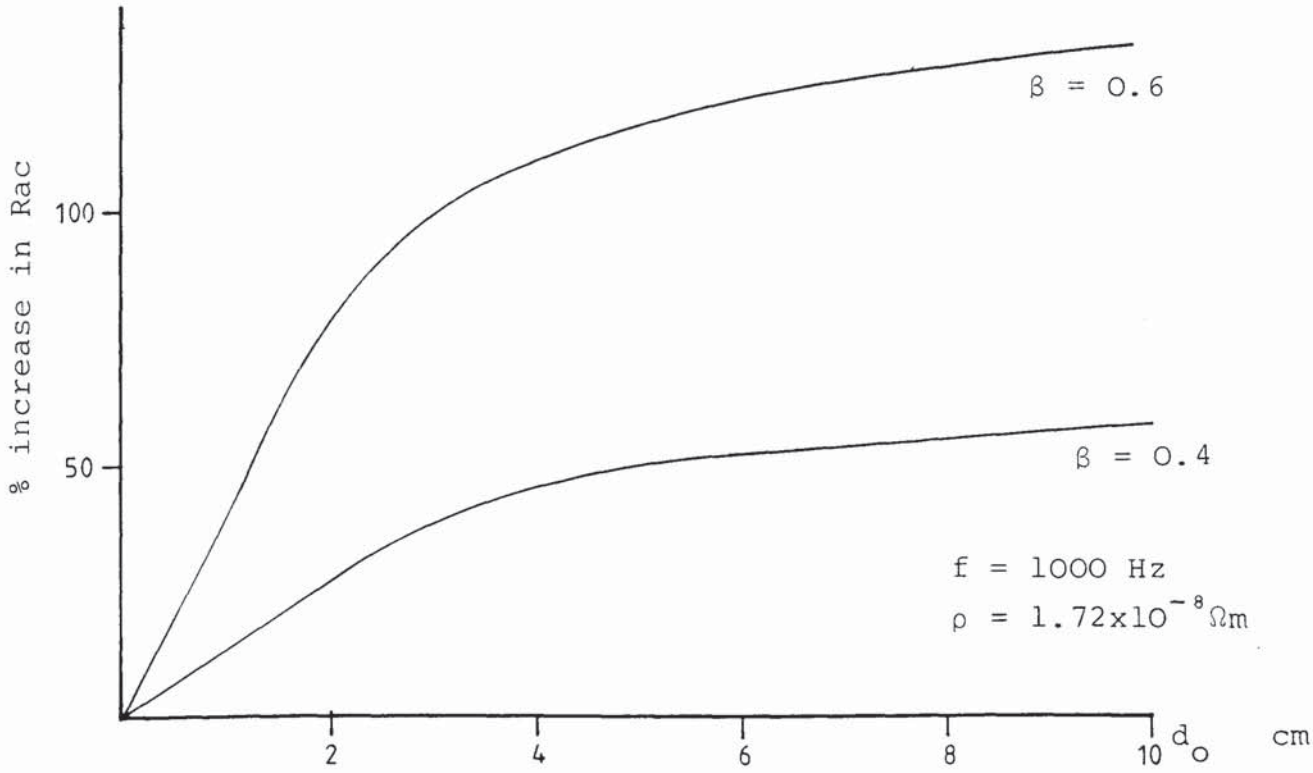

Fig. 4.8 Calculated % increase in effective resistance as a function of external tube diameter - concentric arrangement

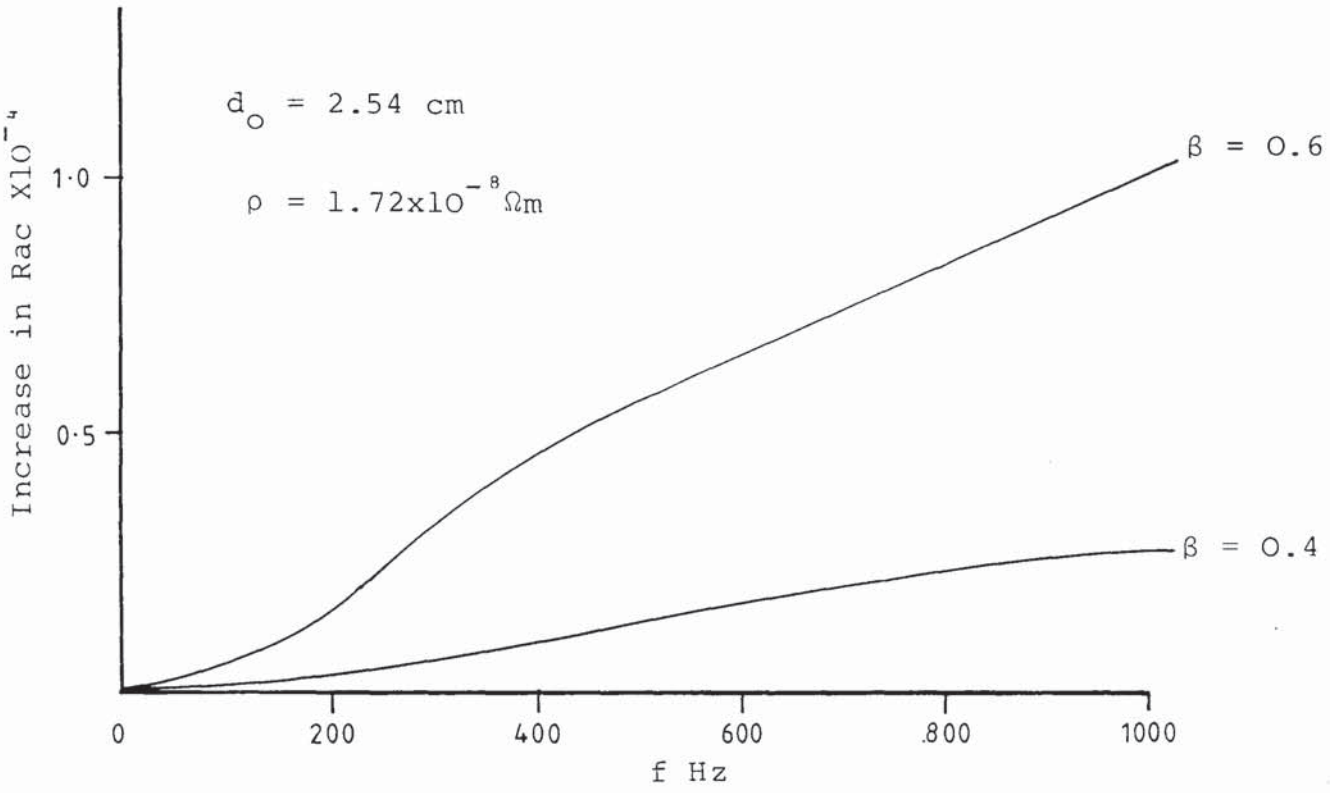

Fig. 4.9 Increase in effective resistance as a function of frequency - concentric arrangement

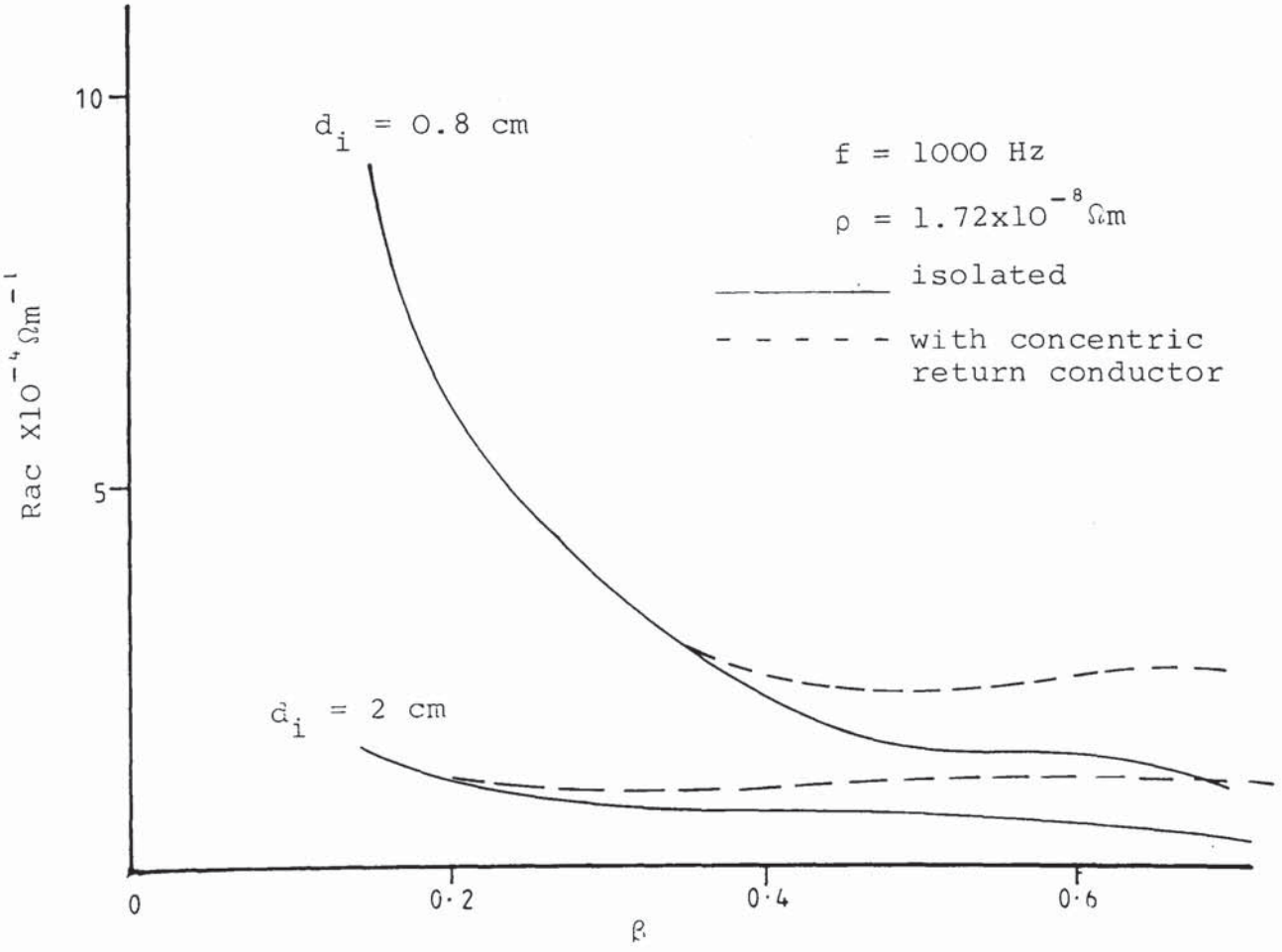

Fig. 4.10 Calculated effective resistance for constant internal diameter and variable wall thickness

CHAPTER 5

MAGNETICALLY NON-LINEAR SOLUTIONS

Chapter Summary

Solutions accounting for the non-linearity of steel and applicable to resistance heating are reviewed, discussed and compared.

Chapter Contents

5.1 Literature Survey

Many solutions have been proposed to account for saturation and magnetic non-linearity in steel, which can be broadly grouped into analytic and numerical methods. Within each group, two subgroups can be identified; one relates to losses by induction on thick and thin plates and the other to losses by conduction on solid or tubular conductors.

The requirements of machine designers and induction heating applications, resulted in the past to attention being directed to the calculation of losses by induction rather than by conduction. Furthermore, it appears that to date, little has been published relating to the concentric arrangement when both or one of the conductors is made from steel.

In Section 4.6, the conditions for the non-magnetic or linear magnetic thick plate solution to apply to finite diameter cylinders have been established. Lim and Hammond [9] define the conditions under which a steel plate can be considered thick and therefore it is possible to apply thick-plate solutions to finite diameter cylindrical steel conductors. An examination of published work in this field is therefore appropriate.

Rosenberg [54] was the first to use a one-dimensional analytic solution for a semi-infinite slab, by representing the magnetisation curve as a step-function. The same model for the B/H characteristic has been used by Agarwal [8] for both thick and thin plates subjected to a sinusoidally varying surface magnetic field. Stoll [45] gives a lucid presentation of the

solution for a thick plate with sinusoidal surface field excitation and explains why the "step-function" method of solution gives loss values 70% greater than the linear solution.

Bowden and Davies [14] give a comprehensive review of one-dimensional analysis and identify the factors which contribute to the eddy-current loss in solid steel.

Lim and Hammond [9][52] also give a review of analytical and numerical methods for the solution of non-linear eddy-current problems in thick plates. They solve numerically the one-dimensional diffusion equation in a non-dimensional form and use the Frohlich representation for the B/H characteristic.

All three methods mentioned above are applicable to conductive heating of steel bars or tubes depending on the values of diameter and wall thickness.

An early bibliography (up to 1916) on steel conductors is given by Kennelly et al [55]. In order to calculate the resistance ratio of steel rails of different profile and of cylindrical conductors carrying alternating currents, they used the formula

$$K = \frac{S}{P_r} \; 2\pi \sqrt{\sigma \mu f}$$

where S is the conductor cross-sectional area and P_r its perimeter. The value of μ had been obtained from the d.c. magnetisation characteristic.

Dwight [56] used the same formula to calculate K for steel tubes and agreement between measured and calculated values of K was found to be poor (see also Section 6.4.1)

Rajagopalan and Murty [18] applied a linear solution to steel conductors of rectangular and circular cross-section, carrying alternating currents. Hysteresis effects were accounted for by means of a complex permeability.

The step-fuction B/H characteristic has also been used for the case of resistance heating of a circular solid conductor by Davies and Bowden [57] and by Burke and Lavers [15]. Davies and Bowden applied it incorrectly to small diameter wires and Burke and Lavers limit their investigation to a one inch diameter bar.

A numerical method applicable to resistance heating of isolated circular conductors or tubes has been developed by Lavers [53] but does not account for the saturation harmonics in the flux density waveform.

Koyanagi et al [6] solve numerically the equations describing the concentric arrangement of two steel tubes, but they consider sinusoidal H throughout the cross-section of the tube and only limited experimental evidence is offered in support.

Although a considerable number of additional alternative theories have been proposed to account for non-linearity, they are not considered here, because they relate to current flow by induction rather than current due to edge to edge contact.

As far as thick plates are concerned and by virtue of the solutions having possible applications to conductive heating, the more up-to-date analysis of Bowden and Davies [14] and Lim and Hammond [9] are examined. Their analyses supersede Agarwal's [8] and avoid having to assign a value to the flux

density required by the "step-function" method. However, they apply only to large diameter bars.

In the following sections available solutions relevant to conductive heating are briefly reviewed, discussed, compared and contrasted.

Particular attention is paid to the step-function method, because it is extended in this thesis to the cases of small diameter wires and to isolated or concentric tubes, which have not been treated previously in the literature by this method.

5.2 The Step-function Magnetisation Characteristic

5.2.1 Description of the magnetic model

The assumptions are:

1. The cylinder has an infinite length.
2. The cylinder carries an axial sinusoidal current $i = \hat{I} \sin\omega t$.
3. The B/H curve is given by $B = (\text{abs } H)\, B_A$

Suppose the cylindrical conductor of radius b is in the steady-state and at t=o the conductor is magnetised to saturation in the negative direction to a value $-B_A$ and to a depth δ_s from the surface because of a preceding cycle of magnetisation; δ_s may have any value between 0 and b but initially it is assumed that $\delta_s < b$. As the current increases from zero, the field intensity H reverses direction at the surface switching the flux density in the surface layer from $-B_A$ to B_A Two regions are therefore defined both of which are magnetised to saturation in opposite directions. The boundary of the two regions determines a cylindrical surface which advances into the conductor during the halfwave of the current at a finite velocity which will be found to be of subsequent interest.

5.2.2 Analysis

Let the surface velocity be v. The distance penetrated by

the separating surface as a function of time is $\Psi(t)$ and at time t equals $|\Psi(t)|$ (Fig. 5.2). $\Psi(t)$ and v are related through

$$v = \frac{d\Psi(t)}{dt}$$

Two further equations describe the problem

$$\oint \bar{E}.dl = -\frac{\partial}{\partial t} \iint_s \bar{B}.\bar{ds} \qquad (5.1)$$

and

$$\oint \bar{H}.dl = \sigma \iint_s \bar{E}.\bar{ds} \qquad (5.2)$$

equation (5.1) gives the flux change in time δt and equation (5.2) the current enclosed by the path over which $\bar{H}$ is integrated.

Since $\bar{E}$ has only one component in the axial direction, equation (5.1) reduces to

$$E = \frac{d\Phi}{dt} = 2\hat{B}_A v = 2\hat{B}_A \frac{d\Psi(t)}{dt} \qquad (5.3)$$

By applying equation (5.2) around the circle of radius r and by substituting (5.3) into (5.2) and re-arranging

$$H_s = \frac{\sigma \hat{B}_A}{r}[r^2 - b^2 + 2b\Psi(t) - \Psi^2(t)] \frac{d\Psi(t)}{dt} \qquad (5.4)$$

for

$$b - |\Psi(t)| < r < b$$

and $Hs = 0$ for $r < b - |\Psi(t)|$

since the current is uniform in the region between b and $b - |\Psi(t)|$ and zero in the region $r < b - |\Psi(t)|$, at the surface, $H_s = \hat{H}_s \sin wt = \frac{\hat{I}}{2\pi b} \sin wt$ and $r = b$

substituting into equation (5.4)

$$\hat{H}_s \sin wt = \frac{\sigma \hat{B}_A}{b} \left[2b\Psi(t) - \Psi^2(t)\right] \frac{d\Psi(t)}{dt} \qquad (5.5)$$

Integrating (5.5) with the initial conditions, $\Psi(t) = 0$ when $t = 0$,

$$\delta_s^2 \sin^2\left(\frac{w \cdot t}{2}\right) = \Psi^2(t) - \frac{\Psi^3(t)}{3b} \qquad (5.6)$$

where $\delta_s = \sqrt{\frac{2\hat{H}_s}{\sigma w \hat{B}_A}}$ is the saturation depth (5.7)

If $\frac{\hat{H}_s}{\hat{B}_A}$ is written as $1/\mu_s$, then δ_s is the non-linear equivalent of the skin depth δ of the linear theory.

If $\delta_s > b$, the separating surface reaches the centre of the conductor before the end of the first half-cycle and at time τ, with $\Psi(\tau) = b$ in equation (5.6)

$$\tau = \frac{2}{w} \sin^{-1}\left[\sqrt{\frac{2}{3}} \frac{b}{\delta_s}\right] \qquad (5.8)$$

If $b/\delta_s = \sqrt{\frac{3}{2}}$

the flux wave reaches the centre of the cylinder at the end of the first half-cycle.

If $b/\delta_s < \sqrt{\frac{3}{2}}$

the centre is reached before the end of the half-cycle.

It is now possible to define the current density as a function of time at any given depth y. During any positive half-cycle of the current, the current density which has only one component in the axial direction, will be zero until the separating surface reaches the depth y, after a time t_y, given

by

$$t_y = \frac{2}{w} \sin^{-1} \left[\frac{1}{\delta_s} \sqrt{y^2 - y^3/3b} \right] \qquad (5.9)$$

If so required, the current density can be defined in the four intervals of time between 0 and $2\pi/w$ and the current density can be expressed as a Fourier series from which the influence of the current density harmonics can be investigated. Stoll [45] carries out this exercise for a thick plate.

5.2.2.1 Power and power factor

The instantaneous power per unit length of cylinder is

$$p(t) = E(t)\, i(t) = 2\hat{B}_A \frac{d\Psi(t)}{dt} \hat{I} \sin wt$$

from (5.5)

$$p(t) = \frac{\hat{I}^2 \sin^2 wt}{\sigma\pi b \left[2\Psi(t) - \frac{\Psi^2(t)}{b}\right]} \qquad (5.10)$$

The instantaneous reactive power per unit length is

$$q(t) = \frac{\hat{I}^2 \sin wt \cos wt}{\sigma\pi b \left[2\Psi(t) - \frac{\Psi^2(t)}{b}\right]} \qquad (5.11)$$

Integrating equation(5.10), the average power is

$$P = \frac{\omega \hat{I}^2}{\pi^2 \sigma b} \int_0^{\pi/\omega} \frac{\sin^2 wt}{\left[2\Psi(t) - \frac{\Psi^2(t)}{b}\right]} dt \qquad (5.12)$$

and integrating (5.11) the average reactive power is

$$Q = \frac{w\hat{I}^2}{\pi^2 \sigma b} \int_0^{\pi/w} \frac{\sin wt \cos wt}{[2\Psi(t) - \frac{\Psi^2(t)}{b}]} dt \qquad (5.13)$$

The power factor is given by

$$\text{p.f.} = \cos\left(\tan^{-1}\frac{Q}{P}\right) \qquad (5.14)$$

5.2.3 General discussion

In the literature survey it was stated that the step-function B/H characteristic has been used for the case of resistance heating of bars by Davies and Bowden [57] and by Burke and Lavers [15]. Burke and Lavers' paper does not refer to Ref. [57] which preceded it and their respective equations differ. The limiting case of the thick plate ($b \rightarrow \infty$) or the condition giving a shallow flux wave penetration $|\psi(t)|$ in comparison with the radius b is worth examining.

This limiting case has not been examined by either of the authors of Ref. [57] and [15] although it serves as a way of proof for the more general solution of the finite radius cylinder.

In equation (5.6) if $|\psi(t)| \ll b$ at the end of the half cycle,

$$\Psi(t) = \delta_s \sin\left(\frac{wt}{2}\right) \tag{5.15}$$

from (5.9) the time for the wavefront to reach a distance y is

$$\frac{2}{w} \sin^{-1}\left(Y/\delta_s\right) \tag{5.16}$$

from (5.16) and (5.12) the average power is

$$\frac{4w\hat{I}^2}{\sigma\pi^2 b2\delta_s} \int_0^{\pi/w} \cos^2 \frac{wt}{2} \sin \frac{wt}{2}\, dt \qquad (W\ m^{-1})$$

$$= \frac{2w\hat{I}^2}{\sigma\pi^2 b\delta_s} \left(\frac{2}{3w}\right) \qquad (W\ m^{-1})$$

The average power per unit surface area P_s, follows and is given by

$$P_s = \frac{8}{3\Pi} \frac{\hat{H}_s^2}{\sigma\delta_s} \tag{5.17}$$

Equations (5.15), (5.16) and (5.17) are in agreement with the thick plate case (see Ref. 8).

Davies and Bowden [57] give the following equations:

$$\delta_s = \frac{\hat{V}}{wB_A} \tag{5.18}$$

$$\tau = \frac{2}{w} \sin^{-1}\sqrt{b/\delta_s} \tag{5.19}$$

$$P = \hat{V}^2 \delta_s b\sigma k_p \tag{5.20}$$

$$I = 2\sqrt{2}\hat{V}\delta_s b\, k_I \sigma \tag{5.21}$$

Some of the symbols have been changed to be consistent with the preceding equations, k_p and k_I are functions of b/δ_s. For the present discussion it is important to note the observations made in Ref. [57] that $k_p \to \pi/2$ as $b/\delta_s \to \infty$ and for $b/\delta_s > 1$ $k_I \simeq 1.47\ k_p$

Thus, it is possible to investigate equations (5.18) to (5.21) for the limiting condition $b/\delta_s \to \infty$

For a direct comparison of corresponding equations the quantity V must be eliminated. From (5.21)

$$\hat{V} = \frac{\hat{I}}{\sigma\, 2\sqrt{2}\,\sqrt{2}\,\delta_s\, b\, k_I}$$

since $\hat{H}_{s1} = \hat{I}/2\pi b$

$$\hat{V} = \frac{\hat{H}_{s1}\, 2\pi b}{4\sigma\,\delta_s\, b\, k_I} \qquad (5.22)$$

substituting (5.22) into (5.18) and with $k_I = 1.07\ \pi/2$

$$\delta_s = \sqrt{\frac{\hat{H}_{s1}}{\sigma\,\omega\,\hat{B}_A\, 1.07}}$$

substituting (5.22) into (5.20) with $k = \pi/2 \simeq k_I$

$$P = \hat{H}_{s1}^2\, \pi b / 2\sigma\delta_s \qquad (W\ m^{-1})$$

or

$$P_s = \hat{H}_{s1}^2 / 4\sigma\delta_s \qquad (W\ m^{-2})$$

For $\hat{H}_{s1} = \hat{H}_s$ this equation gives loss densities 2.4 times smaller than from equation (5.17). The difference arises as a result of the assumed operating conditions which in the case of

ref. 15 is sinusoidal current and in the case of ref. 57 sinusoidal voltage. It should however be noted that the analysis of ref. 57 was applied by the authors to experimental results under sinusoidal current conditions and surprisingly reasonable agreement between measured and calculated loss values was obtained.

5.2.4 Prediction of loss based on the step-function B/H characteristic

The use of the step-function B/H characteristic in calculating eddy current losses results firstly, in predicting higher losses than the linear solution and secondly, changes the phase angle of the first harmonic of the current density from a limiting value of 45° to a value of 26.6°.

The ratio Q/P has been plotted by Burke and Lavers [15] and clearly shows this limiting phase angle.

Although the step-function analysis is an improvement on the linear solution, it fails to correctly predict, either the eddy current loss, or the phase angle. The error arises due to the different layers of the conductor experiencing varying levels of saturation. Whilst the material near the surface of the conductor can be in a state of saturation and the step-function is in this case a reasonable approximation, the inner layers are far from a saturation state.

Agarwal [8] first suggested, on the basis of experimental results, the use of a flux density equal to 0.75 B_s , giving better agreement between measured and calculated values of eddy

current losses on steel plates.

Burke and Lavers [15] used the value of H corresponding to 0.637 $\hat{H}s$ on the basis that it gives the best correlation with test results but their statement before choosing this value is confusing. To quote "the magnetic flux density corresponding to the surface magnetic field intensiy is the appropriate value of B_A . Since the material is non-linear, it is not clear whether one should use the value of B corresponding to the maximum, rms or the average value of surface H or none of these. Agarwal uses 0.75 $\hat{H}s$ . . . ". If B_S is the saturation flux density in the step-function representation, it is a constant for all values of Hs irrespective if Hs is taken to be the rms, peak or average. The adjustment to B can only be made in terms of B_S and Agarwal as stated previously used 0.75 B_S and not 0.75 $\hat{H}_s$.

With $B_S = B_A$ the loss is 70% greater than the linear theory when the measured loss is almost 50% greater . Thus, a reduction in the predicted loss (equations (5.7) and (5.17)) is sought which can be obtained by increasing the value of δ_s for a given value of $\hat{H}_s$. The use of H = 0.637 $\hat{H}_s$ gives a loss 0.587 x the loss obtained with Agarwal's empirical factor.

Bowden and Davies [14] show analytically that $B_A = 0.75\, B_S$ for wide range of $\hat{H}_s$ above the knee of the B/H curve. Lim and Hammond suggest that for very high values of H_s, $B_A = B_S$. They also observe that the empirical factor of 0.75 has been chosen to make some specific allowance for hysteresis loss and therefore it is unlikely to be valid for materials with either very

low or very high hysteresis. However, it is generally accepted that under saturation conditions and for low carbon steels, hysteresis is almost negligible. Agarwal's measurements were carried out under saturation conditions.

Returning to equation (5.12), the function $\psi(t)$ is not available explicitly and therefore (5.12) can only be solved numerically. For a universal application the parameter K is more useful than the loss and Burke and Lavers have plotted a graph of K derived from (5.12) versus b/δ_s.

Because of the assumed B/H characteristic, the "step-function" method, even with an adjustment to the flux density by the Agarwal factor, overestimates the losses at low values of Hs and underestimates them at high values of H .

5.3 One-dimensional Analytic Solution

Bowden and Davies' [14] analysis is applicable to steel bars greater than 7 cm diameter depending on the current, the resistivity and the B/H characteristic of the steel. It takes into account the saturation harmonics by representing the curve relating the fundamental component of the B/H curve, B_1, by $B_1 = AH_1^{b'_1}$ and solving the diffusion equation. With the B/H characteristic represented by $B = a'\hat{H}_s^{b'_1}$ it is shown that $A = \xi a'_1$ and ξ_1 is approximately constant and equal to 1.25 for ENIA steel and $Hs > 5000\ (A\ m^{-1})$. The effect of the change in the value of permeability with depth is accounted for by a factor k_p which is a function of b'_1. The ratio of the non-linear to the linear power loss density is simply given by $k_p \sqrt{\xi_1}$.

Calculated values of loss density show agreement with the measured values to within 4% and agree with the values based on Agarwal's method for $\hat{H}_s > 2500\ (A\ m^{-1})$ but give lower values for $\hat{H}_s < 2500\ (A\ m^{-1})$.

The authors did not attempt to compare their calculated values with those obtained by using the universal loss chart of Lim and Hammond although reference is made to this paper.

5.4 Solution Based on Linear Analysis

Rajagopalan and Murty [18] obtain similarly to Bowden and Davies an effective permeability given by the ratio of the fundamental component of the distorted flux density waveform and the sinusoidal surface magnetic field. The effective permeability is substituted in the linear solution to obtain values of the ratio $M=Rdc/_{Zac}$ Hysteresis effects are considered by means of a hysteresis angle θ.

Agreement between calculated values of M and measured values with steel conductors of circular and rectangular cross-section is rather poor. They fail to consider analytically the effect of the change of permeability with depth but they make the following observation to justify the discrepancy between their measured and calculated values of M. Quoting they note:

"The values of μ and θ corresponding to the amplitude of the magnetising force are used. However, bearing in mind that μ and θ vary with H, it is obvious that the proper choice of μ and θ should be based on an average magnetising force instead of the value at the surface. Tentatively we chose $0.8H_s$ (rms) as the magnetising force for predicting the results."

This ad hoc modification which increases the effective permeability improves the correlation between measured and calculated values of M for $H_s > 1000 \left(A\ m^{-1}\right)$ but has the reverse effect for values of $H_s < 1000 \left(A\ m^{-1}\right)$.

The method of calculation if restricted to values of $H_s > 1000 \left(A\ m^{-1}\right)$ has therefore some potential. It has the further

advantage that the conductor diameter is not restricted to a minimum value. It has the disadvantage that a B/H characteristic is required to be obtained experimentally. This last observation also applies to the method proposed by Bowden and Davies.

5.5 Numerical Solutions

Lim and Hammond [52] solved numerically the non-linear diffusion equation

$$\frac{\partial^2 H}{\partial x^2} = \sigma \frac{\partial B}{\partial H} \frac{\partial H}{\partial t}$$

The shape of different types of B/H characteristics are described by a parameter ξ which can be obtained from a knowledge of the Frohlich curve representation and therefore the solution is applicable to more than one material, By solving the diffusion equation in a non-dimensional form, universal loss charts are produced from which the loss density can be easily calculated. The loss charts are not applicable to circular conductors except under certain conditions. The results of Table 4 of their paper are inadvertently misleading but do not influence the conclusions reached

In the step-function theory, the penetration depth δ_s was defined as the depth below which there is no penetration of field or current. In the linear theory δ was defined as the classical skin depth which is independent of H_s.

Lim and Hammond identify another penetration depth δ which can be obtained from

$$P_s = \frac{\hat{H}_s^2}{\sigma \delta_f}$$

with P_s obtained from the universal loss chart.

They show that if $d/\delta_f > 2$ (d = half thickness of plate) the steel plate can be considered thick. This criterion is stricter than the criterion of $d/\delta_s > 1$ applicable to the step-function

theory.

Lavers' numerical solution (Sec. 4.10.1) is not a true non-linear solution. The permeability of each annular ring is obtained from the d.c. magnetisation characteristic but a different value is assigned to each ring and therefore the change of permeability with depth is considered.

Burke and Lavers compare, by means of a graph, calculated values of Rac/Rdc based on the step-function theory, with results obtained from their numerical model. Reference to these results is made in Section 6.4.1.

Gillot and Calvert [7] replaced the non-linear partial differential equation describing conductive heating by a finite difference equation.

The differential equation is

$$\frac{\partial^2 H_\theta}{\partial r^2} + \frac{1}{r}\frac{\partial H_\theta}{\partial r} - \frac{H_\theta}{r^2} = \frac{1}{\rho}\frac{\partial B_\theta}{\partial t} \qquad (5.23)$$

where H_θ and B_θ are functions of θ and t. (This equation can be derived simply from equation (4.5)).

Unfortunately they did not compute or measure the power loss. They however investigated the case of the round rod with an externally supplied sinusoidal mmf. For their computations they used the actual B/H curve and the results show that their computed values for loss were lower at high field strengths and higher at low field strengths than the measured values. Better agreement between measured and calculated values was obtained at 400 Hz.

Koyanagi et al [6] used equation (5.23) with the appropriate

boundary conditions to solve the coaxial pipe problem. However, they replace $\partial/\partial t$ by jw i.e. neglecting harmonics.

In place of μ they use an effective permeability given by

$$\mu = \int_{o}^{H} \mu_{d.c.}\ (H)\ \frac{dH}{H}$$

where $\mu_{d.c.}$ is the permeability obtained from the static characteristic. The right hand side of equation (5.23) becomes

$$jw\left\{\mu(|H_\theta|) - \frac{d\mu(|H_\theta|)}{d|H_\theta|} H_\theta\right\} H_\theta$$

For details of the solution, Koyanagi et al make reference in their paper to publications which proved to be unobtainable. The experimental work is rather inconclusive and the theoretical analysis suffers from the same limitations as Lavers' except that the inner pipe in the coaxial system is likely to operate in the unsaturated region of the B/H curve.

The coaxial pipe system is reconsidered in Sect. 6.4.1.

5.6 Comparison of Theories

For infinite half-space, three alternative theories have been identified and therefore a comparison of calculated loss values based on each theory should be possible. Such a comparison has not been reported in the literature.

For the comparison to be made possible, the B/H characteristic of the material is required and experimental results must be available.

Lim and Hammond [9] tested their theory by measurements on toroids, whilst Bowden and Davies [14] checked their theory by measuring the losses on a steel bar carrying alternating currents. The bar diameter was sufficiently large to ensure that it was electrically appearing as a semi-infinite slab, with an accuracy of 4%.

Since both sets of authors compare calculated values with those obtained by Agarwal's method, either author's experimental results can be used to compare alternative theories.

Lim and Hammond's [9] loss curves are universal and therefore an independent check of their applicability is an attractive possibility. To apply Bowden and Davies analysis for ENIA steel to Lim and Hammond's test results referring to mild steel, the value of k_p and ξ_1 must be known. Whilst k_p is easily calculated from the B/H characterstic, the value of ξ_1 is more difficult to establish. The results of Bowden and Davies will therefore be used for the comparison of theories.

On first examining the universal loss chart of Ref. 9 , it

appears that it cannot be applied to the results of Bowden and Davies, since the value of the parameter η based on the radius of bar (3.8 cm) is outside the published range of η . However, the thickness to be considered in Lim and Hammond's dimensionless parameter η does not have to correspond to the radius of the bar. Provided sufficient depth is allowed for the magnetic field to decay, the value of η corresponding to this depth can be used to calculate the loss.

On the basis of the Frohlich representation of the B/H characteristic for ENIA steel given by $B = \frac{\hat{H}_s}{288+0.51\hat{H}_s}$, the value of the saturation flux density (Sect. 4.12) is 1.96T and the parameter ξ equals 565. Choosing values for η equal to 10 and 20 to avoid interpolation, the corresponding values of d (half thickness of plate) are 3.31 mm and 4.68 mm respectively. The corresponding loss values obtained from the loss chart for the 7.6 cm diameter bar are shown in Table 5.1 together with the values published by Bowden and Davies [14].

Since the loss chart is universal, the loss values corresponding to η = 10 and η = 20 should be equal. Any deviation could be due to one or a combination of three reasons.

1. There is an error in reading the value of dimensionless loss P_n from the loss chart.
2. Insufficient depth has been allowed for complete field penetration.
3. There is an inherent error in deriving the loss chart.

Any error due to the first cause cannot be ascertained, but

it cannot lead to the large differences observed. If insufficient depth has been allowed, the loss should be larger in the case of d = 3.31 compared to the case of d = 4.68.

Lim and Hammond compared results obtained from the loss chart with results calculated using Agarwal's method. They observe that the chart gives smaller losses at low values of H_s and larger ones at higher values of H_s than those obtained by Agarwal's method. The reason they put forward is that Agarwal's approximation depends very much on the empirical factor of 0.75 which for high values of H_s should be nearer to unity. The results of Table 5.1, show the same trend between loss values based on Agarwal's method and the one obtained by using the loss chart. They also observe that their measured loss on mild steel toroids is consistently larger than the calculated losses. In the case of the results of Table 5.1, this consistency does not exist; for some values of H_s the measured loss is smaller than the value based on the loss chart, while for others it is larger. Their assertion that the higher measured losses in their investigation are due to hysteresis, is not substantiated by the present comparison, even allowing for the difference in levels of field strength. The reason is more likely to be due to the toroids used in their experimental investigation not fully approximating to the semi-infinite slab condition or due to inherent errors in the loss chart.

If the result for d = 4.68 mm in Table 5.1 is considered, maximum error between the measured and calculated values is 9.4% as compared to 3.6% for the values calculated by Bowden and

Davies (the loss value corresponding to H_s = 2950 $(A\ m^{-1})$ is not considered since it is supposed to be in error).

So far, the theories applicable to thick plates have been compared. Lavers' [53] numerical method (not limited by diameter size) can also be applied to the results of Bowden and Davies and therfore a further comparison can be made between alternative theories. The calculated values using the numerical method, are shown in Table 5.2 and correspond to the same data of Table 5.1. The computer programme developed for this purpose has been used for the calculation of loss values on the basis of the B/H characteristic representation used by Bowden and Davies over the three ranges of H_s.

In Table 5.2, the significance of the wall thickness is the depth at which a current density is assumed to begin the iteration process. Care must therefore be taken to ensure that this depth is adequate for total penetration bearing in mind that it varies with the level of excitation.

One hundred iterations proved adequate and a replacement of the three-range B/H representation in the computer programme by a single Frohlich type showed a difference of 1.4% on the calculated value of loss for H_s = 11,800 $(A\ m^{-1})$. Increasing the wall thickness and at the same time the number of iterations to 500 did not alter the results indicated in Table 5.2.

The maximum error between the calculated values in Table 5.2 and the measured values of Table 5.1 is 7.7%, again disregarding H_s = 2950 which gives an error of 14%.

Whilst the predicted loss values via the numerical route are

in reasonable agreement by engineering standards with the measured losses, it comes as a surprise that the numerical method gives results consistently higher for all values of H_s except 1000. This is contrary to expectations, since the numerical method does not take into account the effect of saturation harmonics. Bowden and Davies have shown that the linear loss has to be multiplied by $\sqrt{\xi_1}$ to account for these harmonics. If this factor is neglected, a reduction in the calculated loss values should result.

The phase angle between the fundamental component of the surface current density and surface magnetic field strength calculated by Bowden and Davies is constant and equal to 36.7° . This constancy results from the dependency of the phase angle only on the value of the exponent of H_s in the functional representation of the B/H characteristic used in their analysis which assumed that the exponent is independent of Hs above the knee of the saturation curve.

Examination of Table 5.2 indicates that the calculated value of phase angle is not constant but decreases as the level of saturation increases. Lim and Hammond's [9] calculated results show a similar reduction on the value of phase angle and in addition its dependence on the shape of the saturation curve and the amplitude of the surface field. They observe that when the non-linearity of the B/H curve is not pronounced, the phase angle approaches the 45° of the linear theory, while at deep saturation it comes closer to 26.6° the value in the step-function (Agarwal) theory.

Laver did not use his numerical model to compute phase angles nor did he test his method in different steels or different size conductors.

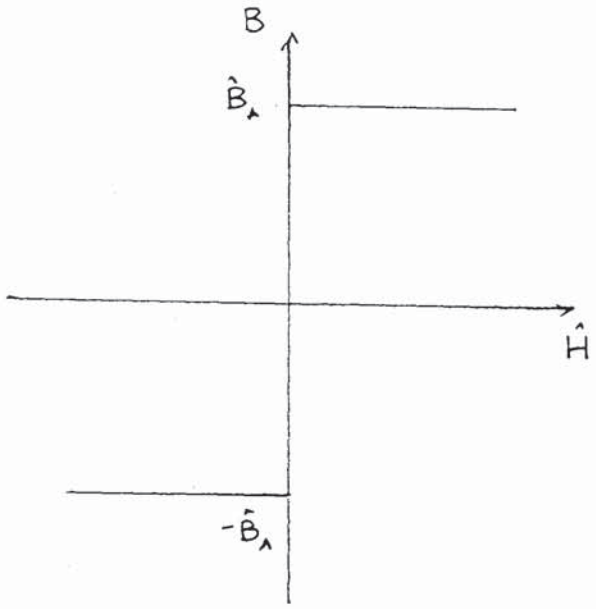

Fig. 5.1 Step-function B/H characteristic

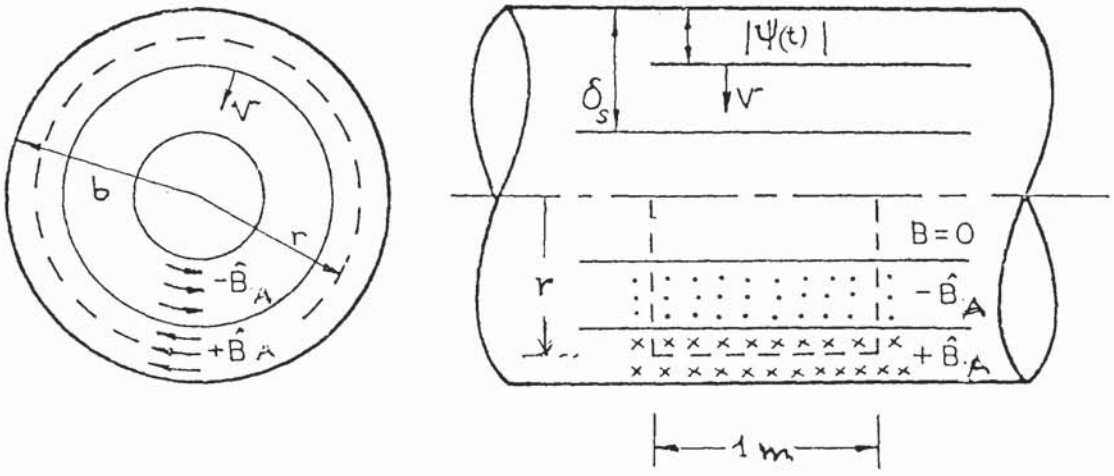

Fig. 5.2 Details of cylindrical conductor for step-function magnetisation model.

Table 5.1. Calculated Loss Values by Different Theories for a 7.6 cm Diameter Steel Bar

Bar Excitation $\hat{H}_s$ Am^{-1}	Loss Density kWm^{-2}				
	Bowden and Davies [14]		Agarwal's Theory [8] from Ref. [14]	Lim and Hammond Loss Chart [by author]	
	Measured	Calculated		$\eta = 10$ $d = 3.31$ mm	$\eta = 20$ $d = 4.68$ mm
1000	0.13	0.128	0.142	0.121	0.118
2000	0.43	0.417	0.447	0.413	0.406
2950	0.71	0.72	0.72	0.775	0.777
5900	2.34	2.38	2.38	2.4	2.4
8850	4.42	4.45	4.46	4.5	4.45
11800	7.05	6.85	6.86	7.36	6.9
14720	10.10	9.74	9.78	11.17	10.56

Table 5.2. Calculated Loss Values by Numerical (Lavers) Method for a 7.6 cm Diameter Steel Bar as for Table 5.1.

Bar Current A	Wall Thickness mm	Power Factor	Phase Angle Degrees	Calculated [by author] Loss Density kW m^{-2}
168.7	4	0.730	43	0.121
338	4	0.766	40	0.42
498	4	0.777	39	0.812
996	5	0.797	37	2.51
1494	5	0.800	36.8	4.76
1992	6	0.807	36.2	7.48
2485	8	0.809	36	10.56

CHAPTER 6

PROPOSED METHODS OF SOLUTION

Chapter Summary

In Chapter 5, the review of contemporary solutions relevant to magnetic non-linear steel identified their limited applicability to the problems under consideration and two methods are now developed.

The first (effective permeability method), is based on the linear solutions of Chapter 4 and is extensively tested on experimental results published by other workers. By expressing the power loss in dimensionless form, an effective permeability is derived and the possibility of scaling is considered. On the basis of this method it is predicted that the index of variation of H_s in the power density/H_s relation is a function of tube diameter and wall thickness.

Depth of penetration and the influence of conductor diameter on its value are evaluated. In the absence of experimental results to test this method for its applicability to the concentric configuration, the step-function approximation method (Chapter 5) is extended to this case and in addition to thin-wall tubes and wires.

Chapter Contents PAGE

6.1 Classification of Methods

In Chapter 5, a common feature of the methods considered, for the calculation of losses in steel conductors, was the requirement for a B/H curve. Despite the fact that a B/H curve is obtained experimentally, these methods were classified as analytic or numerical.

In contrast, Thornton's [17] formula for losses in steel pipes is entirely empirical. His attempt to provide formulae describing the performance of steel pipes in the dual role of a means of transportation and as "heating element", was the first to be reported, but inevitably lacked generality of application.

The proposed effective permeability method, which is developed in subsequent sections, can be described as semi-empirical. This classification is appropriate because, whilst the effective permeability is derived in the first instance from Thornton's experimental results, the loss is calculated on the basis of this permeability and formulae resulting from analytic solutions.

The second method, since it is based on the step-function theory, can be described as analytic.

6.2 Effective Permeability

An effective permeability is explicitly or implicitly involved in the methods described in Chapter 5. In Bowden and Davies' method [14], the step-function method [15] and Lim and Hammond's numerical technique [9], an effective permeability is the outcome of an analytic or numerical solution. In the case of Rajagopalan and Murty [18], an effective permeability has to be established first, before a solution can be obtained.

Rajagopalan and Murty failed to derive an effective permeability which fully accounts for the magnetic non-linearity of steel (for comments see Section 6.3.3.1) and their solution is based on equations applicable to magnetic-linear steel.

The approach adopted in this thesis is in line with that of Rajagopalan and Murty, except that the effective permeability can be accurately determined from experimental results.

In the context of this thesis, effective permeability is defined as a conceptual permeability, which when substituted in the equations applicable to magnetically-linear steel, allows the loss to be predicted.

There are considerable advantages in adopting this approach. Firstly, solutions for linear steel exist for tubes (a solid is a special case of a tube) in isolation and in a concentric configuration (Chapter 4).

Secondly, the effective permeability, if derived from experimental data, is bound to account for the effects of non-linearity.

Thirdly, a B/H curve is not required if the loss in a sample can be measured.

6.3 Derivation of Effective Permeability

6.3.1 Preliminary investigation

Fig. 6.1 (plot b) shows a log/log plot of the relative permeability μ_r as a function of Hs for 0.1% and 0.19% carbon and also typical mild steel. The data have been obtained mainly from references [58] and [59].

The graph is representative of low carbon steels, but some deviation exists between data obtained from various other references which are not listed.

Fig. 6.1 (plot b) shows that $\mu_r / \hat{H}s$ is linear for a wide range of Hs (this is also observed by Davies and Simpson [19] p.336) and also, that the linearity does not hold for H <1000 ($A\ m^{-1}$). The point at which the $\log \mu_r / \log \hat{H}_s$ graph starts to curve, will be termed the turning point for ease of reference.

An examination of $\mu_r / \hat{H}_s$ data from various sources and in particular from Lozinski [60] indicate that as the carbon content increases, the turning point occurs at higher values of $\hat{H}_s$. This observation is important when in Chapter 7, the measured and calculated loss values are discussed.

Having established the shape of the $\mu_r / \hat{H}_s$ curve, it is reasonable to believe, that μ_{reff} will follow a similar pattern. μ_{reff} should be greater than μ_r, since it is well known that loss calculations based on μ_r, give lower values than the measured ones.

In Chapter 4, K-z graphs were obtained for different values

of β . Since K and z are dimensionless, the graphs are universal. If now a K-f graph for a steel tube is obtained experimentally and plotted on the same graph, the possibility of deriving an effective permeability can be investigated.

In order to obtain a K-f graph for a steel tube, Arnold's [47] measuring technique was employed (Fig. 6.2). To gain confidence in the accuracy of the measuring circuit, preliminary measurements were carried out with shunts of known resistance and the following results were obtained.

Nominal Resistance (Ω)	Measured Resistance (Ω)	% Error
0.0505	0.0512	+1.4
0.00125	0.00128	+2.4
0.000625	0.000620	-0.8

Having established that the measuring technique could measure with reasonable accuracy, values of resistance of an order likely to be encountered with steel tubes, measurements were carried out with a mild steel tube having the following parameters

$$d_o = 2.67 \text{ cm}$$

$$d_i = 2.18 \text{ cm}$$

$$t = 2.45 \text{ mm}$$

$$\beta = 0.183$$

The d.c. resistance of the tube was measured with a Kelvin double bridge and the conductivity, calculated from the tube dimensions, was 0.7×10^{7} ($S\ m^{-1}$). The measurements were carried

out with the return conductor sufficiently remote to eliminate proximity effects. The current was supplied by a variable frequency oscillator through current lugs brazed on the ends of the tube and kept at approximately 50 mA. A bridge oscillator detector was used as the null detector tuned to the operating frequency. Measurements were carried out at frequencies between 50 and 500 Hz.

The measured values of K are plotted in Fig. 6.3(plot a) on a base of frequency. Fig. 6.3(plot b) is the calculated K-z graph corresponding to $\beta = 0.183$ (the value applicable to the steel tube) and to arbitrary values of z.

For the two graphs to be coincident for say f = 100 Hz, z must be equal to 8.

Since

$$z = 2\pi f t^2 \sigma \mu_{r,eff} \mu_0$$

$$\text{or} \quad 8 = 2\pi \times 100 \times 2.45^2 \times 10^{-6} \mu_{r,eff} 4\pi \times 10^{-7}$$

with $\sigma = 0.7 \times 10^7$ (S m^{-1}) $\qquad \mu_{r,eff} = 241$

If the exercise is repeated for frequencies up to 300 Hz, the same value of $\mu_{r,eff}$ is obtained which confirms as expected, that $\mu_{r,eff}$ is constant for a constant current and suggests that it is independent of frequency up to 300 Hz. The change in $\mu_{r,eff}$ beyond 300 Hz is not due to a dependency of $\mu_{r,eff}$ on f, but due to measurement errors at the higher frequencies, when complete balance was difficult to achieve.

This simple investigation, has shown that calculated K-z

graphs based on magnetic-linear solutions can be used to obtain the effective permeability of a steel tube provided corresponding K-f graphs can be obtained experimentally for values of current encountered in practice.

6.3.2 Effective permeability based on Thornton's results

The current used for the measurements of Section 6.3.1 was chosen arbitrarily at a very low value to test a hypothesis; namely that μ_{yeff} is independent of frequency and is constant for a given current.

Arnold's measuring technique requires a constant tube temperature which is not possible practically if the tube current is large. Two options are available; either to generate experimental results by using an alternative method of measurement, or seek available results. Since Thornton published experimental results under variable current, variable frequency conditions, it was decided to use his results (test 1-15) in the first instance, to derive an effective permeability for mild steel as a function of H_s. This effective permeability could then be used to calculate loss values and compare them with published experimental results. As a final check of the method of calculation, calculated loss values would be compared with experimental results obtained independently.

Thornton's results are not ideal, since resistance ratios at constant current are sought, with the frequency as the variable parameter and at constant frequency, with the current as the

variable.

Inspection of Thornton's results (test 1-15), shows that neither of the above conditions is entirely satisfied. Furthermore, details of his method of measurement are not given and therefore his results must be used with caution.

Figs. 6.4 and 6.5 are derived from Thornton's test results (1-15). The similarity of the curves in Fig. 6.4, to the K-z curves is apparent. The nature of the curve of Fig. 6.5 is peculiar to steel conductors, because of the change of μ_r with current. Comparable curves to 6.4 for non-magnetic conductors, would be horizontal lines.

In order to obtain a functional relation between $\mu_{r,eff}$ and H_s, Thornton's results have been processed in two ways. These will be described briefly.

Firstly, for a given tube, of wall thickness t, with current I and conductivity σ,

$$z = \lambda f$$

where λ is a quantity to be determined for different values of I, from which the corresponding value of $\mu_{r,eff}$ can be calculated. For each frequency and for constant current conditions

$$z/f = \lambda = \text{constant}$$

Thus, if the value of z is used which gives the measured value of K, λ can be calculated. The average of the values of λ obtained are

Nominal current (A)	200	500	800
λ	1.1	0.59	0.386

from $$\lambda = 2\pi t^2 \sigma \mu_{r,eff} \mu_o$$

and with $\sigma = 0.7 \times 10^7$ (S m^{-1}) and $t = 0.3556 \times 10^{-3}$ m

the following values of $\mu_{r,eff}$ are obtained:-

Nominal Current (A)	200	500	800
H_s (A m^{-1})	1055	2638	4222
$\mu_{r,eff}$	1576	845	553

These values are plotted in Fig. 6.1 (plot a) giving a functional relationship on the basis of a straight line, described by

$$\mu_{r,eff} = 575 \times 10^3 H_s^{-0.83}$$

Alternatively, the same procedure as in Section 6.3.1 can be used. On Fig. 6.4, the K-z curve (not shown) for $\beta = 0.118$ is superimposed on the K-f curves. For each constant current characteristic, the value of z which makes the K-f and K-z curves coincident is obtained. The following values of $\mu_{r,eff}$ are calculated.

Nominal current (A)	200	500	800
$\mu_{r,eff}$	1430	812	546

The above values are not in total agreement with the ones previously calculated. The value of β used in establishing the second set of $\mu_{r,eff}$ values was obtained from the quoted nominal external diameter and a wall thickness calculated by weight. If the measured external and internal diameters are used, β = 0.158 and t = 0.476 cm. If the K-z curve corresponding to β = 0.158 is used, instead of β = 0.118 the values of $\mu_{r,eff}$ obtained, will be somewhat higher and therefore in closer agreement with the first set.

Excluding the first value of $\mu_{r,eff}$ corresponding to H_s =1055 which is in the vicinity of the non-linear part of the log μ /log H_s characteristic only two points are available to obtain the relationship between $\mu_{r,eff}$ and H_s. This together with the previously made remarks regarding Thornton's results, throw some doubt as to the accuracy of the method for obtaining $\mu_{r,eff}$. However, there is a way of checking the correctness of $\mu_{r,eff}$ using the dimensionless parameter $\frac{\rho\sigma}{H_s^2 t}$. Since $\frac{\rho\sigma}{H_s^2 t}$ - z, for a given β and d_o, is a unique curve, the curve in Fig. 6.6 should encompass all the results of tests (1-15). On the same graph the calculated values based on $\mu_{r,eff} = 575 \times 10^3 H_s^{-0.83}$ are shown. The point corresponding to z = 0, represents d.c. conditions and therefore is independent of current and frequency.

The experimental errors involved in Thornton's results, are evident from the scatter of the experimental points in Fig. 6.6. It appears that $\mu_{r,eff} = 575 \times 10^3 H_s^{-0.83}$, gives slightly high calculated loss values, but in view of the spread in the

experimental points and the uncertainty in the value of β, little can be gained by readjusting the expression for $\mu_{r\,eff}$.

6.3.3 Effective permeability derived from loss measurements and a known B/H curve

In section 6.3.2 it was shown that if the measured losses are expressed in dimensionless form, the need to undertake measurements at variable frequency can be avoided. This is possible because a given value of z can be obtained by varying the current at constant frequency. Since the dimensionless parameters $\frac{P\sigma}{H_s^2 t}$ and z are related for a given diameter by a unique curve it should be possible to derive an effective permeability on the basis of measured values of power loss on a sample and a knowledge of its B/H curve. The method can be demonstrated by using the experimental results of ref. [14], which also includes a B/H curve. These results have been processed and are shown in Table 6.1.

In Fig. 6.7, the measured losses Pm in dimensionless form and the calculated losses P_{cL} using Arnold's equations of Chapter 4, have been plotted against the parameter z.

For the calculation of P_{cL}, the permeability is obtained from $\mu_r = 525 \times 10^3 \hat{H}_s^{-0.89}$ (ref. [14]) and for each value of current, the value of μ_r is used to calculate z.

Referring to Fig. 6.7, for a given value of the dimensionless loss parameter, let z_2 be the value of z corresponding to $\frac{P_{cL}\sigma}{H_s^2 t}$ and z_1 the value of z corresponding to

$$\frac{P_m \sigma}{H_s^2 t}$$

For P_m to be equal to P_{cl}, z_1 must be increased until it is equal to z_2.

Since $z_2 > z_1$

$$z_2 = z_1 \times \text{multiplying factor} \qquad (6.1)$$

For a given current, frequency, conductivity and diameter,

$$z_1 \propto \mu_v \qquad \text{and}$$

if the equations for magnetic-linear steel are to predict the losses,

$$z_2 \propto \mu_{veff}$$

hence in (6.1), $\mu_{veff} = \mu_v \times$ multiplying factor

The multiplying factors obtained from the graphs of Fig. 6.7 are listed in Table 6.1.

6.3.3.1 Discussion

The measured loss values used in Section 6.3.3 have been obtained from ref. [14] and therefore, the values of μ_{veff} calculated in 6.3.3 can be discussed in the context of the findings in this reference.

Bowden and Davies [14] define an effective permeability given by,

$$\sum_1 a_1' \hat{H}_{s1}^{(b_1'-1)}$$

where $\hat{H}_{s1}$ is the fundamental component of H_s. For sinusoidal H, it is equal to $\sum_1 a_1 \hat{H}_s^{(b_1'-1)}$

Table 6.1. Measured (ref 14) And Calculated (Thesis) Linear-Steel Loss For ENIA Bar

Bar Current I (A)	Surface Excitation H_S (Am^{-1})	Relative Permeability μ_r	Measured Power Loss Pm (Wm^{-2}) ref. 14	$\bar{z}$ based on μ_r	Calculated Power Loss for Linear Steel P_{CL} (Wm^{-1}) Present Method	Effective Permeability Derived From Fig. 6.7 x μ_r	$\frac{P_m \sigma}{H_S^2 t}$ x10^3	$\frac{P_{CL} \sigma}{H_S^2 t}$ x10^3
338	1415	605	102.6	1814	73	1.97	7.09	5.04
498	2085	429	183.8	1285	134	2.04	5.85	4.27
996	4171	231	559	693	397	2.04	4.44	3.16
1494	6257	161	1055	483	751	2.01	3.73	2.65
1992	8343	125	1683	374	1180	1.87	3.34	2.34
2485	10407	102	2411	307	1671	1.7	3.08	2.13

$2b = 7.6$ (cm)

$\sigma = 0.526 \times 10^7$ (S m^{-1})

$f = 50$ Hz

$\mu_r = 525 \times 10^3 \hat{H}_S^{-0.89}$

$\xi_1 = 1.25$ for $H_s > 5000$ (A m^{-1}), but reduces for smaller values of H. If this definition of effective permeability is accepted, it does not differ in concept from that of Rajagopalan and Murty's. The reason is, that ξ_1 accounts only for the saturation harmonics. In fact, the ingredients are available in Bowden and Davies' paper, but they did not carry the argument to its conclusion and define a truly effective permeability, which accounts also for the change in permeability with depth. Examination of the loss equation for non-linear steel in ref. [14] indicates that the true effective permeability is

$$(k_p^2 \xi_1) \mu_r \qquad (6.2)$$

For ENIA steel, Bowden and Davies calculated the values

$$k_p = 1.32$$
$$\xi_1 = 1.25$$

From (6.2) the effective permeability is thus $2.18\mu_r$ for $H_s >$ 5000 (A m^{-1}) and reduces with a reduction in H. Whilst k_p is assumed to be constant above the knee of the B/H curve, the value of ξ_1 reduces for $H_s < 5000$ (A m^{-1}) and therefore there is a reduction in the effective permeability value.

Examination of the values of μ_{reff} in Table 6.1, shows that the multiplying factor for μ_r varies between the values 1.7 and 2.04, with the low values occurring at the high value of H. From the foregoing, this is contrary to expectations, but since experimental points are not available between z = 0 and 307, the calculated multiplying factors, for the higher values of H_s, depend on the "correct" extrapolation of the $\frac{P_m \sigma}{H_s^2 t}$ curve of Fig.

6.7 and therefore is subject to errors.

One would be justified in making the following comment;

> "what is the point in using measured loss values to obtain $\mu_{r,eff}$, which is then used to calculate the measured loss? If the losses can be measured, they need not be calculated."

The purpose of the exercise is to be able to predict the losses of different size conductors, of constant (chemical) composition and similar work history, under varying operating conditions (sect. 6.4). Measurements on one size of conductor are required to make this possible and it has been shown how $\mu_{r,eff}$ can be obtained.

The methods developed so far for establishing $\mu_{r,eff}$ require either a K-f graph to be obtained experimentally, or the B/H curve of the steel to be known.

A method will now be described which dispenses with the above prerequisites.

6.3.4 Effective permeability derived from loss measurements

Once again the experimental results of ref. [14] will be used to demonstrate the procedure. The present method relies on the uniqueness of the $\frac{P_{cL}\sigma}{H_s^2 t}$ - z curve, irrespective of the B/H characteristic. Since with all other factors remaining constant, $z \propto \mu f$, a plot of $\frac{P_{cL}\sigma}{H_s^2 t} \sim f$ with $\mu_r = 1$ can be used to derive $\mu_{r,eff}$ in the following manner.

P_{cL} is calculated for a 7.6 cm diameter conductor with $\mu_r = 1$,

Table 6.2. Calculated (Thesis) Loss Values for Non-Magnetic Solid Bar

f (Hz)	P_c (W m^{-1})	$\frac{P_c \sigma}{Hs^2 t}$ x10^3	z
6,000	1157	2.3	360
10,000	1482	2.95	600
15,000	1805	3.59	900
20,000	2078	4.13	1,200
25,000	2318	4.61	1,500
30,000	2535	5.04	1,800
35,000	2734	5.44	2,100
40,000	2920	5.8	2,400
45,000	3095	6.15	2,700

$d = 7.6$ cm $\quad \mu_r = 1$

σ = 0.526 x10 (S m^{-1}) and different frequencies.

The results are shown in Table 6.2 and plotted in Fig. 6.8

Let $$z_1 \propto \mu_1 f_1$$

and $$z_2 \propto \mu_2 f_2$$

with the suffixes 1 and 2 referring to calculated and measured conditions respectively.

For P_{cl}, $\mu_1 = \mu_0$ and f_1 is variable

For P_m, $\mu_2 = \mu_{yeff}\mu_0$ and f_2 = 50 Hz

For P_m to be equal to P_{cl},

$$\frac{P_m \sigma}{H_s^2 t} = \frac{P_{cl}\sigma}{H_s^2 t} \quad \text{and}$$

$$z_1 = z_2$$

or $$\mu_{yeff} = f_1/50$$

Hence for each value of $\frac{P_m \sigma}{H_s^2 t}$ in Table 6.1, the corresponding frequency is obtained from Fig. 6.8.

This value divided by 50, gives the effective permeability. The calculated values of μ_{yeff} for different surface excitations are shown in Table 6.3. Fig. 6.9 shows a log/log plot of μ_{yeff} and $\mu_r \sim H_s$ from which

$$\mu_{yeff} = 404 \times 10^{3} H_s^{-0.815}$$

or $\mu_{yeff} = 516 \times 10^{3} H_s^{-0.843}$ if the two extreme values of μ_{yeff} are used.

The multiplying factors in Table 6.3 are more accurate than the ones included in Table 6.1, but still not in agreement with the value of 2.18 obtained by the analysis of ref. [14]. There are three reasons for this difference.

Table 6.3. Effective Permeabilities for Data of Table 6.1.

Bar Excitation H_s (Am^{-1})	$\frac{p_m \sigma}{H_s^2 t}$	Frequency f_1 (Hz)	$\mu_{r}'eff$	Multiplying Factor $\frac{\mu_{r}'eff}{\mu_r}$
1415	7.09	57000	1140	1.88
2085	5.85	40800	816	1.9
4171	4.44	23600	472	2.04
6257	3.73	16600	332	2.06
8342	3.34	13000	250	2.08
10407	3.08	10600	212	2.08

Firstly, ξ_1 is derived on the basis of the fundamental of the flux density waveform and ignores the higher harmonics.

Secondly, in Bowden and Davies' analysis k_p is assumed to be independent of H_s (the constancy of k_p also affects the phase angle - see Section 5.6. Chapter 5).

Thirdly, the value of 2.18 is dependent on the accuracy of the functional representation of the B/H characteristic over the range of H_s considered.

The accuracy of the method developed in this section, is only limited by the accuracy of the experimental results.

6.3.5 Effective permeability of a steel derived from a knowledge of its B/H curve and the effective permeability of another steel

Since B/H curves for some steels are available in the literature, the possibility of a method for calculating μ_{eff} without having to carry out measurements, is an attractive proposition. It has been shown that for mild steel of conductivity 0.7×10^7 (S m^{-1}), the effective permeability is given by $575 \times 10^3 H_s^{-0.83}$. Thornton did not measure the B/H curve of the tube material he tested. Fortunately, Agarwal gives B/H values for one of the mild steel samples he tested, which also has a conductivity of 0.7×10^7 (S m^{-1}) and therefore it is reasonable to assume that the two mild steels have almost identical B/H curves.

Lim and Hammond matched a Frohlich curve to Agarwal's B/H

Table 6.4. Relative Permeability of Mild Steel and ENIA Steel

Surface Excitation $\hat{H}_s$ (Am^{-1})	Mild Steel $\sigma = 0.7 \times 10^7$ (Sm^{-1})		ENIA Steel $\sigma = 0.526 \times 10^7$ (Sm^{-1})	
	μ_r from Agarwals B/H Data	μ_r from $[(207 + 0.576\hat{H}_s)\mu_o]^{-1}$	$525 \times 10^3 \hat{H}_s^{-0.89}$	μ_r from $[(288 + 0.51\hat{H}_s)\mu_o]^{-1}$
314	1723	2052	3146	1776
629	1404	1397	1696	1307
1102	946	945	1029	936
1575	717	714	749	729
3150	391	394	404	420
4724	273	272	282	295
6299	210	207	218	227
9449	147	141	152	156
12598	114	107	118	118
15748	93	86	96	96

values and give the Frohlich constants as a_1 =20.7 and b_1 = 0.57 (the value of a_1 should have been 207). The permeabilitie obtained from Agarwal's data and from the Frohlic representation are shown in Table 6.4. In the same table th corresponding values for ENIA steel have been included fc comparison. For the case of ENIA steel the B/H representation given by Bowden and Davies have been used.

Since in Section 6.3.2 μ_{yeff} has been derived frc measurements (Thornton's) on a material with a certain B/H curv and conductivity, it will only apply to that material. Howeve it was pointed out that for a given diameter, the $\frac{P_\sigma}{H_s^2 t} \sim z$ curve is unique irrespective of the B/H representation frequency, conductivity and current.

Suppose now that $\frac{P_{c1}\sigma}{H_s^2 t}$ is plotted for the steel of known μ_{yeff}, conductivity and B/H curve. For corresponding values c H_s, the parameter $\frac{P_{c1}\sigma}{H_s^2 t}$ is also calculated on the basis of th B/H representation of the steel of unknown μ_{yeff}, and plotte against the z values of the first steel. An expression can b derived for the unknown μ_{yeff} which will be shown to be the sam as that of the known μ_{yeff}, but multiplied by a constar factor.

The procedure will be illustrated by a way of a 2 c diameter steel bar made from "Thornton's" material of know μ_{yeff} and a 2 cm diameter bar made from "Bowden and Davies material of unknown μ_{yeff}.

The dimensionless power loss for the two steels ha been calculated for assumed currents, and are shown in Tabl

6.5. In Fig 6.10, the loss parameters for the two steels hav been plotted against z based on the values of z obtained fc M.S. for different currents. If the two steels had identica parameters, the two curves of Fig. 6.10 would be coincident. I is therefore possible to make the two steels apparentl identical, by using for ENIA steel and for a given current, th corresponding z value for M.S., but reduced by a factor K_o. Th use of $K_o z$ will then give the loss for ENIA steel. Since μ_{reff} $575 \times 10^{3} H_s^{-0.83}$ gives a reasonable prediction of the losse for M.S. of $\sigma = 0.7 \times 10^{7}$ (S m^{-1}), the use of $\mu_{reff} = K_o \times 575 \times 10^{3} H_s^{-0.83}$ wil also give a reasonable prediction for ENIA steel of $\sigma = 0.526 \times 10^{7}$ (S m^{-1}).

From the curves of Fig. 6.10, the value of K_o can b established, by making the two curves coincident. K_o varie slightly between low and high values of z, but the accuracy c the predicted losses is not affected to any extent by taking K as constant and for ENIA steel ($\sigma = 0.526 \times 10^{7}$ (S m^{-1})) i is equal to 0.79.

Whilst the permeability calculated from the two B/H curv representations of the ENIA steel differ (Table 6.4), the los parameters are very nearly equal (Table 6.5) because the loss i not very sensitive to changes in permeability. For the purpos of plotting the curves in Fig. 6.10, it makes little differenc which set of values is used.

A comparison of the values of μ_r for mild stee ($\sigma = 0.7 \times 10^{7}$ (S m^{-1})) and for ENIA steel show very smal

Table 6.5. Dimensionless Linear Loss For Two Steels

	Thornton's Material $\sigma = 0.7 \times 10^7$ (Sm^{-1}) $a_1 = 207$) Frohlich $b_1 = 0.576$) Constants			Bowden and Davies Material $\frac{P_{cL}\sigma}{H_s^2 t}$ $\sigma = 0.526 \times 10^7$ (Sm^{-1})	
Bar Current I (A)	Surface Excitation H_s (Am^{-1})	z	$\frac{P_{cL}\sigma}{H_s^2 t}$	$a_1 = 288$) Frohlich $b_1 = 0.51$) Constants	$\mu_r = 525 \times 10^3 \hat{H}_s^{-0.89}$
80	1273	177	6.22	5.52	5.55
100	1591	146	5.7	5.1	5.06
140	2228	109	4.96	4.48	4.4
180	2865	86.6	4.47	4.06	3.97
220	3500	71.9	4.1	3.74	3.65
260	4138	61.5	3.82	3.49	3.43
300	4775	53.7	3.59	3.3	3.24

differences (Table 6.4). Yet, their respective values of $\mu_{r,eff}$ differ. This suggests that $\mu_{r,eff}$ is a function not only of the B/H curve and hence permeability, but also of conductivity. Bowden and Davies analysis shows that $\mu_{r,eff}$ is a function of the B/H curve only, since ξ_1 and k_p are independent of σ. It has been shown that this is not the case. Further experimental evidence is required before the dependence of $\mu_{r,eff}$ on σ is confirmed or otherwise.

6.4. Comparison with Published Experimental Results

In order to test the validity of the method of calculating losses on the basis of an effective permeability, calculated values of surface loss density and resistance ratios have been compared with experimental results published by various authors. The results of this comparison are given in Tables 6.6.to 6.13.

6.4.1. Discussion

The results in Tables 6.6, 6.7 and 6.8 are Thornton's experimental results on which he based his empirical formulae for resistance heating of mild steel pipes. He does not give details of his measuring technique, or the resistivity of the pipes tested. He states however, that careful measurements on a number of steel pipes, gave resistivity values between 13.7 and 14.3×10^{-8} (Ω m). On this basis, the resistivity used for calculating the loss values in Tables 6.6 - 6.8, was 14.3×10^{-8} (Ω m).

The difference between measured and calculated values of loss density is less than 10%, excluding results in the vicinity of 1000 ($A\ m^{-1}$), when the effective permeability derived from $575 \times 10^{3}\ H_s^{-0.83}$ is not valid.

Tables 6.9 and 6.10 incorporate the results of tests carried out by Dwight [56], on two pipes and at two frequencies.

Dwight's measured values have been referred to 20°C, by using the temperature coefficient of resistance, which he quotes

Table 6.6. Surface Power Loss In Tubular Steel Conductors
Measured and Calculated Values

Conductor Current I (A)	Conductor Excitation H_s (Am^{-1})	Loss Density ($W\ cm^{-2}$)		
		Measured Thornton	Calculated present theory	% Difference from measured values
800	5940	0.40	0.398	- 0.5
640	4754	0.28	0.279	0.3
480	3566	0.179	0.176	- 1.6
320	2377	0.095	0.0922	- 2.9
160	1189	0.031	0.0306	- 1.3

Outside diameter	4.286 cm	
Wall Thickness	0.556 cm	$\beta = 0.26$
Frequency	50 Hz	
Conductivity	$0.7 \times 10^7\ S\,m^{-1}$ (assumed)	

Table 6.7. Surface Power Loss In Tubular Steel Conductors
Measured And Calculated Values

Conductor Current I (A)	Conductor Excitation H_s (Am^{-1})	Loss Density (W cm^{-2})		
		Measured Thornton	Calculated Present Theory	% difference From Measured Values
800	5259	0.306	0.326	+ 6.5
640	4207	0.214	0.229	+ 7.0
480	3155	0.137	0.144	+ 5.1
320	2104	0.072	0.076	+ 5.5
160	1052	0.022	0.025	+ 13.6

Outside diameter	4.842 cm	
Wall Thickness	0.516 cm	$\beta = 0.21$
Frequency	50 Hz	
Conductivity	0.7×10^7 S m^{-1}	(assumed)

Table 6.8. Surface Power Loss in Tubular Steel Conductors
Measured And Calculated Values

Conductor Current I (A)	Conductor Excitation H_s (Am^{-1})	Loss Density ($W\ cm^{-2}$)		
		Measured Thornton	Calculated Present Theory	% Difference From Measured Values
800	2864	0.1186	0.1227	+ 3.4
640	2291	0.083	0.0861	+ 3.6
480	1718	0.0527	0.0545	+ 3.4
320	1145	0.0282	0.0286	+ 1.4
160	573	0.00846	0.0091	+ 7.5

Outside Diameter	8.89 cm	
Wall Thickness	0.635 cm	β =0.143
Frequency	50 Hz	
Conductivity	$0.7 \times 10^7\ S\,m^{-1}$ (assumed)	

as approximately equal to 0.004 per degree C. The conductivities of the two pipes tested were given in per cent of that of copper. Since this figure differs slightly in the literature and information is not given as to how these conductivities were obtained, there is some doubt as to the accuracy of the values used in calculating the results of Tables 6.9. and 6.10.

Below H_s = 1000 (A m^{-1}), the calculated values are not reliable. As the measured values of resistance ratio in Tables 6.9. and 6.10. have been obtained from the graphs of Dwight's paper, they are subject to a reading error. In view of the above, agreement between Dwight's measured values and those calculated by the method developed in the thesis are reasonable.

Table 6.11 incorporates the measured values obtained by Burke and Lavers [15] for a solid bar of 1020 steel. The B/H curve and the conductivity have not been given for the bar tested and therefore, for calculation purposes, the conductivity has been assumed to be 0.7 x10^7 (S m^{-1}). The measured values of resistance ratio, have been obtained from Burke and Lavers graphs and therefore are subject to a reading error. Their calculated values were plotted on the same graph, but it is very difficult to ascertain their accuracy. A comparison of measured and calculated (thesis) resistance ratios shows good agreement.

Since Lavers [53] numerical method was used in Section 5.6 with reasonable success, it was decided to test it on Burke and Lavers results, as information was not given in their paper regarding the way their numerical model was used.

In order to undertake the calculations, a B/H representation

Table 6.9. Comparison Of Calculated And Measured Values Of Resistance Ratio

Tubular Steel Conductor

Conductor Current I (A)	Conductor Excitation H_s (Am^{-1})	Resistance Ratio								Power Density (Wm^{-2})
		Measured Dwight		Calculated Dwight		Calculated Thornton		Calculated Present Method		Calculated Present Method Frequency 50 Hz
		Frequency		Frequency		Frequency		Frequency		
		60 Hz	25 Hz	60 Hz	25 Hz	60 Hz	25 Hz	60 Hz	25 Hz	
100	312	14.7	10	8.5	5.6	14.2	9.2	13.8	8.95	363
200	625	10.2	7	7.7	5.1	10.5	6.8	10.4	6.72	109
300	937	8.7	5.7	6.5	4.2	8.82	5.7	8.7	5.69	208
500	1562	7.0	4.6	5.0	3.2	7.13	4.6	7.1	4.61	468
600	1875	6.6	4.2	4.6	3.0	6.57	4.26	6.6	4.28	625
800	2500	-	3.7	-	2.6	5.82	3.76	-	3.80	-
900	2800	-	3.5	-	2.5	-	3.57	-	3.63	-

Outside diameter of pipe 10.18 cm

Wall Thickness 5.1 mm $\beta = 0.1$

Conductivity 0.7×10^7 S m^{-1}

Table 6.10. Comparison Of Calculated And Measured Values Of Resistance Ratio

Tubular Steel Conductor

Conductor Current I (A)	Conductor Excitation H_S (Am^{-1})	Resistance Ratio										Power Density (W/m^2)
		Measured Dwight		Calculated Dwight		Calculated Thornton		Calculated Present Method				Calculated Present Method
		Frequency		Frequency		Frequency		Frequency				
		60 Hz	25 Hz	60 Hz	25 Hz	60 Hz (1)	25 Hz (1)	60 Hz		25 Hz		
								(2)	(3)	(2)	(3)	(3)
100	432	13.5	7.7	8.2	5.2	12.39	8.1	11.5	12.2	7.45	8.03	62.7
200	865	9.0	5.5	6.6	4.4	9.22	5.99	8.65	9.18	5.60	6.04	188
300	1290	7.4	4.8	5.5	3.6	7.75	5.03	7.31	7.76	4.74	5.01	347
500	2160	6.0	3.8	4.2	2.7	6.23	4.04	5.93	6.29	3.85	4.5	809
600	2600	5.3	3.5	3.7	2.3	5.76	3.74	5.50	5.84	3.58	3.85	1081
800	3450	-	3.0	-	2.0	-	3.3	-	5.19	3.19	3.43	1710

Outside diameter of pipe 7.36 cm
Wall Thickness 4.93 mm $\beta = 0.134$

(1) Calculations based on $= 0.79 \times 10^7 S\ m^{-1}$

(2) Calculations based on $\mu_{reff} = 575 \times 10^3\ H_S^{-0.83}$ and $\sigma = 0.7 \times 10^7\ S\ m^{-1}$

(3) Calculations based on $\mu_{reff} = 575 \times 10^3\ H_S^{-0.83}$ and $\sigma = 0.79 \times 10^7\ S\ m^{-1}$

Table 6.11. Surface Power Loss And Resistance Ratios In Solid Steel Conductor

Measured And Calculated Values

Conductor Current I (A)	Conductor Excitation H_s (Am^{-1})	Resistance Ratio				Calculated Surface Power Loss at 60 Hz ($W\ cm^{-2}$) Present Method	Calculated Surface Power Loss at 50 Hz ($W\ cm^{-2}$) Present Method
		Measured Burke & Lavers	Calculated Present Theory	Calculated Thornton Formula Power Index			
				1.57	1.59		
500	6260	5.5	5.47	5.14	5.69	0.48	0.44
1000	12500	4.2	4.17	3.81	4.28	1.47	1.35
2000	25063	3.1	3.20	2.83	3.22	4.52	4.16
3000	37595	2.75	2.75	2.38	2.73	8.74	8.05
4000	50127	2.45	2.47	2.10	2.43	13.97	12.91
5000	62659	2.2	2.28	1.91	2.21	20.14	18.56
6000	75191	2.1	2.13	1.76	2.05	27.08	25.23
7000	87723	2.0	2.02	1.65	1.93	34.98	32.14

Conductivity $0.7 \times 10^7\ Sm^{-1}$ (assumed)

μ_{reff} $= 575 \times 10^3\ H_s^{-0.83}$

Diameter of steel bar (1020) 2.54 cm

is needed. On the basis of the μ_r values in Table 6.4, it was decided to use the B/H representation $0.66\,\hat{H}_s^{-0.89}$ which gives at high field strengths agreement with the μ_r values for the Thornton/Agarwal M.S. The calculated surface power densities were found to be too small. The B/H representation function for $H_s > 2500$ was then increased by a factor 1.25 and the calculations repeated. The results which are shown in Table 6.12 are in good agreement with the values of K measured by Burke and Lavers. The dependency of the power factor on H has already been mentioned and is also evident in the results of Table 6.12. What remains unexplained, is the factor 1.25 which was not used previously, when the results of Table 5.2 were obtained.

A plausible explanation is that the numerical technique takes care of the change in permeability with depth and the factor 1.25 takes care of the effect of saturation harmonics. It is too much of a coincidence that the factor 1.25 is the value of ξ_1 quoted in ref. 14. If this explanation is accepted it poses the question:
why is it that the same numerical technique used in Chapter 5, gave losses <u>higher</u> than the measured ones included in Table 5.1?

It must be accepted that the assumed conductivity of 0.7×10^7 (S m^{-1}) is correct, since when used with the thesis method and the corresponding B/H representation, it gave results in agreement with the measured values (Table 6.11). Any error in the assumed B/H curve for 1020 steel cannot account for the factor 1.25 because such large differences in permeabilities

Table 6.12. Calculated (by P.T.) Parameters Based on Laver's Numerical Model

Current (A)	Surface Power Density ($W\ cm^{-2}$)	Power Factor	Resistance Ratio K
500	0.504	0.798	5.67
1000	1.52	0.810	4.32
2000	4.58	0.821	3.25
3000	8.71	0.826	2.74
4000	13.98	0.829	2.44
5000	19.64	0.833	2.23
6000	26.49	0.836	2.07
7000	33.83	0.838	1.95

Bar diameter 2.54 cm
1020 steel, $\sigma = 0.7 \times 10^{7}$ ($S\ m^{-1}$) (assumed)
Calculations based on 100 iterations.

Table 6.13. Comparison Of Measured And Calculated Values Of Surface Power Density

Solid Steel Conductor

Conductor Current A	Conductor Excitation H_s (Am^{-1})	Loss Density (kW/m^2)				
		Measured Bowden and Davies [14]	Calculated Bowden and Davies [14]	Calculated Present Theory		
				(1)	(2)	(3)
338	1415	0.427	0.417	0.410	0.419	0.412
498	2085	0.71	0.72	0.762	0.775	0.764
996	4171	2.34	2.38	2.31	2.32	2.3
1494	6257	4.42	4.45	4.42	4.42	4.39
1992	8343	7.05	6.85	7.01	6.99	6.95
2485	10408	10.10	9.74	9.99	9.93	9.89

Conductor diameter 7.6 cm (nominal)

Frequency 50 Hz

Conductivity 0.526×10^7 Sm^{-1}

(1) Calculation based on μ_{reff} = $403618\ H_s^{-0.815}$

(2) Calculation based on μ_{reff} = $516053\ H_s^{-0.843}$

(3) Calculation based on μ_{reff} = $0.79 \times 575 \times 10^3\ H_s^{-0.83}$

which would result, are not known to exist with low carbon steel.

The only conclusion to be drawn from the above discussion is that Laver's numerical model can give wrong results in some cases (see Chapter 5) depending on the value of H_s (the respective maximum values of H in tables 5.1 and 6.11 are 14,720 and 87,723 respectively and this observation may be significant in view of the findings in reference 14 that ξ_1 the factor accounting for the saturation harmonics, is dependent on the value of H_s).

The calculated values of loss density using the method developed in this Chapter and the findings of Section 6.3.4 and 6.3.5 are compared with Bowden and Davies' results in Table 6.13 (note the discrepancy in the measured value for H_s = 2950 $(A\ m^{-1})$) where good agreement is shown.

In their book, Lammeraner and Stafl [61] include Fig.6.11 which can be used as a further check of the findings so far. The calculated values of resistance ratio based on the effective permeability method, show good agreement with the measured values indicated in Fig. 6.11 (plot 1).

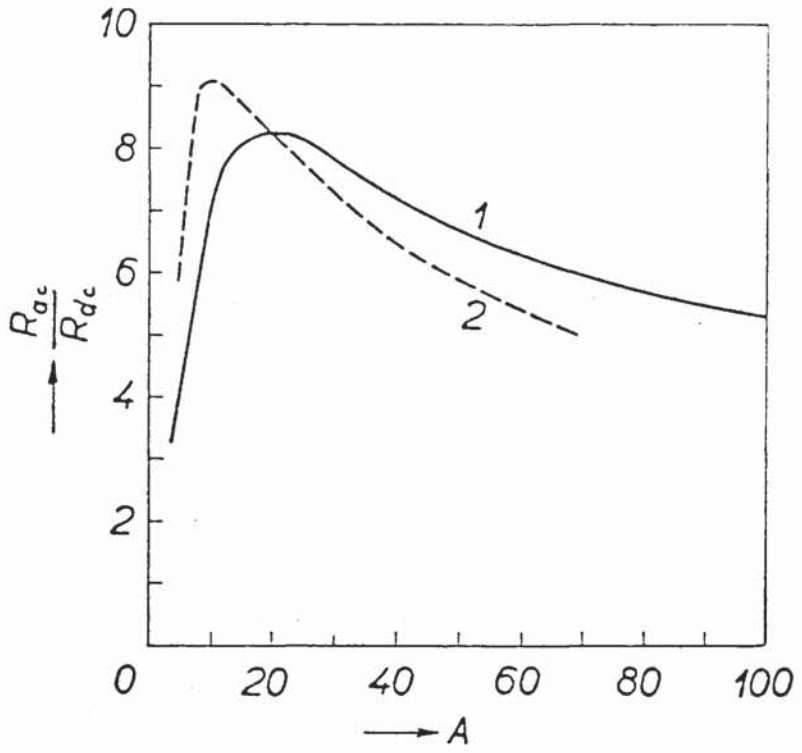

Fig. 6.11 Resistance ratios for an iron rod:

1 - experimental curve

2 - curve obtained by Rosenberg

b = 0.795 cm (ref. 61)

$\rho = 13.4 \times 10^{-8}\ \Omega\ m$

$\mu_{reff} = 575 \times 10^{3}\ H_i^{-0.83}$

f = 50 Hz

I (A)	Calculated (Thesis) K = Rac/Rdc
30	8.4
40	7.5
50	6.8
60	6.3
70	6.0
80	5.7
90	5.4
100	5.2

Davies and Bowden [57] reported measurements on a 2.54 mm diameter steel wire having a resistivity of 11.1 $\times 10^{-8}$ (Ω m). The calculated values based on an effective permeability given by

$$575 \times 10^{3} H_s^{-0.83}$$

are shown below, where the agreement with the measured values is better than the corresponding ones of ref. [57]

I (A)	P_m (ref [57]) (W m^{-1})	P_c (ref [57]) (W m^{-1})	P_c (thesis) (W m^{-1})
23.6	12.1	15.6	13.2
34	26	30.8	26.4
39.7	34.3	38.2	35.6
44.7	42.8	47.8	44.8
48.7	51.4	54.5	53

Koyanagi et al [6], reported one power measurement obtained for a current of 400 A with a coaxial arrangement of two pipes having the following dimensions

Inner Pipe	Outer diameter	165.2 mm
	Wall thickness	11.0 mm
Outer Pipe	Outer diameter	355.6 mm
	Wall thickness	11.1 mm

Unfortunately they do not state the resistivity but a value of about 14×10^{-8} (Ω m) is a commonly encountered value for a steel transport pipe.

For the coaxial heating system, the heat is generated in the inner pipe and the power developed for a given current is unaffected by the presence of the outer pipe. Thus for calculation purposes, the inner pipe can be treated as an isolated tube and the measured power of 68 (W m^{-1}) quoted by the authors can be compared with a calculated value based on an effective permeability of $575 \times 10^{3} H_s^{-0.83}$ and the equations of Chapter 4.

Now for a current of 400 A, the surface magnetic field strength is 772 (A m^{-1}) which is below the value of approximately 1000 (A m^{-1}) corresponding to the turning point of most low carbon, unalloyed steels.

Since at H_s = 1000 (A m^{-1}), μ'_{reff} = 1860, at 772 (A m^{-1}) can be taken as 1700 say.

The following calculated values of power are obtained for a current of 400 A which are close to the quoted value.

μ'_{reff}	ρ (Ω m)	P (thesis) (W m^{-1})
1800	14×10^{-8}	69.1
	14.5×10^{-8}	70.3
1700	14×10^{-8}	67.2
	14.5×10^{-8}	68.4

The authors do not quote the power developed in the outer tube. This is an important quantity because it does not contribute to the useful heat. Neither do they discuss the contribution of hysteresis to the measured value of loss which is obtained by a calorimetric method and therefore included in the measurement.

For the range of field strengths applicable to the coaxial pipe heating system, the hysteresis cannot be completely ignored because it can contribute between 4 and 8% of the total loss depending on the steel. In the effective permeability method, hysteresis loss is reflected in the effective permeability function and therefore it is to some extent taken into account.

6.5 Scaling

Measurements on a scaled model will give the same response as the original if the dependent variables describing the original, are grouped in a dimensionless parameter, which has equal value for the original and scaled model.

This technique has been used with copper conductors [64], whereby the increase in resistance of a large cross-section conductor at 50 Hz was deduced from measurements on a small cross-section conductor at high frequency. The case of ferromagnetic conductors is not as simple since the effective resistance is also current dependent.

The dimensionless parameter $\frac{P\sigma}{H_s^2 t}$ has been calculated for a number of conductor diameters with all conductors having the same conductivity of 0.7×10^7 (S m^{-1}) and a B/H characteristic resulting in $\mu_{r\,eff} = 575 \times 10^3 H_s^{-0.83}$. The results are shown in Fig. 6.12.

Fig. 6.12 can be identified as equivalent to the universal loss chart of Lim and Hammond, except that P in Fig. 6.12 is in W m^{-1} instead of W m^{-2}. The shape of the graphs are similar to the universal loss chart because, for a given B/H curve, ξ is constant and therefore, $h_o = \frac{H_s}{\xi}$ in Lim and Hammond's paper is proportional to H_s.

Similarly since $\eta = \frac{\sigma B_s f d^2}{\xi}$, (where in the present case d is the diameter) a constant value of d represents a constant value of η for the appropriate values of ξ and B_s (for M.S, typical values are $\xi = 400$ and $B_s = 1.72$) and therefore a value

of η can be assigned to the curves of Fig. 6.12. For the case when the diameter is sufficiently large to enable the conductor to be approximated to a semi-infinite slab, the loss is independent of d and therefore the appropriate parameter in this case is t_s at constant H resulting in a family of constant η curves. The interesting feature of graph 6.12 is that the points for d = 6, 8, 10, 20 cm which are not shown, lie almost on the same curve. This is not surprising if the variation of H with depth into the conductor is considered or the power for a given excitation as a function of its diameter. Either route shows that beyond a certain value of diameter, the conductor behaves as a semi-infinite slab.

In contrast with copper conductors, this condition is not only dependent on frequency and diameter, but also on the value of current.

For large values of H_s, $\frac{P_e \sigma}{H_s^2 t}$ is slightly larger for d = 6 cm than for d = 20 cm. For smaller values of H_s, when μ_r is large, both conductors appear electrically the same size because of the smaller depth of penetration.

The advantage of using h_o instead of z, as one of the dimensionless parameters, is that it separates the effects of frequency and permeability. Fig. 6.12 also shows the effect of cylindricity and skin depth for a given field excitation and in this respect can be considered as an extension of Lim and Hammond's chart.

Fig. 6.12 can be used for scaling purposes. Suppose it is required to measure the power for a 6 cm diameter bar at some

given value of H. Instead, measurements can be performed on a 0.8 cm diameter bar but at a value of H_s which gives the same value of dimensionless loss. Knowing this value of H and the dimensionless loss, the actual power on the 6 cm bar can be calculated.

If the B/H curve of the material is known, the H_s axis in Fig. 6.12 can be converted to the dimensionless parameter h_o, and the constant d parameter to η but the applicability of the curves in Fig. 6.12 to more than one type of steel, needs to be verified experimentally. As bars with different ξ value are readily available the difficulty experienced by Lim and Hammond in verifying their universal loss charts with toroids of different ξ value does not arise.

6.6 Index of Variation of Surface Power Density with Surface Field Strength

Thornton [17] established from measurements on three different size pipes, that the index of H_s in the surface power density/H_s relationship is 1.57.

In Fig. 6.14, Thornton's measured loss values listed in Tables 6.6, 6.7 and 6.8 have been plotted and the slope is as Thornton states, 1.57.

In Thornton's paper, the best straight line through all the points has been drawn. Although this does not affect the value of slope, it masks the effect of conductivity. The mathematical model shows that for the same surface excitation, the steel with the lower conductivity will develop the higher surface power density.

Examination of Fig. 6.14 shows that one of the steel tubes (Table 6.6) must have a lower conductivity than the other two. This observation also explains the difference in the percentage errors listed in Tables 6.6, 6.7 and 6.8, since the calculations were all based on an assumed conductivity of 0.7×10^{7} ($S\ m^{-1}$).

Bowden and Davies also consider the power index of H_s and show that for ENIA steel the theoretical value is 1.56.

In Fig. 6.15 the calculated loss values of Table 6.11 have been plotted and also some of the measured losses by Bowden and Davies. The slope is 1.61.

It should be pointed out that the index of H_s depends on the level of saturation and it is a function of diameter, wall

thickness, frequency and conductivity.

This point has been missed by Thornton and Bowden and Davies' analysis excludes a number of these variables.

For low value of H_s, Thornton's loss values do not lie on the straight line of Fig. 6.14 and the reason he puts forward is experimental error. A correct explanation is that for values of H_s below the turning point in the $\log \mu_r / \log \hat{H}_s$ curve, the power index of H in the surface power density expression changes.

Figs. 6.16, 6.17 and 6.18, are based on calculated loss density values which show the influence on the index of H_s of the parameters mentioned previously.

Figs. 6.16 and 6.17 refer to tubes of equal external diameter, but different wall thickness and show the effect of change in conductivity and wall thickness. With the thinner wall tube, as the field strength increases, the penetration increases and therefore the skin effect reduces to the point when eventually the a.c. and d.c. resistance are equal, leading to an index of 2.

The same effect is present with solid conductors and the diameter size decides at a given frequency and conductivity the value of index. Fig. 6.18 shows that as the conductor radius is reduced from 15 mm to 3 mm, the value of index increases to 2.

The surface power density values of Tables 6.6 to 6.13 are plotted against surface field strength in Fig. 6.13.

6.7 Depth of Penetration

In the case where steel conductors are used to carry alternating currents, a knowledge of the depth t_s beyond which the power density is zero is important. A knowledge of the value of this parameter enables the use of tubes of the correct dimensions.

Depending on the current and for a given diameter, the wall thickness for minimum loss is slightly smaller than t_s. This can be deduced from the nature of the curves in Fig. 4.5.

In Section 4.4.1 it was argued that for the same current, t_s for the concentric arrangement will be greater than for the isolated tube. For the saddle tube heating system, safety considerations dictate a wall thickness in excess of t_s. Depth of penetration for the concentric arrangement is further discussed in section 7.9.3.

Equation 4.40 has been used to calculate t_s and the results have been plotted in Figs. 6.19 and 6.20.

Consider first Fig. 6.19. At constant current as d increases, H_s decreases and therefore μ_{reff} increases resulting in smaller penetration. For a given diameter, as the current increases, H_s increases, resulting in a smaller μ_{reff} and therefore larger penetration. Thus Fig. 6.19 supports the qualitative treatment of the concept of penetration depth which differs in magnitude from the skin depth of the linear theory.

For the linear relationship to be valid in Fig. 6.19, certain limits have to be imposed. For any given diameter, the

maximum value of t_s is d/2 and for a given current, the diameter is limited to a value which makes H_s larger than the value corresponding to the turning point . Fig. 6.19 only applies to the steel for the stated parameters and a reduction in σ will increase t_s.

As for δ , t_s is a function of temperature. Under steady-state temperature conditions, the value of σ will be constant at some different value. For low temperatures and for small penetration depths associated with steel, the different conductor layers are almost at the same temperature and therefore temperature effects can be taken into account by adjusting the value of σ to correspond to the operating temperature.

The results of Fig. 6.19 and 6.20 can be shown in a more useful form in Fig. 6.21 which can be converted into a universal penetration chart by changing the d values to η ($\eta \propto d$) and the H_s values to h_o ($h_o \propto H_s$).

Since depending on the value of d, f, μ, σ and I a conductor of finite diameter may appear as a semi-infinite slab, in Fig. 6.21, as d increases t_s will be independent of d. For values of H_s below the turning point, t_s/d increases and then falls to zero.

Lim and Hammond [9] published graphs similar to 6.21 for thick steel plates except they plot

$$\frac{\delta_F}{\text{1/2 plate thickness}}$$

instead of t_s/d. In Lim and Hammond's work δ_F is the field penetration depth based on the solution for magnetic non-linear steel. They also observe that as η increases, there is a

reduction in field penetration. η can be increased by increasing f or by reducing ξ. For constant H, the smallest value of ξ is obtained with the step-function approximation and therefore it gives the smallest estimation of field penetration.

The reader must be reminded that t_s is not equal to Lim and Hammond's δ_f, to the step-function theory's δ_s, or to the skin depth δ.

In the linear theory, H and J decay exponentially with depth at the same rate which is defined by δ. At a depth equal to 3δ the power density reduces to zero. Since t_s is a measure of the decay of power and δ_f a measure of the decay of H in a semi-infinite plate, with almost zero H at $2\delta_f$ (ref. 9), it should be expected that for the magnetic non-linear steel,

$$2\delta_f > t_s < 3\delta$$

A numerical comparison between $2\delta_f$ and t_s is possible by calculating t_s for a large diameter conductor (say 7 cm) from equation 4.40 and compare it with the value of $2\delta_f$ obtained from Lim and Hammond's universal penetration depth curves.

Fig. 6.21 shows also the effect of cylindricity on the depth of penetration. For a given H, the value of t_s increases as d decreases. Thus, the effect of taking into account the cylindricity of the conductor is to increase the depth of penetration.

6.8 Method of Solution for Concentric Arrangement of Conductors

For the case of the isolated solid or tubular conductor, in Section 6.3 an effective permeability was derived as a function of the surface field strength.

For a given conductor current, the calculated surface field strength has a different value, if the external or internal diameter of the tube is used.

Since in the concentric arrangement, the current is carried by the inner skin of the tube, the internal diameter should be used in calculating H .

The concentric configuration has three effects:

1. For the same current, the inner surface of the tube is in a higher state of saturation than the outer surface of the isolated tube.
2. There is an increase in loss depending on the wall thickness.
3. The current density decays outwards.

Since the previously derived $\mu_{r,eff}$ expressions were obtained for different operating conditions, it is reasonable to expect, that they will not apply to the case of the concentric arrangement.

Unfortunately, experimental results for the concentric configuration have not been published and therefore, there is no basis on which to evaluate expressions for $\mu_{r,eff}$, as a function of the internal surface field strength.

It is expected however, that for a given tube the expression

for $\mu_{r,eff}$ in the concentric arrangement will be the same as the one applicable to the isolated case, but multiplied by a factor which accounts for all the effects of concentricity. This factor will have to be a function of tube wall thickness, since as the wall thickness is reduced, the isolated and concentric arrangements approach the same loss.

The experimental results of Chapter 7, should be of some assistance.

6.9 Advantages of Proposed Method

The measurements required in order to produce B/H characteristics are replaced by measurements of losses on a rod sample.

A restriction on diameter size does not have to be imposed.

The method is valid for solid or tubular conductors.

The method can accommodate the concentric configuration.

Induction losses in thick steel plates due to sinusoidal surface field excitation can be predicted.

6.10 Alternative Method of Solution

6.10.1 Introduction

In Chapter 5 the step-function theory was used to develop equations for the case of a solid magnetic conductor of circular cross-section. These equations were previously published by Burke and Lavers. However, to date, as far as the writer is aware, the step-function theory has not been applied to the case of tubes in isolation or in a concentric arrangement. Furthermore, the analysis for the solid conductor has not been examined for its validity in the case of small diameter conductors. These cases will now be considered.

6.10.2 Solid conductor

The equations of section 5.2 only apply if $\sqrt{\frac{2}{3}}\ \frac{b}{\delta s} \geq 1$.

If the separating surface reaches the centre before the end of the half-cycle i.e. $\sqrt{\frac{2}{3}}\ \frac{b}{\delta s} < 1$,

$$\text{average power } P = \frac{\omega}{\pi}\left[\int_0^{\tau} \frac{\hat{I}^2 \sin^2\omega t\,dt}{\sigma\pi b\left[2\psi(t)-\frac{\psi(t^2)}{b}\right]} + \int_{\tau}^{T/2} \hat{I}^2 \sin^2\omega t\ R\,dt\right] (Wm^{-1}) \quad (6.3)$$

where R is the d.c. resistance and $\tau = \frac{2}{\omega}\sin^{-1}\left(\sqrt{\frac{2}{3}}\ \frac{b}{\delta s}\right)$

$$\text{or } P = \frac{\omega}{\pi}\left[\int_0^{\tau} \frac{\hat{I}^2 \sin^2\omega t\ \ dt}{\sigma\pi b\left[2\psi(t)-\frac{\psi^2(t)}{b}\right]} + \frac{\hat{I}^2}{2\sigma\pi b^2}\left(\frac{T}{2}-\tau+\frac{\sin 2\omega\tau}{2\omega}\right)\right] \quad (Wm^{-1}) \quad (6.4)$$

For a given b, ω and I, τ is fixed and the second term of equation (6.3) is fixed. The integral in equation (6.4) has to be solved numerically with $\psi(t)$ obtained from equation (5.6) for the different time intervals. The reactive power and hence the power factor can also be evaluated.

(Note that the statement before equation 6 of Burke and Lavers' paper is misleading since $t_c = \frac{2}{\omega} \sin^{-1}\left(\sqrt{\frac{2}{3}}\ \frac{R}{\delta_s}\right)$ is the time to reach the centre and is unspecified in relation to the half-cycle until the value of $\sqrt{\frac{2}{3}}\ \frac{R}{\delta_s}$ is calculated.)

6.10.3 Isolated tube

For this case equation (5.6) is still valid. The time taken for the separating surface to reach the inner radius of the tube is in this case obtained by substituting in (5.6)

$$|\psi(t)| = |b-a| .$$

$$\delta_s^2 \sin^2 \frac{\omega t}{2} = (b-a)^2 - \frac{(b-a)^3}{3b}$$

$$= (b-a)^2\left[1 - \frac{b-a}{3b}\right] = (b-a)^2\left[\frac{2b+a}{3b}\right]$$

$$\text{or } \tau = \frac{2}{\omega} \sin^{-1}\left[\frac{b-a}{\delta_s}\sqrt{\frac{2}{3} + \frac{a}{3b}}\right] \text{ for solid } a \to 0$$

giving equation 5.8.

Equation 5.12 is valid for a tube if

$$\left(\frac{b-a}{2\delta_s}\right)\sqrt{\frac{2}{3} + \frac{a}{3b}} \geq 1.$$

If <1, then the limit of integration is τ instead of T/2 and a second term is added similar to that of equation (6.4) except that in this case the resistance is that of a tube.

6.10.4 Concentric arrangement

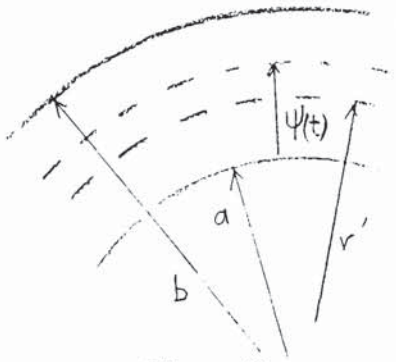

The separating surface is now moving outwards towards b.

$$E(t) = 2\hat{B}_A \frac{d\psi(t)}{dt} \quad \text{for } a < r' < a + \psi(t)$$

and $\quad o \quad$ for $r' > a + \psi(t)$

Since the current is uniform between radii $a+\psi(t)$ and r' and applying Amperes law along the perimeter of radius r',

$$H2\pi r' = \sigma E(t)\, \pi \left[[a+\psi(t)]^2 - r'^2 \right]$$

$$= \sigma 2\hat{B}_A \frac{d\psi(t)}{dt} \pi \left[a^2 + \psi(t)^2 + 2a\psi(t) - r'^2 \right]$$

$$\text{or} \quad H = \frac{\sigma \hat{B}_A}{r'} \frac{d\psi(t)}{dt} [a^2 + \psi(t)^2 + 2a\psi(t) - r'^2] \tag{6.5}$$

$$\text{at } r' = a \qquad H = \hat{H}_s \sin\omega t = \frac{\hat{I}}{2\pi a} \sin\omega t.$$

Substituting in (6.5)

$$\hat{H}_S \sin\omega t = \frac{\sigma \hat{B}_A}{a} \left[\psi(t)^2 + 2a\psi(t) \right] \frac{d\psi(t)}{dt} \tag{6.6}$$

Integrating and noting that $\psi(t) = o$ when $r' = a$

$$\sin^2\left(\frac{\omega t}{2}\right) = \frac{\sigma \hat{B}_A \omega}{2\hat{H}_s} \left[\frac{\psi^3(t)}{3a} + \psi^2(t) \right] \tag{6.7}$$

$$\text{with } \delta_s = \sqrt{\frac{2\hat{H}_s}{\sigma\omega\hat{B}_A}}$$

equation (6.7) becomes

$$\delta_s^2 \sin^2\left(\frac{\omega t}{2}\right) = \psi(t)^2 + \frac{\psi^3(t)}{3a} \tag{6.8}$$

The time to reach the outer surface can be obtained by substituting

$|\psi(t)| = |b-a|$ in equation (6.8) giving

$$\delta_s^2 \sin^2\left(\frac{\omega t}{2}\right) = (b-a)^2 + \left(\frac{b-a}{3a}\right)^3$$

$$= (b-a)^2 \left[1 + \left(\frac{b-a}{3a}\right)\right]$$

$$= (b-a)^2 \left[\frac{2a+b}{3a}\right]$$

$$= (b-a)^2 \left[\frac{2}{3} + \frac{b}{3a}\right]$$

$$\text{or } t = \frac{2}{\omega} \sin^{-1}\left[\left(\frac{b-a}{\delta_s}\right)\sqrt{\frac{2}{3} + \frac{b}{3a}}\right]$$

The instantaneous power $p(t) = 2\hat{B}_A \frac{d\psi(t)}{dt} \hat{I} \sin\omega t$ (6.9)

from equation (6.6), $\frac{d\psi(t)}{dr}$ can be obtained and substituted in (6.9) to give

$$p(t) = \frac{\hat{I} \sin^2\omega t}{\sigma\pi a \left[\frac{\psi(t)}{a} + 2\psi(t)\right]} \qquad (Wm^{-1})$$

The average power $= \frac{\omega\hat{I}^2}{\sigma\pi^2 a} \int_0^{T/2} \frac{\sin^2\omega t}{\left[2\psi(t) + \frac{\psi^2(t)}{a}\right]} dt$

which is valid if $\left(\frac{b-a}{\delta_s}\right)\sqrt{\frac{2}{3} + \frac{b}{3a}}$ is > 1. If < 1 the same comments as for the isolated tube apply.

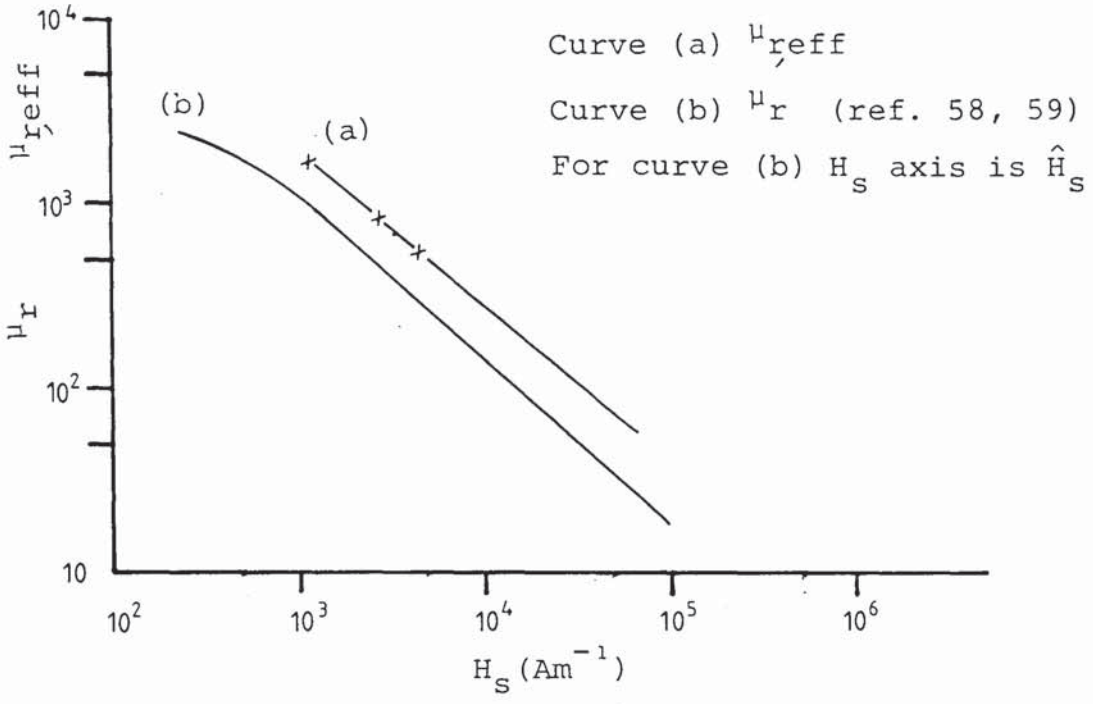

Fig. 6.1 Permeability and effective permeability for mild steel

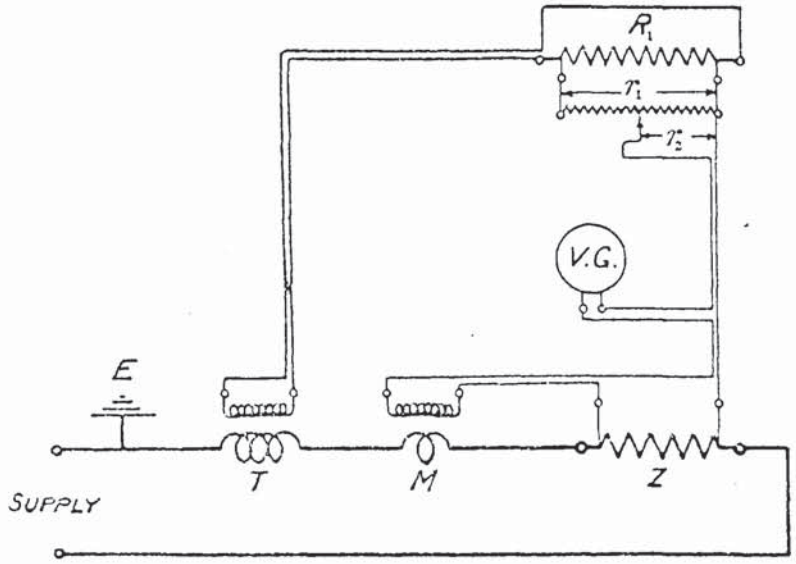

Fig. 6.2 Alternating-current bridge for measurement of low impedances.

E = earth point; T = current transformer; M = mutual inductance; Z = impedance to be measured; V.G. = vibration galvanometer; R_1 = 4-terminal resistance; r_1 = Thomson–Varley potential divider; r_2 = tapped-off portion of divider.

Curve (a) measured K ~ f

Curve (b) calculated K ~ z for linear steel

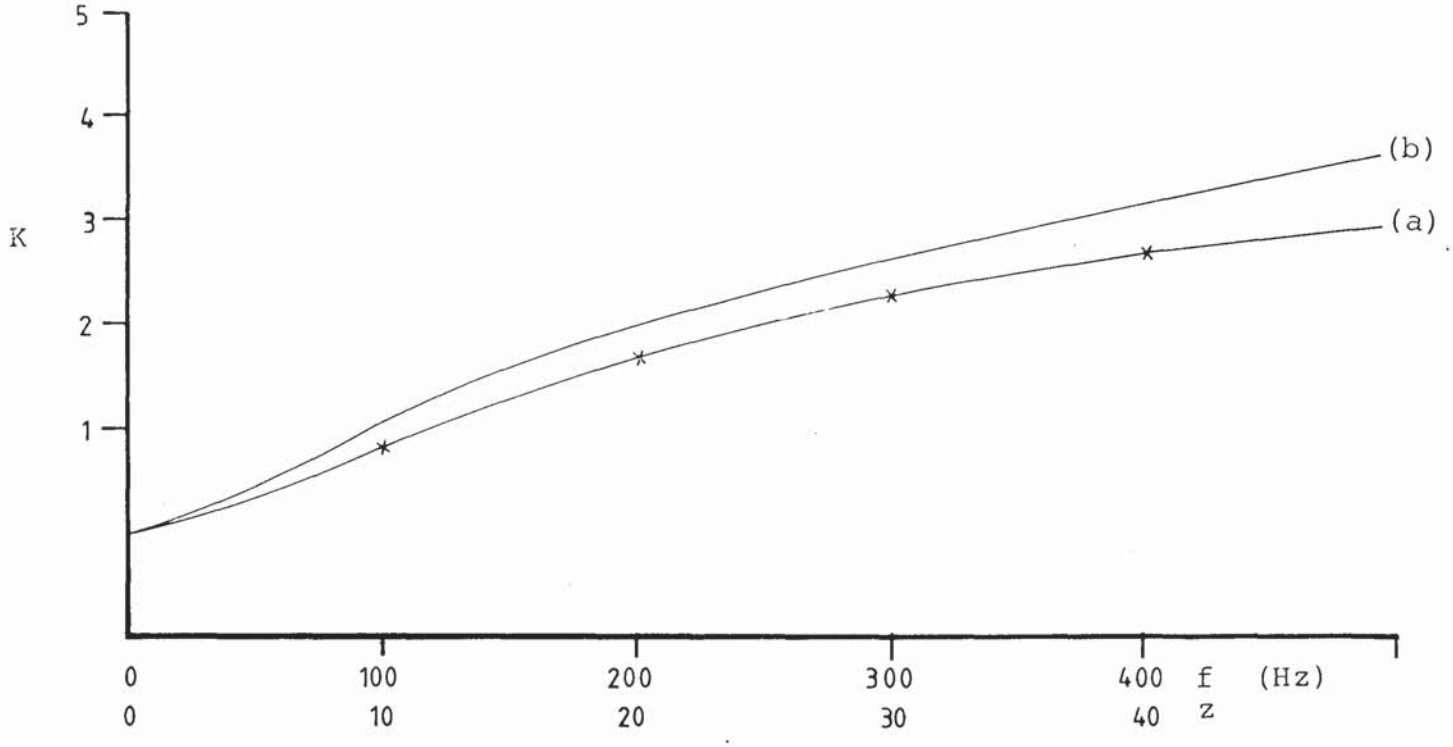

Fig. 6.3 Resistance ratio curves for a steel tube β = 0.183

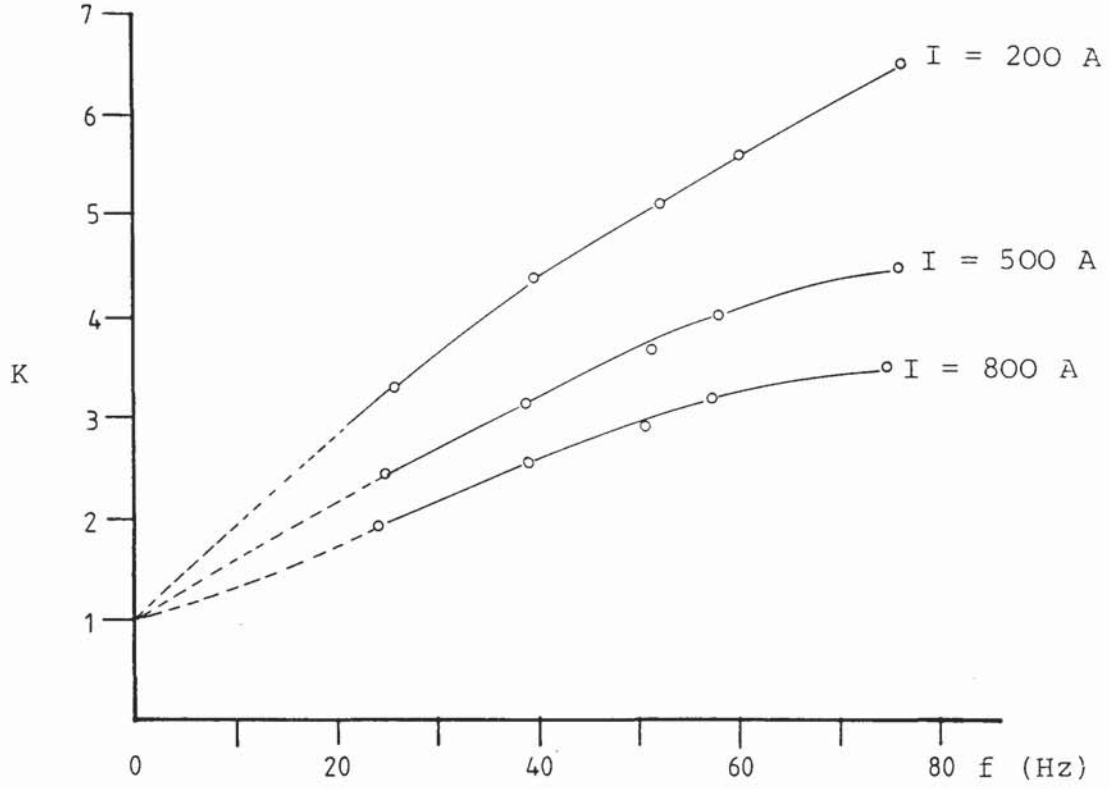

Fig. 6.4 Resistance ratio as a function of frequency and constant current for a steel tube from experimental results of Ref.17

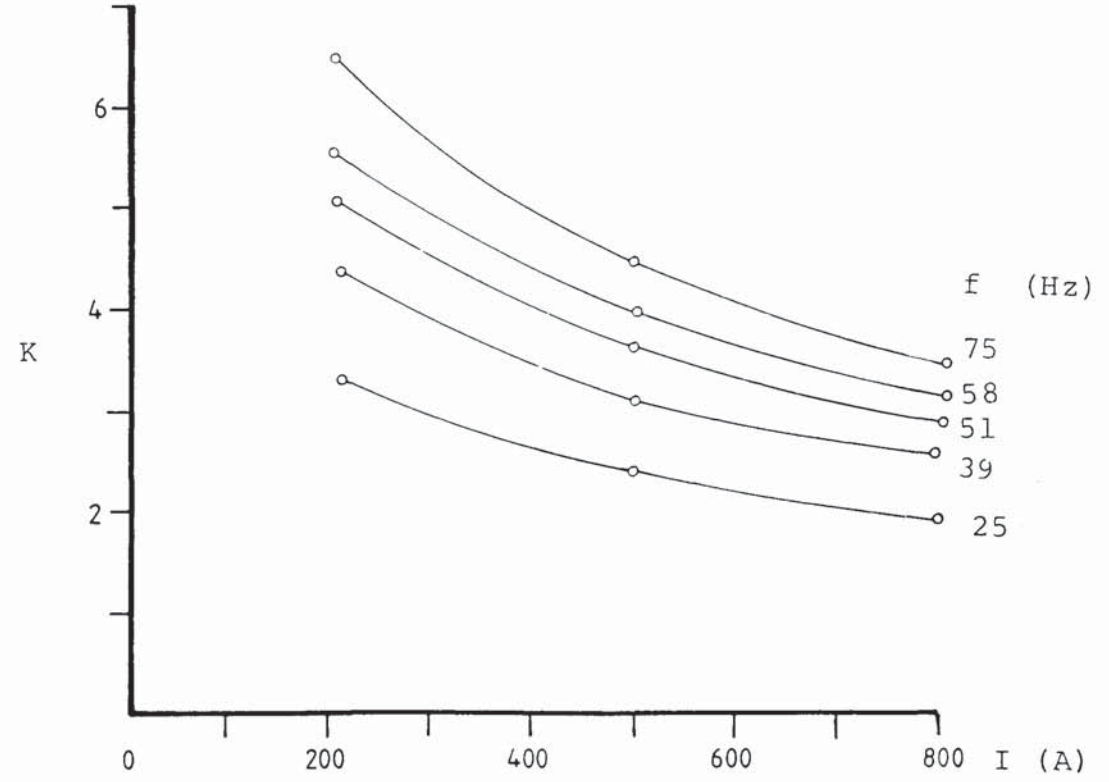

Fig. 6.5 Resistance ratio as a function of current and constant frequency for a steel tube from experimental results of Ref.17

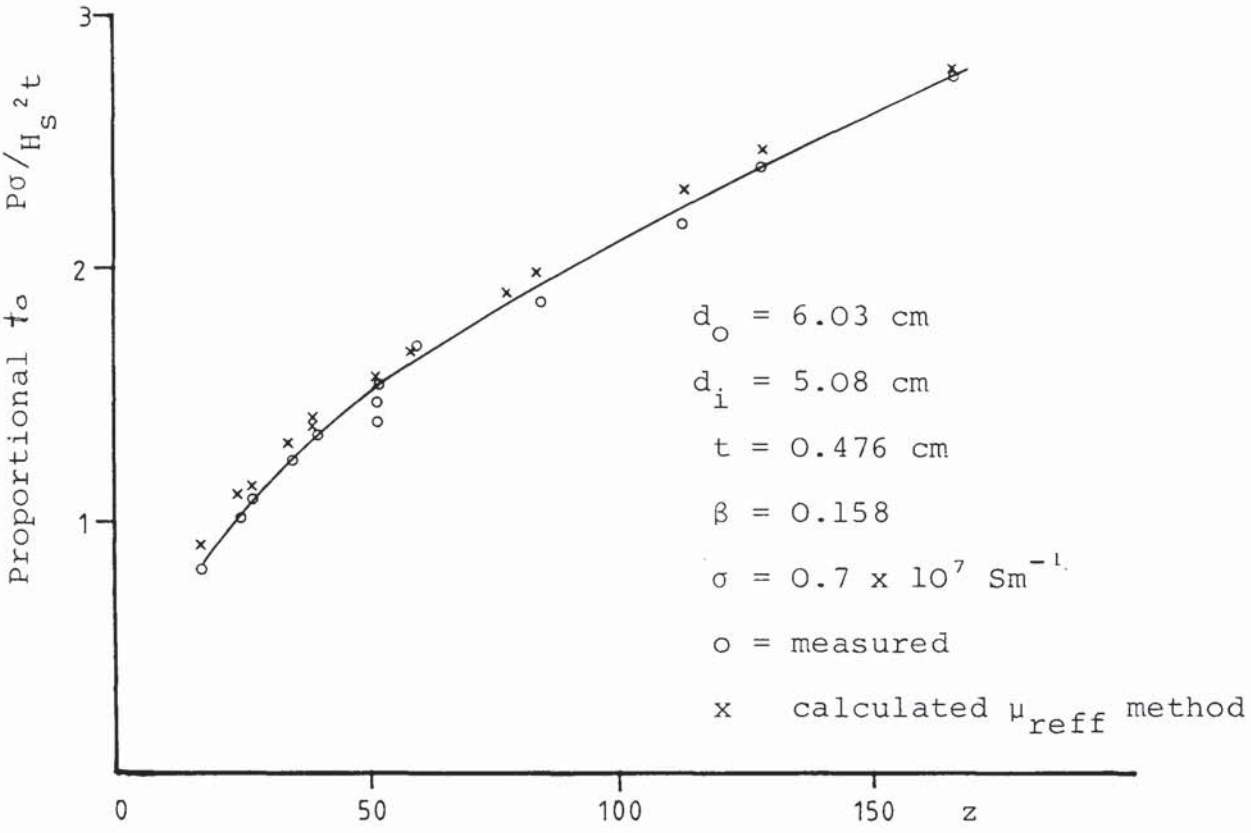

Fig. 6.6 Results of tests 1-15 of Ref.17 plotted in terms of dimensionless parameters

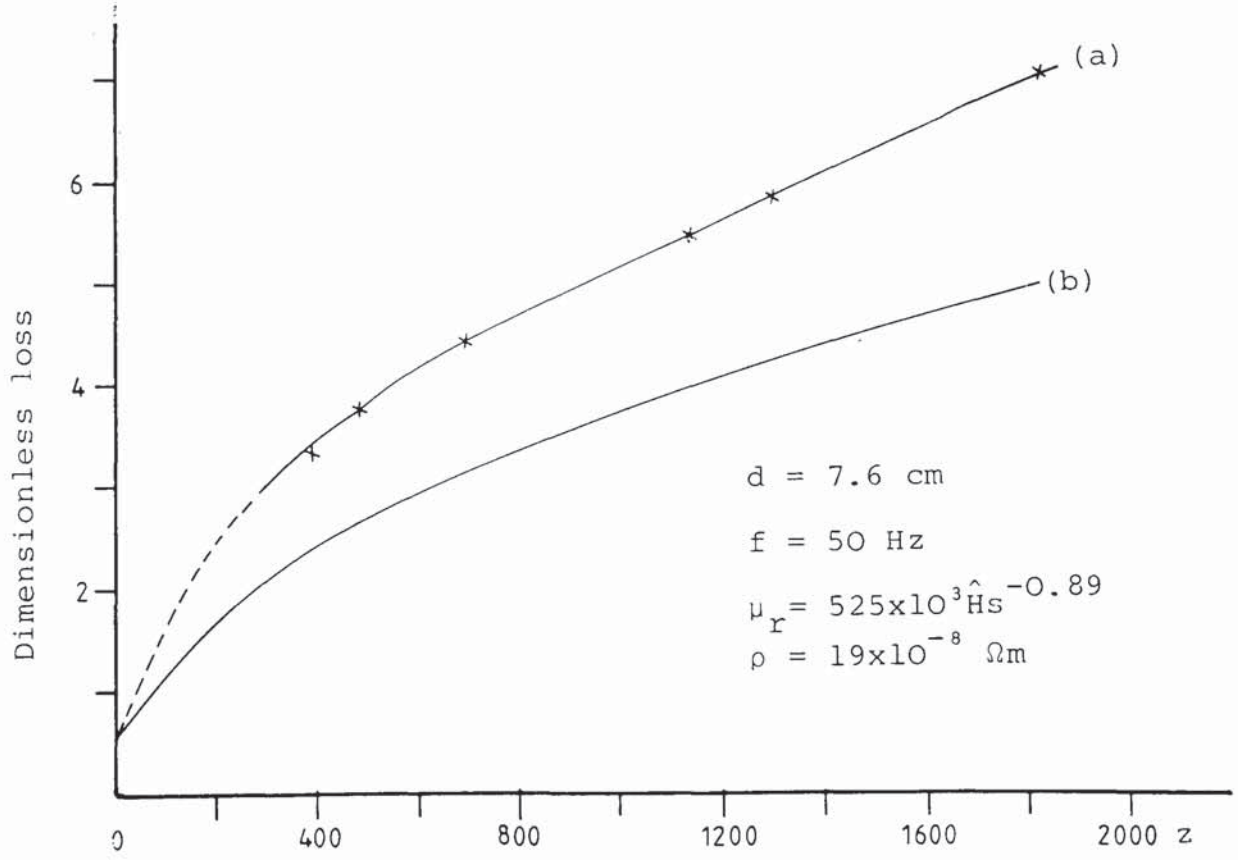

Fig 6.7 Curve (a) Dimensionless measured loss versus z from experimental results of Ref.14

Curve (b) Dimensionless calculated loss versus z based on equations for linear steel

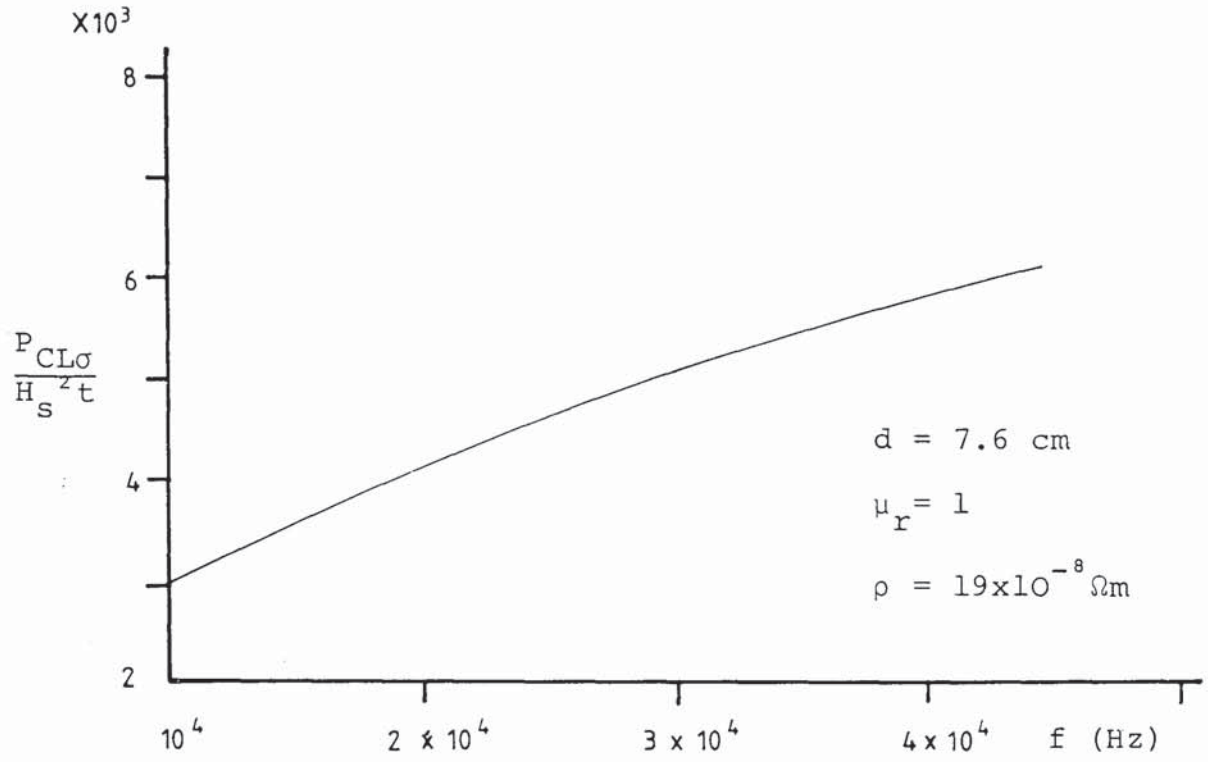

Fig. 6.8 Dimensionless calculated loss as a function of frequency for non-magnetic bar

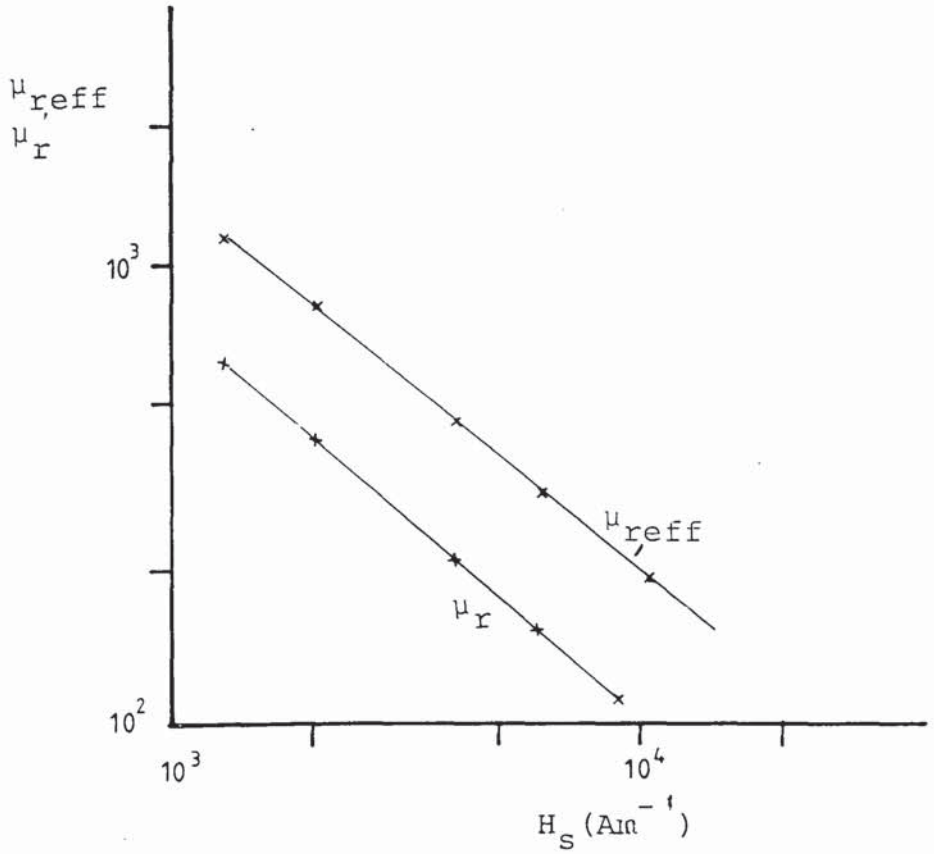

Fig. 6.9 Permeabilities as a function of surface magnetic field strength for ENIA steel μ_r from Ref.14

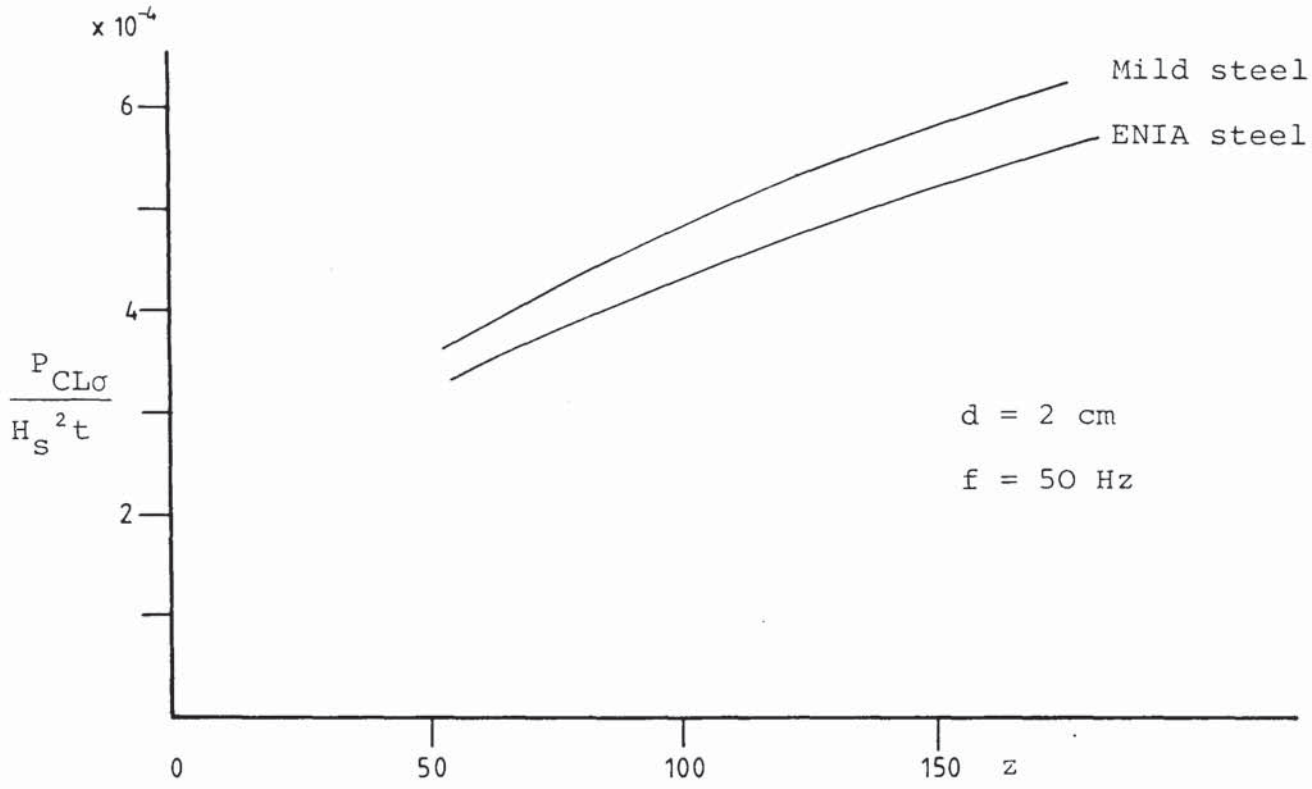

Fig. 6.10 Calculated dimensionless loss as a function of z-linear steel

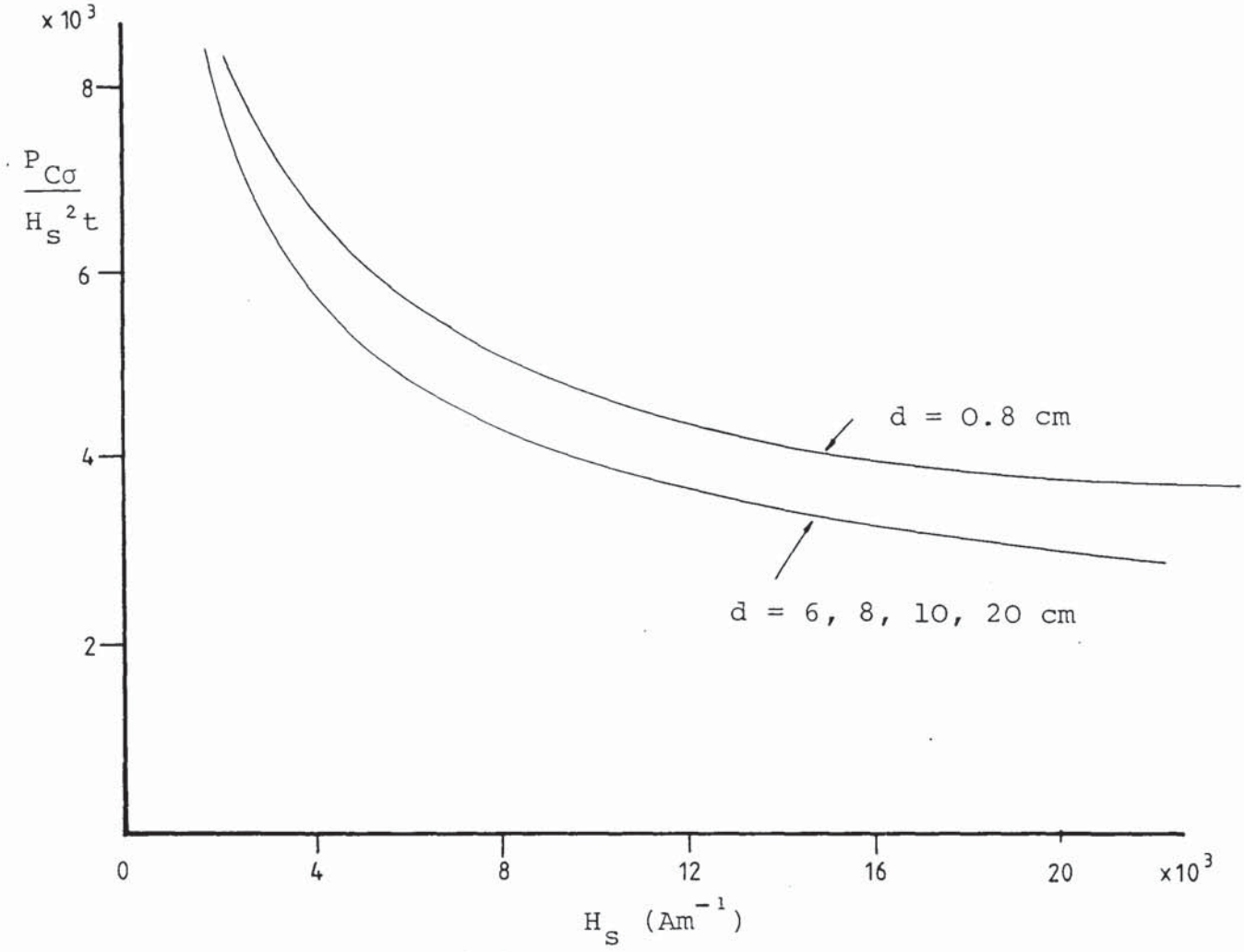

Fig. 6.12 Calculated dimensionless loss as a function of surface field strength for constant bar diameter

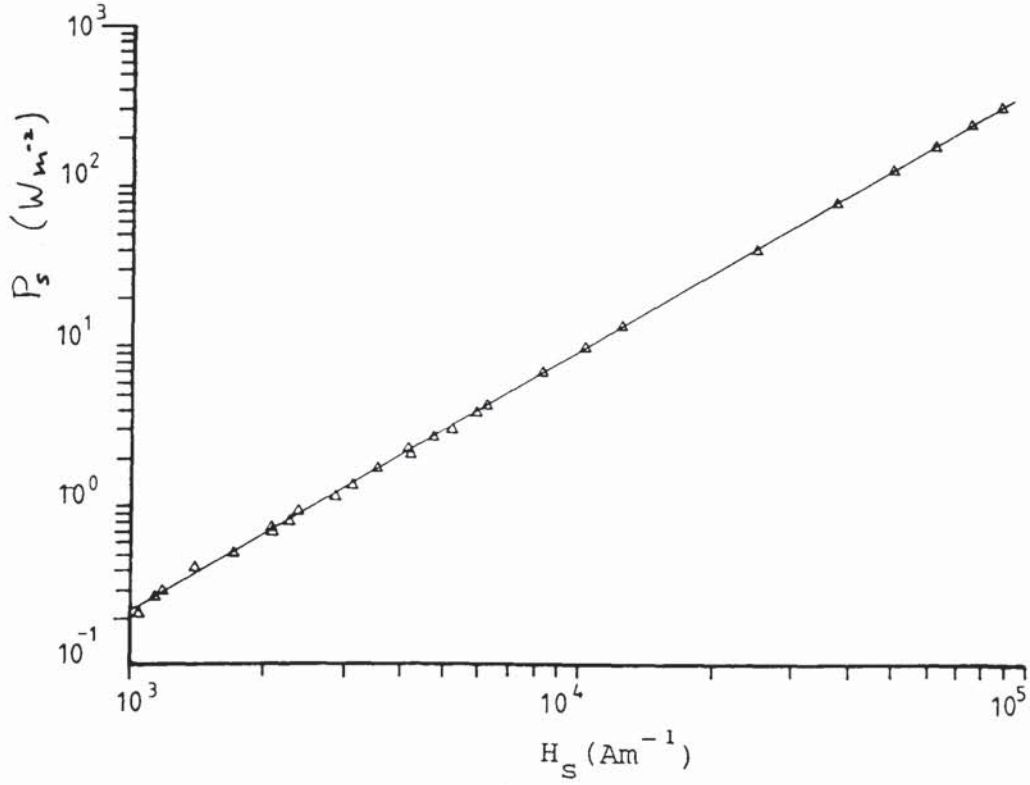

Fig. 6.13 Surface power density versus surface field strength. Results of Ref. 14, 15, 17.

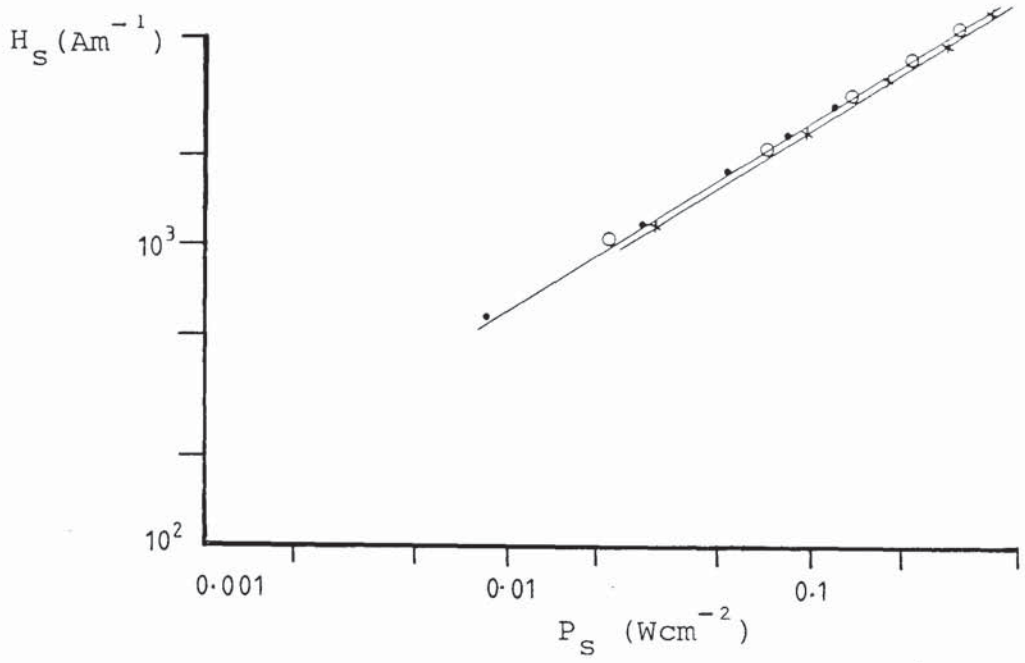

Fig. 6.14 Surface power density as a function of surface magnetic field strength from experimental results of Ref.17

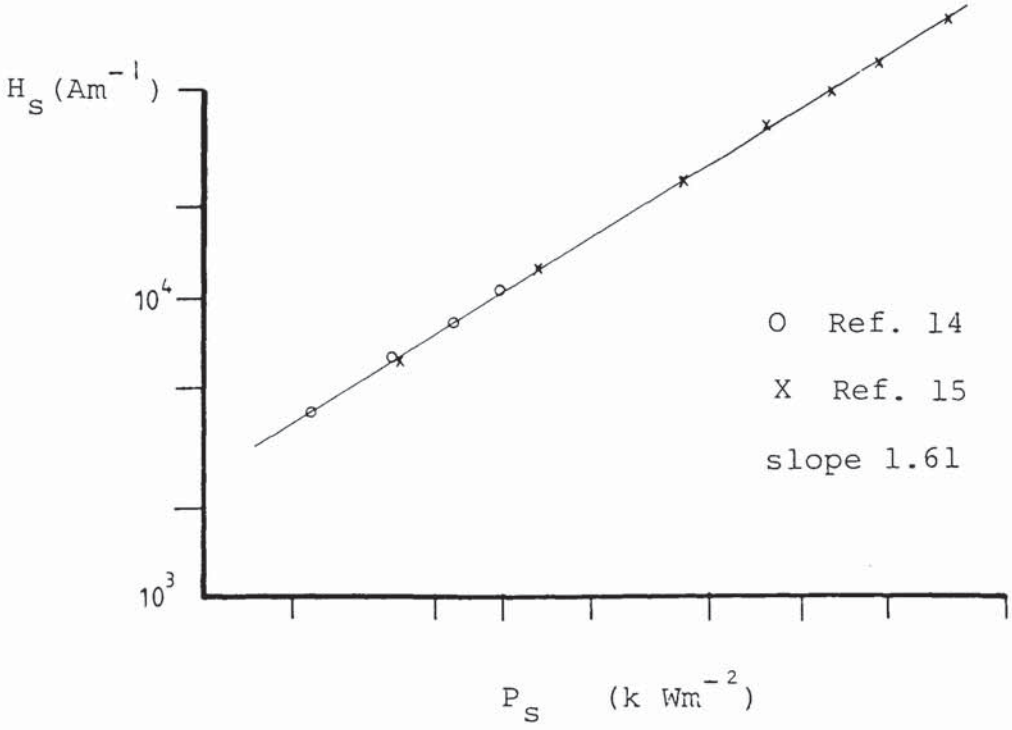

Fig. 6.15 Experimental results of Ref. 14 and 15

Curve (a) $\beta = 0.25\ \sigma = 0.9 \times 10^7\ Sm^{-1}$ slope 1.57

Curve (b) $\beta = 0.25\ \sigma = 0.53 \times 10^7\ Sm^{-1}$ slope 1.58

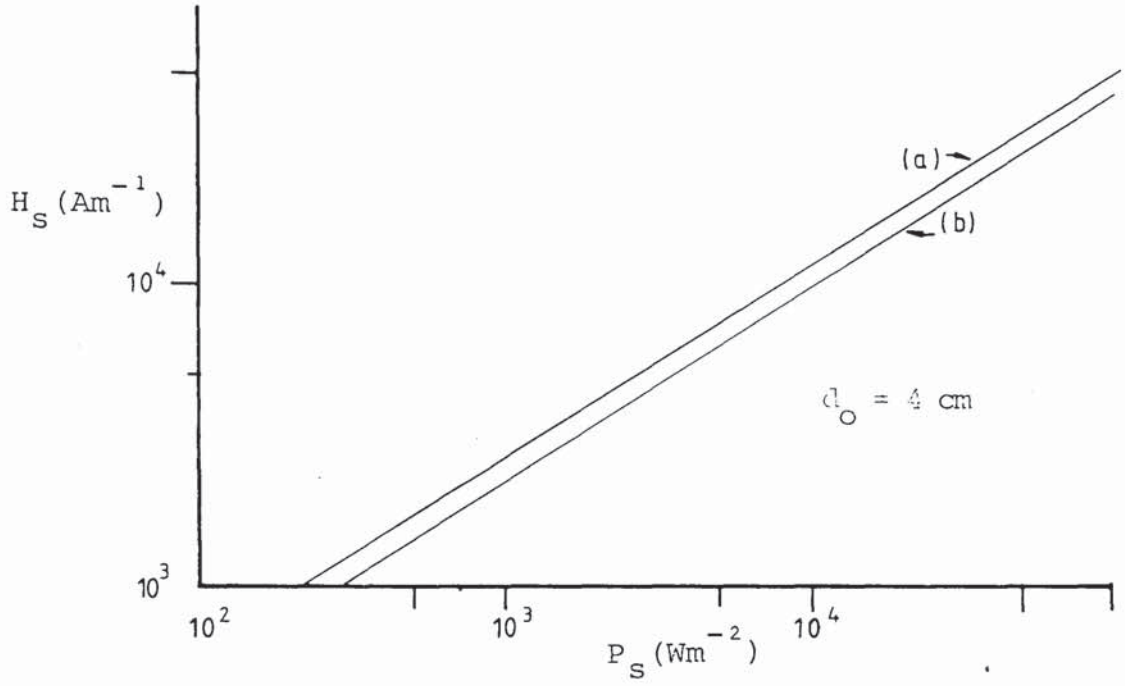

Fig. 6.16 Calculated surface power density (effective permeability method) at 50 Hz, as a function of surface field strength for a tubular steel conductor

Curve (a) $\beta = 0.1\ \sigma = 0.9 \times 10^7 (Sm^{-1})$ slope 1.59 and 1.84

Curve (b) $\beta = 0.1\ \sigma = 0.53 \times 10^7 (Sm^{-1})$ slope 1.59 and 1.84

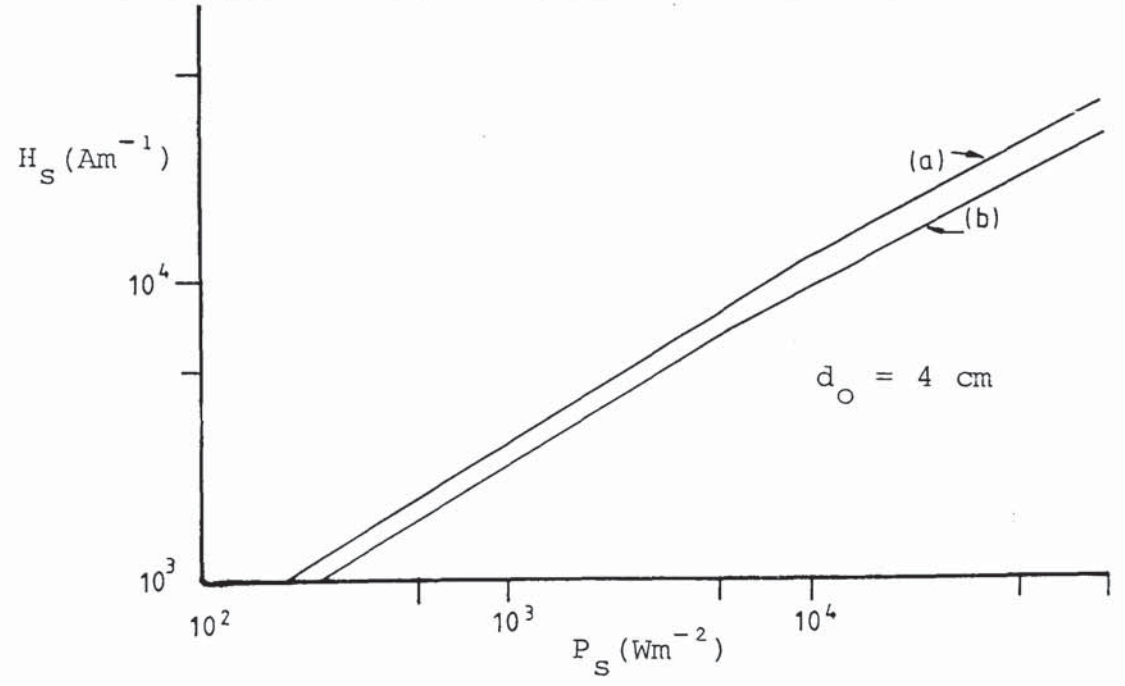

Fig. 6.17 Calculated surface power density (effective permeability method) at 50 Hz, as a function of surface field strength for a tubular steel conductor

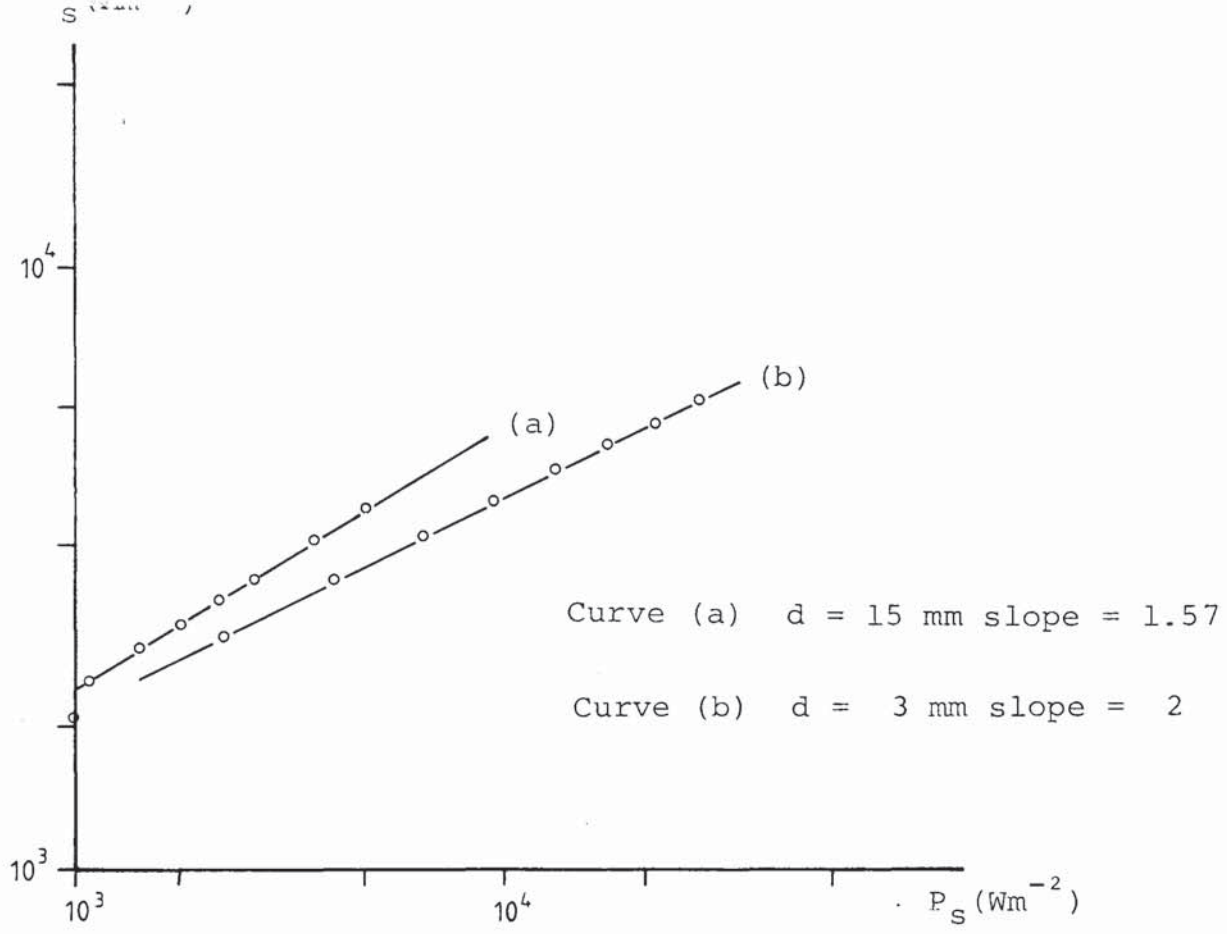

Fig. 6.18 Calculated surface power density at 50 Hz (effective permeability method) as a function of surface field strength for a solid conductor

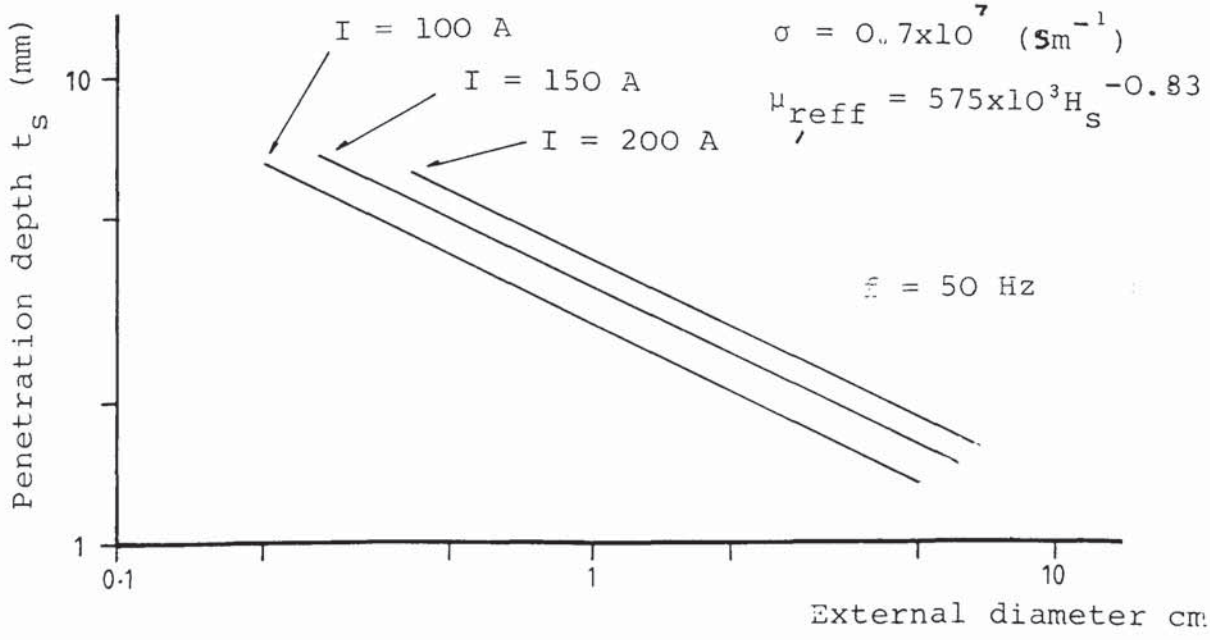

Fig. 6.19 Calculated penetration depth as a function of conductor diameter at constant current

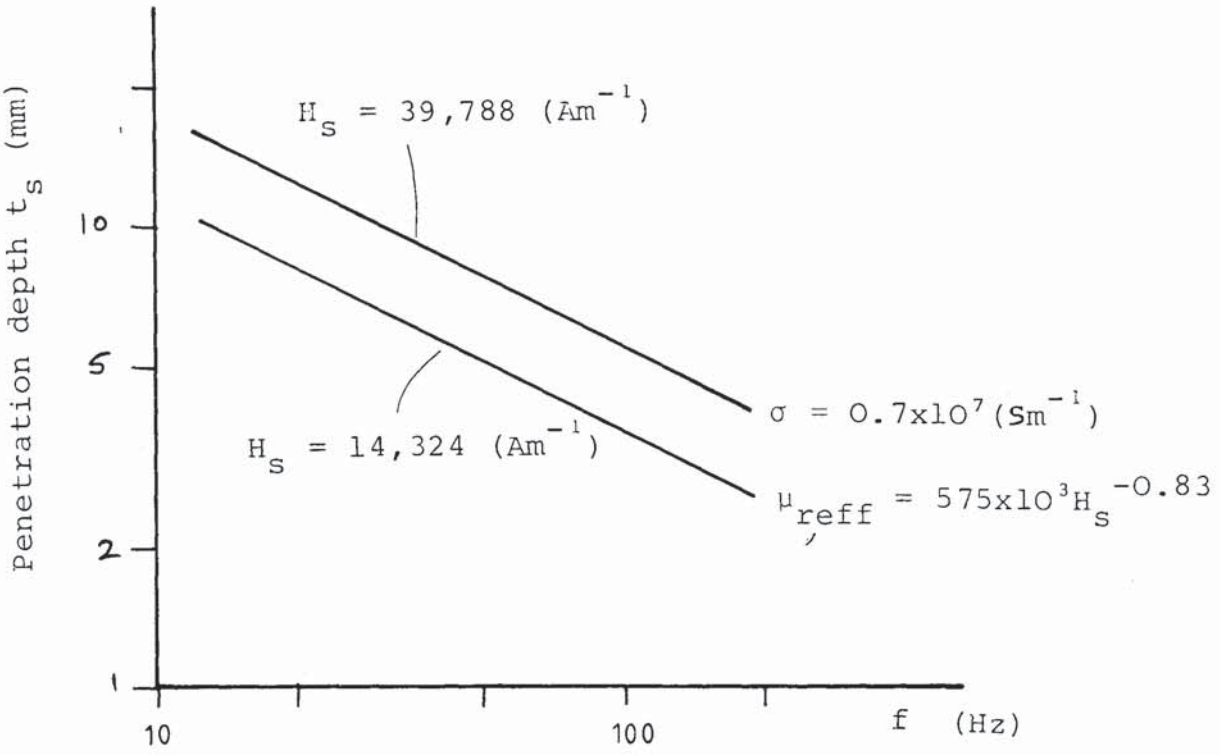

Fig. 6.20 Calculated penetration depth as a function of frequency at constant magnetic field

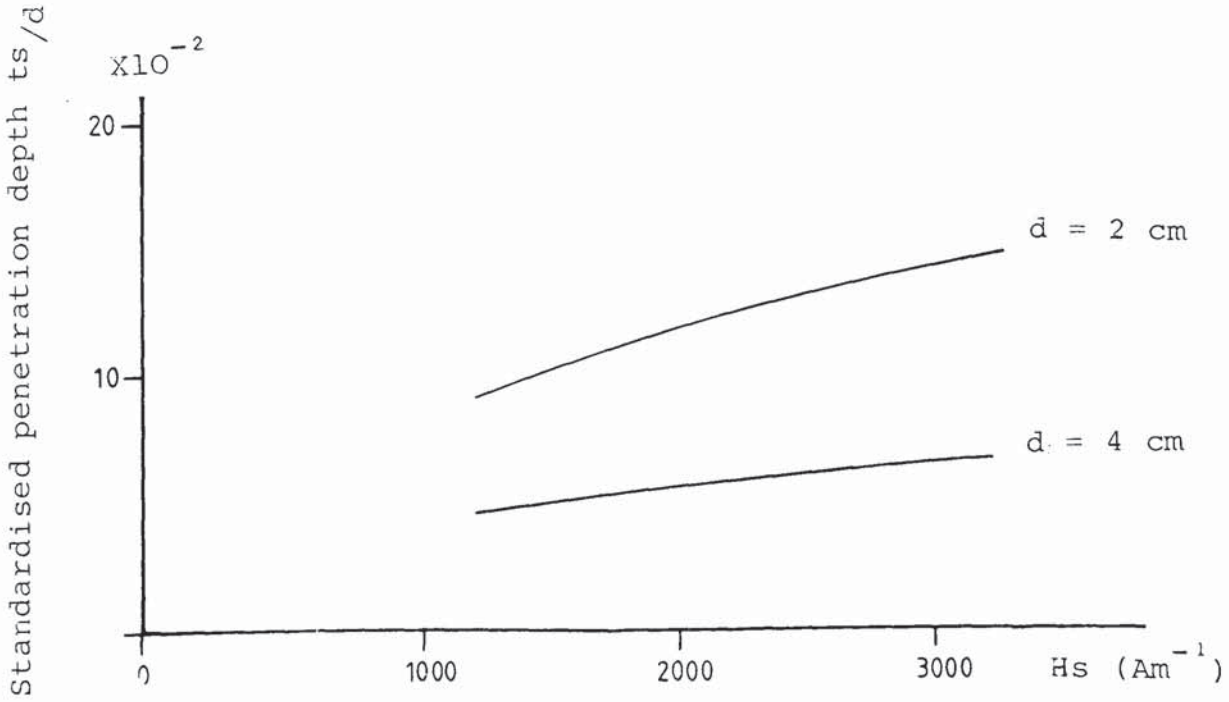

Fig. 6.21 Standardised penetration depth at 50 Hz as a function of surface magnetic field.

CHAPTER 7

EXPERIMENTAL WORK

Chapter Summary

The objectives of the experimental work are stated and a method for measuring power loss is selected.

Calculated and measured loss values are compared for the conductor configurations under investigation, the observed waveforms explained and in some cases predicted.

Chapter Contents

7.1 Scope of Experimental Work

One of the solutions proposed in this thesis, was devised on the premise that available magnetic linear solutions could be simply modified, to accommodate steel conductors. Experimental work is required to establish the validity of this method and its limitations. Equally the validity of the step-function theory to the cases considered must be tested.

The case of the isolated non-magnetic conductor of circular cross-section, solved by Maxwell in 1873, with the solution first tested and proved correct in 1915, is a case where an exact solution can be obtained. The accuracy of Arnold's formulae discussed in Chapter 4 can be established by comparing the answers obtained by the rigorous and approximate solutions, and therefore experimental verification of his formulae is not strictly necessary.

Once a formula is well established so that its accuracy is no longer questioned, discrepancies between calculated and experimental results may be used to infer errors in the initial assumptions such as lack of homogeneity of the conductors, temperature gradients, or additional factors which were not apparent in the formulation of the problem.

It can be stated with confidence, that the formulae applicable to non-magnetic conductors, discussed in Chapter 4, are correct and adequately tested by experiment.

In the case of steel conductors, the solutions discussed in Chapter 5, are based on a number of assumptions and experimental

work is therefore required to ascertain their validity.

If a discrepancy which is greater than the maximum possible experimental error should be found, between the experimental work and the mathematical solution, then the source of the discrepancy will be either in the initial assumptions, or in the mathematical development. Equally, if experiment and theory disagree, it should not be inferred that the experiment is necessarily right. In such cases, the problem should be regarded unsolved, until experiment and theory agree within the limits of accuracy required.

In many cases, the maximum possible experimental error is difficult, if not impossible to establish and details of experimental work are not often included in published papers. Published experimental results are therefore often of limited value in testing an analytical method particularly if as in the case of the effective permeability method it is semi-empirical. Neverthless, published experimental results can be used in the first instance, specially if the experimental work is involved and time consuming. The requirement of independent tests on steel conductors is therefore obvious and leads to the first objective of the experimental work. Within this objective, a number of experiments are necessary, in order to investigate the influence of various parameters on the development of loss. These parameters are:

conductor material properties and composition;

supply frequency;

dimensions;

temperature;

position of return conductor.

Of particular interest, are measurements on electrically thin-walled tubes and the investigation of the concentric arrangement of steel tube and return copper conductor, which have not been considered previously.

The second objective of the experimental work is to establish, if possible, a relationship between the effective permeability and the material parameters of different steels.

7.2 Selection of Method of Measurement

Experimental work reported in the literature refers to copper, aluminium and steel conductors and involves the measurement of effective resistance, impedance and phase angle, or power. The methods adopted are bridge [47][62], and resonance techniques [64], co-ordinate potentiometer [18][63][65], thermal [56][63][66][67][68] and electronic multipliers [14].

In the bridge method and for copper conductors, the current need only be sufficiently large to give the required sensitivity for balance purposes. For steel conductors, the effective resistance must be measured at different values of current. Salter's measuring technique [62] can be used for isolated conductors, provided that the conductor is cooled or measurements are made after the conductor has reached a steady-state temperature. Preliminary measurements with shunts of known values showed that balance was achieved after a number of adjustments and that the balance settings were sensitive to the relative position of the bridge components, and in some cases to stray capacitance effects.

In the case of the concentric arrangement, because of the small diameters of steel tubes used, access to the internal surface of the tube was not possible in order to connect potential leads. The possibility of connecting potential leads by means of steel pins inserted through holes in the manner shown in Fig. 7.1 was dismissed because the potential leads loop

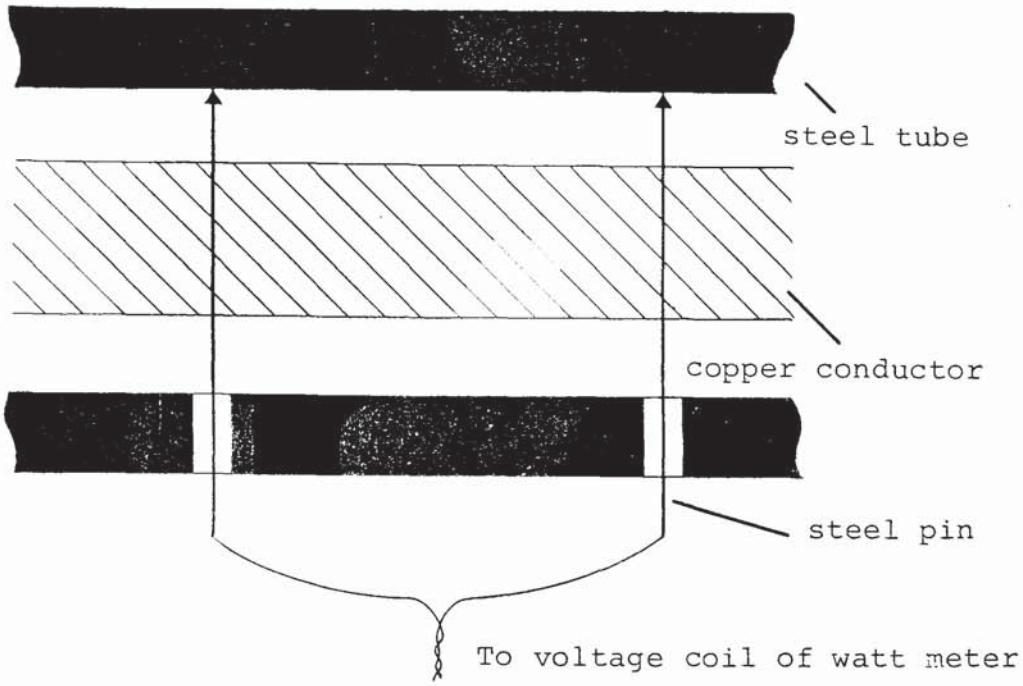

Fig. 7.1 Possible arrangement of potential leads

would enclose a large component of flux due to the external conductor and thus give erroneous results. In addition, the same problems regarding balance would be encountered as in the case of the isolated conductor. Cooling in water would require insulating the internal surface of the tube and the internal conductor. The cross-sectional area of the internal conductor had to be sufficiently large to carry currents up to 300 A without excessive heating and again because of the range of internal diameters considered, insufficient space was available for insulation and adequate circulation of water.

Dwight's [56] or Jackson's [63] thermal method, applied to the isolated tube, is time consuming and in the case of the concentric configuration, impractical. Particularly with short

lengths of test specimen, serious errors are introduced due to heat conduction through the current lugs and cables. The accuracy of the method which uses the slopes of the time/temperature curves, is influenced by temperature gradient across the tube wall and by heat conduction through the end connections. Additional complications would arise in the case of the concentric arrangement, since the temperature rise of the steel tube will be partly due to the heating of the internal conductor, which is in close proximity.

For the order of magnitude of currents anticipated for the present investigation and at low frequencies, the use of a linear coupler has no advantage over the conventional current transformer and in addition, it has to be constructed and calibrated.

Forbes and Gorman's [64] scaling and resonance technique cannot be applied to steel conductors, because the resistance is a function of current .

Having examined and rejected the reported measuring techniques, a method was devised which could give the magnitude of the effective resistance and the angle between the fundamental component of the voltage across the potential leads and the sinusoidal supply current. The circuit used is shown in Fig. 7.2. T is a three-phase phase-shifting transformer, whose secondary phase RN is connected through a variable resistor, to the current coil of a dynamometer wattmeter W. The unknown impedance Z, is connected in series with a standard resistor and supplied with a current, which can be varied by means of a

variable output transformer. With the wattmeter voltage coil connected across the standard resistor and the phase angle of the transformer adjusted to give zero deflection on the wattmeter, the phasor diagram is shown in Fig. 7.3. With the voltage coil connected across the unknown impedance Z, the phasor diagram is shown in Fig. 7.4. The phase angle of the transformer is again adjusted to give zero wattmeter reading. This corresponds to the condition when I_c (Fig. 7.4) has been rotated through angle θ, since for zero wattmeter reading, I_c is perpendicular to I_v.

The difference in the two transformer phase angles, which can be read on a dial marked in degrees lead and lag, gives θ, the phase angle of the impedance Z.

The current through the wattmeter current coil is adjusted to suit the rated current of the current range in use. For measurements on steel tubes the voltage when the potential leads are connected to the tube, needs to be amplified and filtered. Since for a sinusoidally varying supply current, the wattmeter responds to the fundamental component of voltage from the potential leads, the phase angle measured is between the fundamental voltage and current..

The magnitude of Z is obtained from

$$|Z| = \frac{V_{1,rms}}{I}$$

where $V_{1,rms}$ is the rms value of the fundamental component of voltage from the potential leads and

$$Rac = |Z| \cos\theta$$

The sensitivity of the phase angle adjustment can be

improved by the use of a wattmeter calibrated for low power factor, since as the wattmeter reading approaches zero, the power factor approaches zero and therefore, for given voltage and current signals, such a wattmeter will produce a larger deflection.

This measuring technique was tested with a circuit of known phase angle and it was established that the phase angle could be measured to within ±1%. The accuracy in measuring |Z| depends on the voltmeter and ammeter used and the overall experimental error could be kept to under ± 3%. The method however was not adopted as the time required to make measurements was comparable to the bridge technique and could not be adopted for the concentric configuration. The same arguments apply to the case of an electronic phase meter and in fact, the last technique described , constitutes an electro-mechanical phase meter with a built-in filter.

After taking all factors into consideration, it was decided to measure the power loss, since from the heating point of view the parameter of interest is the power developed. This can be measured by a wattmeter. In the past, a wattmeter would not be considered because of the need to amplify the small output voltage signals from the potential leads - a feature overcome in Fig. 7.6.

7.3 Apparatus and Test Procedure

7.3.1 General discussion

The steel tube under test, was connected to the secondary of a transformer and in series with a copper rod, by means of stranded flexible cables. The cables were connected to the tube, by means of easily removable current terminals, which were designed to accommodate different size diameters (Fig. 7.5).

The tube current could be set to a desired value, by means of a variable ratio transformer and was measured by a moving iron ammeter, connected in series with the current coil of a precision dynamometer wattmeter and the secondary of a C.T. (Fig. 7.6).

The input of the potential leads P_1 P_2 was amplified by means of a variable gain amplifier and connected to the voltage coil of the wattmeter W. Resistor R was selected to have a measured resistance value of 1kΩ, so that the amplifier gain was given directly, by the resistance setting on the 0.1% decade resistance box.

The test procedure was to carry out first a dummy run, whose purpose was to note for different test currents, the amplifier gain required, to give without clipping the waveform, a voltage of 2.5 V. This was the smallest voltage range on the wattmeter, which indicates the average power irrespective of the voltage waveform.

At intervals, the circuit was tested for pickup from stray fields, by checking that with the circuit de-energised, the output of the amplifier was zero.

For measurements in air, the tube was allowed to cool between successive readings, but under high ambient temperature conditions, measurements had to be made at temperatures above 20° C.

The potential leads P_1 P_2 served two purposes. They provided the voltage signal for the wattmeter and an output proportional to the surface current density [69]. In order to satisfy the second role, the potential leads were made from two lengths of 36 SWG enamel wire and one end of each length was spot welded to the tube. The other ends were run along the surface and to the middle of the tube and from there twisted together to avoid induced emf's before connecting them to the amplifier input.

The tube current and surface current density waveforms, were displayed on a double beam storage oscilloscope, provided with a digital readout for waveform amplitude and time.

For measurements on the concentric arrangement of tube and return copper rod, the dynamometer wattmeter was replaced by an electronic type which gave a d.c. output proportional to power. Although the accuracy of the electronic wattmeter was inferior to that of the dynamometer type, a high resolution could be obtained by recording the wattmeter output direct voltage on a five digit programmable voltmeter. The readings were recalled at the end of a test run.

It was possible to overload the electronic wattmeter with deflections below full scale on its analogue meter and this was overlooked with some readings in the early stages of the experimental work. Because of the problem in locating the

potential leads in the case of the concentric arrangement, an alternative method of measuring the tube loss had to be devised. The method consisted of measuring the total power dissipated in the circuit beyond terminals ab (Fig.7.6), firstly with the tube some distance away from the copper rod and secondly, with the rod inserted within the tube, in both cases retaining the same cables and connections. To keep the rod concentric, pvc tape was wound round each end and the middle of the rod.

If for a given current,

W_1 = Watts measured for isolated arrangement

W_{T1} = power developed in the tube for isolated arrangement

Wc = power in circuit abc (Fig. 7.6) excluding steel tube

W_2 = watts measured for concentric arrangement

W_{T2} = power developed in tube for concentric arrangement

then $W_1 = W_{T1} + Wc$

and $W_2 = W_{T2} + Wc$

the increase in power ΔW developed in the steel tube due to the concentric arrangement is

$$\Delta W = W_1 - W_2$$

7.3.2 Experimental errors

For the isolated conductor, the power per metre is given by

$$\frac{\text{Wattmeter reading x C.T. ratio x Wattmeter multiplying factor}}{\text{Amplifier gain x distance between spot welds}}$$

The experimental error is thus mainly due to the wattmeter which had a f.s.d. error of 0.5%. The error due to the C.T. and the amplifier can be considered negligible.

Two additional errors are introduced; the first by converting the watts measured into Watts per metre and the second by the slight drift in the wattmeter reading. The first error was due to the uncertainty in the effective distance between the spot welds and the second due to the increase in tube temperature while the current was set to the required value. The overall error is estimated to be better than 3%, which by engineering standards is acceptable.

The method of measurement for the case of the concentric arrangement, is inherently inaccurate since it relies on the difference of two large quantities. Particularly with thin-wall tubes and for large currents, the quantity sought, ΔW, is of the order of the experimental error in the measurement of W_1 and W_2.

For the quantity Wc to be equal in the two conductor configurations, the temperature of the cables should be equal, but its value is not important. Although the cable temperature was not monitored, the problem of temperature rise in the cables was partly overcome, by ensuring as far as possible that the time taken over a set of readings with and without the concentric return conductor, was the same. For each set of measurements, the tube surface temperature is not an indication

that the connecting cables are at the same temperature, because of the location of the current carrying skin and more importantly due to the considerable contribution of heat from the inner conductor.

Since an alternative measuring technique could not be devised, it was decided to proceed with the above method and repeat the measurements a number of times, in the hope that the errors will average out. Particularly for thin-wall tubes and for high currents, there was a considerable spread in the individual measured values of ΔW to make any meaningful statement regarding the percentage experimental error. Further comments are made when the results of these tests are discussed.

7.3.3 Samples tested

Initially, measurements were performed on two steel tubes and a solid steel bar which were of unknown origin. Tubes of known specification were therefore needed of the same material but of different wall thickness. To obtain a range of β values, two lengths of tube were purchased having a nominal external diameter of 3/4" and wall thickness of 1/4" and 14G respectively. These tubes were manufactured to B.S. 980, CDS2 or CDS1, both specifications referring to mild steel and to hard as drawn and annealed conditions respectively.

The thick-walled tube was annealed. Fig. 7.7 photograph (a) and Fig. 7.7 photograph (b) show photomicrographs of the two samples tested which are designated sample A and sample B

respectively.

The manufacturing tolerances were:

outside diameter	± 0.004"
wall thickness for sample A	± 2%
wall thickness for sample B	± 0.003"

Preliminary tests showed that the two samples were behaving differently and therefore could not be considered for investigational purposes as made from the same material. (In the event the analysis proved to be different and is shown below.)

	SAMPLE A	SPREAD ON A	SAMPLE B*
C	0.13	0.159 - 0.093	0.079
M	1.60	1.67 - 1.53	0.46
S	0.38	0.41 - 0.35	0.148
S	0.014	0.018 - 0.011	0.044
P	0.018	0.02 - 0.015	0.013
C	0.11	0.10 - 0.119	0.158
N	0.12	0.131 - 0.103	0.112
A	0.012	0.014 - 0.010	0.036
M	0.022	0.031 - 0.016	0.046
C	0.016	0.018 - 0.014	0.015
B	0.001	0.0023 -<0.0005	0.0004
W	0.06	0.081 - 0.035	0.045
V	0.02	0.032 - 0.011	0.016
N	0.013	0.018 - 0.006	0.009
A	0.024	0.033 - 0.017	0.025
P	0.006	0.008 - 0.0035	0.005
C	0.34	0.42 - 0.32	0.21
S	0.02	0.023 - 0.017	0.017
T	0.003	0.006 -<0.001	0.029

* Sample was sufficiently coherent to produce insignificant spreads.

The only way to ensure material compatibility, was to produce samples of different radial dimensions from the same tube length, by machining the outside diameter to successively smaller sizes and by boring the tube to successively larger internal diameters.

The maximum length of tube which could be processed in this way to give the different sizes, was approximately 60 cm and all subsequent tests were performed on two lengths of tubing 60 cm long, whose radial dimensions were changed for each test run.

To ensure as much as possible a uniform current distribution over the relatively short tube lengths, the plates previously mentioned were constructed (Fig. 7.5).

7.3.4 Measurement of resistivity

With all the samples tested, difficulties were experienced in establishing their resistivity. Initially, the resistance to direct current of a section, was measured by a voltmeter/ammeter method and by a Kelvin double bridge.

For the large cross-section conductors and for small lengths of tube, balance was obtained with the smallest range. In addition, the lengths of the potential leads which were used to make 4-terminal measurements, were found to influence the value of resistance measured and had to be kept to a minimum in order to obtain agreement between the two methods.

With sample B and tubes made from sample A, the resistance to be measured was even smaller and the readings obtained by the two methods were inconsistent.

For each tube produced from sample A, the resistance of a known tube length was measured. Although there was some variation in the measured resistance values, the order of magnitude was established, but a value could not be quoted with

confidence.

This problem was resolved by measuring the d.c. power with the same precision wattmeter used in the a.c. tests. For maximum accuracy, the direct current (which was obtained from a variable 50 V, 10 A, rectified a.c. power supply) and the gain of the two-stage operational amplifier, were adjusted to give maximum deflection on the wattmeter. This method gave repeatable results and the resistivities quoted for samples A and B are based on this method.

Irrespective of the method of measurement, the resistivity is obtained from the measured value of resistance and the measured dimensions of the rod or tube. With tubes, the internal diameter cannot be measured except at the ends and because of manufacturing tolerances, the cross-sectional area is not uniform throughout its length. It can be shown that a 1% change in the external diameter can give a maximum of 6% change in resistivity and for a 1% change in the internal diameter, the corresponding maximum is 3.8%. The implications of these changes are discussed when the test results are considered. Thornton measured the wall thickness of a tube and calculated it from its weight. The difference was 25%!

7.3.5 Measurement of temperature coefficient of resistance

A knowledge of the temperature coefficient of resistance is required for a temperature correction factor to be applied to the value of resistivity. For steels, the temperature

coefficient is within the range 0.0025 to 0.0047/ °C with the lower resistivity steels having the higher temperature coefficient.

Since the larger number of tests were made with tubes from sample A, this steel was selected for the measurement of the temperature coefficient.

The procedure adopted was to heat the tube to steady state temperature, by passing an alternating current through it. By a change-over switch, a direct current was passed and the power measured. The resistivity at a given temperature was calculated from the d.c. power and the tube dimensions. The procedure was repeated for different steady state temperatures.

Special precautions were not taken to exclude any draughts of air on the basis of Dwight's findings [56]. A fall in the surface temperature occurred during the change-over period and the time taken to read the meters. The fall in surface temperature was more significant at temperatures above 60° C, when the heat losses from the surface were sufficiently high, to make the results unreliable. The results for temperatures below 60 °C, showed a straight line relationship between resistivity and temperature and the temperature coefficient of resistance was calculated and found to be 0.003477 per °C at 20 °C.

7.4 Isolated Steel Bar

7.4.4.1 Introduction

The only experimental work identified in the literature on steel bars is that of Bowden and Davies [14], Rajagopalan and Murty [18] and Burke and Lavers [15]. Burke and Lavers' method of test has not been mentioned in Section 7.2, since their method was not reported.

Since the theory developed by Bowden and Davies is restricted to a semi-infinite slab, their experimental work was conducted on a 7.6 cm diameter bar which was electrically equivalent to a semi-infinite slab (see also Sect. 4.6). High currents were required for these tests in order to achieve field strengths in excess of 10,000 (A m^{-1}) . It was therefore decided, for the purpose of independent experimental work, to carry out tests on a solid bar of approximately one cm diameter, at 50 Hz and at variable frequency. Thus the required field strength could be achieved by smaller currents obtainable with available equipment.

The purpose of the variable frequency tests was to confirm or otherwise that:

1. The power developed could be predicted at all frequencies within the range used.
2. The electrical performance of the bar at variable current or frequency conditions, can be described by the dimensionless parameters developed in Sect. 4.9.1.

3. Thornton's assertion

surface power density = constant x $H_s^{1.57}$ x $\sqrt{f}$ (7.1)

is valid.

4. The power index of H_s is independent of frequency.

In addition variable frequency tests introduce a scaling factor. The important parameter in induction and resistance heating is the "skin" depth and increasing frequency effectively increases the diameter of the test specimen.

7.4.2 Experimental procedure

A bright mild steel bar, which was available in the laboratory, was used for these tests. The bar diameter was measured with a micrometer on a number of places along the length of the bar which was 1.5 m long. The average of these readings was 1.11 cm.

The current was supplied to the bar through copper end plates which were bolted onto the bar ends. The secondary of a transformer was connected to the bar by means of flexible cables, which were attached to the end plates by a bolt and nut arrangement.

The spot welded ends of the potential leads, were 50 cm apart and the instrumentation was as described in Sect. 7.3.1. The return conductor was left in the same position throughout the power loss tests.

For the 50 Hz tests, the current was adjusted to the desired

value by varying the supply voltage to the transformer by means of a variable output transformer.

For the variable frequency tests, a synchronous generator was used, driven by a variable speed d.c. motor, whose speed could be adjusted by means of coarse and fine manual speed control.

The generator frequency could be varied between 22 and about 70 Hz, but the output of the generator was limited at the extreme frequency ranges, since it was unable to supply the necessary voltage at low frequencies and the current at high frequencies. After some exploratory tests, it was found that only two currents could be accommodated throughout the frequency range. The bar current was varied by changing the generator 's field excitation.

Adjustment of the speed to give a desired frequency, was in some instances made difficult by sudden changes in the d.c. supply provided by a d.c. motor-generator set. This was due to the voltage regulator becoming inoperative prior to commencing the tests. Since the variable frequency tests commenced towards the end of the project, the measurements could not be delayed and it was decided to proceed. Although this situation caused some inconvenience, the results were not unduly affected, since readings were taken quickly and only if the required frequency was indicated. The frequency was not accurately measured, as it was read off from an analogue meter with a scale calibrated in speed and corresponding generator frequency. Further inaccuracy was introduced by a small drift in the wattmeter and

Table 7.1. 50 Hz Test Results On Steel Bar Immersed In Water

I	H_s	Decreasing Current		Increasing Current		Pms	Pc	Pdc	z	$\frac{P_m \sigma}{H_s^2 t} \times 10^3$	K	Remarks
		P_m	Bar Temp.	P_m	Bar Temp.	$W m^{-2}$	$W m^{-1}$	$W m^{-1}$				
A	Am^{-1}	Wm^{-1}	°C	Wm^{-1}	°C							
42	1204	10	19.1	10.1	18.6	286	11.3	2.75	117	8.22	3.65	Bar Diameter 1.11 cm
48	1376	12.8	19.2	12.9	19.1	368	13.9	3.6	105	8.1		Restivity 15.1×10^{-8} Ω m
54	1548	16	19.7	16	19.5	459	16.9	4.5	95	7.96		Calculated Losses
60	1720	19.2	19.9	19.2	19.8	550	20	5.6	87	7.74	3.42	Based On
72	2065	26.2	20.1	26.4	20.1	751	26.9	8.7	75	7.36		$\mu_{reff} = 536 \times 10^{-3} H_s^{-0.833}$
84	2409	34	20.2	34	20.3	975	34.5	11	66	6.99	3.1	
96	2753	42.2	20.4	42.5	20.8	1213	42.9	14.4	59	6.66		Frequency 50 Hz
108	3097	51.5	21	52.3	21.1	1485	51.9	18.2	53	6.44	2.84	
120	3441	61.5	21.2	62.1	21.6	1772	61.6	22.5	49	6.21		
144	4129	83.1	22	82.7	22.5	2377	83	32.3	42	5.8	2.56	
168	4817	106.3	22.6	106.5	23.7	3040	106.8	44	37	5.47		
192	5506	133	22.3	132.5	24.6	3814	132.9	57.5	33	5.22	2.3	
216	6194	160.8	22.5	160.8	25.5	4611	160.9	72.8	30	5		
240	6882	188.4	22	190.8	26.3	5402	191.2	89.9	27.4	4.74	2.1	

Table 7.2. Variable Frequency Test Results On Steel Bar In Air

I A	H_s Am^{-1}	f Hz	$f^{0.5}$ $Hz^{0.5}$	P_m Wm^{-1}	Bar Temp °C	Pc Wm^{-1}	Pms Wm^{-2}	z	$\frac{P_m \sigma}{H_s^2 t} \times 10^3$	K	Pdc Wm^{-1}	Remarks
96	2753	22	4.69	30.5	24.8	29.8		25.9	4.8	2.12	14.4	
120	3441	"	"	44	28.8	43		21.5	4.33	1.92	22.5	
96	2753	30	5.47	35	27.3	34.2	1000	35.3	5.5	2.43		
120	3441	"	"	51.3	24.9	49.2	1471	29.3	5.17	2.28		Details as in
96	2753	40	6.32	39.6	27.2	38.8		47.1	6.23	2.75		7.1. except
120	3441	"	"	57.9	29	55.8		39.1	5.83	2.57		for frequency
96	2753	50	7.07	43.4	23.8	42.9		58.8	6.83	3.02		
120	3441	"	"	63.9	27.9	61.6		48.9	6.44	2.84		
96	2753	60	7.75	47.7	26.4	46.6		70.6	7.51	3.32		
120	3441	"	"	68.9	29.2	66.9		58.6	6.94	3.07		
96	2753	70	8.37	50.7	27.5	50	1453	82.4	8	3.53		
120	3441	"	"	73.2	27.9	71.7	2099	68.4	7.37	3.26		

ammeter readings due to the increase in the bar temperature while the meters were read.

The bar was supplied from one phase of the generator and to ensure balanced load conditions, two resistors were connected across the other two phases. Because of the high power factor of the test circuit, connecting an inductor in series did not make any difference to the current waveform and therefore a resistive load was used.

The 50 Hz tests were performed with the bar, which was varnished, immersed in a trough filled with water. The potential leads were positioned according to Salter's [62] and Jackson's [63] findings and the bar temperature was measured by a thermo-couple attached to the bar.

The variable frequency tests were carried out in air and the bar was allowed to cool between successive tests. As before, special precautions were not taken to exclude any draughts and it is expected that the bar surface temperatures, measured by a surface temperature probe, are below their true values, which in any case are difficult to ascertain. Because of all the other inaccuracies involved, it was felt that refinements in measuring surface temperatures were not necessary.

7.4.3 Results and discussion

The test results are shown in Tables 7.1 and 7.2. Fig. 7.8(a) and Fig 7.8(b) show the supply current and surface current density waveforms for the currents of 48 A and 216 A

respectively. Although the current density waveform for the higher current is distorted, saturation is not pronounced.

The current waveform has a small third harmonic component but measurements have shown, by deliberately distorting the current waveform, that the contribution of the harmonics to the losses was small.

The calculated values of power loss at 50 Hz, included in Table 7.1, are in good agreement with the measured values above 60 A. The disagreement below 60 A suggests that for this particular steel, the turning point on the μ_r/H-curve occurs at about 1700 (A m^{-1}).

The variable frequency results are shown in Table 7.2, where in this case the calculated values are slightly lower than the measured ones (max. error 3.6%). The dimensionless factors calculated from the variable frequency and variable current tests are plotted in Fig. 7.9. According to the theory of dimensional similarity, irrespective of the value of resistivity, for a given diameter, all points should lie on the same curve. Fig. 7.9 shows that the points from the variable frequency tests lie on a slightly different curve from the points from the 50 Hz tests, although the largest difference is 5.2%. This difference can be explained by temperature effects since the power loss values are measured values. In addition to the experimental error, which is expected to be larger in the case of the variable frequency tests, changes in the bar temperature affect the measured power loss.

The results for 60, 84 and 120 A in Table 7.1 can be used to

demonstrate the influence of temperature. The reason for selecting these particular currents is that the calculated and measured values of power loss at 50 Hz are in good agreement. A temperature correction factor for resistivity can therefore be applied to the calculated values of power, which will reflect the measured loss values, had the temperatures been higher. Allowing for a temperature differential of 7 °C between the 50 Hz and variable frequency tests, the resistivity at 27 °C assuming a temperature coefficient of resistance of 0.004 °C (within the acceptable range for steels), the resistivity is approximately 15.5 $\times 10^{-8}$ (Ω m). The following values of parameters are calculated for a resistivity of 15.5 $\times 10^{-8}$ (Ω m).

I	% Change in Resistivity	P_m	% Change in P_m	z	% Change in z	$\frac{P_m \sigma}{H_s^2 t}$
60	2.6	20.3	1.5	84.5	2.9	7.98
84		43.5	1.4	57.3	2.6	6.67
120		62.5	1.46	47.6	2.7	6.13

The above results show that a 2.6% change in resistivity, produces a change of 1.5% in power loss. However, this combined with the larger change in z, which is reduced, brings the two curves of Fig. 7.9 in line.

It can be concluded that the dimensionless factors $\frac{P_m \sigma}{H_s^2 t}$, z and β which in this case is 1, as predicted, describe the performance of the steel bar at constant temperature.

The power developed as a function of a 50 Hz current is shown in Fig. 7.10 and the power due to a direct current is

included for comparison.

The ratio of a.c. to d.c. resistance as a function of current and for different frequencies is shown in Fig 7.11. The temperature effect on the 50 Hz characteristic is evident. For a constant current, the skin effect is less pronounced at low frequencies, resulting in a lower resistance ratio.

The power as a function of frequency is shown in Fig. 7.12. Since for constant current, the power is proportional to the effective resistance Rac, Fig. 7.12 also shows the Rac/f characteristic.

Fig. 7.13 shows the log/log plot of the surface power density and surface field strength from which the power index of H_s is 1.61. The points for low values of H do not lie on the straight line because the $\log \mu_r / \log H_s$ graph is non-linear, for values of H below the turning point of the μ_r / H curve. Thornton's [17] experimental points for low values of H_s, also deviate from the straight line characteristic, except that he attributed this to experimental errors.

The characteristics of Fig. 7.13 corresponding to different frequencies are parallel, showing that the power index of H_s is independent of frequency.

Thornton [17] carried out tests on a 6 cm O.D. tube in order to investigate the validity of equation 7.1. By reference to Jeans [70] Thornton attempted to explain the effect of frequency. The following is an extract from his paper.

"With constant permeability, the dissipation of heat is proportional to the square root of the frequency of the current,

other things being equal. Although there was no reason to suppose that variation of permeability would affect this law, a test was carried out to verify it. The results are given in Table 2."

The results of this Table have been plotted and are shown in Fig. 7.14. Since the tube tested by Thornton is electrically solid, the experimental results of this section can be used to draw conclusions regarding frequency effects on steel conductors. These results have been plotted and are shown in Fig. 7.16.

Thornton missed a number of points by putting forward equation 7.1. If at all applicable, equation 7.1 will only be valid for the condition f>0 since the currents are not field induced. For f=0, the power loss is not zero but equals the d.c. power corresponding to a particular value of current.

For a discussion on the validity of equation 7.1, the case of the semi-infinite slab can be recalled, where, for constant H_s and μ_r the loss is proportional to $\sqrt{f}$. A small diameter conductor at high frequencies will also behave as a semi-infinite slab and the proportionality of power loss to $\sqrt{f}$ is illustrated in Fig. 7.15. These points were discussed in more detail in Section 4.6 where it was also shown that at 50 Hz and depending on the value of current and resistivity it is possible for a steel conductor of 6 cm O.D. to be indistinguishable in its behaviour from a semi-infinite slab. It is therefore by coincidence, that the tube tested by Thornton, not only behaved as a solid conductor, but also appeared as a semi-infinite

slab.

Examination of Fig. 7.16 shows that for the size of conductor diameter tested (by the author), equation 7.1 does not apply since, as predicted by theory, the projected lines joining the points for a constant current and hence H_s and μ_v, do not pass through the origin.

Thornton's hypothesis that equation 7.1 could be valid is based on a misconception and does not take into account cylindricity effects and the influence of the value of current in altering electrically the dimensions of a tube. However, he observed the effects of hysteresis on the validity of his empirical law. The proportionality of loss to $\sqrt{f}$ is only valid if hysteresis is absent, or a small percentage of the total loss.

The spread of the points on the graphs of Fig. 7.14, are due to experimental errors, which became apparent previously.

The prediction of loss depends on a combination of resistivity and effective permeability. It appears that for a particular value of resistivity there is a corresponding effective permeability function. So far there is insufficient evidence to prove or disprove this statement.

In Section 6.3.5 it has been shown that the power loss can be predicted by modifying the effective permeability function appropriate to the "Thornton steel" by a multiplying factor. The calculated results are shown in Table 7.3 and are in agreement with the measured values. In the same Table the calculated results based on a resistivity of 14×10^{-8} (Ω m) and effective

Table 7.3. Calculated Loss Values At 50 Hz - Steel Bar

Bar Diameter 1.11 cm

Current	Calculated Loss (Wm^{-1})		Measured Loss (Wm^{-1})
(A)	Resistivity 14 x 10^{-8} Ω m Effective Permeability from 575 x 10^3 $H_s^{-0.83}$	Resistivity 15.1 x 10^{-8} Ω m Effecitve Permeability From 575 x 10^3 $H_s^{-0.83}$ x 0.885	
42	11.3	11.1	10.1
48	14	13.8	12.9
54	16.9	16.6	16
60	20.1	19.7	19.2
72	26.9	26.5	26.4
84	34.6	34.1	34
96	42.9	42.3	42.3
108	52	51.3	51.7
120	61.7	60.9	61.7
144	83	82	83
168	106.7	105.5	106
192	132.7	131.3	133
216	161	159.1	161
240	191	189.1	189

permeability given by $575 \times 10^{3} H_s^{-0.83}$ have been included and are also in agreement with the measured values. In fact there are a number of combinations of effective permeabilities and restivities which will predict the measured losses. A knowledge of the correct value of resistivity is therefore important and its value determines a unique effective permeability function.

There is some evidence to believe, that a high value resistivity is accompanied by a lower effective permeability characteristic. This is to be expected, since the high resistivity steels have a lower permeability as derived from their B/H curves. It has been shown, that due to the tolerances in the external and internal diameters of tubes, an accurate measurement of resistivity is difficult to achieve. Whilst for an electrically thick-wall tube the value of the internal diameter is irrelevant to the calculation of power loss, it has an influence on its calculation through the value of resistivity.

7.5 Isolated Steel Tube

7.5.1 Introduction

To the author's knowledge, the only experimental work on steel tubes is that reported by Dwight [56] and by Thornton [17]. Their results have been discussed in Section 6.4. It was therefore considered appropriate to extend the work of the previous section on a solid bar to steel tubes, so that the method of calculation developed in Chapter 6, could be tested on independently obtained experimental results with known limitations (see also Section 6.4.1.).

Loss measurements were performed on two lengths of tubing, commonly known as "water pipes", which had almost identical radial dimensions, but different lengths. Since the two lengths of tubing were not cut from the same length, loss measurements would reveal any differences in the properties of the tube material.

Measurements indicated, that the resistivities of the two samples, within the experimental errors, were of value nearer to Thornton's tube. Thus, the hypothesis, that for a given resistivity and type of steel there exists a particular permeability function, could be tested, since the effective permeability given by $575 \times 10^{3} H_s^{-0.83}$ was based on Thornton's experimental results.

Since subsequent tests on samples A and B were to be carried out in air, measurements made in air and in water, but at the same frequency, would also show the importance or otherwise of

temperature effects.

7.5.2 Experimental procedure

The method of test was as previously described in Section 7.4.2 except that the current was supplied to the tubes by means of copper lugs brazed onto the pipe ends. For one tube, the effect of circulating the cooling water was investigated.

The external diameter was measured in four positions, but the internal diameter at each end. The tube's external surface was originally painted and removing the paint from a small section, revealed that the tube surface was not very smooth.

There is therefore some doubt about the radial dimensions and hence the resistivity. For calculation purposes, it was therefore decided to use for both tubes the same value of resistivity.

7.5.3 Results and discussion

The results for the two tubes are summarised in Tables 7.4, 7.5 and 7.6. Representative waveforms of the current and surface current density are shown in Fig. 7.17.

The calculated and measured loss values are in good agreement for both tubes tested. For the 1m tube, an increase in surface temperature of 13°C produced a change of 4% in the measured loss (result for 300 A). There is some evidence there-

Table 7.4. Measured Loss Values - Steel Tube

I (A)	H_s (Am^{-1})	In Circulating Water				In Air				In Air					
		Decreasing Current		Increasing Current		Decreasing Current		Increasing Current		Decreasing Current		Increasing Current		Middle range of Current	
		Pm (Wm^{-1})	θp °C	Pm (Wm^{-1})	θp °C	Pm (Wm^{-1})	θp °C	Pm (Wm^{-1})	θp °C	Pm (Wm^{-1})	θp °C	Pm (Wm^{-1})	θp °C	Pm (Wm^{-1})	θp °C
90	1059	21.8	19.7	21.7	17.4	22.3	16.6	21.7	12.4	22.7	33.5	22.3	20	-	-
120	1413	34.4	20.1	35.3	17.9	35.3	17	34.3	12.8	36.1	-	35.3	-	-	-
146.4.	1723	47.3	20.9	46.9	18.3	47.8	17.7	46.9	13.2	49.1	-	48.2	-	48.2	27
180	2118	65.3	21.4	66.3	18.8	64.9	18	64.9	13.9	67.3	-	66.3	-	66.3	-
211.2	2486	85	21.9	84.4	19.1	83.9	18.3	83.3	14.4	86.6	-	86.1	-	85.5	-
240	2825	103	21.9	104.2	19.9	102.4	18	101.8	15.1	104.2	-	105.9	-	103	20
264	3108	119.6	21.6	118.3	20.1	117.7	17	118.3	15.9	120	-	122.8	-	-	-
300	3531	143.5	19.5	144.9	20.2	142.8	15.4	143.5	16.7	144	18.5	149.8	31	-	-

Tube length	1 m
Potential leads	20.5 cm
Outside radius	1.352 cm
Inside radius	1.09 cm
Resistivity	14.28×10^{-8} Ω m
Frequency	50 Hz
$\beta = 0.194$	

Table 7.5. Calculated Loss Values Corresponding To Table 7.4.

H_s (Am^{-1})	b = 1.352 cm a = 1.09 cm $\rho = 14.28 \times 10^{-8}$ Ω m Pc (Wm^{-1})	b = 1.352 cm a = 1.09 cm $\rho = 13.99 \times 10^{-8}$ Ω m Pc (Wm^{-1})	Solid b = 1.352 cm $\rho = 14.28 \times 10^{-8}$ Ω m Pc (Wm^{-1})	$\rho = 14.28 \times 10^{-8}$ Ω m Psc (Wm^{-2})
1059	21.8	21.6	21.8	256
1413	34.6	34.3	34.5	407
1723	47.6	47.1	47.5	560
2118	66.2	65.5	66	779
2486	85.4	84.5	85.2	1000
2825	104.4	103.4	104.6	1229
3108	121.3	120.1	121.8	1428
3531	147.5	146.6	149.5	1741

Calculations based on $\mu_{reff} = 575 \times 10^3 \, Hs^{-0.83}$

Frequency 50 Hz

Table 7.6. Calculated And Measured Loss Values - Steel Tube

I (A)	H_s (Am^{-1})	Pm (Wm^{-1})	θ_p (°C)	Pc(Wm^{-1})		Psm(Tube) (Wm^{-2})
				Tube	Solid	
90	1058	22.1	14.3	21.8	21.8	260
103	1210	27.6	14.5	27.1	27.1	324
120	1410	34.9	14.6	34.6	34.5	410
132	1551	40.6	14.7	40	40.2	477
144	1693	46.4	14.8	46	46.2	545
168	1975	59.5	15	59	59.1	699
180	2116	66.2	15.6	66	66	778
192	2257	73.8	16.1	73.3	73.1	867
210	2468	84	16.4	84.6	84.4	987
228	2680	95.4	16.8	96.3	96.3	1121
240	2821	103.8	16.9	104.4	104.5	1220
252	2962	112.8	17.2	112.7	113	1326
276	3244	129.4	17.7	130	130.7	1521
294	3456	141.7	18	143.4	144.6	1666

Outside radius	1.354 cm
Inside radius	1.09 cm
Frequency	50 Hz
Length of Tube	2 m
Potential leads	1 m
Resistivity	14.28×10^{-8} Ω m
Tube immersed in water	
Calculations based on μ_{reff}	$= 575 \times 10^3 H_s^{-0.83}$
β'	= 0.195

fore, that substantial changes in surface temperature, produce a small change in the measured loss. Further tests were carried out to confirm this with the tubes of sample A and B material. This conclusion is important, so far as measurements in air are concerned at different ambient conditions.

The calculated results for a solid of equal external diameter, show that the tubes appear electrically as solid, except for currents beyond 270 A. This is to be expected, since with increasing current and for constant material properties, the depth of penetration increases.

Fig 7.18 shows that the turning point of the μ_r/H curve for this steel, is below 1000 (A m^{-1}). Because of this, the calculated and measured loss values are in agreement over the entire range of the field strengths considered.

This offers further support to the observation that the turning point of the μ_r/H curve depends on the value of resistivity, since for the steel bar of resistivity 15.1 x10^{-8} (Ω m), the turning point was found to be at about 1700 (A m^{-1}). It will be seen that sample A, of resistivity 24.5 x10^{-8} (Ω m), has a turning point at an even larger value of field strength.

Fig. 7.18 shows that the power index of the surface field strength is between 1.57 and 1.58.

The results of this section confirm, that the effective permeability function for a steel of resistivity of approximately 14 x10^{-8} (Ω m), is 575 x10^{3} $H_s^{-0.83}$. Tests on further samples of MS will reveal if this function applies to resistivies other than 14 x10^{-8} (Ω m).

7.6 Isolated Tube - Samples A and B

7.6.1 Fixed frequency tests

The objectives of these tests were:

1. to investigate the effect of altering the bore of a tube of fixed external diameter;
2. to investigate the effect of altering the external diameter of a fixed bore tube, of the same material as in (1);
3. to compare the performance of two tubes of known chemical analysis and equal dimensions;
4. to evaluate any effect the wall thickness might have in predicting power losses;
5. to generate more experimental data in an attempt to establish a relationship between resistivity and effective permeability;
6. to examine the influence of wall thickness on the power index of H_s.

Details of samples A and B and the way of obtaining the tubes of different radial dimensions, has already been reported.

From sample B, only two bore sizes were produced from the original thin-wall tube. From sample A, six bore sizes and five external diameters were produced.

7.6.1.1 Results and discussion

For both sample B specimens, the agreement between the calculated and measured loss values is good. The turning point

of the μ_r/H curve for this steel is between 1000 and 1400 (A m^{-1}).

The calculated loss values for a solid conductor of equal external diameter, included in Table 7.7, indicate that for β = 0.213, the tube is electrically thin for field strengths above approximately 2000 (A m^{-1}).

The equality of the measured loss and the loss calculated based on an equivalent solid (in the case of β = 0.16, table 7.7) can be explained with reference to Fig.4.5.

Examination of Fig. 4.5, shows that there are two values of β for which the power losses are equal. Thus, sample B behaves as predicted in Chapter 4, except that there are only three points on the Power/β curve for constant values of current and therefore, the results are not shown in graphical form.

In Chapter 6, it was predicted (Fig.6.16 & 6.17), that for a tube, depending on the value of H_s and wall thickness, a change in the slope of the surface power density/H_s graph is possible. The corresponding results for sample B have been plotted in Fig. 7.19, where it can be observed that whilst the thickness corresponding to β = 0.213 is not sufficiently small to reflect a change in the slope, for β = 0.16, the change is clearly distinguishable and occurs at approximately 2400 (A m^{-1}).

For samples B, from Fig 7.19 the power index of H_s for the 15 mm bore is 1.58 and for the 16 mm bore it changes from 1.58 to 1.85.

Table 7.7. Measured And Calculated Loss Values. Sample B

Variable Bore

	β = 0.213					β = 0.16				β = 1
H_s (Am^{-1})	Pm (Wm^{-1})	θp °C	Pc (Wm^{-1})	Pc* (Wm^{-1})	Psm (Wm^{-2})	Pm (Wm^{-1})	θp °C	Pc (Wm^{-1})	Psm (Wm^{-2})	Pc (Wm^{-1})
1000	15.8	23.7	16.3	15.5	264	14.3	23.7	15.7	239	16.2
1400	27.2	24.6	27.6	26.2	454	25.2	23.8	26.2	421	27.9
1600	33.8	25.9	33.9	32.1	565	31.7	24	32.1	529	34.5
2000	48.1	28	47.6	45.2	804	46.2	24	45.5	772	49.4
2600	72.1	22.9	71.1	67.4	1205	70.4	24	69.7	1176	75.3
3000	90.8	25	88.6	84.2	1517	90.4	24.2	88.7	1510	94.8
3400	110.5	27	107.6	102.6	1846	112	24.3	110	1871	116
3800	131	25	128.3	122.5	2189	135.5	23.5	133.9	2264	138.7
4000	141	23	139	133.2	2356	149	24.1	146.6	2489	151
4206	152.4	23	150.4	144.3	2546	161.9	24.3	160	2700	163
4400	164.6	24	162.3	155.8	2750	175.2	24.3	174	2927	175
4607	175.8	24.7	174.5	167.8	2937	189.3	24	188.6	3163	188
4807	189	26.7	187.6	180	3158	202.8	24.6	203.8	3384	202
5007	200	26	200	193	3342	219.8	25.1	219.7	3673	216

f = 50 Hz

$\rho = 18.5 \times 10^{-8}\ \Omega$ m at 20°C

Pc based on $\mu_{reff} = 575 \times 10^3\ H_s^{-0.83}$

Pc* based on $\mu_{reff} = 536 \times 10^3\ H_s^{-0.833}$

Fixed external diameter 19 mm

Tables 7.8 to 7.10 incorporate the results of tests at 50 Hz on specimen prepared from sample A of fixed external diameter. It can be observed that for this steel, the turning point of the μ_r/H curve occurs at about 3400 (A m^{-1}), which further supports the statement, that a higher value of resistivity (in this case 24.5 $\times 10^{-8}$ (Ω m), is associated with a turning point occurring at a larger value of field strength.

The method of calculating losses assumes linear $\log \mu_r / \log H_s$ characteristics. Thus, whilst the effective permeability given by $536 \times 10^{3} H_s^{-0.833}$ has been used to calculate the loss beyond H_s = 3400 (A m^{-1}), it is not valid for H_s<3400 (A m^{-1}). For the purpose of calculating the losses in this range of H_s, it has been assumed that $\mu_{r\,eff}$ remains constant below H_s = 3400 (A m^{-1}) when in fact it is not the case. For this reason, while there is good agreement between measured and calculated loss values for H_s>3400, the agreement is lacking for H_s<3400 (A m^{-1}).

The effective permeability functions, used for calculating losses for samples A and B, are shown in Fig 7.21.

The sample A tubes, behave as solid conductors up to a bore size of 12 mm and as the bore size increases, for a constant current, the losses increase, rather than decrease as theory predicts.

The measured and calculated loss values are shown in Fig. 7.22 for three currents. In Fig. 7.23 the calculated values corresponding to 50 Hz and d.c. have been included and the curves merge at about β = 0.1.

Table 7.8. Measured And Calculated Loss Values. Sample A

Variable Bore

		β = 0.666		β = 0.554		β = 0.476		β = 1	β = 0.554
I (A)	H_s (Am^{-1})	Pm (Wm^{-1})	θp °C	Pm (Wm^{-1})	θp °C	Pm (Wm^{-1})	θp °C	Pc (Wm^{-1})	Psm
60	1000	8.4	22.3	9	19.3	9.4	19.6	11.1	150
84	1400	19.8	22.5	21.3	19.9	22	20	21.8	355
96	1600	27.3	23.2	28.8	20.0	30	20.7	28.5	481
120	2000	44.6	24.2	46.9	20.7	48.5	21.4	44.6	783
156	2600	75.3	20.7	78.6	22.9	80	22.9	75.4	1312
180	3000	99	22	101.2	22.3	103.5	21.2	100.4	1689
204	3400	123.4	23.6	127.7	23.9	127.7	23.7	129	2131
228	3800	150.5	24.8	154	25.5	154	26	154.4	2570
240	4000	164.3	23.5	167	22.9	168	26.9	167.8	2787
252	4206	178	21.6	182	24.7	182	24.9	181.6	3038
264	4400	194	32.0	196	26	197	22.5	195.8	3271
276	4607	209	30.0	210.5	28	210	24.8	210.4	3511
288	4807	223	26.4	224.7	25.5	226	26.7	225.5	3751
300	5007	239	24	240	23.4	241	23.9	240.9	4000

f = 50 Hz

$\rho = 24.5 \times 10^{-8}$ Ω m at 20°C

Pc for H_s = 1000-3000 based on $\mu_{reff} = 612$

Pc for H_s>3000 based on $\mu_{reff} = 536 \times 10^3 H_s^{-0.833}$

Fixed external diameter 19.07mm

Table 7.9. Measured And Calculated Loss Values. Sample A
Variable Bore

	β = 0.37			β = 0.269		
H_s (Am^{-1})	Pm (Wm^{-1})	θp (°C)	Pc (Wm^{-1})	Pm (Wm^{-1})	θp °C	Pc (Wm^{-1})
1000	10.4	21	11	11.1	20	-
1400	23.7	22	21.6	25	20.6	-
1600	32	22	28.2	33.4	21	-
2000	50.4	23	44.1	52	22	-
2600	82	24.5	74.5	83.5	23.6	-
3000	105	22	99	106.7	25.2	-
3400	129	22	127.4	131.8	27.8	120.6
3800	156	26	151.4	157.4	22.5	143.6
4000	169	21.6	164	172.6	26.6	155.7
4206	184	24	176.9	185.8	22.9	168.2
4400	198	24	190.2	202.8	25.9	181.2
4607	212	23.5	203.7	216.7	23	194.7
4807	230	26	217.5	235	24	208.5
5007	246	24	231.7	253	27	222.9

f = 50 Hz

$\rho = 24.5 \times 10^{-8}$ Ω m at 20°C

Pc for H_s = 1000 - 3000 based on $\mu'_{reff} = 612$

Pc for Hs>3000 based on $\mu'_{reff} = 536 \times 10^3 H_s^{-0.833}$

Fixed external diameter = 19 mm

The discrepancy between the measured and calculated values cannot be explained by experimental errors, since the same measuring technique has been used for all samples tested. Since the tube material is also the same for the different specimen, the difference in the measured and calculated losses can only be explained by the presence of an additional factor. The extra loss present, will be termed the anomalous loss. From Figs. 7.22 and 7.23, the anomalous loss has been calculated and is shown in Fig. 7.24, as a percentage of the measured loss for the three currents considered.

The anamolous loss increases as β decreases, reaches a maximum and then reduces to zero. Beyond a certain value of β corresponding to very thin tubes, the a.c. and d.c. losses are equal and therefore this equality can only be achieved if the anomally reduces to zero.

In order to examine the effect of wall thickness and material properties on the power index of H_s, the surface power density for $\beta = 0.16$ of sample A, has been plotted in Fig. 7.19. The slope and therefore the power index of H_s, for the high values of H is the same as for sample B of equal β value.

Although a change in the slope occurs at about 2500 (A m^{-1}), the line joining the points corresponding to H_s values below 2500 (A m^{-1}), is not parallel to that for sample A. The reason is that these points correspond to H_s values below the turning point. It is interesting, however, to note that the loss is still described by a straight line characteristic, giving a power index for H_s of 1.85.

Table 7.10. Measured And Calculated Loss Values. Sample A
Variable Bore

	β = 0.213				β = 0.16			
H_s (Am^{-1})	Pm (Wm^{-1})	θp °C	Pc (Wm^{-1})	Psm (Wm^{-2})	Pm (Wm^{-1})	θp °C	Pc (Wm^{-1})	Psm (Wm^{-2})
1000	12.5	19.9	-	209	15.87	23.9	-	265
1400	27.2	20	-	455	30	25.1	-	501
1600	35.6	21.1	-	596	38.6	27	-	645
2000	55.1	22.9	-	923	58	25.5	-	969
2600	88.4	25.5	-	1481	92.1	27.8	-	1539
3000	112	21.2	-	1876	118.4	27.9	-	1978
3400	139.6	24.6	120	2338	150	28.4	133	2506
3800	168.3	23.5	145	2812	182.7	28	163.8	3053
4000	184.6	26.9	158.6	3093	201	30	180.3	3358
4206	198.4	22.6	172.4	3324	218	31	197.7	3643
4400	217.4	26	187	3642	238.5	31	215.9	3985
4607	230.8	24.8	202.3	3866	256	30	234.9	4277
4807	250	27.8	218	4188	283	30	254.7	4728
5007	264	24.1	234.6	4423	307	32	275.4	5130

f = 50 Hz

$\rho = 24.5 \times 10^{-8}$ Ω m at 20°C

Pc based on $\mu_{reff} = 536 \times 10^3 H_s^{-0.833}$

Fixed external diameter = 19 mm

Table 7.11. Measured And Calculated Loss Values. Sample A
Variable External Diameter

	β = 0.626			β = 1		β = 0.576			β = 1
H_s (Am^{-1})	Pm (Wm^{-1})	θp °C	Pc (Wm^{-1})	Pc (Wm^{-1})	H_s (Am^{-1})	Pm (Wm^{-1})	θp °C	Pc (Wm^{-1})	Pc (Wm^{-1})
1123	11	23.2	13.4	-	1273	13.56	21	14.63	-
1573	25.3	23.6	26.2	-	1782	29.44	24.5	28.67	-
1797	34.2	24.1	34.3	-	2037	38.78	22.7	37.45	-
2247	53.3	25.2	53.5	-	2546	60	25.5	58.5	-
2921	87.5	26.5	90.5	-	3310	96	28.6	98.9	-
3370	113	28.1	113.6	114.2	3820	123.6	31.9	124	124.9
3820	139.4	30	140	139.9	4329	150.5	23	152	153
4269	168	31.2	168	167.5	4838	182	26.8	182	183.7
4494	182	28.2	182	182	5093	198	30	197	199.7
4718	197	24.4	197	197	5348	214	29.1	213	216.3
4943	211.6	21.7	211.6	212.6	5602	229	24	229	233.5
5168	228	31.2	228	228.6	5857	248.4	33	246	251.1
5392	246.6	27	246.6	245	6117	268	28.6	263	269.2
5617	264	23.7	264	261.8	6366	285.3	24.9	280.9	287.8

f = 50 Hz

$\rho = 24.5 \times 10^{-8}$ Ω·m at 20°C

Fixed internal diamter 6.35 mm

For β = 0.626 Pc based on μ'_{reff} = 696 for H_s = 1123-2921 ($A\,m^{-1}$)

For β = 0.576 Pc based on μ'_{reff} = 627 for H_s = 1273-3310 ($A\,m^{-1}$)

For all other values of H_s, Pc based on $\mu'_{reff} = 536 \times 10^3\ H_s^{-0.833}$

Table 7.12. Measured And Calculated Values. Sample A
Variable External Diameter

	β = 0.546			β = 1		β = 0.47			β = 1
H_s (Am^{-1})	Pm (Wm^{-1})	θ_p °C	Pc (Wm^{-1})	Pc (Wm^{-1})	H_s (Am^{-1})	Pm (Wm^{-1})	θ_p °C	Pc (Wm^{-1})	Pc (Wm^{-1})
1591	18.5	24.3	16.4	–	1364	15.2	22.2	15.2	–
2228	37.5	25.7	32.1	-	1910	32.2	23	29.9	-
2546	48.2	27.6	41.9	-	2183	42	24	39.1	-
3180	73.7	25.9	65.5	-	2728	64	26.3	61.1	–
4138	117	29.4	117	117	3547	101	25	103.2	104
4775	147.9	27.9	147.7	147.7	4092	129	28	129.5	131.5
5411	182.7	27.2	181.4	181.4	4638	158	27	157.8	161.4
6048	220	28	217.6	217.6	5184	190.7	27	188	193.6
6366	240	28.3	236.6	236.6	5467	206	26	203.8	210.6
6684	260	25	256.2	256.2	5729	222	28	220	228
7000	281.4	26.7	276.4	276.4	6000	240	27	236.8	246.2
7321	308.6	29	297.2	297.2	6275	257	28	254	264.3
7639	330.6	27.7	318.6	318.6	6548	281	29	271.7	283.4
7957	357.3	31	340.5	340.5	6821	300	30	289.8	303

f = 50 Hz

$\rho = 24.5 \times 10^{-8}$ Ω m at 20°C.

Fixed internal diameter 6.35 mm

For β = 0.47 Pc based on $\mu'_{reff} = 520$ for H_s = 1591-3180 ($A\,m^{-1}$)

For β = 0.546 Pc based on $\mu'_{reff} = 592$ for H_s = 1364-2728 ($A\,m^{-1}$)

For all other values of H_s, Pc based on $\mu'_{reff} = 536 \times 10^3\ H_s^{-0.833}$

It appears therefore, that the power index of H_s is independent of material, for values of H_s beyond the turning point of the μ_v/H curve as the wall thickness is reduced.

Fig. 7.20 shows that for sample A tube, the power index for β = 0.554 is 1.63 for $H_s > 2500$ (A m^{-1}) instead of the expected 1.58 and increases to 1.68 for β = 0.213 (15 mm bore). The reason for the higher value in the power index must be the presence of the "anomalous" loss which reduces to zero as the wall thickness becomes progressively less with the result that the power index for both sample A and B tubes equals 1.85 when the bore becomes 16 mm.

The results of variable external diameter tube specimen of sample A, are shown in Tables 7.11 and 7.12. There is good agreement between measured and calculated loss values for $\beta \geq 0.546$, below which the anomaly becomes apparent once more.

Fig. 6.19 has shown that for a constant current and frequency, the depth of penetration is dependent on the external diameter. As the external diameter is reduced, the depth of penetration increases and therefore, for the same value of β and for a given current, the tube with the smaller diameter, will appear electrically thinner. For this reason the "anomaly" with this specimen, occurs at a value of β higher than for the variable bore tubes.

The experimental and measured loss values are shown in Fig. 7.25, showing that the loss/$_\beta$ characteristic is different from the case, when the value of β is obtained by altering the internal diameter. This difference in behaviour was predicted

in Chapter 4 (Fig. 4.6 and Fig. 4.10).

It was previously observed that the effective permeability function depends on the value of resistivity and that the higher the resistivity, the lower is the effective permeability. Two effective permeability functions have been shown in Fig.7.21 and it might be questioned why for sample B tubes, of resistivity 18.5×10^{-8} (Ω m), the effective permeability previously used with a steel of $\rho = 14.3 \times 10^{-8}$ (Ω m), was also used in this case to calculate the results.

In Table 7.7 the calculated values, on the basis of $536 \times 10^{3} H_s^{-0.833}$, have been included for comparison and the maximum error is 7% occurring only twice.

To be consistent with previously made statements regarding effective permeability, an effective permeability function, in between the two characteristics of Fig. 7.21, should have been used with sample B tube. Because of the insensitivity of losses to moderate changes in permeability, it was not considered worthwhile altering the calculated values and in fact the results incorporated in Table 7.7 serve to illustrate the above.

However, the observation made above should be borne in mind when drawing general conclusions regarding the relationship between resistivity and effective permeability function.

7.6.1.2 Additional tests

Temperature effects were further investigated. A 150 A current was supplied to a sample A tube, of 17 mm external diameter and 6.35 mm bore, until the temperature stabilised at 94.5 °C. Measurements showed, that there was an increase of 6.4% in power, between the temperatures of 26°C and 94.5°C.

The exercise was repeated with another sample A tube of 19.07 mm external diameter an 9.5 mm bore, supplied at 120 A. The increase in power, between the temperature of 22.5°C and 90°C, was in this case 7.7%.

These tests support the previous findings, that temperature effect in the measurement of power loss in air, is not very significant, particularly since the temperature variations did not exceed 10 °C. Some temperature/time graphs are shown in Fig. 7.26. In Chapter 2, it was observed that heat treatment can affect the magnetic properties of steel. Since sample A was in the "hard as drawn" state the effect of annealing was investigated by heating a tube, of external diameter 19.07 mm and 15 mm bore, in a furnace for three-quarters of an hour at 650 °C in a neutral atmosphere and then cooling it to room temperature within the furnace. The tube losses were re-measured and compared with the original values. The results showed that whilst the measured loss increased well above the experimental error for low values of excitation, for the higher values it decreased by 2.7 to 5.2%. In view of the consistent repeatability of the measurements, the above differences are not entirely due to

experimental errors, but probably due to changes in the magnetic properties of the steel.

The increase in losses could be explained by a shift in the turning point of the μ/H curve, since this will have the effect of increasing the permeability and hence the power loss. However, the reduction in the power loss cannot be explained. One plausible explanation is that the wall thickness has been electrically changed by the increased permeability, which will make the tube appear thicker and therefore cause a reduction in loss. If this is true, the same effect should be observed by measuring the losses at higher frequencies.

It was suggested that the temperature of 650°C was not sufficiently high to produce significant metallurgical changes in the tube and therefore the same tube (its bore was by then changed to 16 mm) was held at 800°C for 45 minutes and the losses re-measured. This time, the measured losses increased throughout the range of H_s, but the increase was in the range of 2 to 5%; the larger changes occurred at the lower values of H_s. These changes are not sufficiently large to be attributed to changes in the structure of the steel. On the basis of available experimental evidence, firm conclusions cannot be reached and further tests are required in parallel with a metallurgical investigation. What can be concluded however is that the observed anomalous loss was not eliminated by heat treatment, although significant changes were produced in the measured losses particuarly at low field strength.

7.6.2 Variable frequency tests

7.6.2.1 Objectives

The objectives of these tests were:

1. to verify experimentally the condition under which a tube appears as a semi-infinite slab;
2. to attempt to understand the observed anomalous loss associated with sample A tube.

7.6.2.2 Apparatus and experimental procedure

For the low frequency tests (22-70 Hz), the apparatus was the same as reported in Section 7.4.2. With the tubes used, three currents could be obtained over the frequency range.

For the high frequency tests (Ca 400 - 1600 Hz), an inductor alternator was used in place of the synchronous generator. For these tests, the precision wattmeter could not be used because of its frequency limitation and an electronic wattmeter was substituted.

Only one current could be obtained, because the impedance of the loop containing the tube was much higher than for the case of the low frequency tests. The loop was made as small as possible without introducing proximity effects.

The frequency was measured by measuring the period of the current waveform displayed on a storage oscilloscope, which had a facility for a digital display of time.

The tests were performed on two tubes of equal dimensions,

having an external diameter of 19.07 mm and a bore of 15 mm, but were of sample A and sample B material. The tube A material was the same as the one previously heated to 650 °C.

7.6.2.3 Results and discussion

The results are shown in Tables 7.13 to 7.16.

Fig. 7.27 shows the Power/f curves for the two tubes at a constant current of 96 A. The shape of the curves is as expected.

For sample B, the agreement between the measured and calculated loss values for low and high frequencies is of the same order. For sample A there is considerable error between the measured and calculated losses throughout the frequency range (Fig. 7.28).

Fig. 7.29 shows the graphs of Power/ $\sqrt{f}$ for the lower frequency range (22-70 Hz) for samples A and B.

Fig. 7.29 indicates that for sample B the tube appears as a semi-infinite plate for frequencies above 30 Hz and calculations show that it also appears approximately as a solid.

For the high frequency range, both samples A and B appear as semi-infinite plates as indicated in Fig. 7.30 (slope of 2).

For a current of 96 A and for the sample B, the minimum diameter required for the tube to appear as a semi-infinite plate at a frequency of 68 Hz is 1.9 cm, which is the diameter of the tube tested.

For the lower frequencies, the tube diameter is not

Table 7.13. Measured and Calculated Loss Values

Sample B-Variable Frequency Tests

I (A)	H_s (Am^{-1})	f (Hz)	$\sqrt{f}$	Pm (Wm^{-1})	θp °C	Pc (Wm^{-1})	$\mu_{reff} f\sigma \times 10^{11}$	$\frac{Pm\sigma}{H_s^2 t} \times 10^3$
96	1602	22	4.69	23.2	26	21.6	1.49	24.1
180	3000			65.2	27.4	63.4	0.887	19.6
228	3805			113.8	30	97.6	0.73	21.2
		30	5.47	26.1	25	25.3	2.04	27.5
"	"			72.6	27	69.7	1.21	21.8
				107.3	30	104.9	0.99	20
		40	6.34	30.4	26	29.8	2.72	32
"	"			82	29.5	78.9	1.61	24.6
				121	31	116	1.32	22.6
		50	7.1	33.5	23.8	33.9	3.4	35.2
"	"			89	26.5	88.6	2.02	26.7
				129.7	29.4	128	1.65	24.2
		60	7.75	37.5	25.5	37.4	4.07	39.4
"	"			99.4	30.8	98.1	2.42	29.8
				144.7	36	141	1.98	27
		68	8.3	38.8	29.2	39.9	4.62	40.8
"	"			105.5	31	105.5	2.74	21.6
				154.5	35.5	151.2	2.25	28.8
60		72			21		6.6	51.6
72					21.5		5.7	48.3
84					23.4		5	45.2
96		0				15.6		
180						55		
228						88		

Pc based on $\mu_{reff} = 575 \times 10^3 H_s^{-0.83}$, $\beta = 0.213$

Table 7.14. Measured And Calculated Loss Values. Sample B

Variable Frequency Tests

I (A)	f (Hz)	√f	Pm (Wm^{-1})	θp °C	Pc (Wm^{-1})	$\mu_{reff} f_\sigma$ x10^{11}	$\frac{P_m \sigma}{H_s^2 t}$ x10^3
96	452	21.2	102.6	28.7	101	30.7	108
↓	544	23.3	112	27.4	110.2	36.9	118
	611	24.7	119.6	27.4	116.7	41.5	126
	717	26.8	128	26.1	126.3	48.3	135
	826	28.7	137.4	24.7	135.5	56	144
	1099	33.1	162	27.2	156	74.6	170
	1218	34.9	169.7	25	164	82.7	178
	1460	38.2	188	27.1	179.7	99.2	197.7
Results From Table 7.7.							
120	50		48.1			2.83	32.5
156	↓		72.1			2.27	28.7
228			131			1.66	24.5
276			175.8			1.41	22.3
300			200			1.32	21.5

Results From Table 7.13. I = 96A

f	√f/f	Pm	Pm/f
22	0.21	23.2	1.05
30	0.18	26.1	0.87
40	0.16	30.4	0.76
50	0.14	33.5	0.67
60	0.13	37.5	0.625
68	0.12	38.8	0.57

Table 7.15. Measured And Calculated Losses. Sample A

Variable Frequency Tests

I	H_s	f	$\sqrt{f}$	P_m	θp	Pc	Pc*	$\mu'_{reff}\ \sigma f$	$\frac{P_m \sigma}{H_s^2 t}$
(A)	(Am^{-1})	(Hz)		(Wm^{-1})	°C	(Wm^{-1})	(Wm^{-1})	$x10^{11}$	$x10^3$
96	1602	22	4.69	28.1	23.9	24.9	22	1.02	22.3
180	3000			86	26	78.7	77.3	0.61	19.5
228	3805			135	27.7	123		0.5	18.9
		30	5.47	30.8	25.8	27.9	23	1.4	24.5
				94.1	26.7	83	81	0.83	21.3
"	"			139.5	29.4	128		0.68	19.6
		40	6.34	34.6	25.5	32	24.7	1.87	27.3
				100	30.8	89.8	86.7	1.11	22.7
"	"			151.9	30.4	136		0.91	21.4
		50	7.1	37.9	25.4	36	26.6	2.34	30.1
"	"			108.8	29.1	97.5	93.4	1.39	24.7
				163.5	33	145		1.14	23
		60	7.75	40.7	28.9	40.2	28.7	2.81	32.3
"	"			118.4	35	106	100.8	1.66	26.8
				176	38	155		1.36	24.8
		68	8.3	43.5	25.3	43	30.6	3.18	34.6
"	"			123.8	30.9	113	107	1.88	28.1
				183	33	164		1.55	26
60	1000	71		18.66	25.3	21.3		4.92	38
84	1402	70		34.8	25.3	35.8		3.66	36.1
72	1200	70		26.2	25.3	28.2		4.17	37.1
96		0				20.7			16.5
180		0				72.9			
228		0				117			

$\beta = 0.213$ Pc based on $\mu'_{reff} = 536 \times 10^3 H_s^{-0.833}$

Pc* based on $\mu'_{reff} = 612$

Table 7.16. Measured And Calculated Loss. Sample A
Variable Frequency Tests

I (A)	f (Hz)	√f	P_m (Wm^{-1})	θp °C	Pc (Wm^{-1})	Pc* (Wm^{-1})	$\mu'_{reff}{}^{f\sigma}$ x10^{11}	$\mu'_{reff}{}^{f\sigma*}$ x10^{11}	$\frac{P_m \sigma}{H_s{}^2 t}$ x10^3
96	396	19.9	102.8	29.4	103.9	76	18.5	9.9	81.7
↓	537	23.1	117.7	25.9	120.7	88.7	25.1	13.4	93.5
	585	24.2	123.6	28.2	125.9	92.5	27.4	14.6	98.2
	762	27.6	140.8	28.6	143.5	105.3	35.6	19	111.9
	1010	31.8	161.5	28.3	164.8	120.9	47.3	25.2	128
	1282	35.8	185.5	29.2	185.5	135.9	60	32	146.7
	1504	38.8	199.8	30.1	200.7	147	70.4	37.5	158.8
↓	1613	40.6	206.7	28.3	207.8	152.3	75.8	40.2	164
Results From Table 7.10.									
120	50		55.1				1.94		28.1
156	↓		88.4				1.56		26.7
228			168.3				1.14		23.7
300	↓		264				0.91		21.3

β_i = 0.213

Pc based on μ'_{reff} = 536 x 10^3 $H_s^{-0.833}$

Pc* based on μ'_{reff} = 612

$\mu'_{reff}{}^{f\sigma}$ based on 536 x 10^3 $H_s^{-0.833}$

$\mu'_{reff}{}^{f\sigma*}$ based on 612

sufficiently large and therefore some errors will be introduced in the application of the semi-infinite loss formula. Based on this formula the calculated losses Pc_{∞}, for sample B, are shown in Table 7.17 where Pc are the losses calculated based on the actual dimensions of the tube.

Table 7.17 Calculated And Measured Loss Values.

Sample B, 96 A

f (Hz)	P_m (W m^{-1})	$P_{c\infty}$ (W m^{-1})	P_c (W m^{-1})	$\frac{P_m - P_{c\infty}}{P_m}$ %
22	23.2	21.9	21.6	5.6
30	26.1	25.5	25.3	2.3
40	30.4	29.5	29.8	2.9
50	33.5	32.9	33.9	1.8
60	37.5	36.1	37.4	3.7
68	38.8	38.4	39.9	1

As the frequency increases, the error shown in Table 7.17 does not reduce uniformly, although agreement between measured and calculated loss values is good.

Apart from the experimental errors, two additional factors must be considered, in assessing the magnitude of error indicated in Table 7.17. It was stated that, for the lower frequencies, the tube tested is not quite a solid. Hence the measured losses will be somewhat lower than if the tube was

solid. Since the losses calculated on the basis of a finite diameter, are larger than on the basis of a semi-infinite plate, for a diameter smaller than the minimum value corresponding to a particular frequency, the losses will be underestimated. Thus there is a self cancellation of the errors, with the result that agreement between measured and calculated loss values is good, even at frequencies below 68 Hz.

7.7 Anomalous Loss

It has been shown, that the three dimensionless parameters, $\frac{P_m \sigma}{H_s^2 t}$, z, β, describe the tube performance. For a constant β, the other two parameters will therefore show the effect on tube losses of all the variables within the limits of experimental error, where correlation exists. The variables embodied in the independent dimensionless parameters should be independent. However, for steel, μ is a monotonic function of H_s.

If a functional relationship between μ and H is used, as in this case, the three dimensionless parameters are no longer independent and can only apply to another tube under the conditions of equality of β and external diameter. Since this condition is satisfied for the two tubes tested, the absence of correlation between the other two dimensionless parameters will indicate the presence of additional factors which were ignored in the derivation of the dimensionless parameters, such as hysteresis.

The work of Hale and Richardson [71] is partly relevant to this discussion. They measured losses on a number of cores, over a range of frequencies and at flux densities in the middle portion of the magentisation curve. The data were studied by means of dimensionless analysis.

The materials tested were divided into groups with similarly shaped B/H curves and significant correlations were obtained between parameters embodying the classical variables, which are

known to influence core losses. These variables were grouped in the three dimensionless parameters,

$$\frac{P_m}{f J_o} \quad , \quad \frac{f B_o^2 d^2}{\rho J_o} \quad , \quad \bar{\mu}_o \frac{J_o}{B_o^2}$$

where Jo = area of static hysteresis loop in Joules per cubic metre, per cycle at B_o

d = lamination thickness

They overcame the difficulty of the dependence of permeability on H, by assigning an average value $\bar{\mu}_o$, which is the permeability averaged with respect to flux density from 0 to B_o. They also found that the third dimensionless parameter was constant for materials with similar shapes of B/H curve and hysteresis loop .

Thus a plot of $\frac{P_m}{f J_o}$ versus $\frac{f B_o^2 d^2}{\rho J_o}$ shows the effect on core losses of all the independent classical variables. Fig. 7.31 is reproduced from their paper and shows that there is no correlation between curve A, for ingot iron, and curve B for one of the groups of materials tested. They argue that the only plausible explanation is in terms of domain size and a reduction in domain size, leading to a reduction in losses.

They also show that the dimensionless parameters of thinner laminations within one of the group, when plotted produce a curve which is parallel and displaced in the direction of higher losses from that for the thicker laminations. They attributed this to a change in the ratio of domain width to lamination thickness, the domain width not decreasing as rapidly as the lamination thickness.

For the present investigation, the dimensionless parameters used ignore hysteresis loss, but the effective permeability used for the calculation of losses embodies any contribution to the losses by hysteresis. However, the effective permeability was such as to give agreement between the measured and calculated losses for the case of the thick-wall tube of sample A. Thus, if there is an increase in hysteresis loss/cycle due to the reduction in the wall thickness, the same effective permeability function will not give agreement between measured and calculated values for progressively thinner walls.

Since the anomalous loss was not present with sample B tubes, it can be concluded that the tube material has a hysteresis loss/cycle which does not vary with wall thickness, or if it does, it is too small to detect in progressing from the 15 mm, to the 16 mm bore.

It was stated previously, that increasing the frequency alters electrically the dimensions of the tube, so that the tube appears first as solid and secondly as a semi-infinite slab. This was the case for both A and B materials at high frequencies (Fig. 7.30).

Based on the above argument, the calculated losses at high frequencies for the thin-wall sample A tube, should have been in agreement with the measured losses since such agreement existed in the case of thick-wall tubes of identical material. However, examination of the results for sample A steel at 50 Hz and at high frequencies, indicate that for the test current of 96 A, the percentage difference between measured

and calculated values is almost the same and equals about 25% ; it is independent of frequency. This suggests that the extra loss is entirely due to an increase in hysteresis loss, the increase being independent of frequency but related to the physical rather than equivalent electrical wall thickness.

Since the equations developed for the calculation of losses do not account for hysteresis, the extra losses cannot be explained.

There is also the possibility that $\mu_{r,eff}$ is a function of thickness. If this was the case, reducing the wall thickness will lead to a reduction in $\mu_{r,eff}$, since fewer layers of the tube will be in the unsaturated state and thereby reduce the loss.

In Table 7.16, the calculated loss has been obtained on the basis of a fixed value of permeability (as for the results included in Table 7.9) and on the basis of extending the linear relationship of the effective permeability function down to H_s = 1602 (A m^{-1}) giving an effective permeability of 1147 instead of 612. The result calculated with $\mu_{r,eff}$ = 1147 are in good agreement with the measured values (Table 7.16). This however must be providential, since for the low frequency range and for the current of 96 and 180 A the disagreement persists (Table 7.15).

The dimensionless parameters from Tables 7.13 and 7.15, have been plotted in Fig. 7.32 and the impression given is that correlation exists, thus invalidating the previous discussion.

However, the results are distorted by using for sample A, $\mu_{r,eff}$ = 1147 and 680 for the current of 96 A and 180 A

respectively, when correlation is sought with the measured losses referring to the thick-wall tube, where μ_{reff}' was 612 for both currents. This difficulty can be overcome by considering the results corresponding to 228 A only at variable frequency, since for this current both tubes operate in the linear part of the $\log \mu_r'/\log H_s$ characteristic. These results are plotted in Fig. 7.33 and, as it can be seen, there is no correlation.

The lack of correlation cannot be explained as previously by temperature effects and it should also be noted, although it was not plotted, that the variable current fixed frequency points also lie fairly closely to the characteristics of Fig.7.33.

Since both characteristics of Fig. 7.33 refer to constant current and wall thickness, the hysteresis loss per cycle is a constant. As the frequency increases, the hysteresis loss increases, and therefore there is no correlation, as the dimensionless parameters ignore hysteresis.

Since sample A tube has a considerably larger hysteresis loss, as compared to sample B tube tested, it follows that there will be no correlation between the dimensionless parameters.

Fig 7.34 shows the dimensionless parameters obtained from the high frequency results (on the basis of $\mu_{reff}' = 612$ for sample A) and again, there is no correlation for the same reasons as for the low frequency tests.

On the basis of the evidence presented, it can be concluded, that the cause of the anomalous loss, with sample A material, is hysteresis.

The anomalous loss is independent of frequency, but increases with a reduction in wall thickness up to a certain value depending on the current.

The cause of this could be a relationship between the microstructure and wall thickness, but other than Hale and Richardson's [71] observations in support, information in the literature regarding this phenomenon as related to resistance heating is not available.

For sample B material, there is some evidence, that the anomalous loss is not present, but this is based on the results of two wall thicknesses only. The hysteresis loss was small.

From the point of view of heating, tubes made from material A have advantages over material B since it has a larger resistivity but almost equal permeability for (H_s>3400) and extra hysteresis losses below a certain value of wall thickness. The losses however cannot be predicted, unless a method for calculating hysteresis loss is developed.

An interesting observation which does not lead to any conclusions, is that sample A has a higher Si content than sample B; silicon is an element normally associated with a reduction in iron losses.

7.8 Waveforms

7.8.1 General discussion

For all specimens tested, waveforms of the supply current and surface current-density were recorded for different values of current. The current-density waveforms were obtained from current-density probes as described by Burke and Alden [69], which give an output voltage proportional to the surface current-density.

Ideally, a sinusoidal current waveform was desirable, since the equations developed for the calculation of loss assume sinusoidal excitation. In practice, it was found that for some specimens tested their impedance was large compared to the system impedance and therefore some distortion in the current waveform was present.

It has already been mentioned (sec. 7.4.3), that this distortion, which is mainly due to the third harmonic, did not significantly affect the power loss. A bigger kVA transformer than the one used for the tests would have produced sinusoidal currents, by the use of air-cored reactors, but it was unavailable. The slight distortion therefore had to be tolerated.

In Chapter 6, the method developed for the calculation of power loss was based on equations derived from a linear solution. These equations therefore cannot be expected to predict the field distribution within the conductor material. Bearing in mind that the main objective of this thesis is the prediction of losses, the inability to predict or estimate the

current-density distribution within the material may not be consequence, in the case of the isolated conductor. It has however been shown that for this case the depth for complete penetration can be predicted. It will also be shown in the next section, that the step-function analysis can be used to predict, to a reasonable degree of approximation, surface current-density waveforms and, more importantly, explain the observed voltage waveforms obtained in the case of small diameter conductors and thin-wall tubes.

For the case of the concentric arrangement, it is important to be able to predict the electric field at the external surface of the tube, since this value determines the leakage current to earth.

A numerical solution of the field equations describing the system, appears to be the only way to predict accurately the tube surface current-density. A reasonable estimate can be made, using the results of the isolated tube, bearing in mind that for identical external and internal tube dimensions, the depth of penetration for a given H is smaller in the case of the concentric arrangement. The value of δ_s could also be used as a guide to the depth of field penetration since by definition δ_s is the depth below which there is no penetration of field or current. However, this definition is not valid in the case of direct current resistance heating as will be seen later.

7.8.2 Solid conductors

Two typical sets of waveforms have been included in Fig.

7.8 corresponding to different levels of magnetisation, H_s=1370 (A m^{-1}) and H_s=6194 (A m^{-1}). The current-density waveform corresponding to the larger current, shows evidence of saturation, whilst the waveform corresponding to the lower current does not. This observation is in line with the findings of Section 7.4.3 where it was deduced that the turning point for the 1.11 cm diameter bar was in the vicinity of 1400 (A m^{-1}) and therefore the operating point is not in the saturation region.

Whilst the step-function solution for the case of thick and thin steel plates has been superceded by more accurate methods, (Lim and Hammond [52]) (O'Kelly [13]), comparable solutions for a bar of any diameter has not been developed, when the field is produced by the conductor current. However, the analysis based on the step-function B/H characteristic discussed in Chapter 5, can be used in the absence of a more accurate alternative solution.

In Chapter 5, Burke and Lavers and Davies and Bowden's step-function analyses were discussed. None developed expressions for the time variation of electric field strength and therefore an expression will now be developed.

From equations (5.3) and (5.5)

$$E(t) = 2\hat{B}_A \frac{d\psi(t)}{dt} = \frac{2b}{\sigma} \quad \frac{\hat{H}_s \sin\omega t}{2b\psi(t) - \psi^2(t)} \qquad (7.3)$$

Equation 5.6 can be written as

$$\left(\frac{\delta_s}{b}\right)^2 \sin^2\frac{\omega t}{2} = \left[\frac{\psi(t)}{b}\right]^2 - \frac{1}{3}\left[\frac{\psi(t)}{b}\right]^3 \qquad (7.4)$$

in order to introduce the dimensionless parameter δ_s/b

From (7.3) and (7.4) after some manipulation it can be shown that

$$E(t) = \frac{2\hat{H}_s}{\sigma\delta_s}\cos\left(\frac{\omega t}{2}\right) 2\left[\frac{\sqrt{1 - \psi(t)/3b}}{2 - \psi(t)/b}\right] \qquad (7.5)$$

For a thick plate, $b \rightarrow \infty$ and equation (7.5) reduces to equation 20 of Agarwal's paper.

Thus the factor

$$\frac{2\sqrt{1 - \psi(t)/3b}}{2 - \psi(t)/b}$$

takes into account the finite diameter of the bar. As $wt \rightarrow o$, $\psi(t)/b \rightarrow 0$ and therefore the value of E(t) at the start of the half cycle, is the same as if the bar had an infinite radius, or otherwise is equivalent to a thick plate. This observation is in order, since, before the flux has penetrated into the metal, the two situations are indistinguishable. Thus, from equation 7.5, at t=o, the voltage jumps to its peak value. This sudden jump is the result of the assumed B/H curve and this point will be discussed subsequently.

For a given value of wt and δ_s/b, the value of $\psi(t)$ can be calculated from equation 7.4. For small values of wt, $\psi(t)/b$ is $<<1$ and therefore the value of E(t) remains at the peak value. From equation (7.5) E(t) as a function of time can be calculated for different values of the parameter δ_s/b. Fig 7.35 shows E(t) for a few values of δ_s/b. For the second half of the cycle, the

voltage waveform is identical to the first half, except for a displacement in time of π/ω and a sign change. In Fig. 7.35 $\delta_s/b = 0$ corresponds to the infinite radius, or thick plate. In practice, this condition can be achieved by a large diameter bar, whose limiting value is a function of current, frequency and conductor's material parameters. Since the prediction based on the step-function analysis, becomes more accurate as the level of saturation increases, in Fig. 7.35, the characteristic corresponding to $\delta_s/b = 0$, will be a true representation of actual waveforms, in the case of a large diameter bar and high level of saturation. This observation can be substantiated by the waveform (α) of Fig. 7.36 which is reproduced from Bowden and Davies paper [14].

The results reported in Sect. 7.4 refer to a 1.11 cm diameter solid bar and therefore depending on the value of current through the bar, the voltage waveform will lie between the curves corresponding to $\delta_s/b = 0$ and $\delta_s/b = 0.82$. Observations of the oscillogram in Fig. 7.8 indicate that there is no sharp rise in voltage at wt = 0. That this is a consequence of the assumed magnetisation characteristic, can be shown by reference to the papers of Lim and Hammond [52], O'Kelly [13] and Zakrzewski [10] relating to thick and thin steel plates.

In particular, Lim and Hammond compare the waveforms obtained from the step-function solution with the waveforms obtained from a numerical solution of the diffusion equation and a Frohlich representation of the B/H curve. These waveforms are

reproduced in Fig. 7.37 for comparison. Since the power loss mechanism for thick plates is the same as that for conductive heating, it can be argued that a more representative waveform at the start of the half-cycle would be as shown by the dotted lines of Fig. 7.35, which closely resemble the waveform of the oscillogram in Fig. 7.8 under saturation conditions.

So far it has been assumed that the prevailing conditions are such that the wavefront does not reach the centre before the end of the half-cycle, or only just reaches it.

These conditions are represented by $\sqrt{\frac{2}{3}}\, b/\delta_r > 1$ and $\sqrt{\frac{2}{3}}\, b/\delta_s = 1$ respectively, in the equation

$$\tau = \frac{2}{\omega} \sin^{-1}\left(\sqrt{\frac{2}{3}}\, b/\delta_r\right)$$

Under these conditions equation 7.5 applies for the interval $0<t<\pi/\omega$.

Suppose now, that for a constant frequency and diameter, the current is large enough to cause the separation surface to reach the centre of the bar before the end of the half-cycle i.e. $\sqrt{\frac{2}{3}}\, b/\delta_s < 1$. In such a case, for the remainder of the half-cycle, the conductor exhibits a constant resistance equal to its d.c. value and equation 7.5 applies only to the interval $0<t<\tau$.

This observation was made in qualitative terms by McConnell [72] but was not pursued further. This phenomenon was also completely ignored by Davies and Bowden [63] when calculating the losses of a 2.54 mm diameter wire, which show a large error (sect 6.4.1). To test the above prediction, measurements were performed on a 3 mm diameter wire. In addition, the test results would provide a further check for the method of predicting

Table 7.18. Measured And Calculated Loss Values For A 3mm Diameter Wire

I (A)	H_s (Am^{-1})	P_m (Wm^{-1})	P_{c1} (Wm^{-1})	P_{c2} (Wm^{-1})	P_{sm} (Wm^{-2})	$\frac{P_{c2}-P_m}{P}$ %
16	1697	7.14	6.89	6.77	757	- 5.2
24	2546	14.5	14.4	14.1	1538	- 2.7
32	3395	24.8	24.6	24.1	2631	- 2.8
40	4244	38.1	37.7	36.9	4042	- 3.1
48	5093	53.7	53.7	52.5	5704	- 2.2
64	6791	93.6	94.2	92	9931	- 1.7
80	8488	147.2	146.3	142.7	15620	- 3
96	10180	216	209.7	204.6	22920	- 5.3
112	11880	296	284.7	277.7	31406	- 6.1
120	12730	336	326.6	318.5	35651	- 5.2

For P_{c1} $\rho = 15.9 \times 10^{-8}\ \Omega \cdot m$

For P_{c2} $\rho = 15.5 \times 10^{-8}\ \Omega \cdot m$

$\mu_{reff} = 575 \times 10^3 H_s^{-0.83}$

losses and finally confirm that for small diameter conductors, the power index of H approaches 2.

The measured and calculated results are shown in Table 7.18 Fig. 7.38 shows that the power index of H_s is indeed 2.

The measured value of resistivity using a voltmeter/ammeter method was 14.8×10^{-8} (Ω m) $\pm$ 6% and good agreement is obtained between measured and calculated loss values based on a value of resistivity within this range. *

Fig. 7.39 and Fig. 7.40 shows a selection of oscillograms for different levels of saturation. It can be seen that depending on the value of current, the transition during the half cycle from a.c. to d.c. resistance, occurs at different time intervals.

An attempt will now be made, to predict waveform (a) of Fig. 7.40.

Under d.c. resistance conditions, E(t) is given by

$$\hat{I} R_{dc} = \frac{2 \hat{H}_s}{\sigma b} \qquad (7.6)$$

and is in phase with the current through the wire. For a given value of $\hat{H}_s$, equation 7.6 has a definite value. However, the value of E(t) obtained from equation 7.5 is dependent on the value assigned to δ_s.

---

* Although the wire was immersed in water the heat generated within it could not be dissipated in the time required to take readings and the bar temperature was not therefore constant throughout the range of currents.

Now $$\delta_s = \sqrt{\frac{2\hat{H}_s}{\sigma\omega\hat{B}_A}}$$

Assuming $\hat{B}_s$ is 1.72 for mild steel and $\hat{B}_A = 0.75\,\hat{B}_s$, with $\omega = 314$ (rad s^{-1}), $\sigma = 0{,}64 \times 10^{7}$ (S m^{-1}), $\hat{H}_s = 7201$ (A m^{-1})

$$\delta_s = 2.35 \text{ mm}$$

From equation 5.8,

$$\omega\tau = 2\sin^{-1}\left(\sqrt{\frac{2}{3}}\,\frac{1.5}{2.35}\right) = 63^{\circ}$$

which agrees with the value obtained from the oscillogram of Fig. 7.40.

From Equation 7.6

$$|E(t)| = \frac{2 \times 7201}{0.64 \times 10^{7} \times 1.5 \times 10^{-3}} = 1.5 \quad (V m^{-1})$$

The measured value of E(t) = 1.44 which is in agreement within the experimental error.

From equations 7.4 and 7.5 with $\omega t = 63^{\circ}$ $\psi(t)/b = 1$

$$|E(t)| = \frac{4 \times 7201 \times 0.852 \times 0.816}{0.64 \times 2.35 \times 10^{7} \times 1} = 1.33$$

with a measured value of 1.32.

The measured and calculated voltage waveforms are shown in Fig. 7.41. It can only be assumed that the disagreement at the beginning of the half cycle is due to the same reasons given for the case when $\delta_s < b$.

As the current increases, the wire exhibits a resistance equal to its d.c. value for a greater part of the half cycle.

The calculated loss values in Table 7.18 are based on the effective permeability method. The step-function theory can be

used but equation 5.12 developed by Burke and Lavers fails since it applies only if $\sqrt{\frac{2}{3}}\, b/\delta_s \geq 1$

For the case when $\sqrt{\frac{2}{3}}\, b/\delta_s < 1$, the power loss can be calculated from equation 6.4.

The two components of power are shown in Table 7.19 as P_1 and P_2. As the current increases the second component which is due to the d.c. resistance predominates.

In the effective permeabilty method, the calculated values are dependent on the effective permeability and resistivity. In the step-function method, the equivalent flux density B_A and resistivity influence the calculated loss values. All these parameters can be obtained only from measurements and on this basis there is little to choose between the two methods. However, the effective permeability method can be valid for magnetic surface field-strengths as low as 1000 (A m^{-1}), whereas the step-function theory is inaccurate at this range, but can predict reasonably well the waveforms of surface current density.

Additional tests were carried out with two bars of equal 10 mm diameters, but of different resistivities and the results which are not included showed that

1. the losses could be accurately calculated by using a value of $\mu_{reff} = 575 \times 10^{3} H_s^{-0.83}$;
2. there was a unique characteristic relating the dimensionless parameters in contrast with the sample A and B tubes of 15 mm bore;

Table 7.19. Measured And Calculated Loss Values Based On Step-function Theory - 3mm Diameter Wire

I (A)	Hs (Am^{-1})	P_1 (Wm^{-1})	P_2 (Wm^{-1})	Pc (Wm^{-1})	Pm (Wm^{-1})	Pc d.c. (Wm^{-1})	$\frac{(Pc - Pm)}{Pm}$ %
16	1697	6	0.74	6.74	7.14	5.6	- 5.6
24	2546	11	2.77	13.8	14.5	12.7	- 4.8
32	3395	13	14	27	24.8	22.6	8.8
40	4244	15	25.4	40.4	38.1	35.4	6
48	5093	20	39.6	59.6	53.7	50.9	11
64	6791	17	77	94	93.6	90.5	0.4
80	8488	24	126	150	147	141.5	2
96	10180	32	186.7	218.7	216	204	1.2
112	11880	41	259	300	296	277	1.3
120	12730	44	299	343	336	318	2

$$\rho = 15.6 \times 10^{-8}\ \Omega \cdot m$$

$$B_S = 1.72\ T$$

$$B_A = 1.72 \times 0.75\ T$$

$$Pc = P_1 + P_2$$

3. the current density double hump characteristic obtained with the 3 mm wire was also obtained with the 10 mm bars at high values of field strengths.

Tests were also carried out with a 20 mm diameter bar. The results are not reported but confirmed the method of calculating the power loss, indicated that the power index of surface field strength is 1.61 and produced a dimensionless parameter characteristic the same as the one obtained for the thick-wall sample A tube (their respective external diameters differ by only 5% and therefore can be described by the same characteristic). The oscillogram for the 20 mm diameter bar corresponding to H_s = 20,254 is shown in Fig. 7.42. Fig. 7.43 shows the calculated waveform with the two points obtained from the oscillogram of Fig. 7.42. The calculations were based on a value of $\hat{B}_A$ = 2 in view of the high level of magnetisation. The good agreement between the measured and calculated waveforms for bars of different diameters confirmed the derived expressions for the calculated surface electric field waveforms, which to the author's knowledge have not been published previously.

In the step-function theory and for a thick plate with a surface excitation produced by a current external to the plate, the depth of penetration is the maximum value of $|\psi(t)|$ which is attained at the end of the half period. The field is zero beyond this depth if $|\psi(t)|$ is less than the half thickness of the plate. If the excitation is produced by a current flowing as in the case under consideration through a bar, and the conditions

are such that $|\psi(t)|$ at the end of the half cycle is less than the radius of the bar, the field beyond $|\psi(t)|$ is not zero. This is because the current flows through the bar throughout the half-cycle. In the case of large diameter bars, where the centre is not reached by the end of the half cycle, a better definition of depth of penetration can be obtained in terms of the power loss and this concept has been used in deriving in Chapter 4 the equation for complete penetration.

7.8.3 Isolated tubular conductor

At the beginning of the half-cycle, the flux penetrating into the surface cannot distinguish between a bar and a tube. The centre of the bar is now replaced by the inner surface of the tube and the time taken to reach it has been shown to be

$$\tau = \frac{2}{\omega} \sin^{-1}\left[\frac{(b-a)}{\delta_s}\sqrt{\frac{2}{3}+\frac{a}{3b}}\right] \qquad (7.7)$$

If $\left(\frac{b-a}{\delta_s}\right)\sqrt{\frac{2}{3}+\frac{a}{3b}} \gg 1$

the current density waveform will be similar in shape to the ones obtained from solid bars, for a corresponding level of saturation. This is confirmed by the oscillograms in Fig. 7.44, A to D, where it can also be observed that the phase angle between the voltage and current becomes zero as the tube-wall thickness is reduced. This is to be expected since with deep penetration and thin-wall tubes Rac approaches Rdc.

The phase angle is also a function of the level of magnetisation and this can be observed by comparing the oscillograms of Fig. 7.44 (A) and Fig 7.45 (A).

If $$\left(\frac{b-a}{\delta_s}\right)\sqrt{\frac{2}{3}+\frac{a}{3b}} < 1$$

the same phenomenon is observed as with small diameter bars, i.e. the tube at some interval within the half-period, exhibits a constant resistance equal to its d.c. resistance.

Equation 7.5 is valid but only up to $t = \tau$

Considering Fig. 7.44 (E), which refers to a sample A tube of 19 mm and 16 mm external and internal diameter respectively, and applying equation 7.7 with $\delta_s = 2.63$ mm

$$\omega\tau = 67^\circ$$

the peak value under d.c. resistance condition is

$$|E(t)| = \frac{2b\hat{H}_s}{\sigma(b^2-a^2)} = 1.27 \quad (V\,m^{-1})$$

with a measured value of 1.28. This agreement also confirms the value of resistivity.

(The temperature at which the oscillogram of Fig. 7.44 (E) was obtained was 35 °C and therefore a temperature correction was made with a temperature coefficient of resistance of 0.0037/°C).

The peak value under a.c. resistance conditions is 1.34 ($V\,m^{-1}$) with a measured value of 1.36 ($V\,m^{-1}$). Similarly for the sample B tube of equal radial dimensions (Fig. 7.46 (B)) and with $\delta_s = 2.55$ mm

$$\omega\tau = 70^\circ$$

The peak value under d.c. resistance conditions is 0.95 ($V\,m^{-1}$)

with a measured value of 0.93 ($V\ m^{-1}$).

Under a.c. resistance conditions the calculated voltage is 1.05 ($V\ m^{-1}$) and the measured value 1.08 ($V\ m^{-1}$).

7.9 Concentric Arrangement

7.9.1 Results and discussion

The method of measurement and its accuracy have already been discussed in Section 7.3.1.

Tables 7.20 and 7.21 show the measured and calculated loss values for four bore sizes of sample A tubes. For the isolated case, it was found that for sample A material and for large values of β, agreement between measured and calculated loss values was obtained on an effective permeability given by $536 \times 10^{3} H_{s}^{-0.83}$.

In Chapter 4, the criteria for the use of Arnold's or Dwight's formula for the concentric arrangement have been established and on this basis, for the β values considered in the experimental work, Dwight's formula is the more appropriate to use. The use of this formula together with the above effective permeability, fails to predict the results correctly. This is not surprising; in the case of the isolated tube, the effective permeability was the result of the field decaying inwards whilst in the case considered here, the field is decaying outwards. Thus for the same surface field strength, successive conductor layers in the concentric case are less strongly magnetised than in the isolated case. Since the effective permeability takes into account the change in permeability with depth, it should be expected that the effective permeability in the concentric arrangement will have to be

increased. It will also be shown later that for the same surface magnetic field-strength, the depth of penetration is smaller in this case. Since the depth of penetration is related to permeability, reduction in depth of penetration, reflects an increase in permeability and therefore the above observations do not contradict the physical laws describing resistance heating.

The mathematical equations developed in Chapter 4, showed that the resistance of the outer tube in the concentric arrangement increases. In the absence of permeability effects, the increase in resistance can be explained rather simply; since the area of cross-section available to current in the inner surface is smaller than at the outer surface, the effective resistance of the tube should be higher than when the current flows in the outer surface. The reduction in the depth of penetration due to an increase in permeability, enhances this effect further.

Having established that the effective permeability is not the same as in the isolated case, it remains to quantify its value. By calculating the losses, it was found that the effective permeability had to be modified by a constant factor h for a given β value. That this factor will have to vary for different β values, can be deduced from the fact that at some value (depends on the external diameter), the tube resistance should be equal for the two configurations (Fig 4.7).

The multiplying factors h, are shown in Tables 7.20 and 7.21 for each tube size tested and when plotted against β, a straight line relationship is obtained.

The loss as a function of β for constant current is shown in Fig. 7.47. The increase in loss ΔW, as a function of current is shown in Fig.7.48 and as a percentage of the measured loss of the isolated case, in Fig. 7.49. As the current increases, the percentage increase is reduced due to the increased penetration.

In Tables 7.20 and 7.21, the values of ΔW are based on a series of repeated tests, but as already mentioned, for high values of currents and thin tubes, they become less reliable. In drawing the graphs of Fig. 7.48 corresponding graphs of Chapter 4 have been used as a guide to their shape. This is because in the case of non-magnetic conductors, the equations used to calculate the increase in loss, have been experimentally verified in the past.

In the case of the isolated tube, it was found that as the wall thickness was reduced, the measured loss was higher than calculated, with the discrepancy increasing with a reduction in wall thickness. For the concentric arrangement, this discrepancy becomes apparent again, for the same β value of 0.37. However, if the difference between calculated and measured loss values for the isolated tube are added to the calculated loss values in Table 7.21, for $\beta = 0.37$ agreement is once again obtained with the measured loss values.

Since the depth of penetration is a function of the diameter, reducing the external diameter of the tube, will reduce the increase in loss for the same current. Thus a thin wall tube of large external diameter can experience at a fixed current the same increase in resistance as a thick wall tube of

Table 7.20 Measured and Calculated Loss Values - Concentric Arrangement

	d_o = 19 mm d_i = 6.35 mm h = 1.25				d_o = 19 mm d_i = 8.50 mm h = 1.2			
I (A)	Pm (Wm^{-1})	ΔW (Wm^{-1})	Pm + ΔW (Wm^{-1})	Pc (Wm^{-1})	Pm (Wm^{-1})	ΔW (Wm^{-1})	Pm + ΔW (Wm^{-1})	Pc (Wm^{-1})
60	8.4	20	28.4	30.6	9	15.7	24.7	26.7
84	19.8	29.4	49.2	50.9	21.3	22	43.3	44.7
96	27.3	33	60.3	62.2	28.8	24.3	53.1	54.9
120	44.6	42	86.6	87.1	46.9	30	76.9	77.2
156	75.3	54	129.3	129.3	78.6	17	115.6	115
180	99	61	160	160.3	101.2	41	142	143
204	123.4	70	193.4	193.3	127.7	44	172	172
228	150.5	77	227.5	228	154	48	202	203
240	164.3	82	246	246	167	50	217	219
252	178	85	263	264.5	182	52.5	234.5	236
264	194	90	284	283	196	54	250	252
276	209	93	302	302	210.5	56	266	269
288	223	97	320	322	224.7	58	282	286
300	239	102	341	341	240	60	300	304

Sample A Tube

$\rho = 24.5 \times 10^{-8}\ \Omega\ m$

$\mu_{reff} = 536 \times 10^{3}\ H_s^{-0.833}$

Table 7.21 Measured and Calculated Loss Values - Concentric Arrangement

	d_o = 19 mm d_i = 10 mm h = 1.17				d_o = 19 mm d_i = 12 mm h = 1.13			
I (A)	Pm (Wm^{-1})	ΔW (Wm^{-1})	Pm + ΔW (Wm^{-1})	Pc (Wm^{-1})	Pm (Wm^{-1})	ΔW (Wm^{-1})	Pm + ΔW (Wm^{-1})	Pc (Wm^{-1})
60	9.4	13	22.4	24.5	10.4	9.5	19.9	22.2
84	22	17.5	39.5	41.3	23.7	12	35.7	37.4
96	30	19	48	50.7	32	13	45	46
120	48.5	21	69.5	71.5	50.4	14	64.4	64.6
156	80	25	105	106.7	82		96	95.3
180	103.5	27.5	131	132	105		119	117.4
204	127.7	30	157.7	159	129		143	140.5
228	154	32.5	186.5	187	156		170	164.7
240	168	33.5	201	202	169		183	177
252	182	34	216	217	184	15	199	190
264	197	35	232	232	198		213	203
276	210	36	246	247	212		227	216
288	226	37	263	262	230		245	230
300	241	38	279	278	246	16	262	243

Sample A

$\rho = 24.5 \times 10^{-8}$ m

$\mu_{reff} = 536 \times 10^{3} \; H_s^{-0.833}$

Table 7.22 Calculated and Measured Loss Values Using Step-function Method

	ISOLATED TUBE		CONCENTRIC ARRANGEMENT		
I (A)	Pm (Wm^{-1})	Pc (B_A=1.72 x 0.75)	Pm (Wm^{-1})	Pc (B_A=1.72 x 0.75)	Pc (B_A=1.72 x 0.75 x 1.25)
60	9	19	28	29	33
84	21.3	32	49	47	54
96	28.8	40	60	57	65
120	46.9	56	87	80	90
156	78.6	84	129	116	131
180	101	104	160	142	162
204	128	126	193	170	193
228	154	150	227	201	225
240	167	162	246	213	245
252	182	175	263	230	260
264	196	187	284	248	280
276	210	201	302	259	300
288	225	215	320	276	314
300	240	228	341	292	334

Sample A

$\rho = 24.5 \times 10^{-8}\ \Omega$ m

$d_o = 19.07$ mm

$d_i = 6.35$ mm

Table 7.23 Percentage Increase In Loss Due To Concentric Configuration

	d_o = 19 mm d_i = 6.35 mm			d_o = 19 mm d_i = 8.5 mm		
I (A)	H_{si} (Am^{-1})	Psmi (Wm^{-2})	% Increase in Loss	H_{si} (Am^{-1})	Psmi (Wm^{-2})	% Increase in Loss
60	3,007	1,424	238	2,247	925	174
96	4,812	3,018	121	3,595	1,990	84
120	6,001	4,334	94	4,494	2,880	64
180	9,000	8,007	62	6,740	5,317	40
240	12,000	12,310	50	8,987	8,126	30
264	13,230	14,210	46	9,886	9,362	27.5
300	15,000	17,066	42.5	11,234	11,230	25

	d_o = 19 mm d_i = 10 mm			d_o = 19 mm d_i = 12 mm		
60	1,910	713	138	1,591	528	91
96	3,056	1,559	63	2,546	1,194	41
120	3,819	2,212	43	3,183	1,708	28
180	5,729	4.169	26.5	4,774	3,156	13
240	7,639	6,398	18.7	6,366	4,854	8.2
264	8,403	7,385	17.7	7,000	5,650	7.6
300	9,549	8,880	16	7,958	6,950	6.5

Sample A

$\rho = 24.5 \times 10^{-8}\ \Omega\ m$

smaller external diameter.

The increase in loss due to the concentric configuration, can also be shown by considering the step-function theory. It has been shown in Chapter 6 that the increase in power under the condition that the wavefront does not reach the inner or outer tube surfaces before the end of the half-cycle, is given by

$$\Delta W = \frac{\omega \hat{I}^2}{\sigma \pi^2}\left[\int_0^{T/2} \frac{\sin^2(\omega t)_c}{2a\,\psi(t)_c + \psi^2(t)_c}\,dt - \int_0^{T/2} \frac{\sin^2(\omega t)_i}{2b\,\psi(t)_i - \psi^2(t)_i}\,dt \right]$$

where T is the period and the subscripts i and c refer to the isolated and concentric arrangement respectively. For a constant b, as a is reduced (i.e.thicker wall), ΔW increases.

Considering the first term in the equation above, which refers to the concentric arrangement, it can be observed that it is independent of b up to a certain value (see Section 6.10.4).

Thus, if a is constant and the wall thickness is reduced by reducing b, the loss will remain constant for a given current. This explains the constancy of Rac in Fig. 4.10 as β reduces. However, if the variation in β is obtained by reducing a, as β increases, there is a considerable increase in Rac and hence power loss.

Because of the need to use a multiplying factor in the effective permeability method in order to obtain agreement between measured and calculated loss values, it was decided to calculate the losses by means of the equation derived on the basis of the step-function theory. The validity of this analysis was first checked on the experimental results obtained

for an isolated tube. The results referring to the sample A tube of dimensions a = 6.35 mm and b = 19 mm (β = 0.666) was selected for this check on the basis that the experimental results are more reliable than for the thinner wall tubes of the same material.

For the calculations, $\hat{B}_s$ was taken as 1.72 T and $\hat{B}_A$ as 1.72 x 0.75 = 1.29 T. To check the correctness of $\hat{B}_A$, the loss of the isolated tube was first calculated and the results are shown in Table 7.22.

The agreement between measured and calculated values is good in the saturation region and fails as expected in the unsaturated region. Using the same value of $\hat{B}_A$, the losses were calculated for the concentric arrangement and agreement with the measured values was not obtained. In view of the comments made previously regarding the experimental results, it could be argued that the measured values are in error. Fig. 7.50 shows the band of experimental results which were obtained from repeating the measurements on nine different runs. The results of Fig. 7.50 indicate that the calculations must be in error.

$\hat{B}_A$ was then increased by a factor of 1.25 (equivalent to increasing μ by 1.25) and the results re-calculated (Table 7.22).

Agreement is now obtained. However, in this case the factor of 1.25 has a different origin. In Chapter 5, the significance of the factor of 0.75 was explained. This factor is a function of the level of saturation and for very high field strengths it

tends to unity. Thus the effect of 1.25 is to increase the factor of 0.75 to 0.75 x 1.25 $\simeq$ 0.94. In the concentric arrangement the appropriate surface magnetic field is that developed on the inner surface of the tube. For the tube considered, the inner diameter is small and therefore for a given current, the internal surface field strength is much larger than in the case of the isolated tube. Thus there is some justification in the factor of 1.25.

In the case of the effective permeability method, the higher surface field strengths involved in the concentric arrangement, necessitate a shift of the operating points beyond the turning point of the μ_v/H curve, thus enabling the use of the effective permeability function throughout the range of currents considered.

Fig 7.51 shows the internal surface power density as a function of the internal surface field strength. The experimental points for different values of β lie almost on the same characteristic. As the wall thickness is reduced, for a given current, the internal surface field is almost equal to the external and the increase in loss ΔW tends to zero. Thus the straight line of Fig. 7.51 is not expected to apply to all values of β but it covers the range of β = 0.37 to 0.66. Fig. 7.51 can therefore be used to estimate the tube dimensions and current to give a required power. Obviously for different steels, the same characteristic does not necessarily apply and further tests are required with different tube radial dimensions and materials (see also Appendix B).

Fig. 7.53 shows the voltages proportional to the external surface current-density as the tube bore is increased. As the bore increases, these values tend to those obtained for the isolated case. This is to be expected since, as the current increases the penetration increases, and therefore the surface current density increases. The case when the external diameter is reduced, is shown in Fig.7.54.

Fig. 7.55 compares the voltage outputs (not corrected for amplifier gain) from the current density probes, for two isolated tubes of the same material and external diameter, but of different bore sizes. In both cases, the characteristics are made of straight line portions meeting at different values of current. The change in slope is due to saturation, with the thinner wall tube saturating at a lower value of current. The corresponding characteristics for the concentric arrangement are shown in Fig. 7.56 and Fig 7.57. In this case, the two straight line portions of each characteristic, meet at the same corresponding current values as for the isolated case, except that the slopes of the upper portion increase rather than decrease. A plausible explanation could be that for low values of current the tube surface is magnetised along the initial part of the B/H curve and as the current increases, along the upper part. The surface layer does not reach saturation level because of the attentuation of the field as it reaches the surface.

7.9.2 Waveforms

The oscillograms obtained with sample A tubes of different internal and external diameters are shown in Figs. 7.58 and 7.59 for two values of current. The phase shift of the current density waveforms for different tube wall thicknesses can be observed and increases with wall thickness. The peak of the waveforms are also displaced in time (some current density waveforms are 180° out of phase because the oscilloscope leads were reversed). Since for a constant current, the level of magnetisation depends on the internal diameter of the tube, the oscillograms of Fig. 7.60 were therefore obtained in order to examine the attenuation of current density with depth into the material for constant magnetisation conditions. For this exercise, two sample A tubes were connected in series and excited by a concentric conductor. Both tubes had an internal diameter of 6.35 mm and the nominal values of the external diameters were 19 mm and 12 mm.

A comparison of the oscillograms of Fig. 7.60 with the waveforms of Fig. 7.37 shows a distinct difference in behaviour of field penetration. Whilst the phase shift with depth is present in both cases, in the case of a bar carrying current, the peak of the displaced waveform is not enclosed by the same envelope. This could be due to the larger tube wall thickness associated with the waveforms of Fig. 7.37, or it could be a cylindricality effect.

Examination of Fig. 7.59 (E) shows the same interesting phenomenon which was observed previously with isolated thin wall

tubes, namely that at some instant during the half cycle, the a.c. resistance reverts to the d.c. value and produces a voltage in phase with the excitation current.

The step-function theory can be used to establish the time interval at which this transition occurs.

Analysis shows that for the concentric arrangement

$$\tau = \frac{2}{\omega} \sin^{-1}\left[\left(\frac{b-a}{\delta_s}\right)\sqrt{\frac{2}{3}+\frac{b}{3a}}\right] \qquad (7.8)$$

Equation (7.8) which has not previously appeared in the literature, gives the following values for $\omega\tau$

Current 288 A

Tube dimensions b (mm)	a (mm)	$\omega\tau$ measured degrees	$\omega\tau$ calculated degrees	Fig.No.
9.5	8	63	59	7.59 (E)
↓	7.5	90	81	7.59 (D)
	6.95	126	107	7.59 (C)

For smaller values of a, the wavefront does not reach the outer surface. The calculated values are of the right order but consistently smaller than the measured values. The calculated values are weakly dependent on the value of δ_s but strongly dependent on the tube dimensions. Since the different bores were obtained by drilling the tube, there is some uncertainty in the value of the internal diameter. Similarly, since the

measured values of $\omega\tau$ have been obtained from the respective oscillograms, these are subject to a reading error.

The main reason for the disagreement between measured and calculated values of $\omega\tau$ is that $\omega\tau$ is calculated for the inner surface, whilst the oscillograms of Fig. 7.59 are obtained from probes at the outer surface. The phase shift with depth is not therefore considered in calculating and as it increases with wall thickness, the discrepancy in $\omega\tau$ increases. It is interesting to compare equations (7.8) with (7.7). In Chapter 4, when the formula for the impedance of the outer tube of a concentric arrangement was quoted, it was stated that the expression was the same as for the isolated tube, except that a and b were interchanged and the sign in front of the formula changed. Examination of equations (7.7) and (7.8) shows that (7.8) is the same as (7.7) with the above changes made.

For the same values of parameters present in equations (7.7) and (7.8) equation (7.8) gives a higher value of arc sin. Since this value cannot exceed unity, it follows that when the conditions are such as to enable the wavefront to reach the inner surface of the isolated tube, for the same surface field-strength, in the concentric configuration, the wave will not reach the outer surface. This confirms that the "depth of penetration" is smaller in the concentric arrangement.

For this case and at the inner surface of the tube,

$$E(t) = \frac{4\hat{H}_1}{\sigma\delta_1}\cos\left(\frac{\omega t}{2}\right)\left[\frac{\sqrt{1+\psi(t)/3a}}{2+\psi(t)/a}\right] \qquad (7.9)$$

with $\psi(t)$ obtained from

$$\delta_s^2 \sin^2\left(\frac{\omega t}{2}\right) = \psi(t) + \frac{\psi^3(t)}{3a} \qquad (7.10)$$

The voltage due to the d.c. resistance is the same as for the isolated tube under identical conditions.

The oscillograms of Fig. 7.59 (A) shows that even with a wall thickness of 6.3 mm, there is some finite surface field.

7.9.3 Depth of penetration

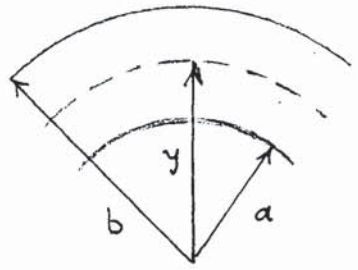

If $$\left(\frac{y-a}{\delta_s}\right)\sqrt{\frac{2}{3}+\frac{y}{3a}} = 1 \qquad (7.11)$$

The separating surface will reach the depth y at the end of the half-cycle. Substituting for δ_s in (7.11) and simplifying

$$y^3 - 3ya^2 + 2a^3 = \frac{3\hat{I}}{\omega\pi\sigma B_A} \qquad (7.12)$$

By definition the distance $(y-a)$ is the depth of penetration given by the step function theory.

For the case of sample A tube with 2a = 6.35 mm, $\sigma = 0.406 \times 10^7 (S\ m^{-1})$, I=288 A, B_A = 1.72 T, from equation (7.12) y= 6.82 mm. Thus at the end of the half-cycle, the separating surface penetrated to a depth of

$$6.82 - 3.17 = 3.65 \text{ mm}$$

The wall thickness of the tube considered for the above example is 6.36 mm and therefore, since the wall thickness is

greater than 3.65 mm the current density should be zero at the surface. The oscillogram of Fig. 7.59 (A) shows that the surface current density is finite. In this respect the discussion of Section 6.7 is relevant.

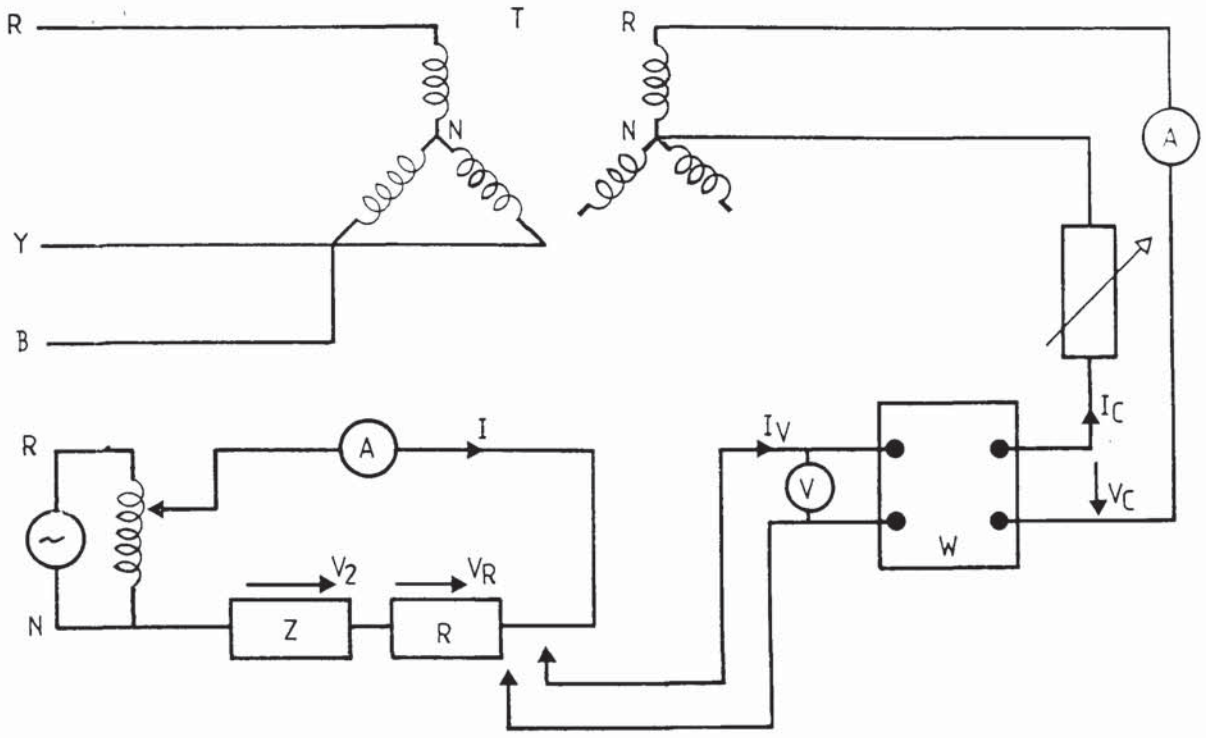

Fig. 7.2 Circuit for measuring magnitude and phase angle of an impedance

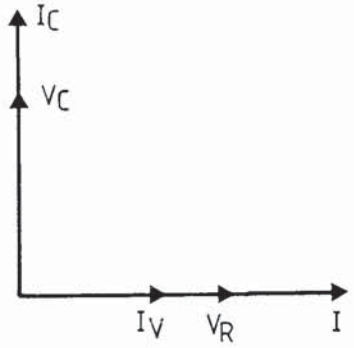

Fig. 7.3 Phasor diagram for zero reading on watt meter voltage coil across standard resistor (Fig 7.2)

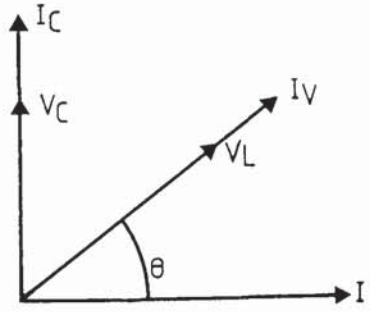

Fig. 7.4 Phasor diagram when voltage coil is connected across impedance Z (Fig 7.2)

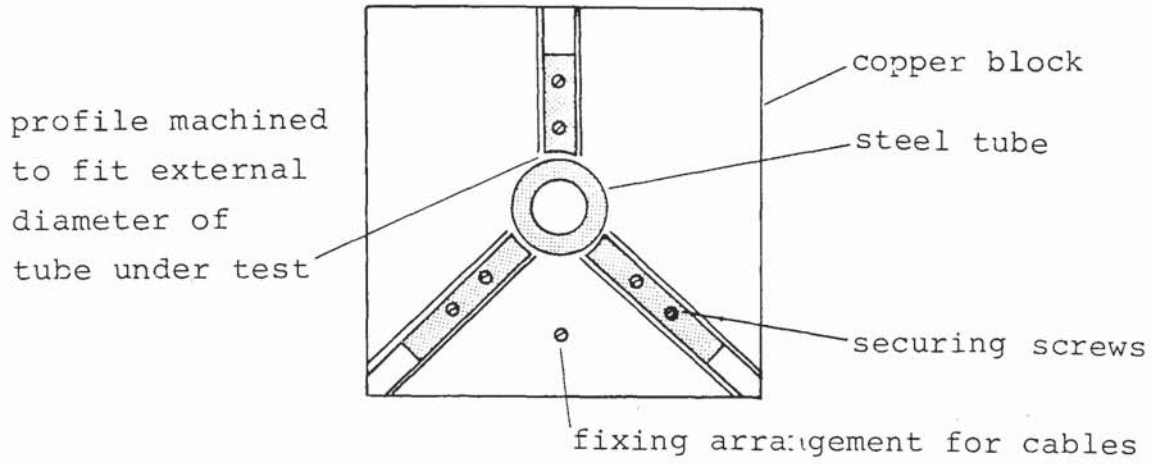

ig. 7.5 Contact arrangement for supplying current to a tube

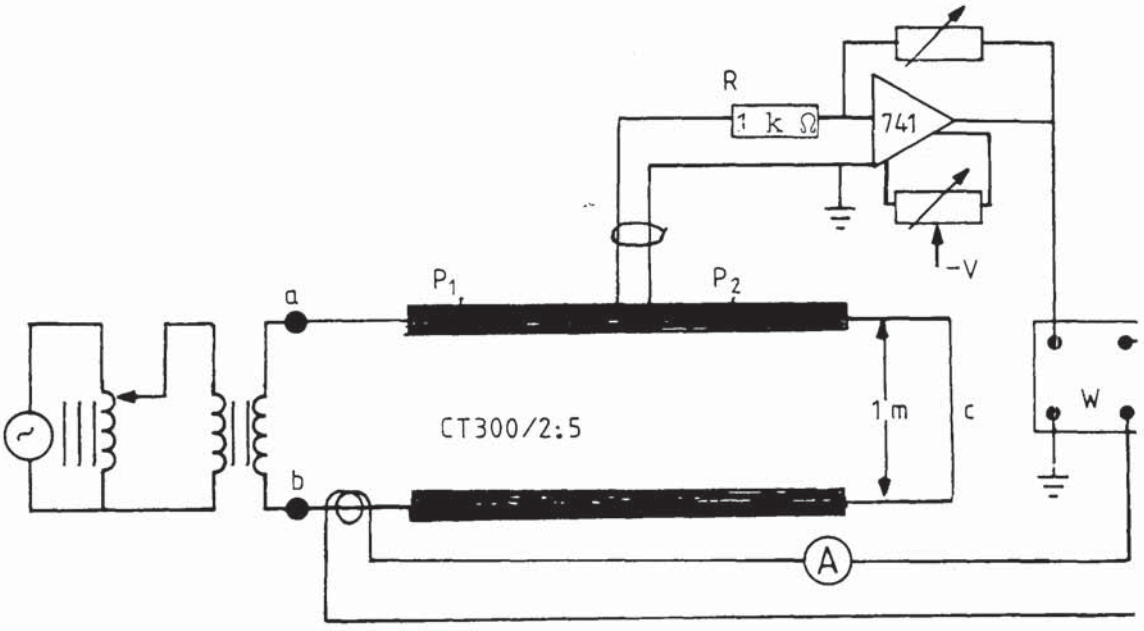

Fig. 7.6 Circuit for measuring power loss in steel conducto

Magnification x 200

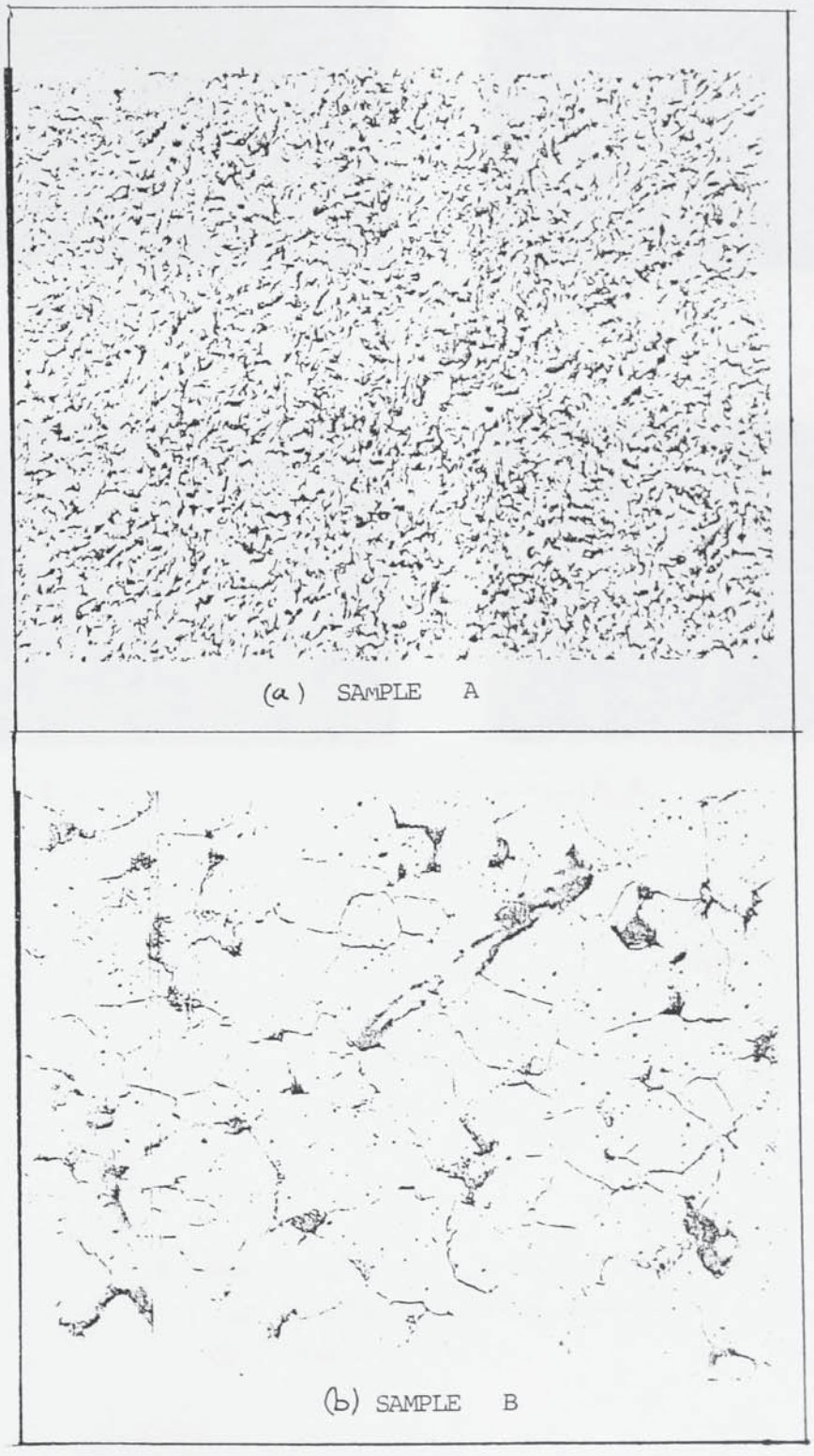

(a) SAMPLE A

(b) SAMPLE B

Fig. 7.7 Photomicrographs of sample A and B material

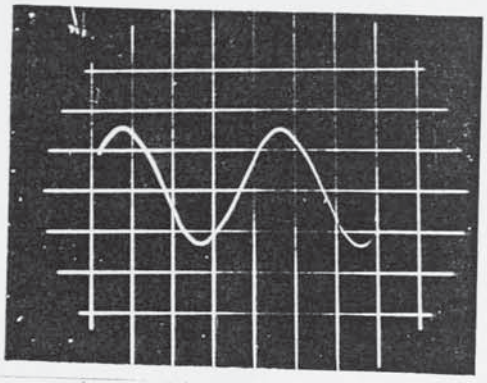

I = 48 A

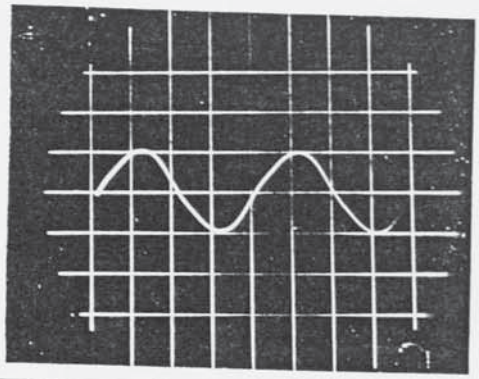

I = 48 A

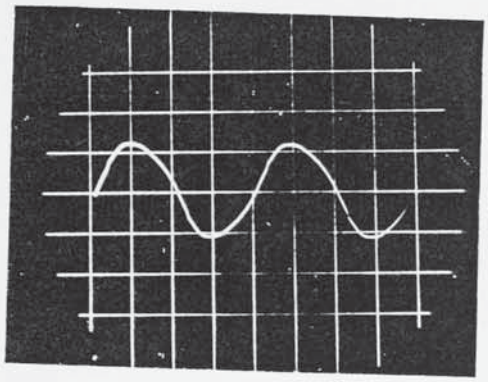

I = 216 A

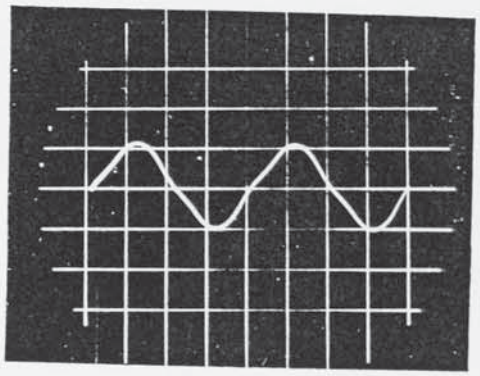

I = 216 A

(a)

(b)

7.8 Oscillograms - isolated conductor
(a) Surface current density
(b) Supply current

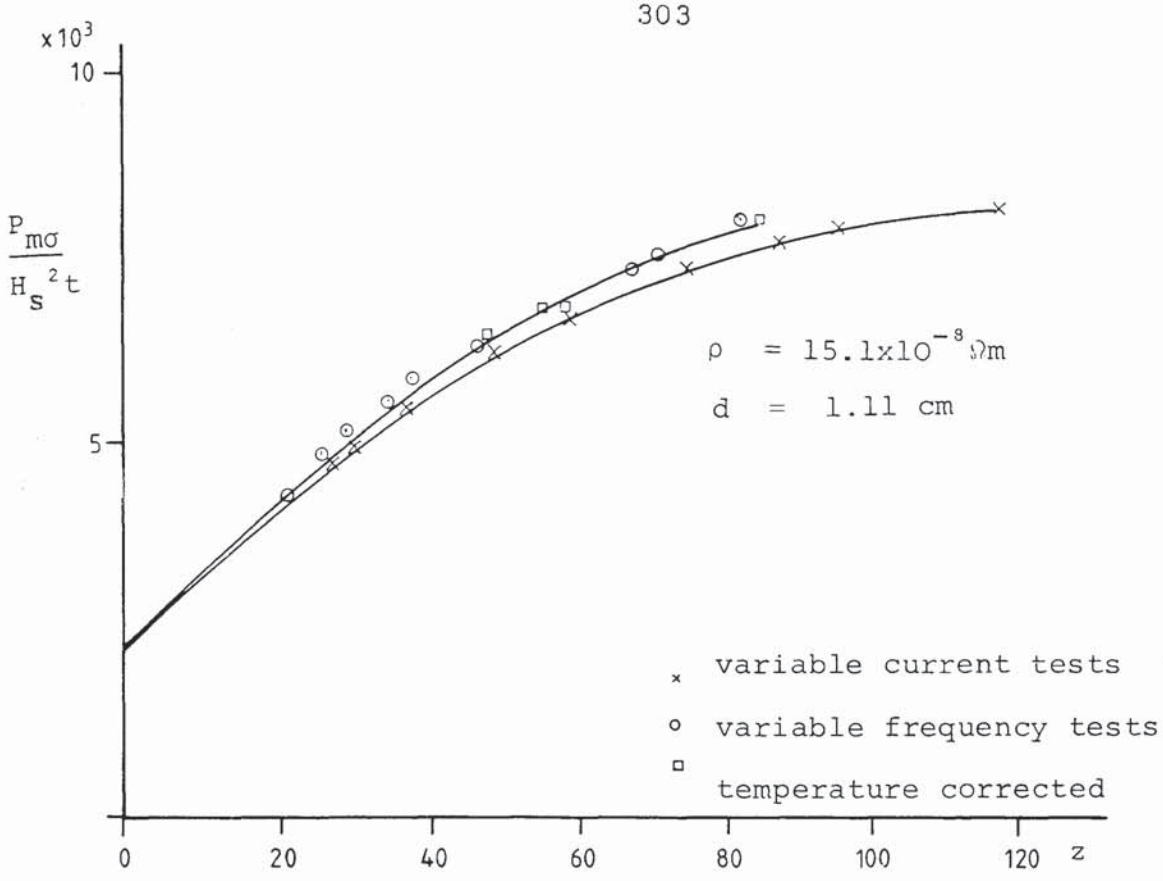

Fig. 7.9 Dimensionless factors describing a steel bar

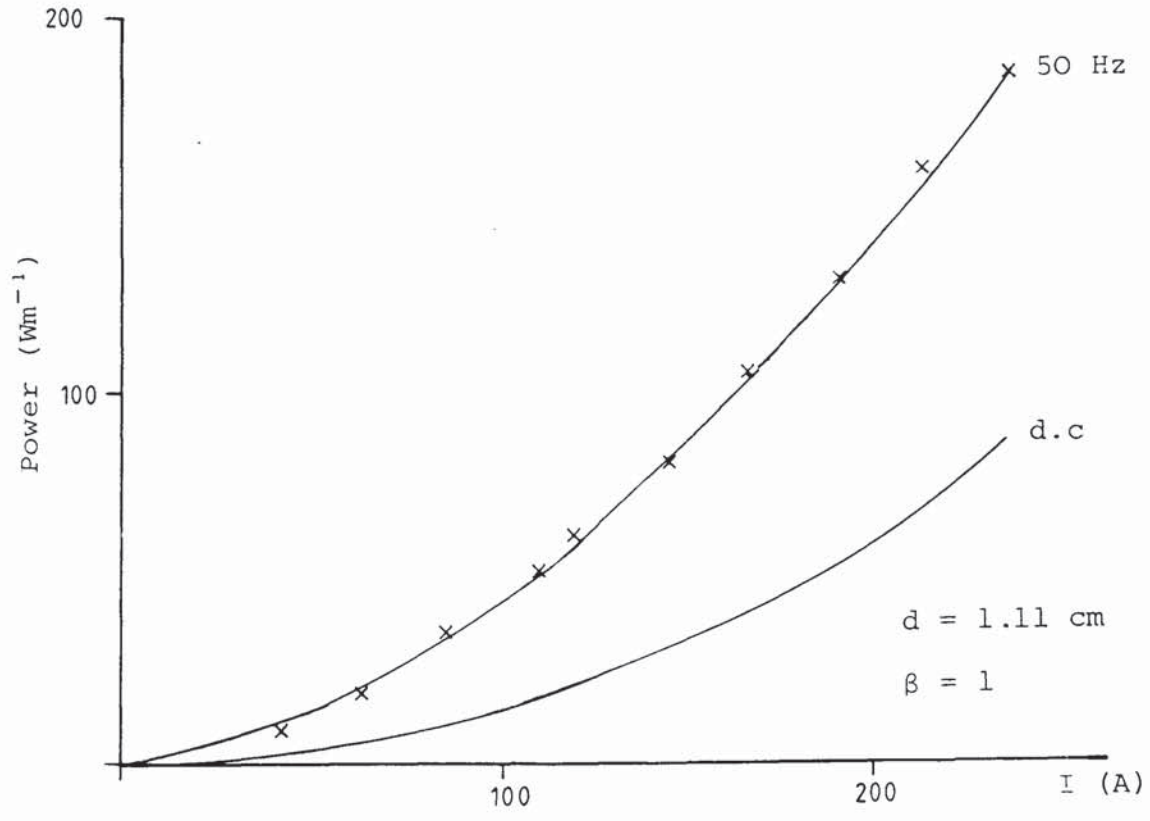

Fig. 7.10 Measured a.c. and calculated d.c. power as a function of current.

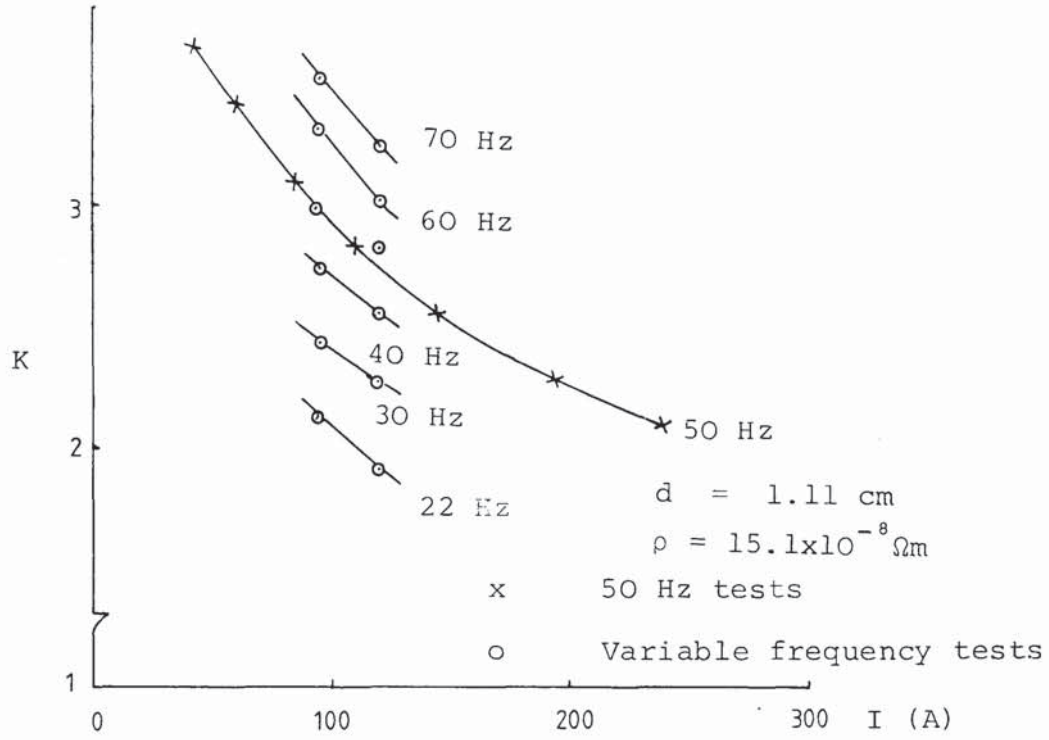

Fig. 7.11 Ratio of a.c. to d.c. resistance at constant frequency, as a function of current for a steel bar - measured values

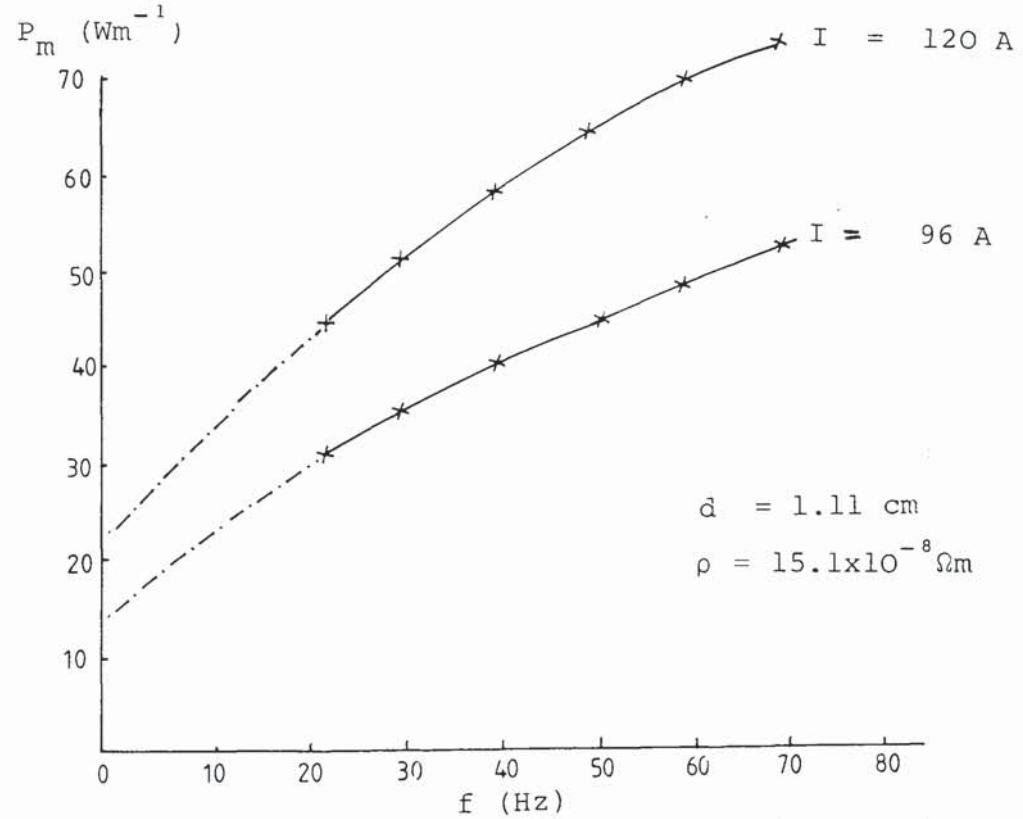

Fig. 7.12 Measured power developed at constant current as a function of frequency for a steel bar

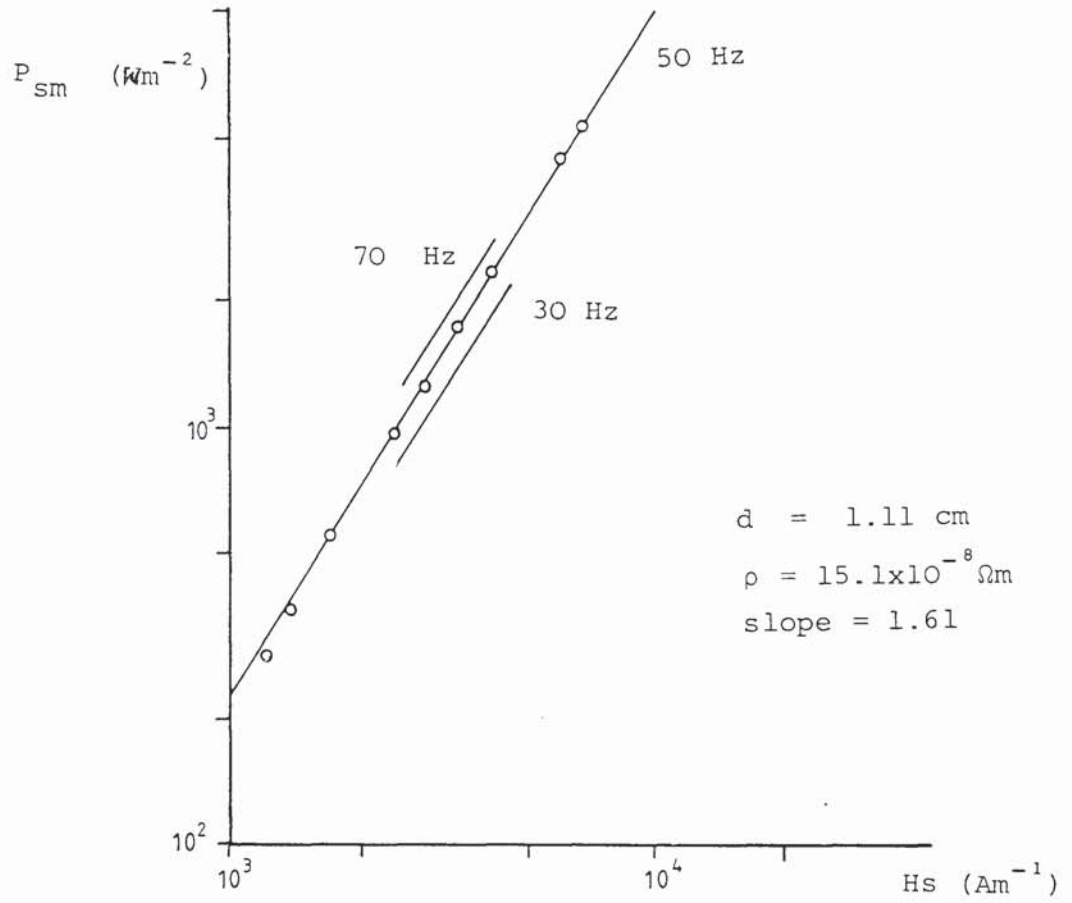

Fig. 7.13 Determination of the power index of surface magn field strength for a steel bar

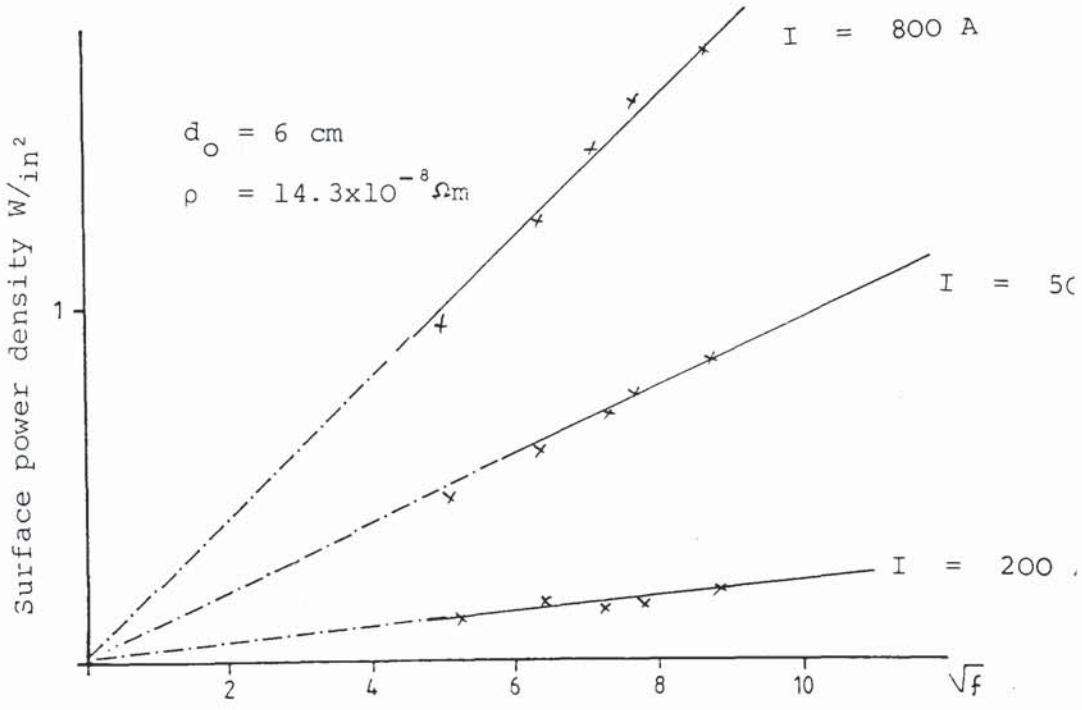

Fig. 7.14 Measured surface power density as a function of square root of frequency from results of ref.17

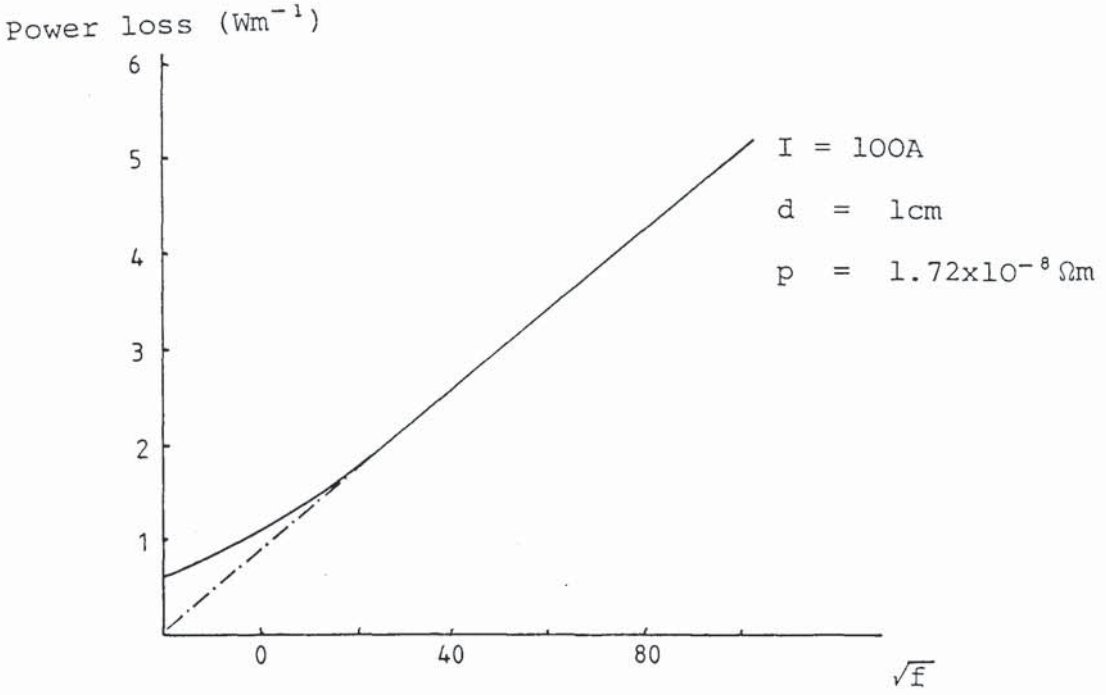

Fig. 7.15 Calculated power loss as a function of square root of frequency for a copper bar

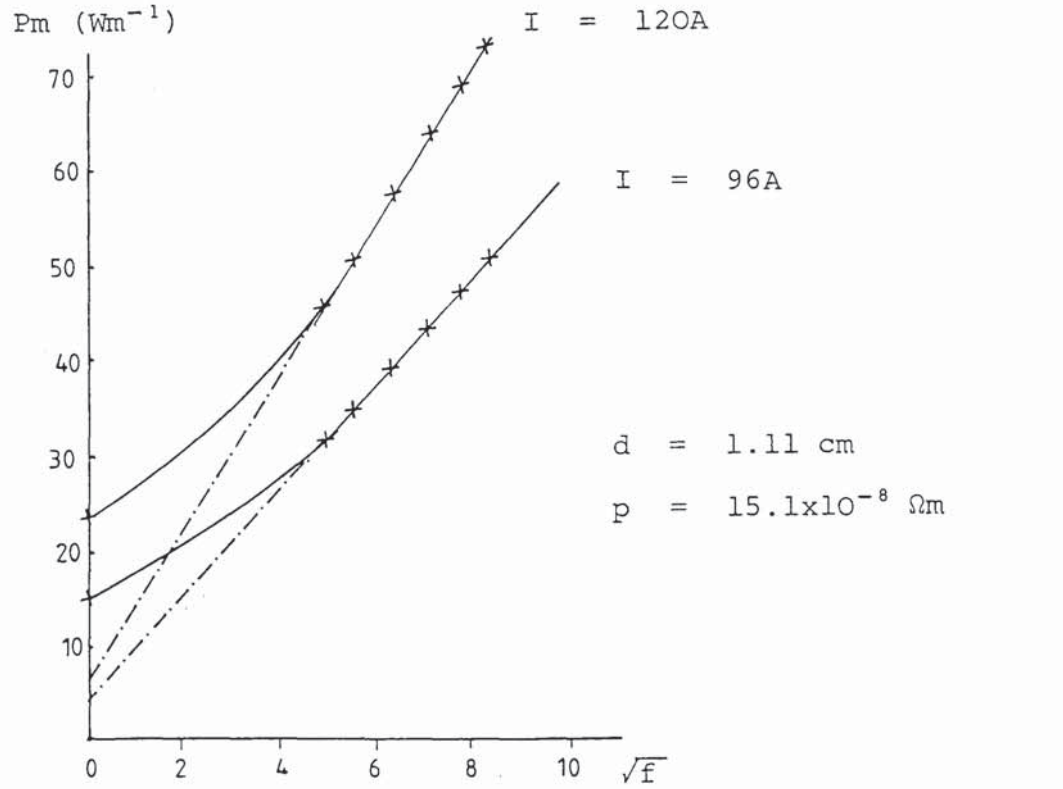

Fig. 7.16 Measured power loss as a function of $\sqrt{\text{frequency}}$ and at constant current for a steel bar

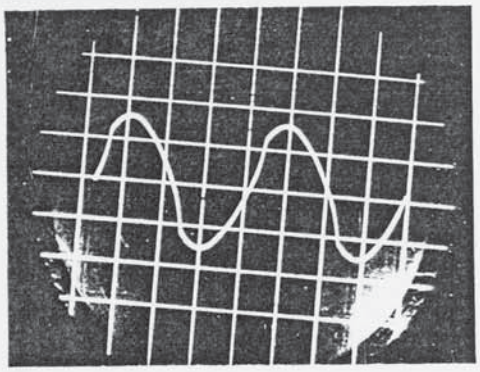

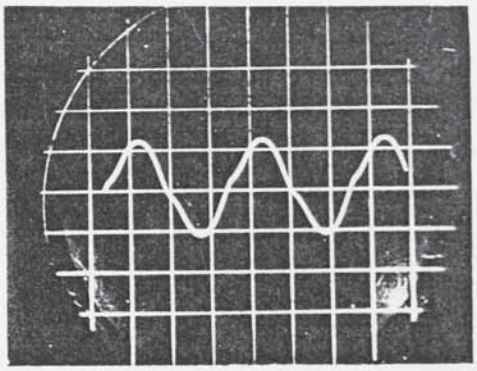

(a_1) Surface current density for I = 103 A

(b_1) I = 103 A

2 m length tube

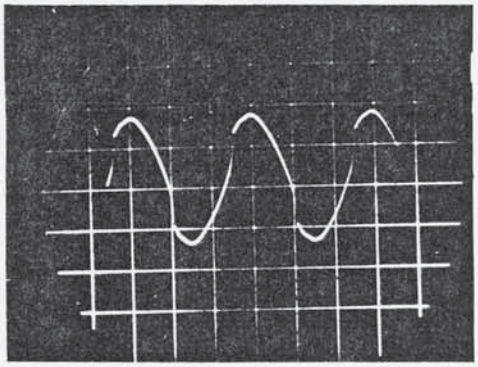

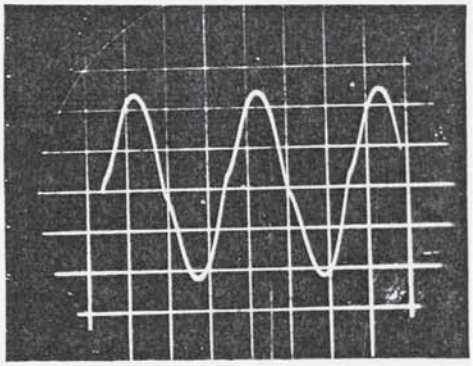

(a_2) Surface current density I = 210

(b_2) I = 210 A

2 m length tube

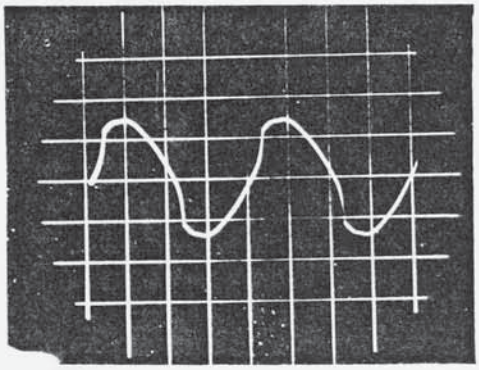

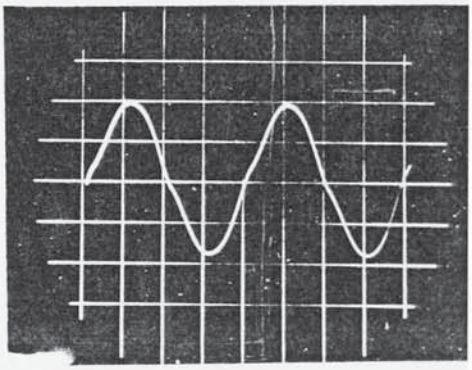

(a_3) Surface current density I = 180 A

(b_3) I = 180 A

1 m length tube

Fig. 7.17 Oscillograms of current and current density waveforms for an isolated tube

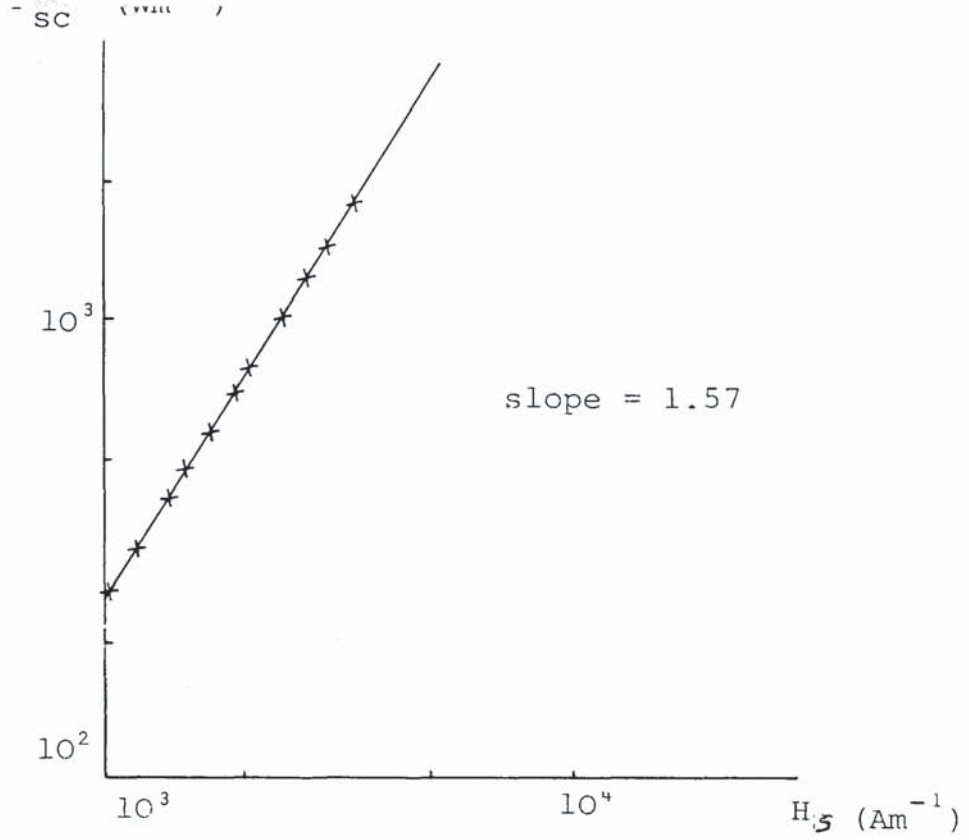

Fig. 7.18 Power index of surface field strength from results of Table 7.5

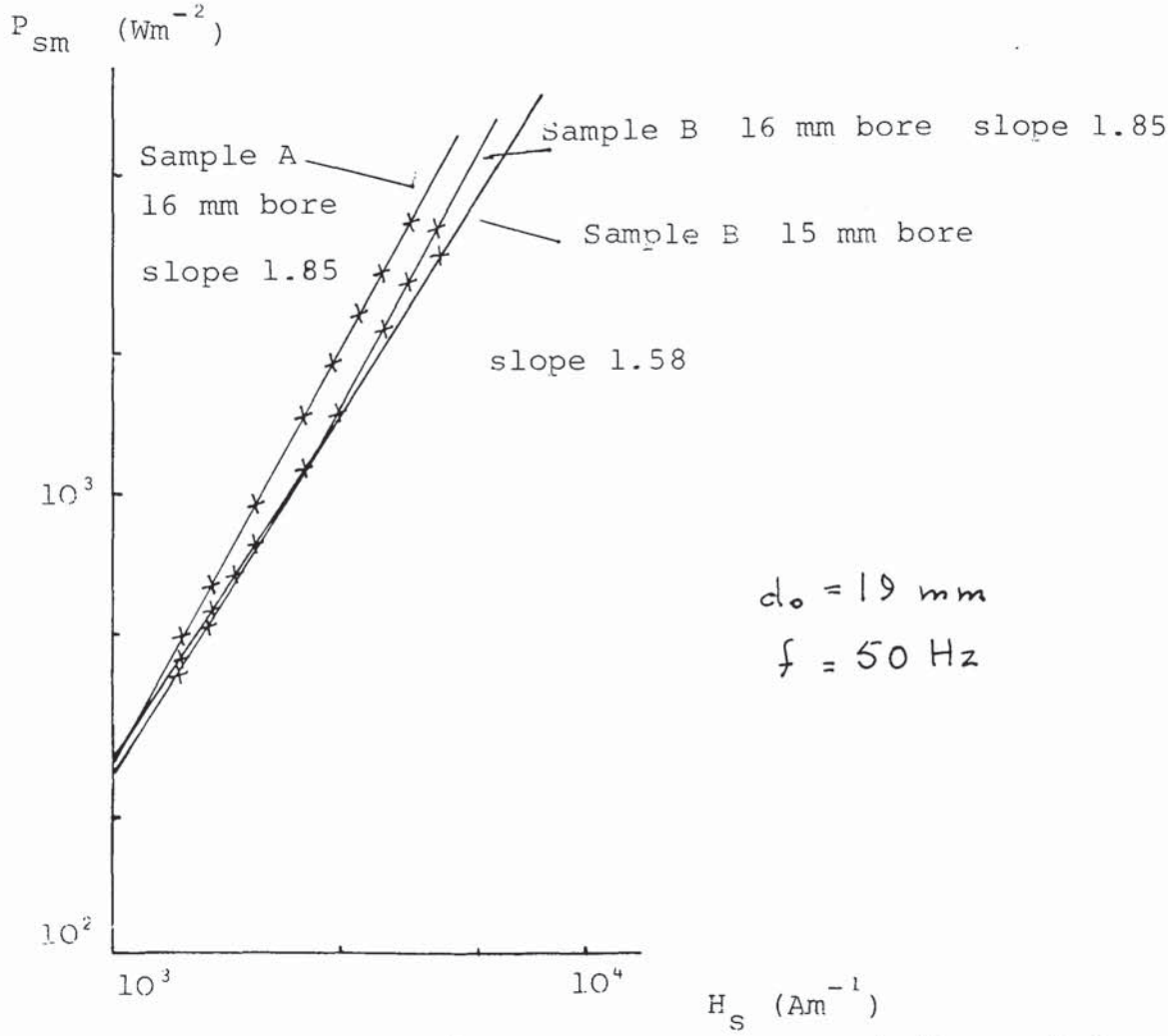

Fig. 7.19 Effect of wall thickness on power indices of H_s for samples A and B. Results from Tables 7.7 and 7

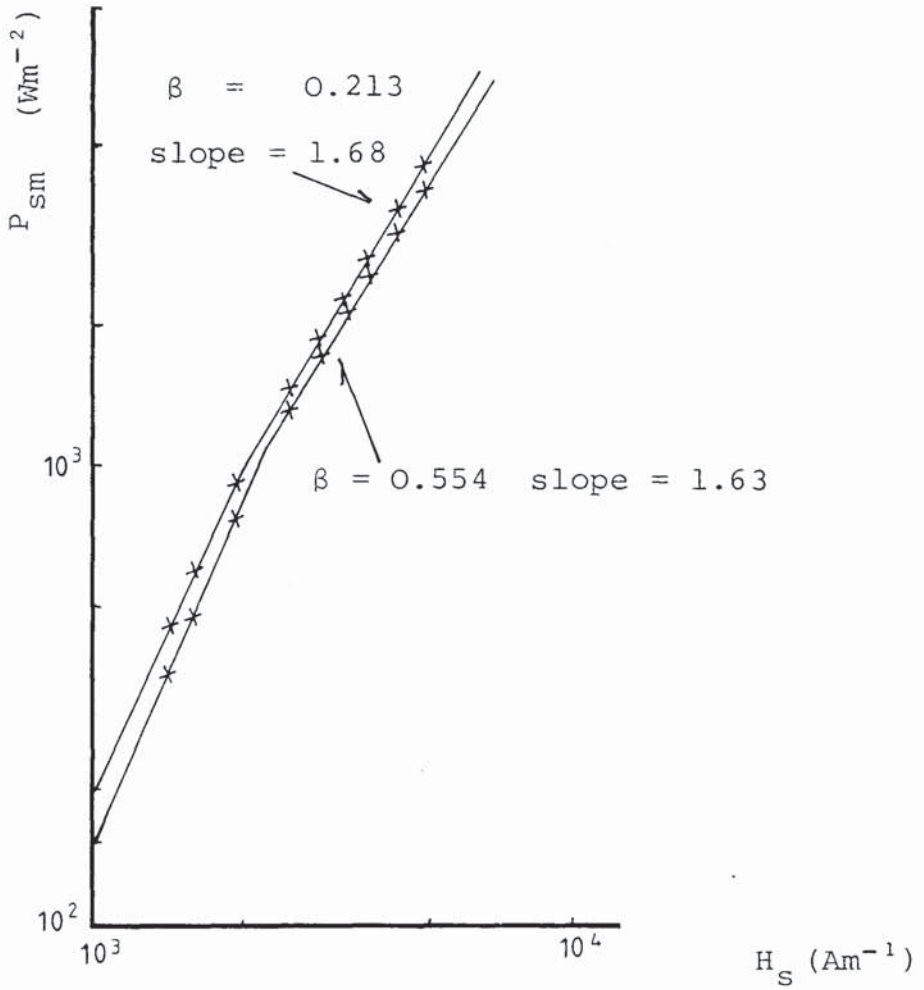

Fig. 7.20 Effect of wall thickness on power indices of H_s for sample A. Results from Tables 7.8 and 7.10

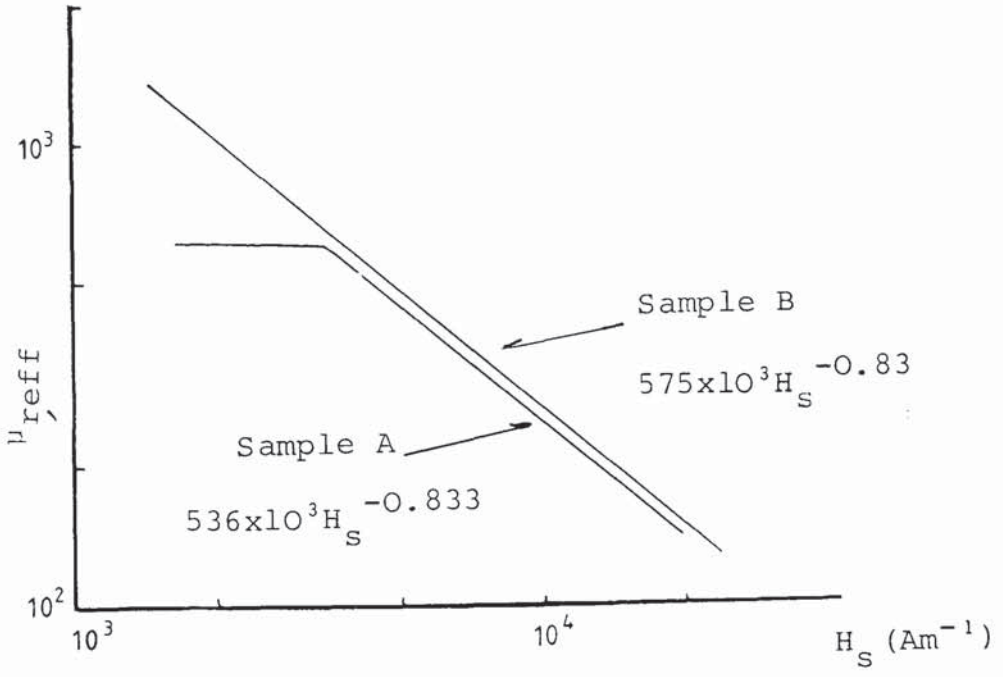

Fig. 7.21 Effective permeability function for sample A and B material

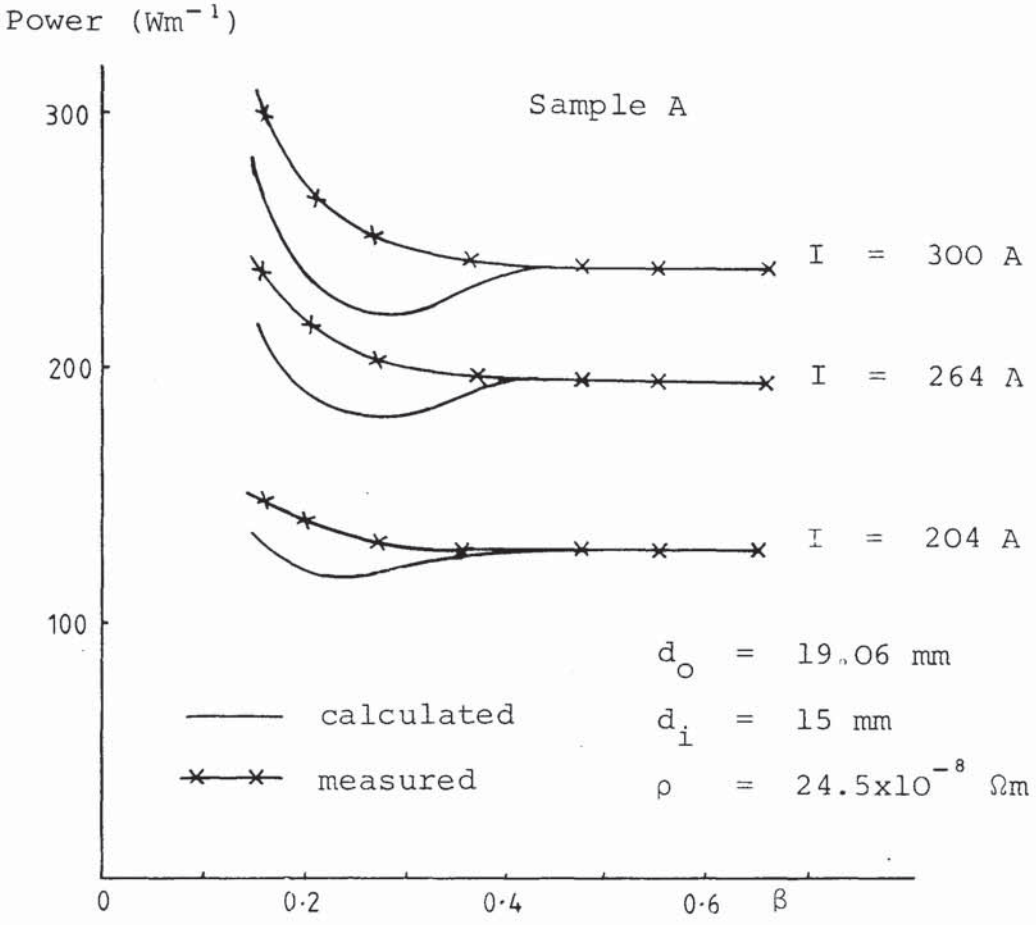

Fig. 7.22 Measured and calculated powers as a function of β and constant current

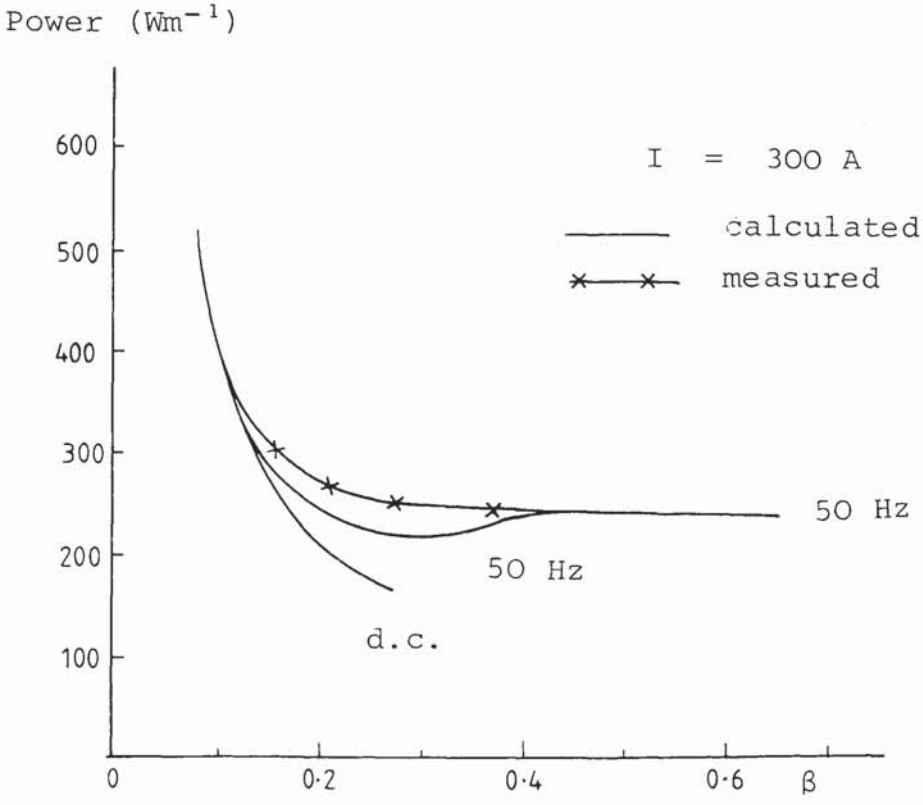

Fig. 7.23 Measured and calculated power loss at constant current of 300 A as a function of β

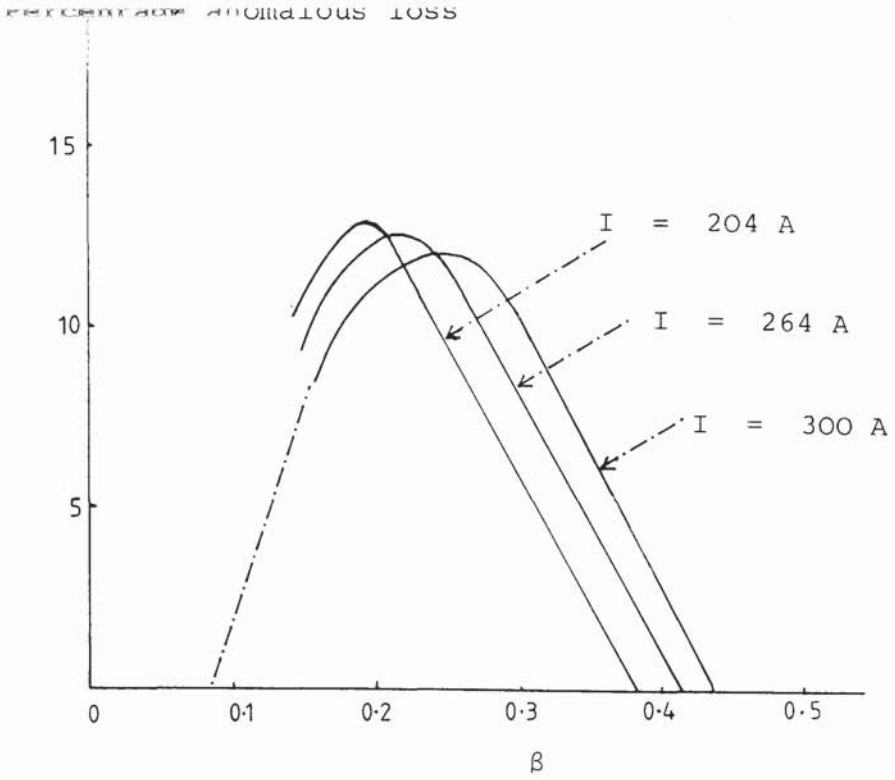

Fig. 7.24 Anomalous loss as a function of β and tube current - sample A material

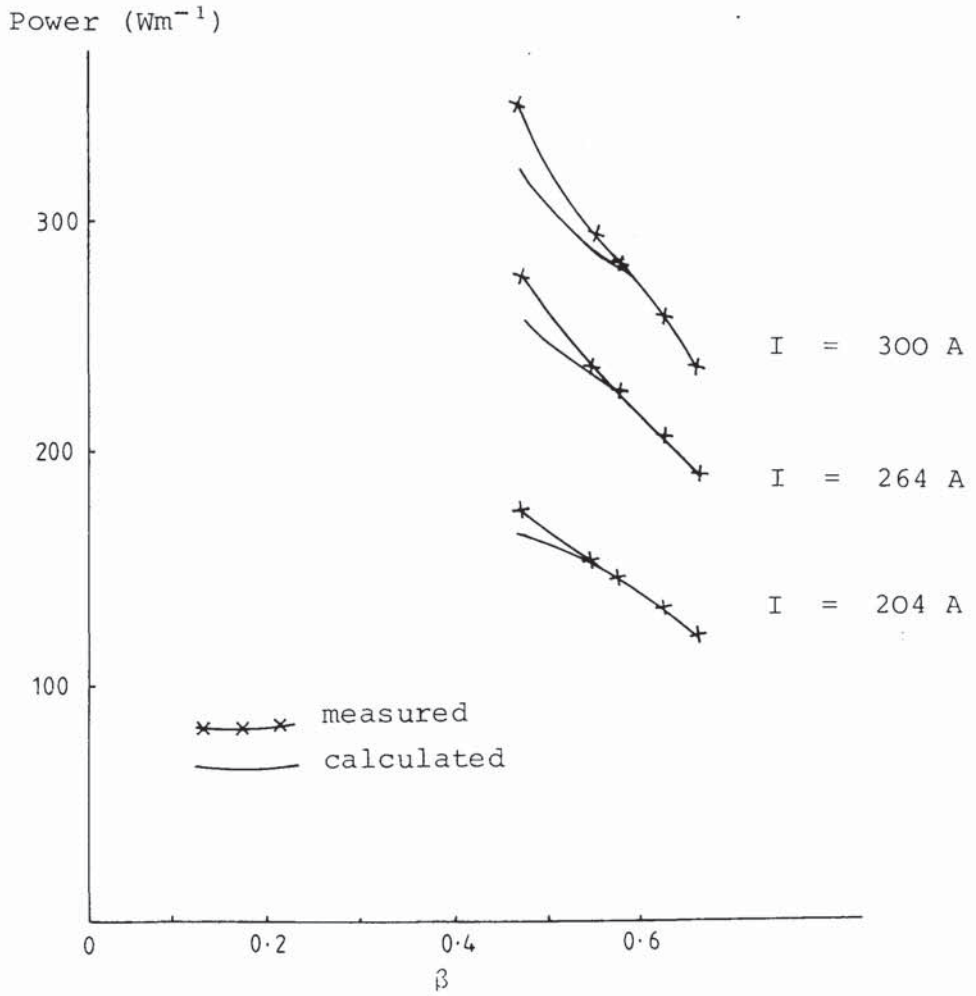

Fig. 7.25 Comparison of measured and calculated losses for sample A material and variable external diameter

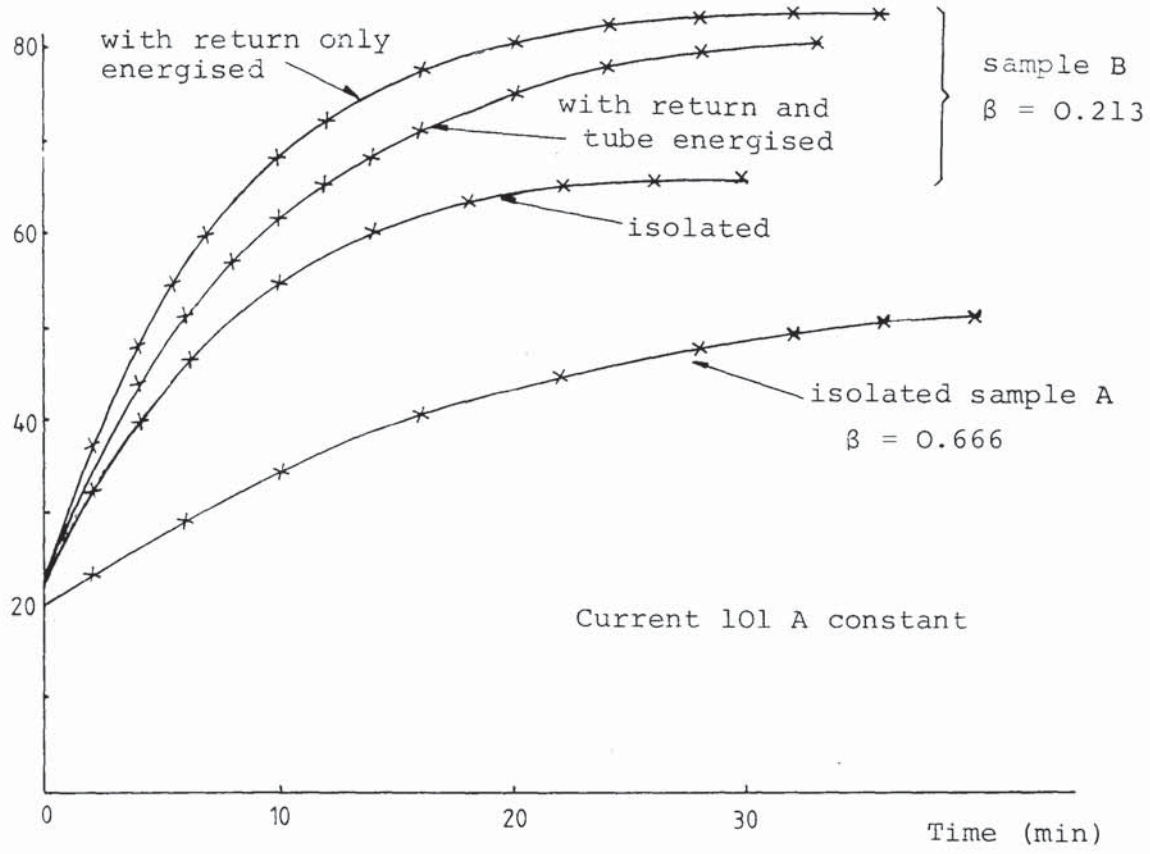

Fig. 7.26 Representative temperature rise curves of tube samples tested

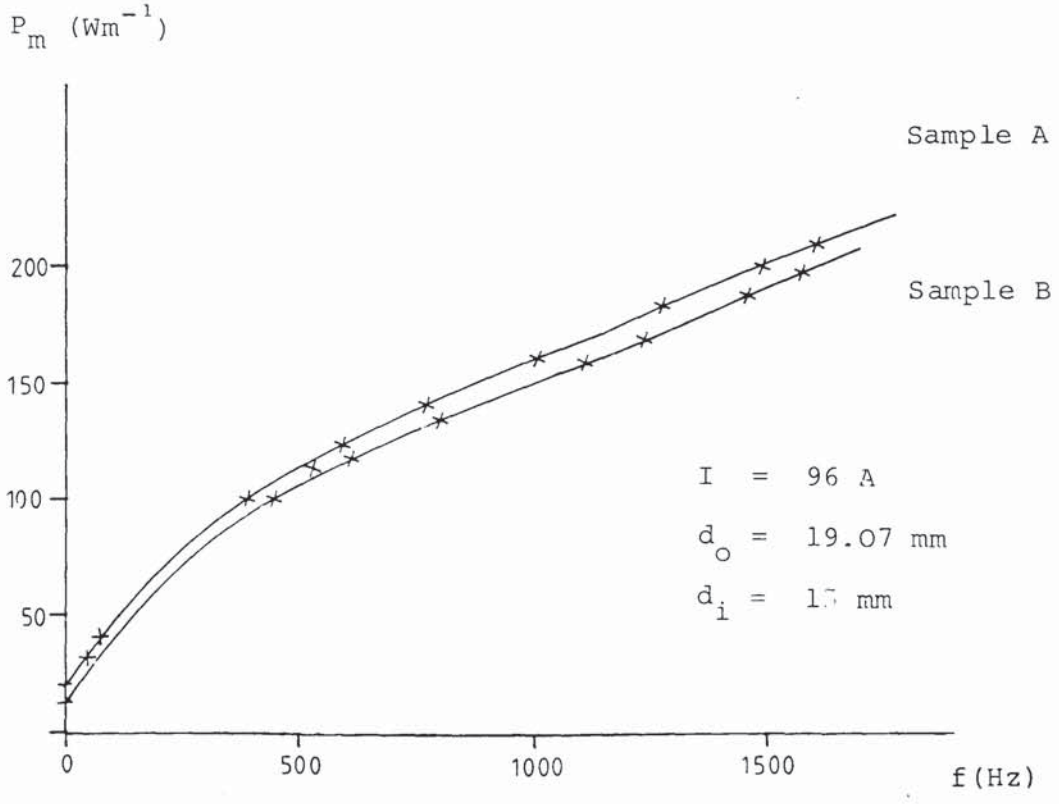

Fig. 7.27 Measured loss as a function of frequency for t current

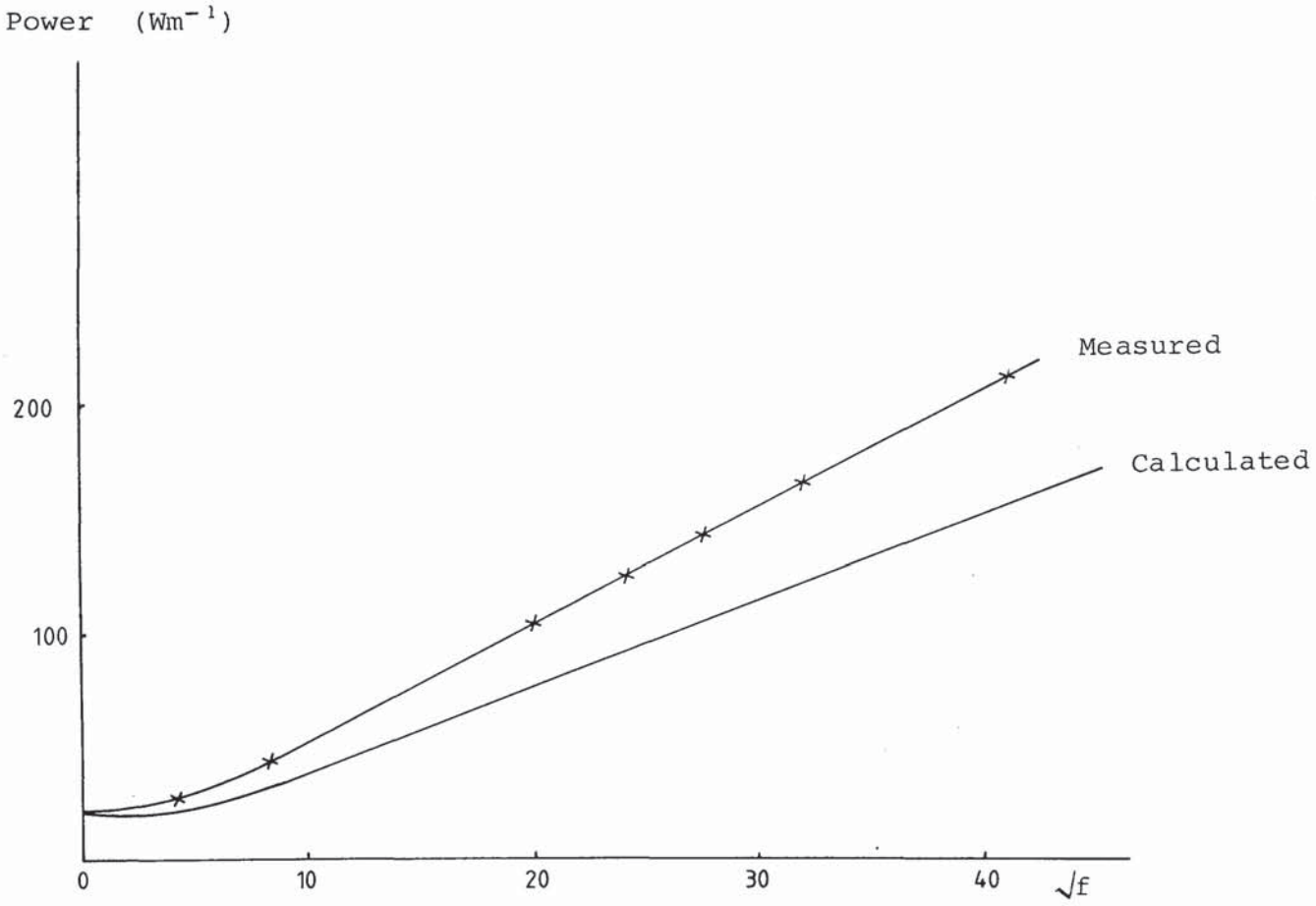

Fig. 7.28 Comparison of measured and calculated powers - sample A 96 A

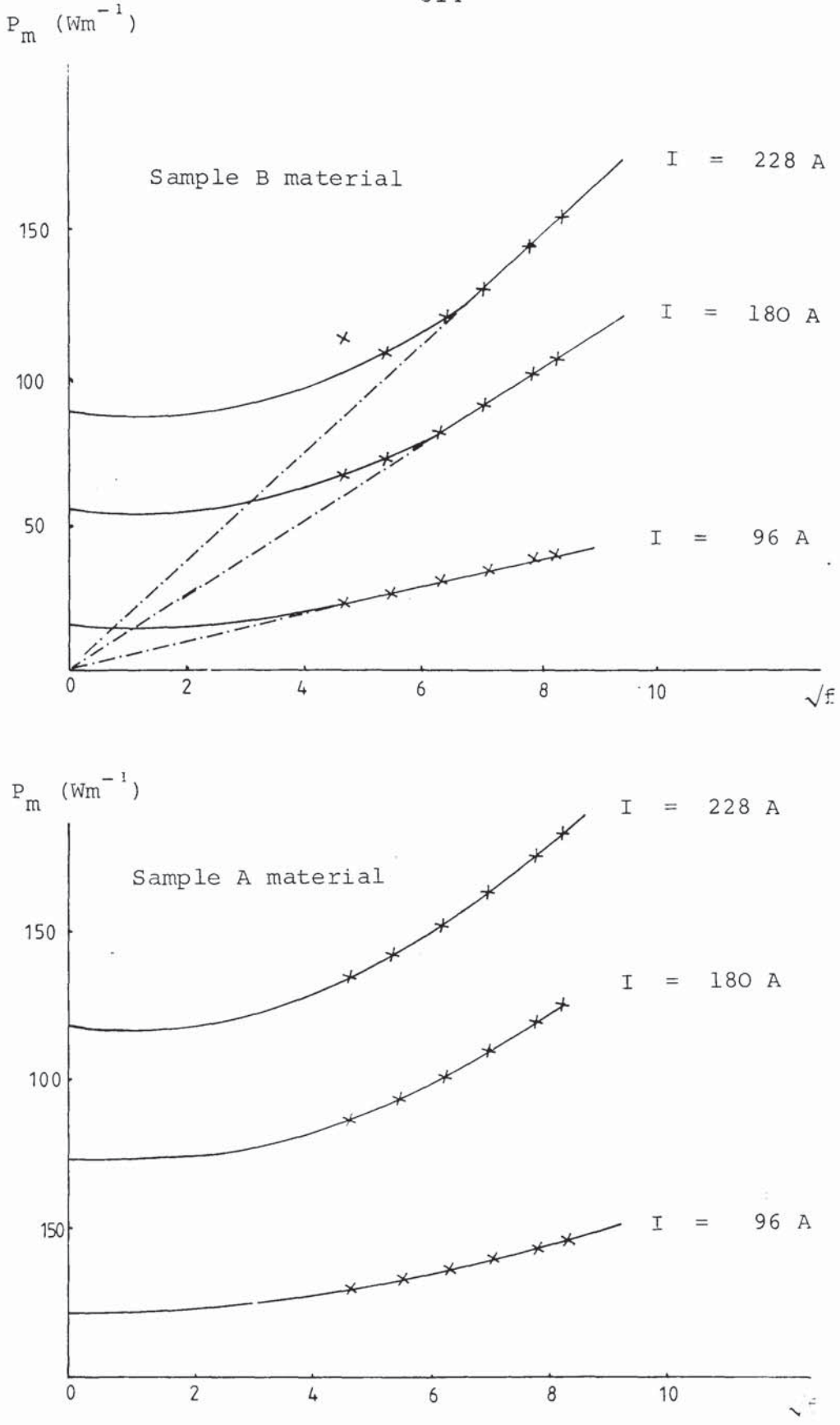

Fig. 7.29 Influence of material on conditions for a tube to be equivalent to a solid

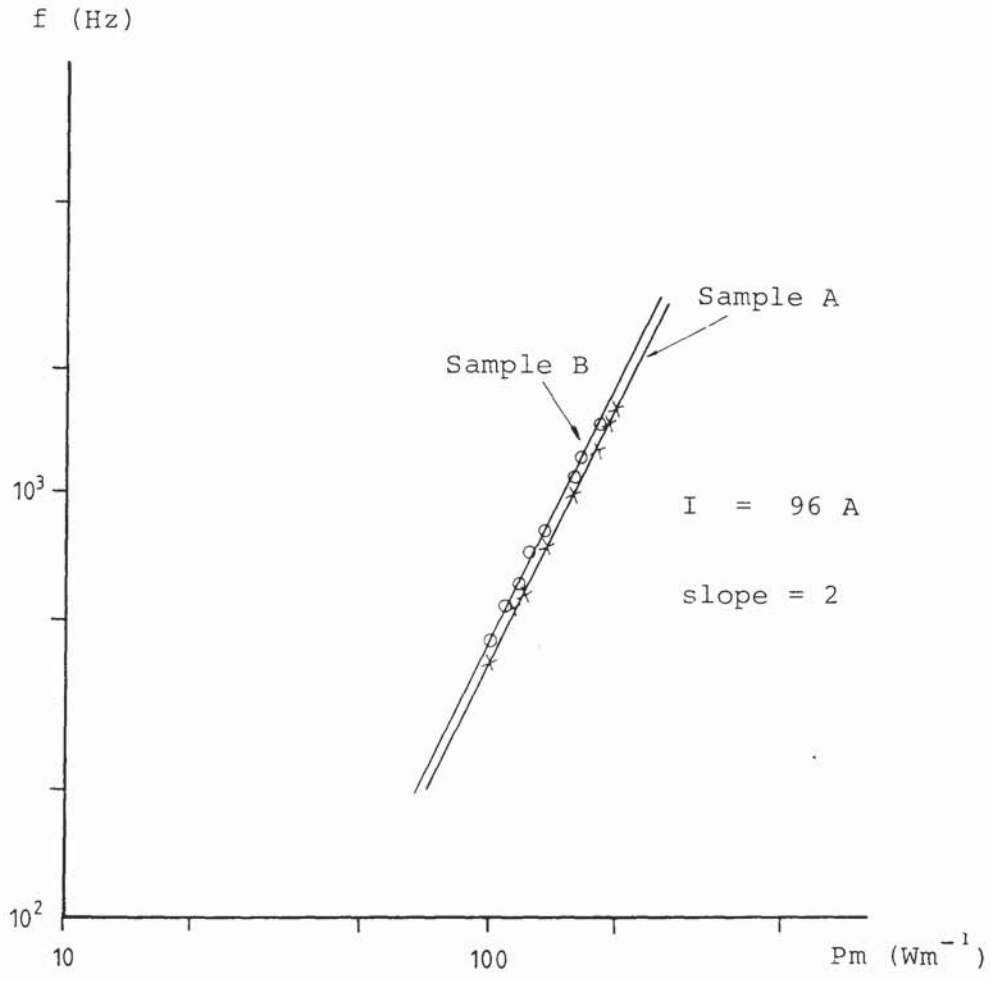

Fig. 7.30 Experimental results showing proportionality of Pm to $\sqrt{f}$ as f increases

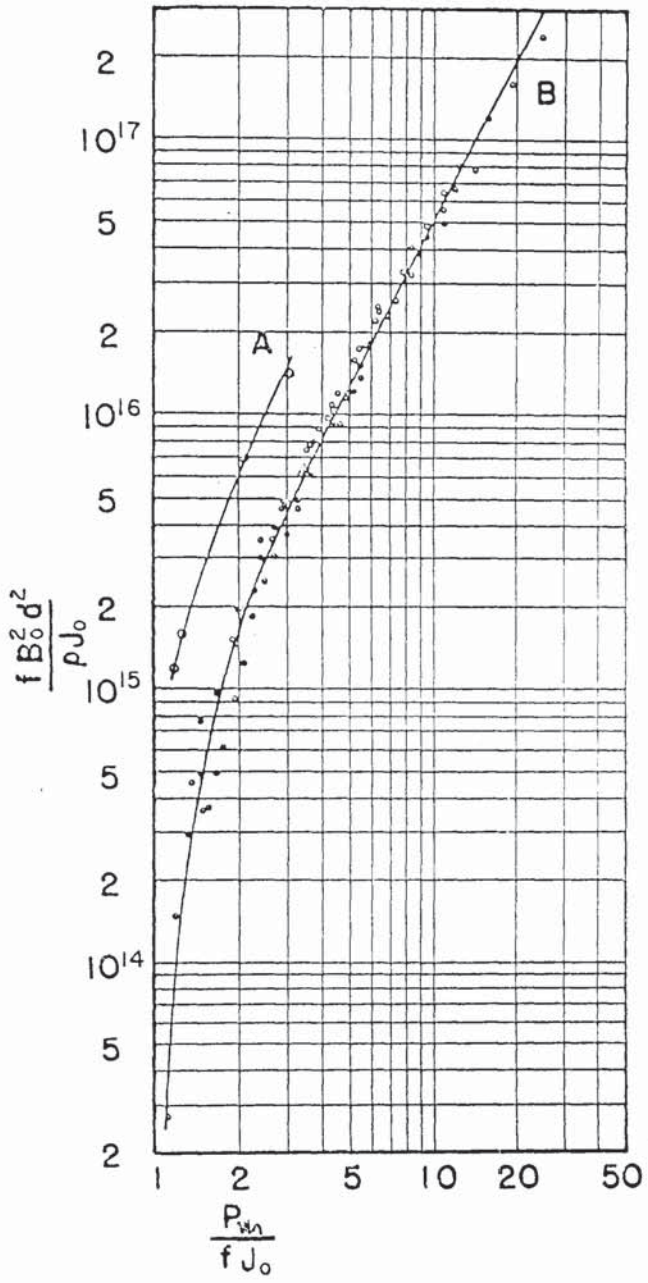

Fig.7.31 Measured values of the dimensionless parameters for ingot iron (curve A) and for various steels (curve B) (Ref.71)

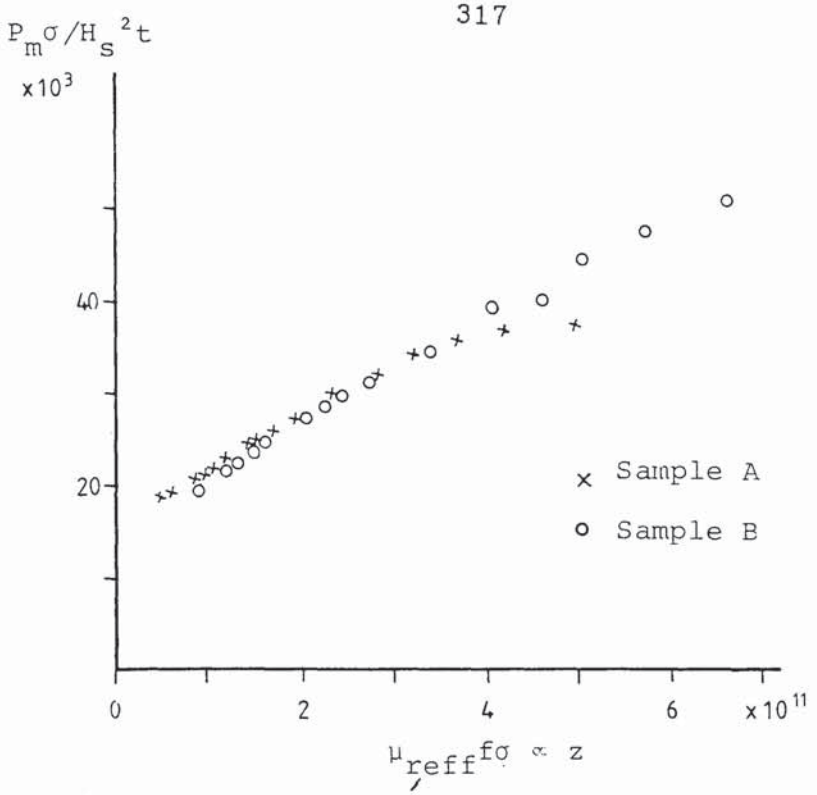

Fig. 7.32 Measured dimensionless power loss for sample A and B material. Tubes of equal radial dimensions

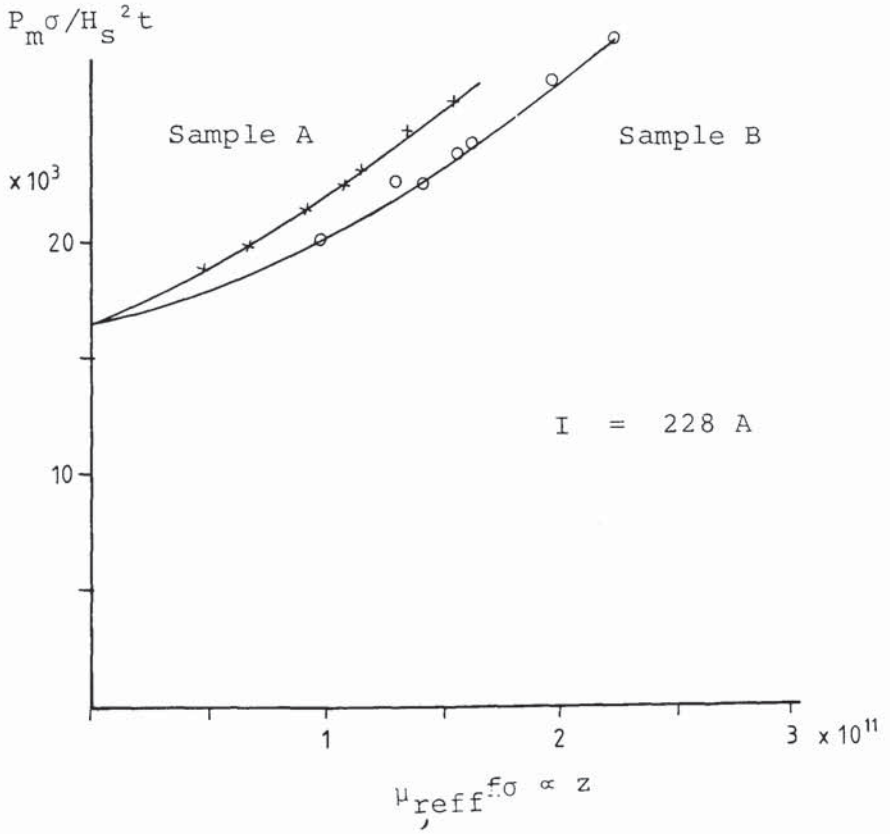

Fig. 7.33 Correlation of dimensionless parameters for samples A and B tubes at constant I and β; low frequency test results

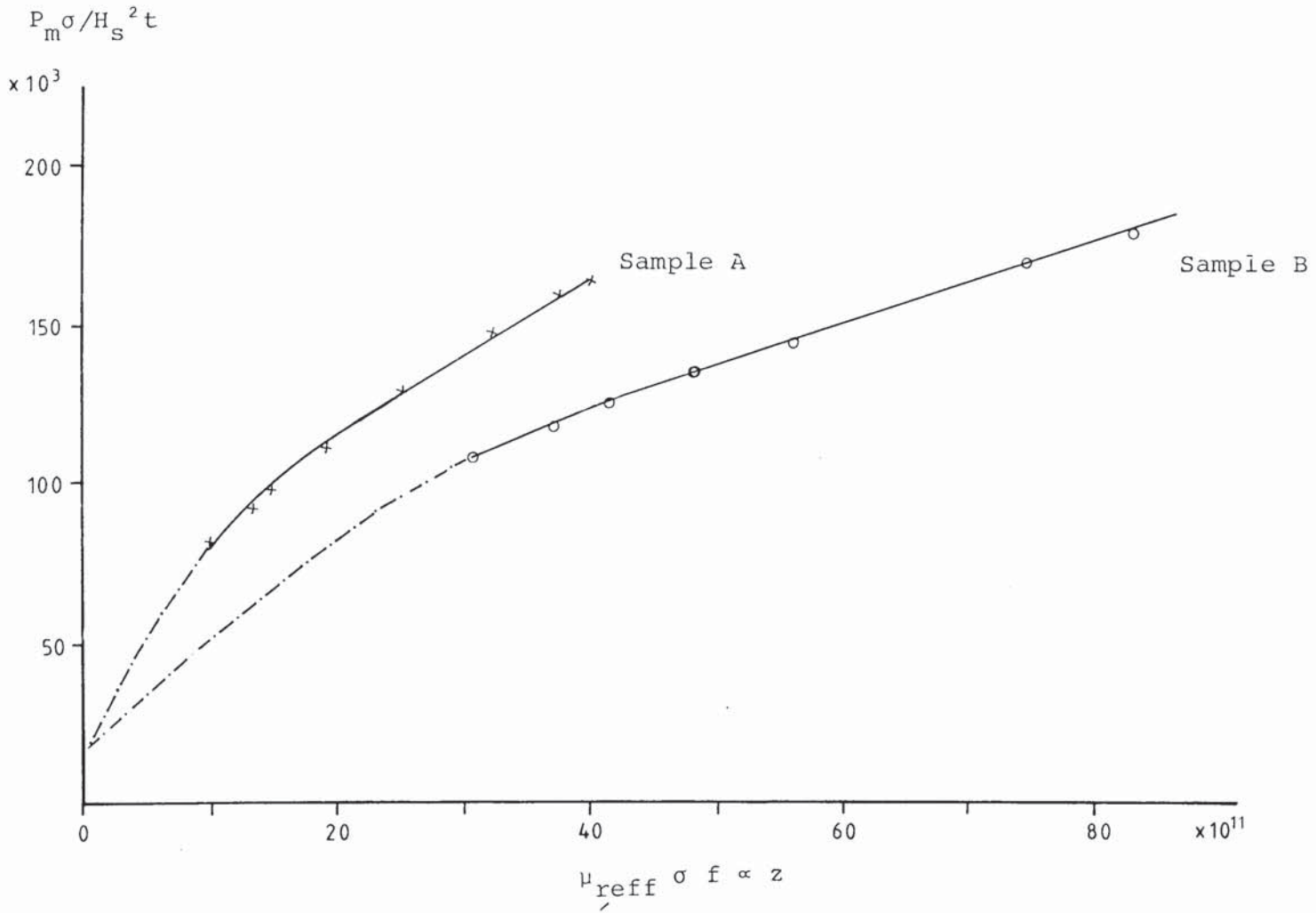

Fig. 7.34 Correlation of dimensionless parameters for sample A and B tubes at constant I and β; high frequency test results

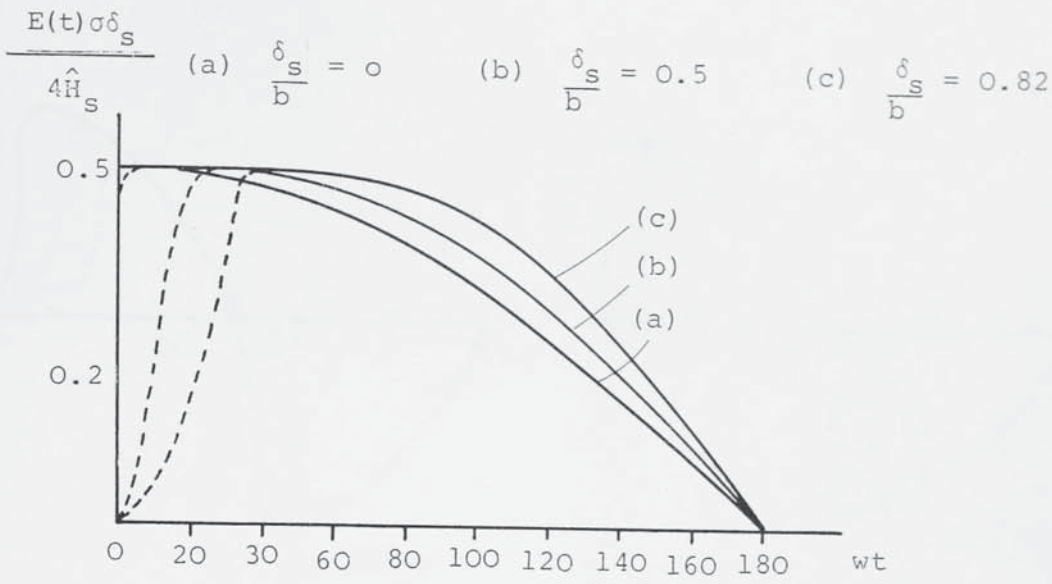

Fig. 7.35 Calculated waveforms of surface electric - field strength proportional to surface current-density

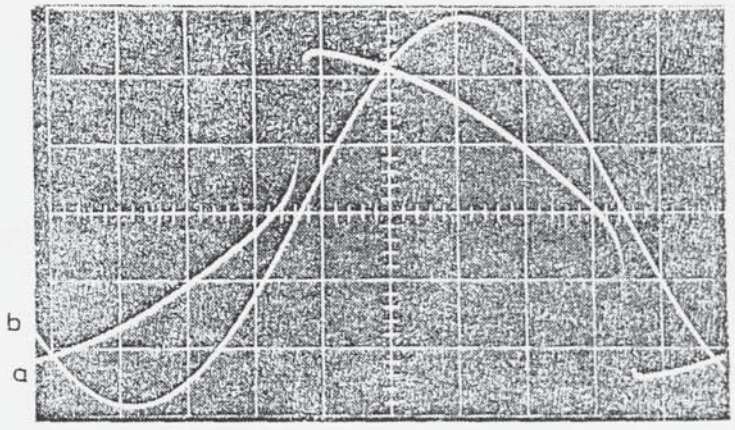

Fig. 7.36 Oscillogram of voltages proportional to the current density

Waveform(a): current density at the surface of the bar

Waveform(b): current through the bar

$\hat{H}_5$= 11800 A/m

(Ref 14)

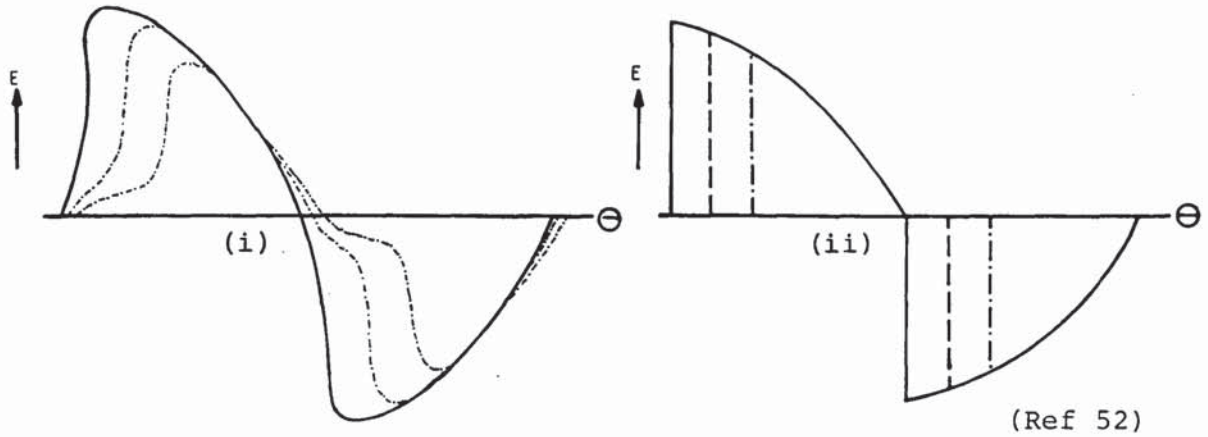

(i) Frohlich

(ii) Agarwal ——— $\tilde{x}$ = 0 ····· $\tilde{x}$ = 0.24 ------ $\tilde{x}$ = 0.48

Fig. 7.37 Waveforms of electric-field strength

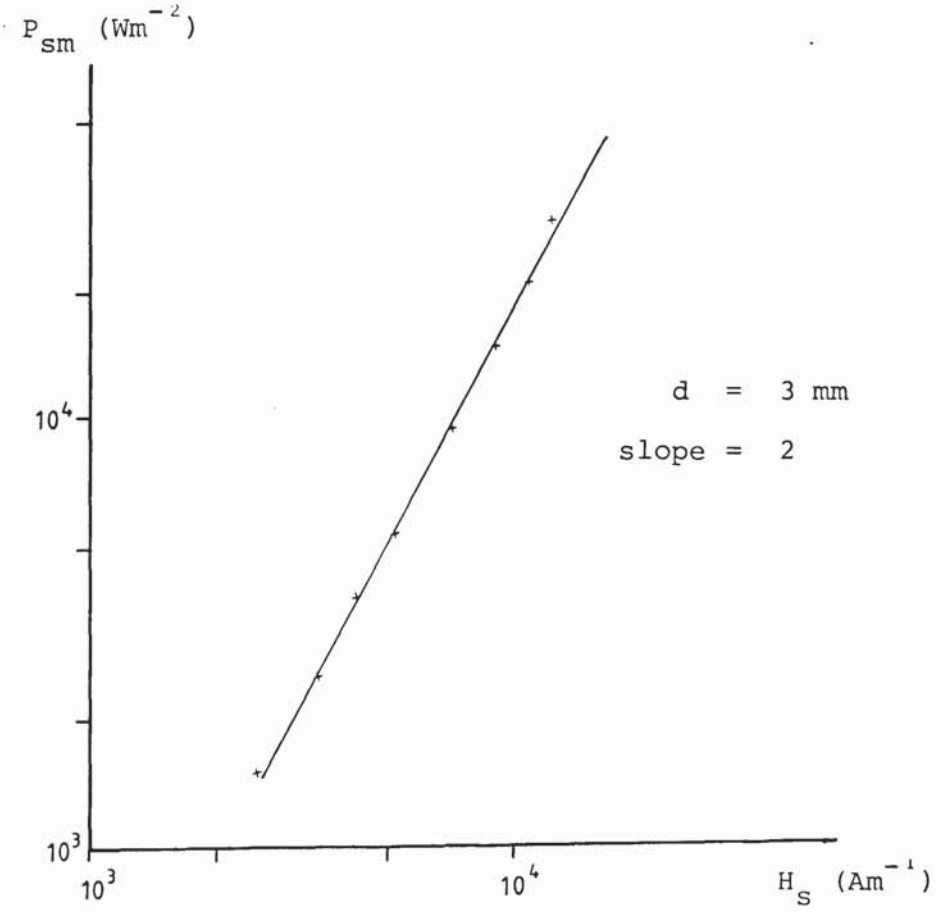

Fig. 7.38 Measured surface power density as a function of surface magnetic field strength for a solid steel wire.

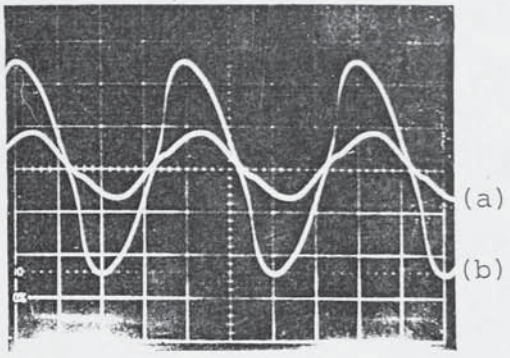

Oscillogram (A) Current 16 A

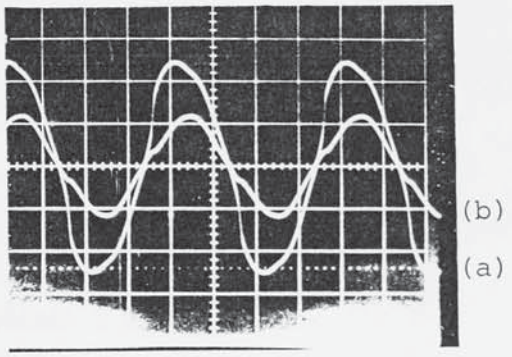

Oscillogram (B) Current 24 A

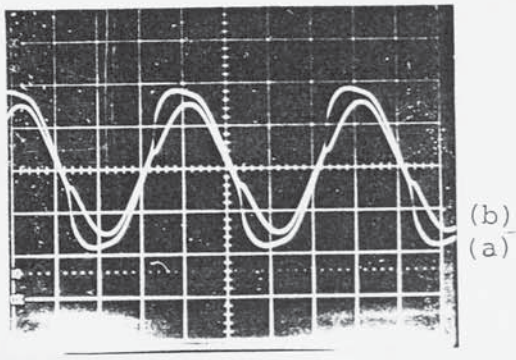

Oscillogram (C) Current 32 A

Wire diameter 3 mm

Waveforms (a) current-density

Waveforms (b) current.

Fig. 7.39 Oscillograms of voltages proportional to surface current-density and current.

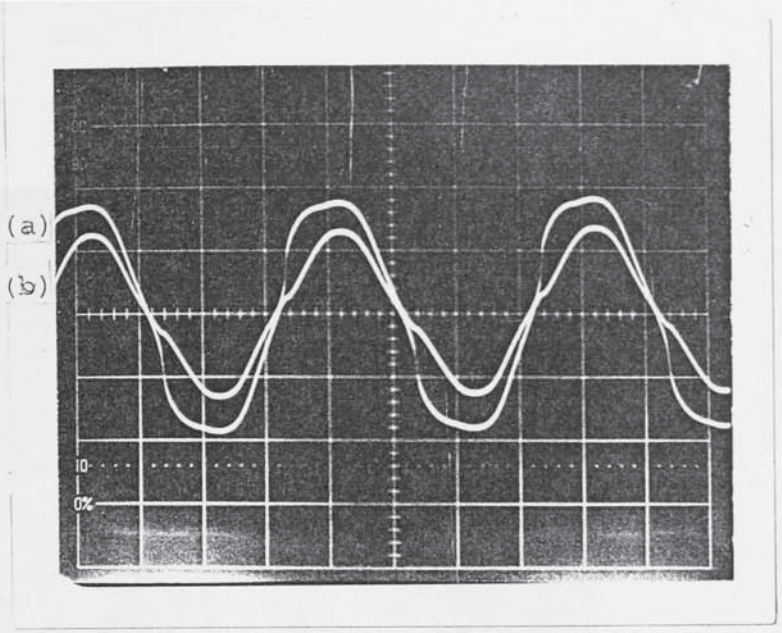

Fig. 7.40 Oscillograms of voltages proportional to surface current-density and current

Waveform (a) current-density Amplifier gain 5 . 2V/cm

Waveform (b) current

Wire diameter 3 mm

Current 48 A

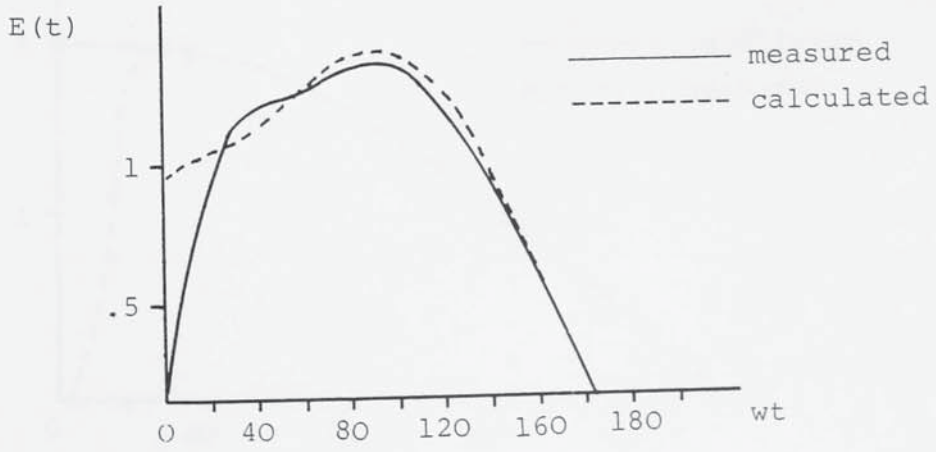

Fig. 7.41 Comparison of measured and calculated surface current-density waveforms

Wire diameter 3 mm

Current 48 A

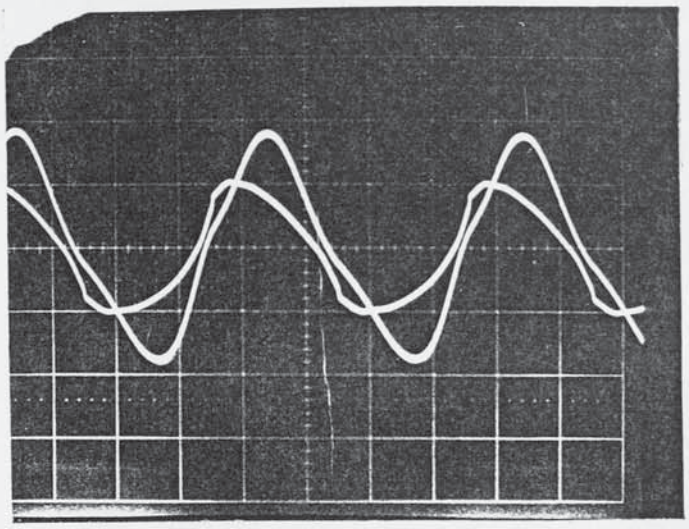

Bar diameter 20 mm

$\hat{H}_s$ = 20,254 Am^{-1}

Fig. 7.42 Oscillograms of surface electric field strength and bar current
Waveform (a) electric field 2V/cm amplifier gain 2
Waveform (b) current

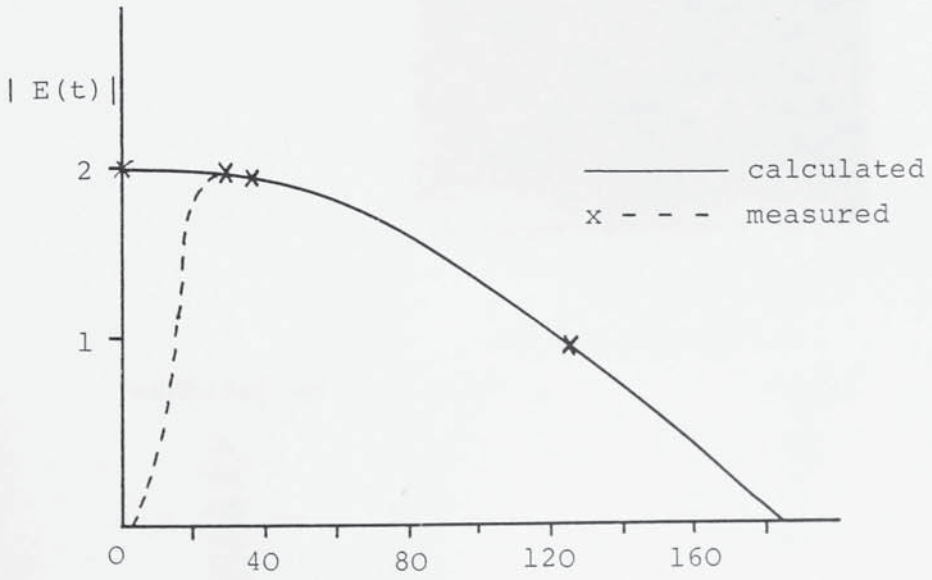

Fig. 7.43 Waveforms of surface electric - field strength
Bar diameter 20 mm $\hat{H}_s$ = 20,254 Am^{-1}

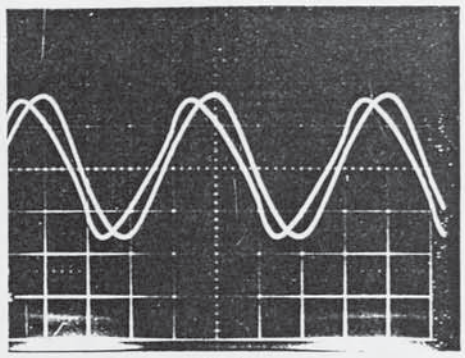

(A)

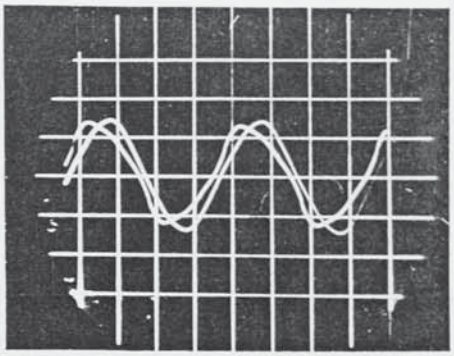

(B)

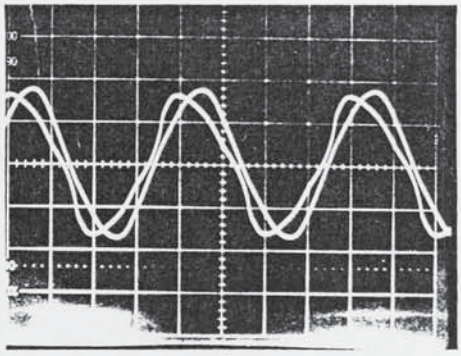

(C)

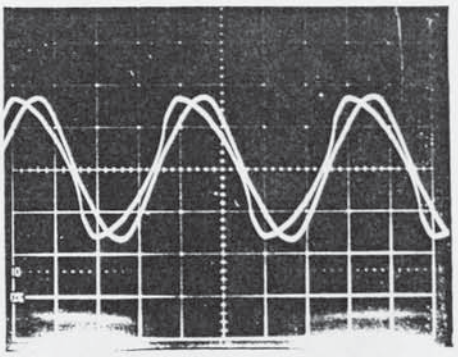

(D)

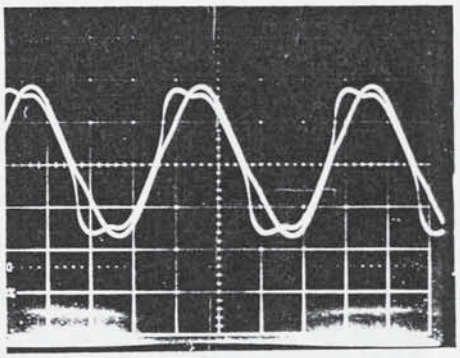

(E)

Tube dimensions

Oscillogram	d_i (mm)	d_o (mm)
(A)	6.35	19
(B)	10	|
(C)	13.9	|
(D)	15	|
(E)	16	

Oscillograms (A) to (E) current 288 A

for (E) gain 10, 2v/cm

Fig. 7.44 Oscillograms of surface current density and current of isolated tubes sample A

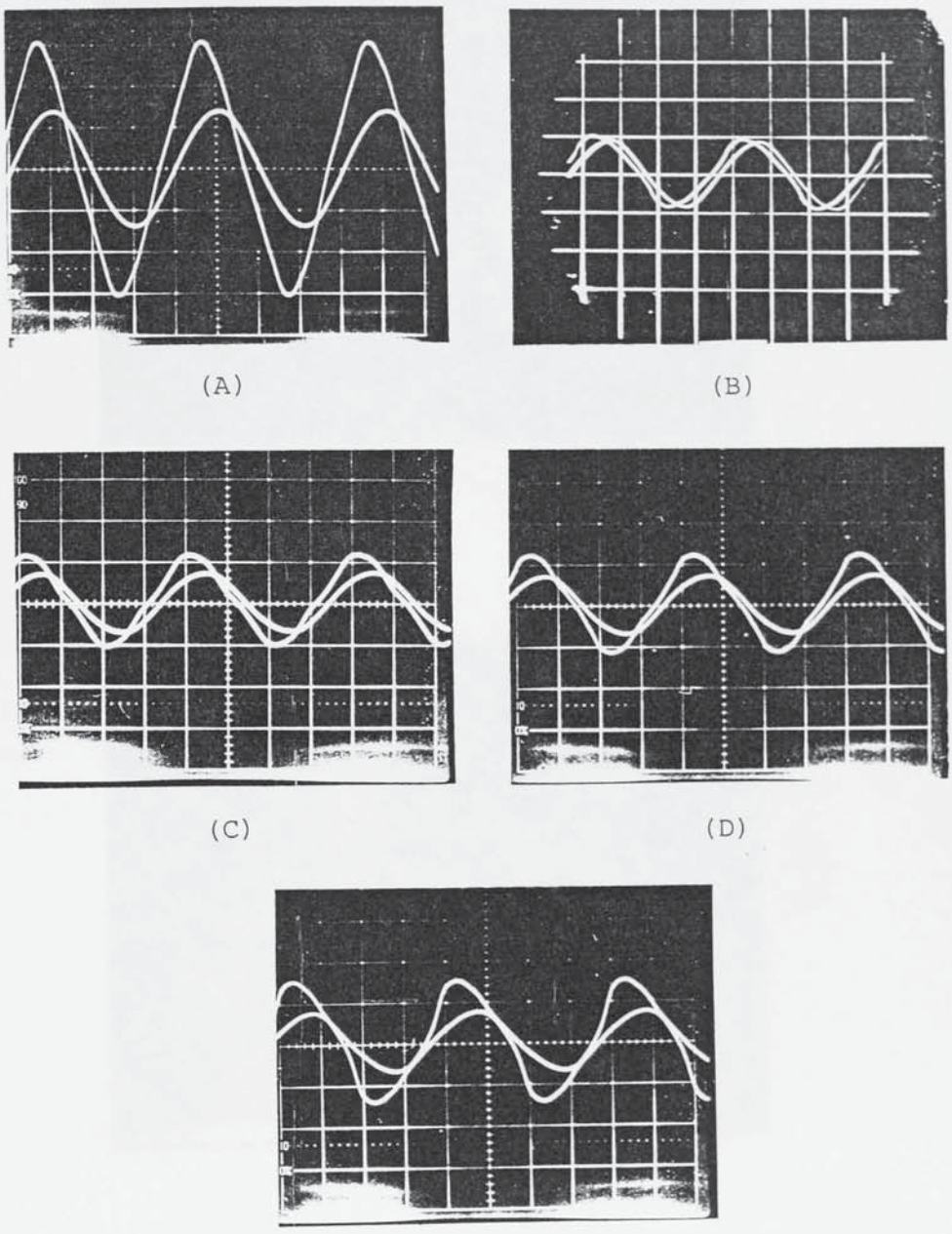

(A) (B)

(C) (D)

(E)

Oscillogram	Tube dimensions d_i (mm)	d_o (mm)
(A)	6.35	19
(B)	10	|
(C)	13.9	|
(D)	15	|
(E)	16	|

Oscillograms (A) to (E) current 60 A

Fig. 7.45 Oscillograms of surface current density and current of isolated tubes sample A

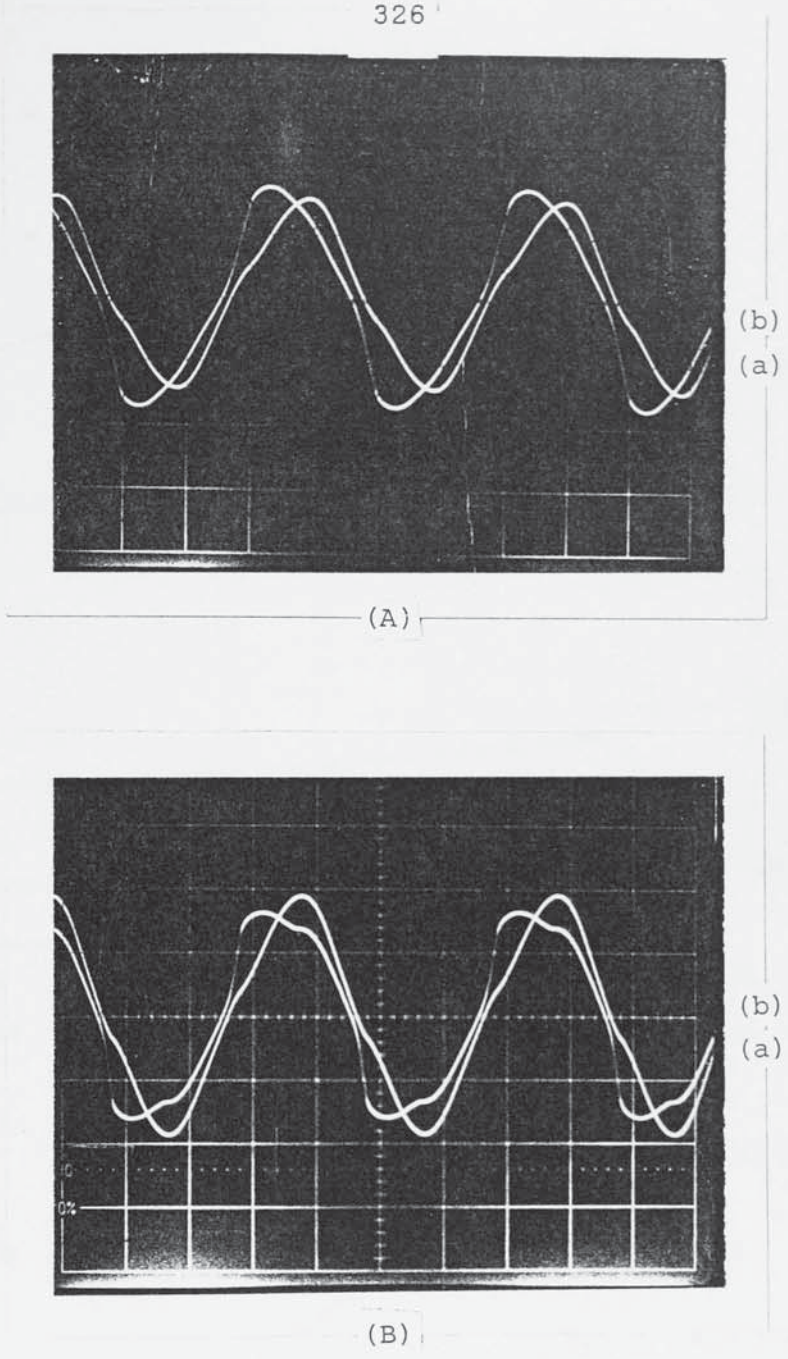

Fig. 7.46 Oscillograms of voltage and current waveforms.
Sample B tube 19 mm external diameter 16 mm bore

Waveform (a) Current
Waveform (b) Surface current - density 2V/cm

Oscillogram (A) bar current 120 A, amplifier gain 22

Oscillogram (B) bar current 300 A, amplifier gain 12

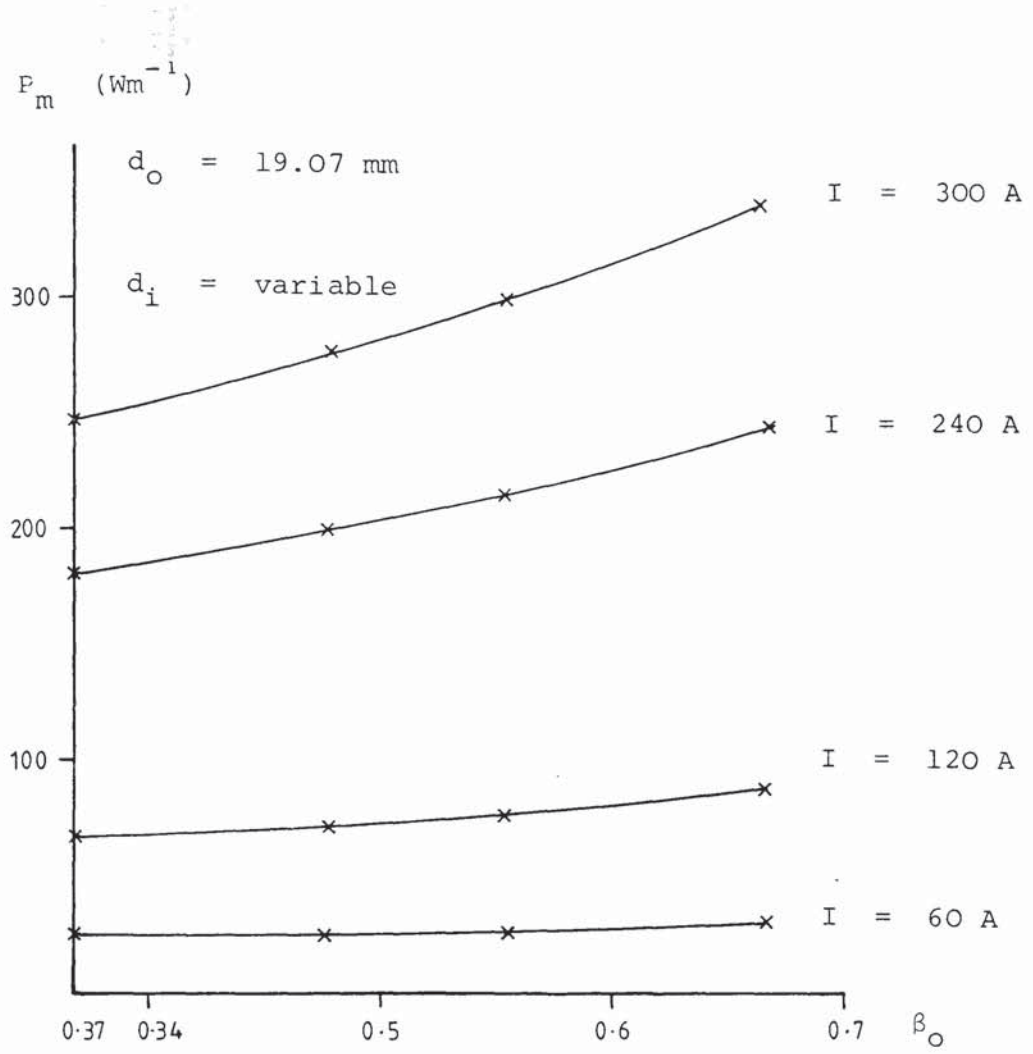

Fig. 7.47 Power developed for constant current as a function of β_o; concentric arrangement

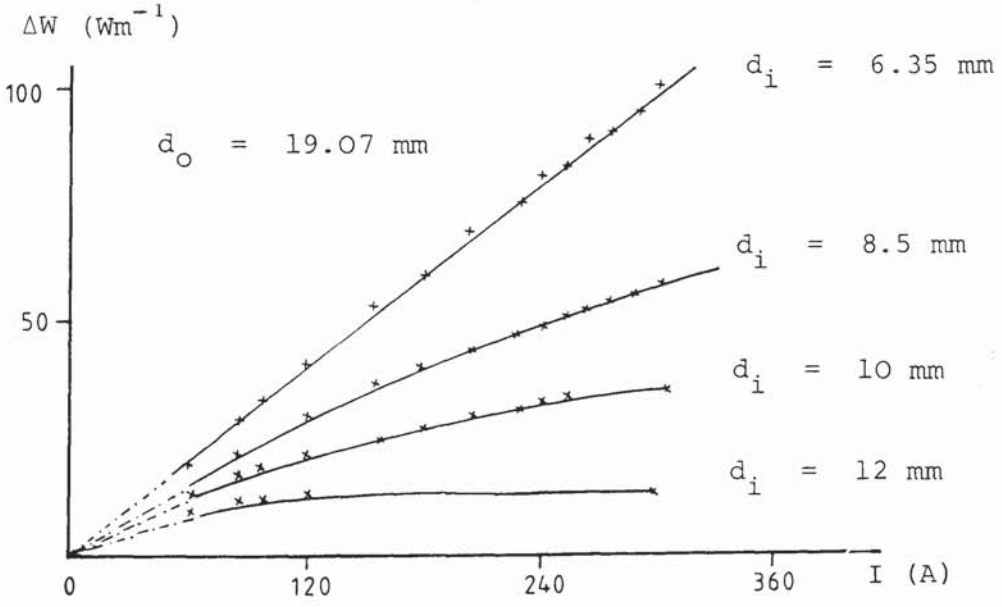

Fig. 7.48 Increase in power loss as a function of current for different internal diameters; concentric arrangement

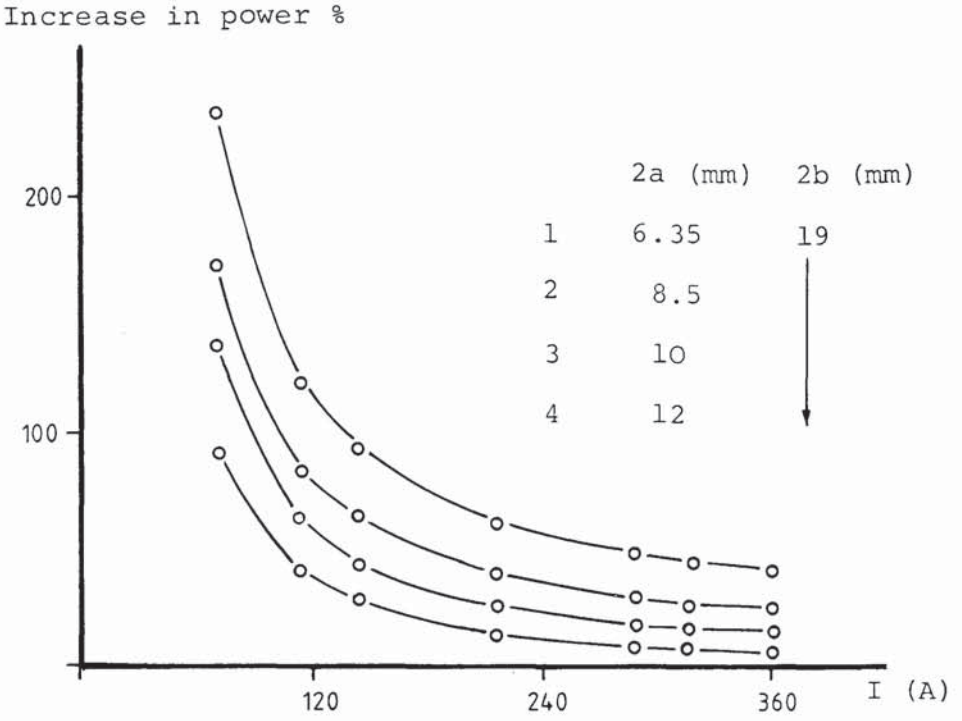

Fig. 7.49 Measured percentage increase in power as a function of current; concentric arrangement

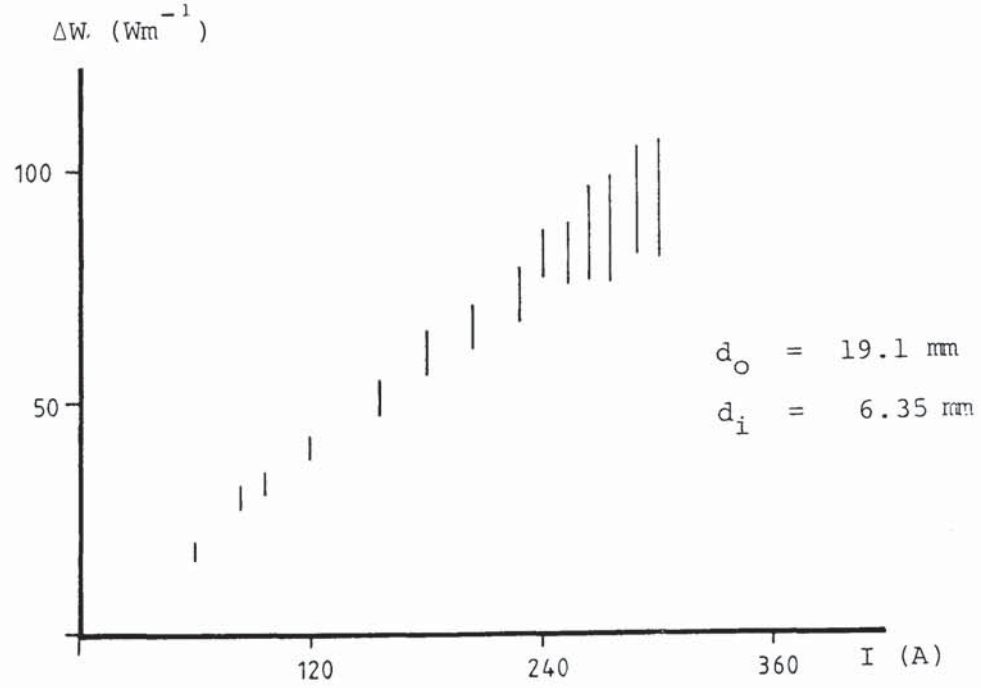

Fig. 7.50 Spread of experimental results in the measurement of increase in loss ΔW

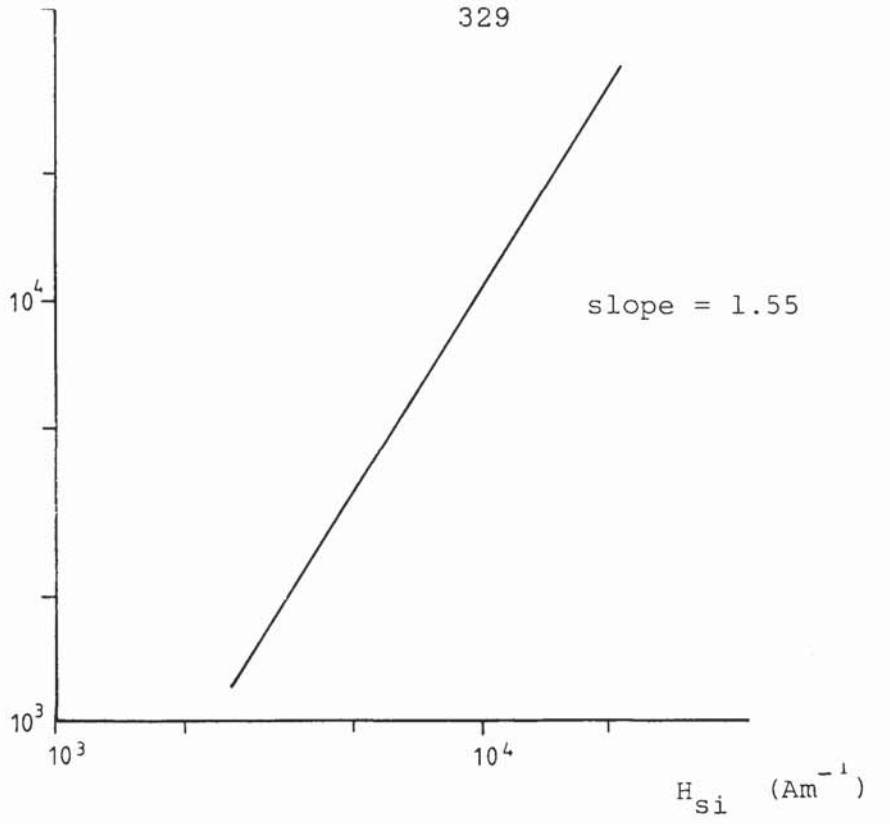

Fig. 7.51 Internal surface power density for different values of β, as a function of internal surface magnetic field ; concentric arrangement

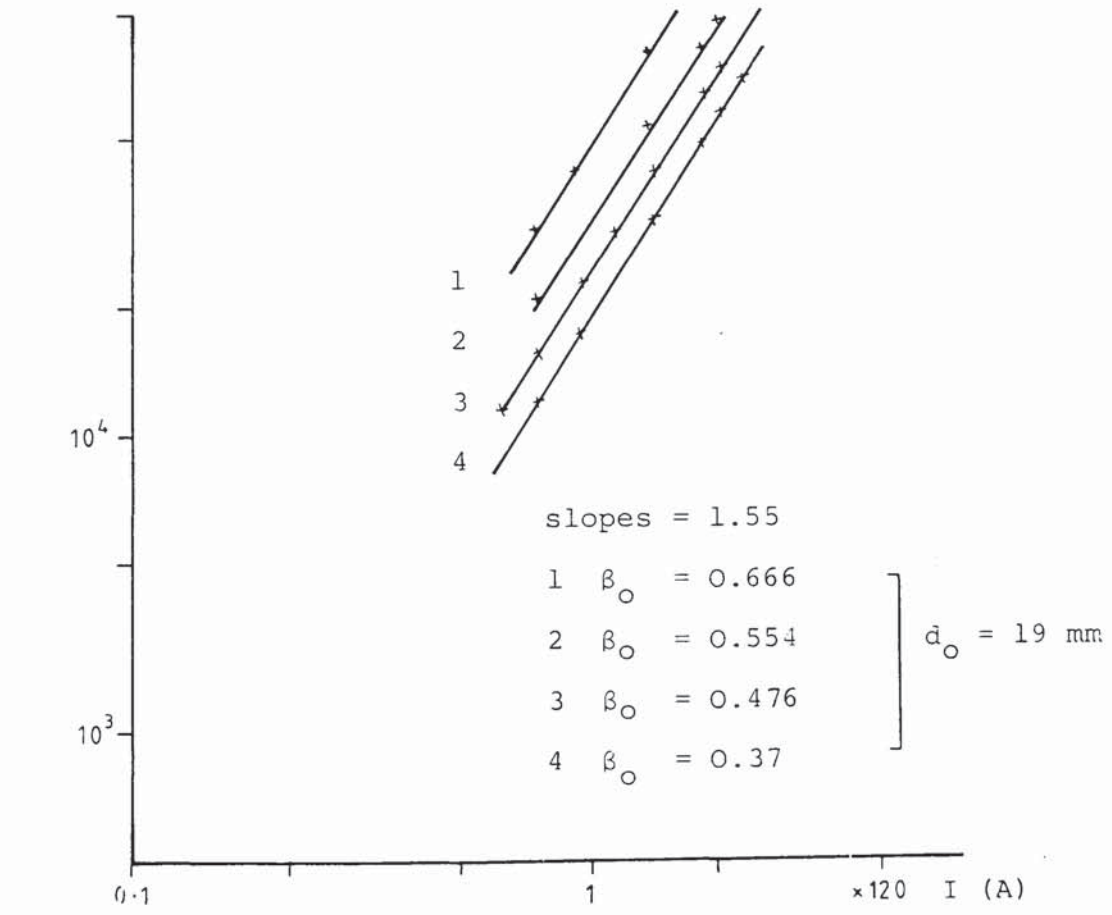

nal surface power density as a function
rrent for constant values of β_o

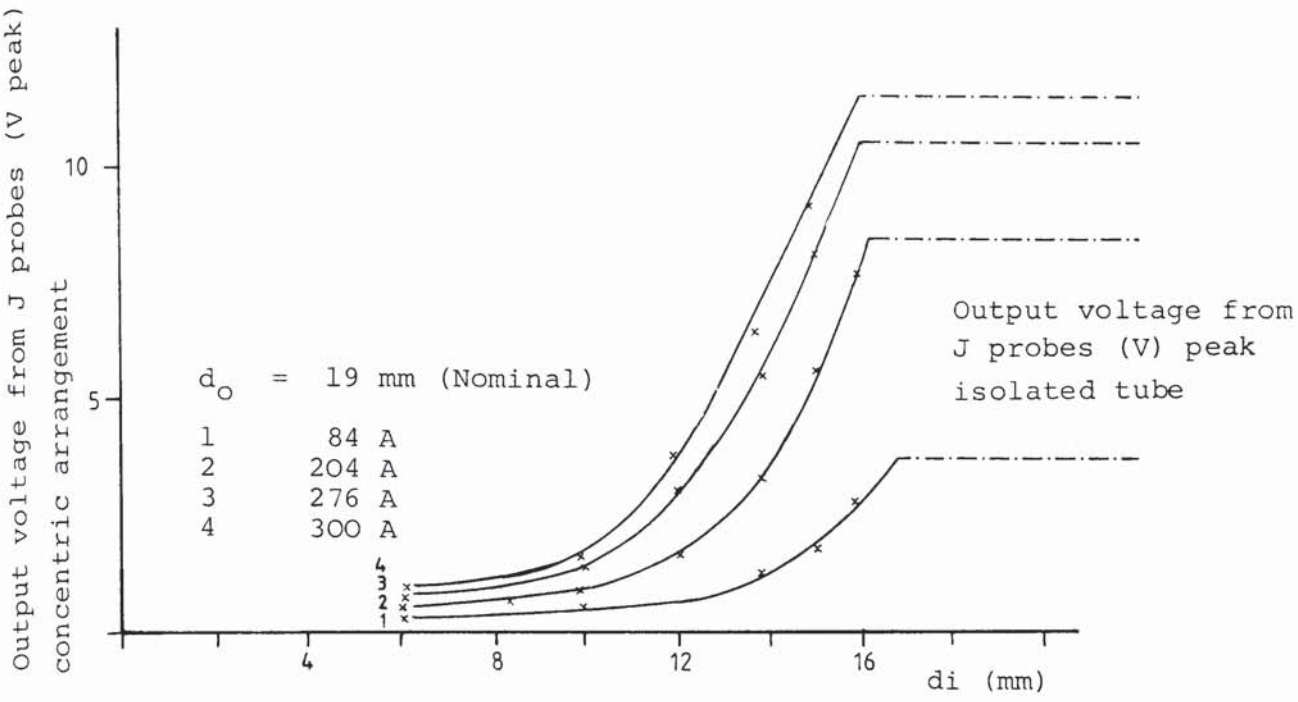

Fig. 7.53 Variation of voltage proportional to surface electric field strenth as a function of internal diameter at constant current.

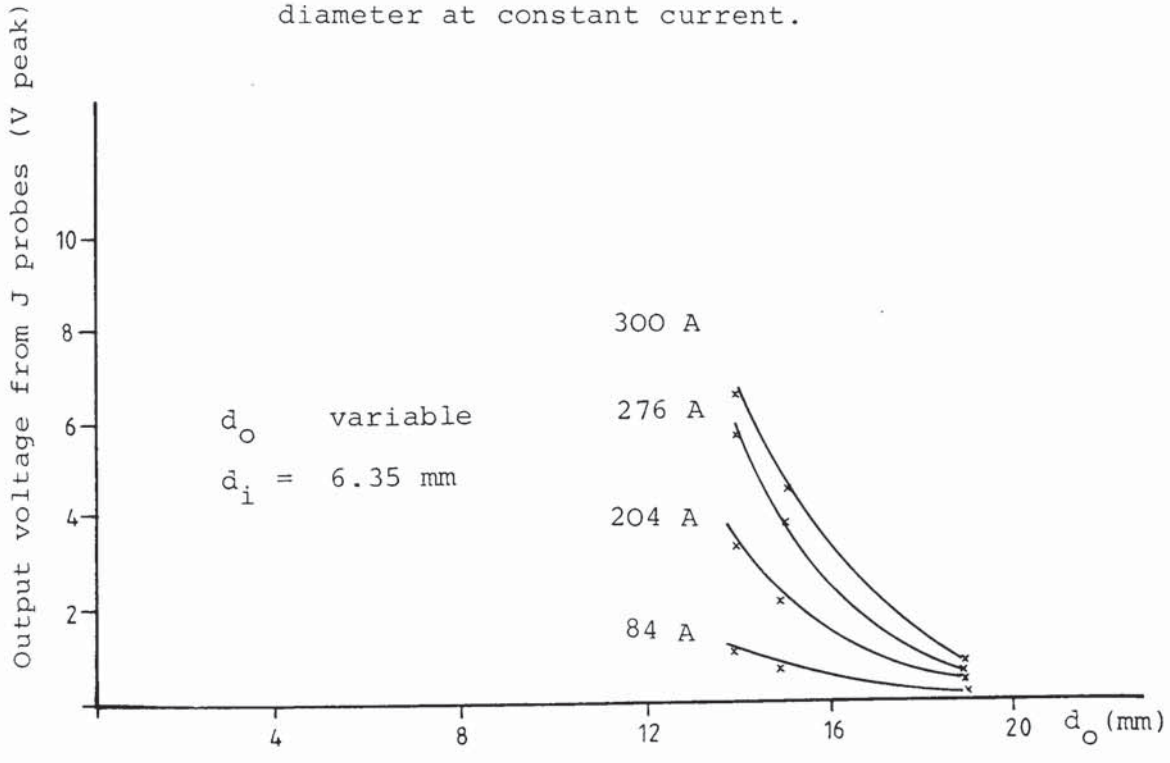

Fig. 7.54 Variation of voltage proportional to surface electric field strength as a function of external diameter at constant current - concentric arrangement

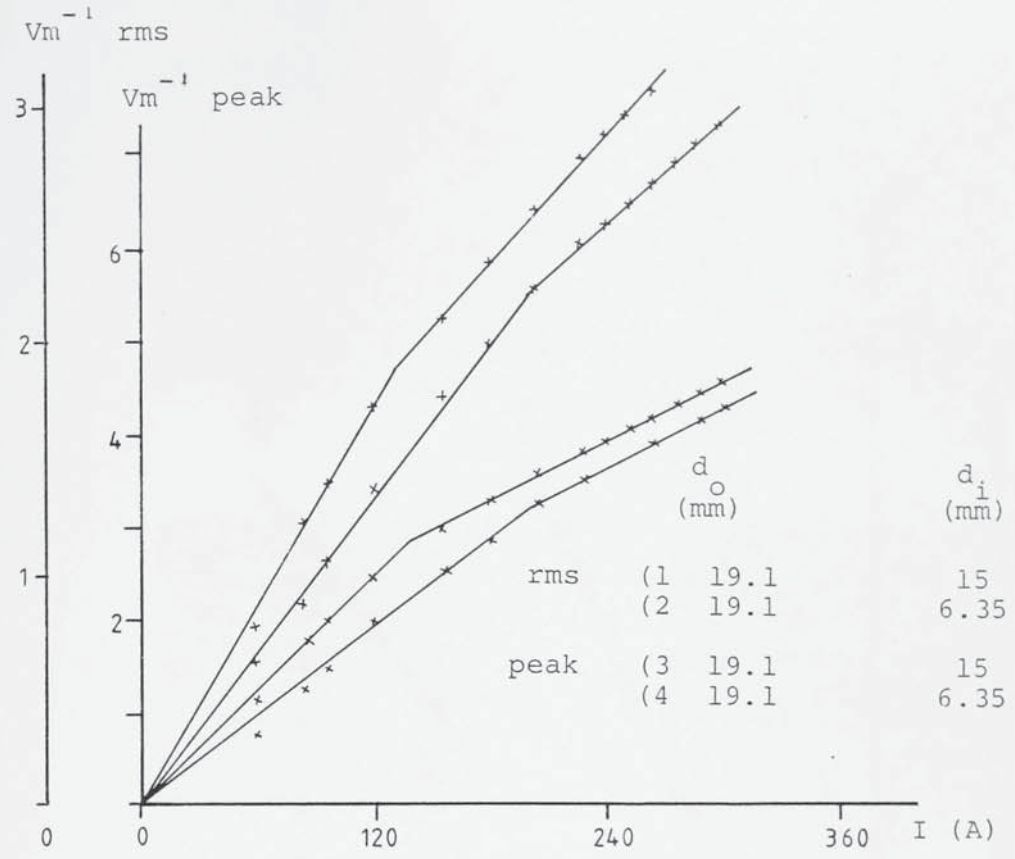

Fig. 7.55 Voltages proportion al to electric field at the surface of an isolated tube

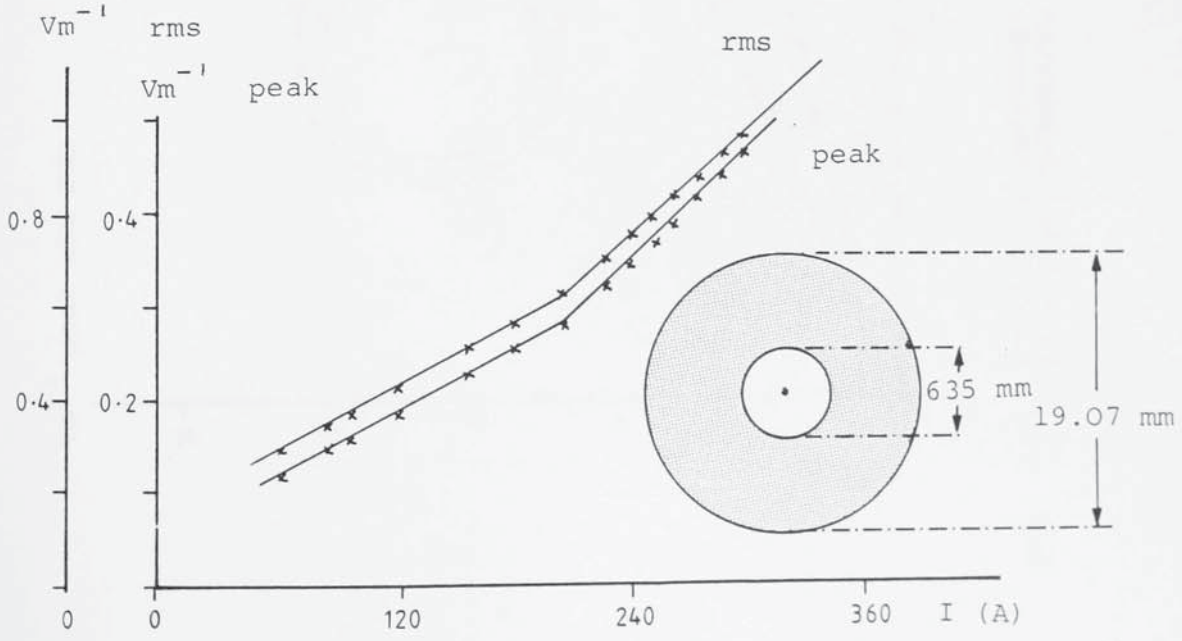

Fig. 7.56 Voltages proportional to electric field at the surface of a tube concentric with a copper conductor

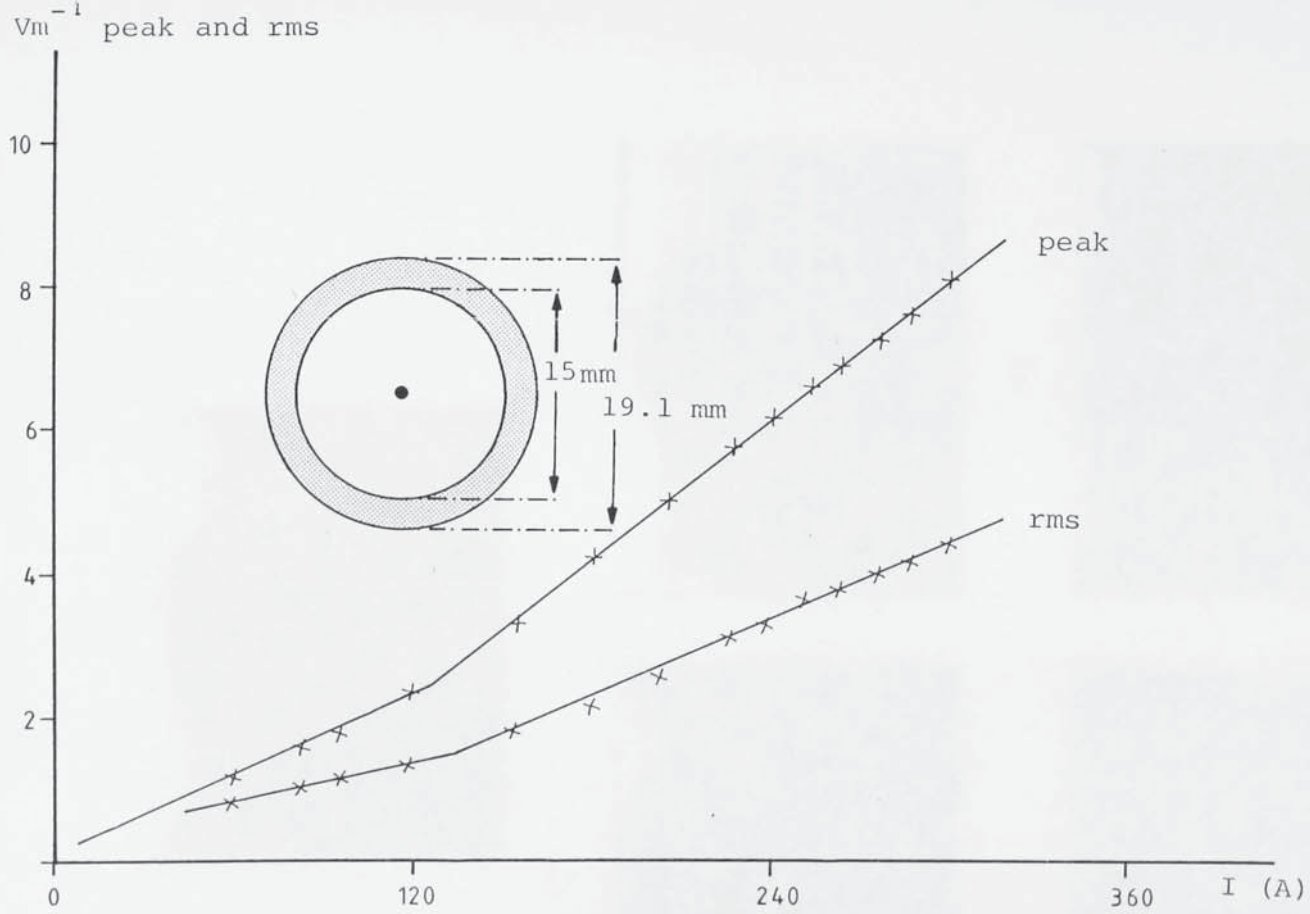

Fig. 7.57 Voltage proportional to the electric field at the surface of a tube concentric with a copper conductor

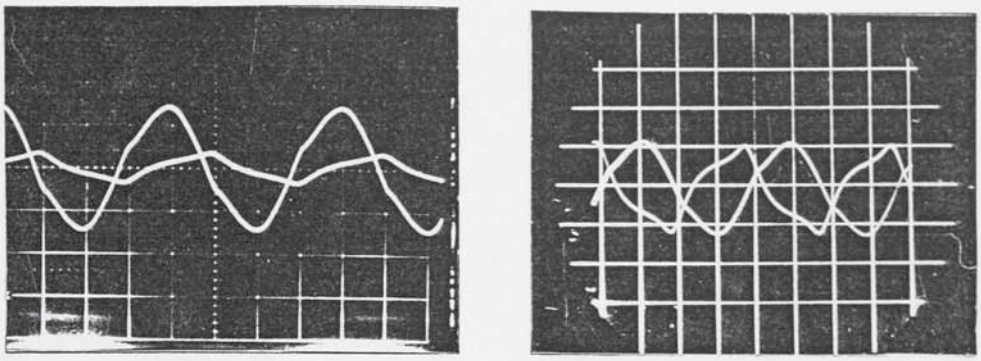

(A) (B)

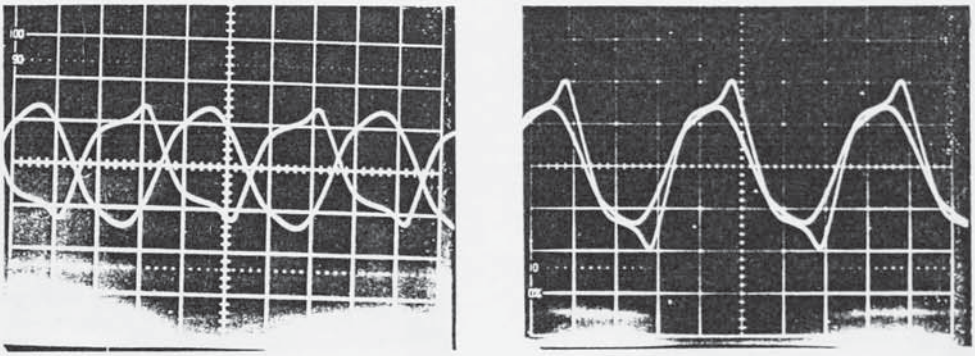

(C) (D)

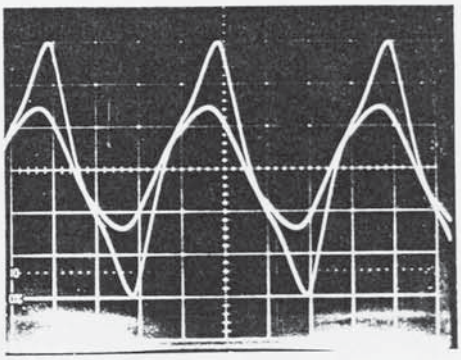

(E)

Oscillogram	Tube dimensions d_i (mm)	d_o (mm)
(A)	6.35	19
(B)	10	|
(C)	13.9	|
(D)	15	|
(E)	16	|

Current 60 A

Fig. 7.58 Oscillograms for tubes sample A with concentric conductor

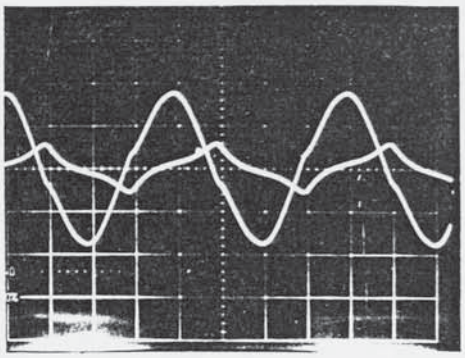

(A)

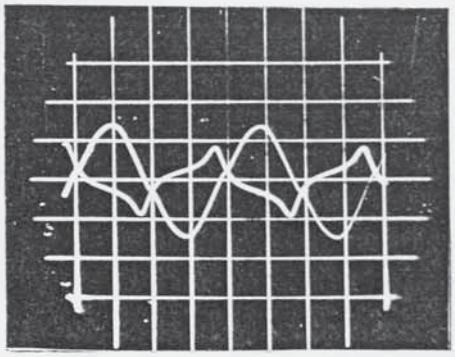

(B)

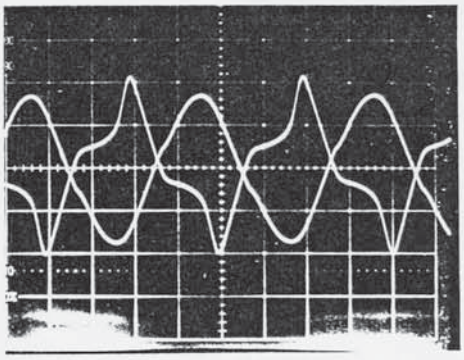

(C)

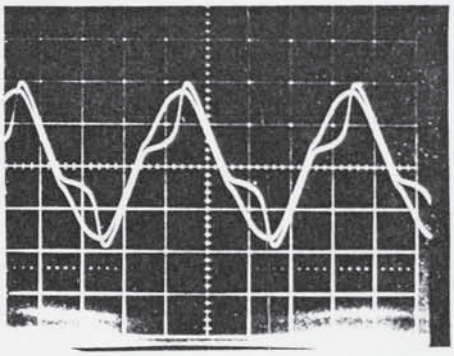

(D)

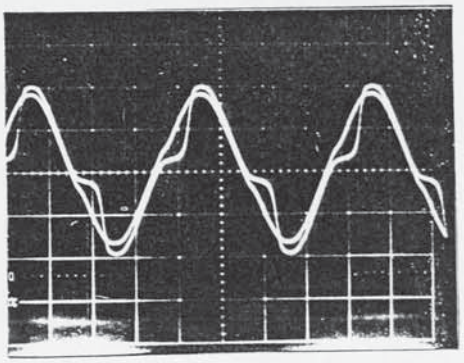

(E)

Oscillogram	Tube dimensions d_i (mm)	d_o (mm)
(A)	6.35	19
(B)	10	|
(C)	13.9	|
(D)	15	|
(E)	16	|

Current 288 A

Fig. 7.59 Oscillograms for tubes sample A with concentric return conductor

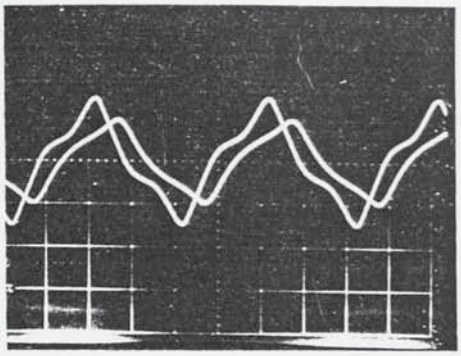

(a) 0.5V/cm
(b) 0.IV/cm

(A) Current 60A Amplifier gain 14

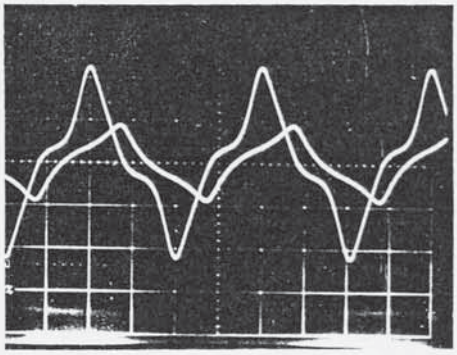

(a) 1V/cm
(b) 0.2V/cm

(B) Current 156A Amplifier gain 14

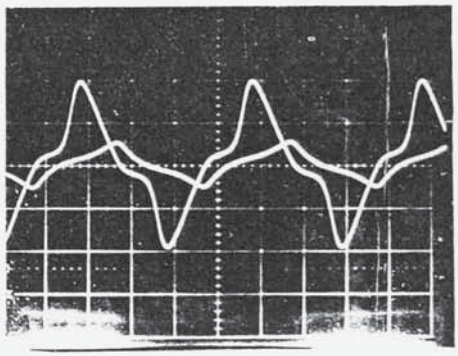

(a) 2V/cm
(b) 0.5V/cm

(C) Current 240A Amplifier gain 14

Fig. 7.60 Oscillograms of J_s waveforms of two tubes in series
Waveform (a) 12 mm outside diameter 6.35 mm bore
Waveform (b) 19 mm outside diameter 6.35 mm bore

CHAPTER 8

CONCLUSIONS

Known solutions applicable to a thick plate in the presence of an alternating magnetic field parallel to its surface can be applied to the resistance heating problem provided the diameter and wall thickness of a tube are above a minimum value. Hitherto unpublished equations (4.40 and 4.48) have been derived for the purpose of calculating these values. These equations, although based on Arnold's resistance ratio formulae referring to non-magnetic circular conductor, have been shown to be applicable to magnetic conductors by replacing μ by μ_{eff}

The presence of the inner conductor in the concentric arrangement increases the resistance of a tube. This resistance can be calculated from Arnold's formula provided $\beta_o \ll 0.3$. Dwight's high frequency formula was shown to apply to the case when $\beta_o > 0.3$ provided $b/\delta > 5$ and $z > 9$.

For a constant external diameter, the resistance continues to increase with β_o . The larger the external diameter, the smaller is the value of β_o at which the resistance begins to increase. For a constant internal diameter, the resistance remains constant beyond a certain value of β_o . This value decreases with an increase in the external diameter of a tube.

For the concentric arrangement of two pipes, the effective resistance of the inner pipe is unaffected by the presence of the outer pipe and therefore it can be considered to be in isolation for the purpose of calculations.

The depth into a conductor at which the power density reduces to zero, is smaller than the depth at which the magnetic field reduces to zero. These depths increase with a reduction in diameter. For the same value of surface field strength and tube dimensions, the depth of penetration is smaller in the concentric configuration. For steel conductors, the classical skin depth has no meaning.

It has been shown that if an effective permeability is used in conjunction with formulae applicable to magnetic-linear material, the losses can be predicted with an accuracy better than 10%. For field strengths beyond the turning point in the $\log \mu_v / \log H_s$ characteristic, the effective permeability is a simple function of the surface field strength and can be derived by simple measurements on a small diameter sample. A knowledge of the B/H curve is not required. The turning point occurs at a higher value of H_s with a sample of higher resistivity. The effective permeability is a function of the B/H characteristic and resistivity and is independent of frequency and the geometrical dimensions of a conductor. The same effective permeability function may apply to steels of different specification as a result of their corresponding values of μ and σ. The same effective permeability function cannot be used for the concentric configuration and must be increased by a factor which for a given internal diameter reduces with a reduction in wall thickness.

The effective permeability method cannot predict the depth at which the magnetic field attenuates to zero. Equally the step-function method underestimates this depth with the error

increasing as the conductor diameter decreases.

In the absence of hysteresis, three dimensionless parameters embodying all the variables, describe the electrical performance of a conductor supplied with a sinusoidal current. Alternative sets of parameters are possible. One set enables the effective permeability function to be derived and the other to produce universal loss charts.

Losses by induction in thick steel plates can be calculated simply by substituting μ_{reff} for μ_r in the loss formula for a semi-infinite magnetic-linear material.

A numerical solution for magnetic non-linear steel bar of any diameter is not available. Laver's numerical model fails to predict the losses correctly in some cases but further investigation is required to establish the limits of applicability.

The power loss in an isolated conductor varies with the surface field strength to a power index in the region 1.57 to 2. This index is a function of t, d_s, σ, f, H_s and the B/H characteristic of the material and is not a constant for a given B/H curve. For a non-magnetic solid conductor an index of 2 indicates that the conductor is equivalent to a semi-infinite slab and for a magnetic non-linear steel conductor it indicates the absence of skin effect.

It has been shown that equations developed on the basis of the step-function theory, can predict the losses for the cases considered with an accuracy depending on the range of magnetic field strengths. New equations have been developed for thin-

wall tubes and small diameter wires. For these cases the power is given by the sum of two components. The first is due to the effective resistance of the conductor and the second due to its d.c. resistance. As the current increases the second component predominates. In addition and for the first time the step-function method has been applied to the concentric configuration. The nature of the surface current density waveforms depends on the ratio of depth of penetration to conductor radius. For tubes it is also dependent on the wall thickness. "Thick" wall tubes and "large" diameter steel bars have surface current density waveforms similar in shape to the ones obtained for a thick steel plate in the presence of a magnetic field parallel to its surface. This similarity disappears as the wall thickness in the case of a tube and the diameter in the case of a bar is reduced. Under these conditions for part of the current half-cycle, the resistance of the bar or tube becomes equal to its d.c. resistance.

The design parameters of a saddle-tube or coaxial pipe heating system, can be specified by means of the characteristics of Fig. 6.12 and B.3. Alternatively, for large diameter tubes or pipes Lim and Hammond's characteristics can be used.

A given power output from a saddle-tube system can be obtained by different combinations of current, tube dimensions and material. The steel with the highest permeability and resistivity will produce the maximum power for a given current. The volume of steel and the current required are smaller for the smaller diameter tube, but the required supply voltage for a given length of pipeline and power is greater.

For one of the samples tested, an extra unaccounted loss is present as the wall thickness is reduced. This is believed to be due to hysteresis effects but further evidence is required from tests on samples of a specification resulting in similar behaviour. This anomally does not affect the results of the saddle-tube system since for safety considerations the wall thickness must be sufficiently thick to ensure that the surface field is almost zero. This wall thickness as stated previously reduces as the internal diameter increases.

CHAPTER 9

FURTHER WORK

Two surface heating systems based on saddle tube and coaxial configuration have been considered. The theoretical investigation was limited to a concentric arrangement and the experimental work was restricted to the saddle-tube system. Additional experimental work is thus desirable with the coaxial system for complete quantitative comparison to be made possible.

The effects of eccentricity need to be investigated theoretically and experimentally. Although of limited relevance to the saddle tube system, it is of importance in the case where the transport pipe itself acts as the heat tube, with the return conductor inside the pipe.

The above systems and many other variations based on the skin effect phenomenon, differ only in their heat transfer characteristics and in their manufacture and installation costs. A scientific investigation is required to quantify these characteristics and evaluate their influence on the performance of the different systems.

Very few solutions are truly general. In seeking a universal or general solution, there is the danger that a solution will not emerge, because of the complexity of the required theoretical models. However the establishment of a general theory must remain a long term objective of any work in this area.

In this thesis a simple approach has been adopted towards

finding a solution by utilising the concept of an effective permeability and by adopting an approximate non-linear solution, but possibly at the expense of generality. It is therefore important to test the boundaries of their applicability by further tests.

The aim of these tests would be to relate the B/H characteristic, resistivity, chemical composition, heat treatment and radial dimensions to the production of power loss. From the academic point of view this investigation need not be limited to particular types of steel, but in practice, cost considerations will automatically exclude many steel specifications. These tests will also establish the relationship between effective permeability in the concentric arrangement as influenced by the tubes' radial dimensions. An important restraint in carrying out these tests will be to secure different tube dimensions from identical steel specifications.

An analytic technique for an isolated steel tube can also be used for the concentric arrangement of two tubes since only the boundary conditions need to be changed. Thus the analytic method of reference 14 could be extended to the case of coaxial tube of "large" diameters and "thick" walls. Such a solution will establish analytically an effective permeability function and also enable current densities to be calculated over the entire range of the B/H characteristic.

A numerical solution of the differential equations describing the two systems is also an attractive proposition, particularly if it is performed in a dimensionless form, leading

to design curves as a function of supply conditions, material parameters and tube dimensions.

Further measurements on field penetration are required and the accuracy of measuring the power in the saddle tube needs to be improved.

APPENDIX A

B.S. 980 : 1950

As altered May, 1954

B.S. reference number	Description	Chemical composition							
		C per cent	Si per cent	Mn per cent	Ni per cent	Cr per cent	Mo per cent	S per cent	P per cent
CDS–1	Mild steel, soft	0·20 max.	—	—	—	—	—	max. 0·050	max. 0·050
CDS–2	Mild steel, hard	0·20 max.	—	—	—	—	—	0·050	0·050
CDS–3	Low carbon case-hardening	0·18 max.	0·05/ 0·35	0·4/ 0·7	—	—	—	0·050	0·050
CDS–3A	Low carbon case-hardening	0·18 max.	0·05/ 0·35	0·4/ 0·7	—	—	—	0·050	0·050
CDS–4	Low carbon case-hardening (free machining)	0·10/ 0·18	0·05/ 0·35	0·6/ 1·0	—	—	—	0·070	0·050
CDS–5	'30' carbon, soft	0·20/ 0·40	0·35 max.	0·3/ 0·9	—	—	—	0·050	0·050
CDS–6	'30' carbon, hard	0·20/ 0·40	0·35 max.	0·3/ 0·9	—	—	—	0·050	0·050
CDS–7	'45' carbon, soft	0·40/ 0·55	0·35 max.	0·3/ 0·9	—	—	—	0·050	0·050
CDS–8	'45' carbon, hard	0·40/ 0·55	0·35 max.	0·3/ 0·9	—	—	—	0·050	0·050
CDS–9	Carbon-manganese, soft (suitable for welding)	0·26 max.	0·35 max.	1·2/ 1·7	—	—	—	0·050	0·050
CDS–10	Carbon-manganese, hard (suitable for welding)	0·26 max.	0·35 max.	1·2/ 1·7	—	—	—	0·050	0·050
CDS–11	'26' carbon-manganese-molybdenum (suitable for welding)	0·26 max.	0·35 max.	1·2/ 1·7	—	—	0·15/ 0·25	0·050	0·050
CDS–12	1 per cent chromium-molybdenum (suitable for welding)	0·26 max.	0·35 max.	0·4/ 0·8	—	0·8/ 1·2	0·15/ 0·30	0·050	0·050
CDS–13	1 per cent chromium-molybdenum, hard	0·25/ 0·45	0·35 max.	0·5/ 1·0	—	0·8/ 1·2	0·15/ 0·30	0·050	0·050
CDS–14	3 per cent nickel, hard	0·30/ 0·45	0·35 max.	0·3/ 0·7	2·75/ 3·5	—	—	0·050	0·050

NOTE 1. Reduced mechanical properties if subsequently annealed, brazed, or welded.
NOTE 2. Reduced mechanical properties if subsequently annealed or brazed.
NOTE 3. Optional elements Mo, Ti, W, Cb and V.
NOTE 4. Titanium not less than 5 × C or niobium (columbium) not less than 10 × C. Optional elements, Mo, W and V.

Table A1 Physical Properties of Steels (Ref.58)

Material and condition Composition %	Temperature °C	Specific gravity g/cm³	Thermal properties (see Notes)			Electrical resistivity μΩ cm
			Specific heat J/kg K	Coefficient of thermal expansion 10^{-6}/K	Thermal conductivity W/m K	
Carbon Steels						
C 0.06 }	RT	7.87	—	—	65.3	12.0
Mn 0.4 }	100		482	12.62	60.3	17.8
	200		520	13.08	54.9	25.2
Annealed	400		595	13.83	45.2	44.8
	600		754	14.65	36.4	72.5
	800		875	14.72	28.5	107.3
	1 000		—	13.79	27.6	116.0
C 0.08 }	RT	7.86	—	—	59.5	13.2
Mn 0.31 }	100		482	12.19	57.8	19.0
	200		523	12.99	53.2	26.3
Annealed	400		595	13.91	45.6	45.8
	600		741	14.68	36.8	73.4
	800		960	14.79	28.5	108.1
	1 000		—	13.49	27.6	116.5
C 0.23 } En 3	RT	7.86	—	—	51.9	15.9
Mn 0.6 } 060A22	100		486	12.18	51.1	21.9
	200		520	12.66	49.0	29.2
Annealed	400		599	13.47	42.7	48.7
	600		749	14.41	35.6	75.8
	800		950	12.64	26.0	109.4
	1 000		—	13.37	27.2	116.7
C 0.42 } En 8	RT	7.85	—	—	51.9	16.0
Mn 0.64 } 060A42	100		486	11.21	50.7	22.1
	200		515	12.14	48.2	29.6
Annealed	400		586	13.58	41.9	49.3
	600		708	14.58	33.9	76.6
	800		624	11.84	24.7	111.1
	1 000		—	13.59	26.8	122.6
C 0.80 }	RT	7.85	—	—	47.8	17.0
Mn 0.32 }	100		490	11.11	48.2	23.2
	200		532	11.72	45.2	30.8
Annealed	400		607	13.15	38.1	50.5
	600		712	14.16	32.7	77.2
	800		616	13.83	24.3	112.9
	1 000		—	15.72	26.8	119.1
C 1.22 }	RT	7.83	—	—	45.2	18.4
Mn 0.35 }	100		486	10.6	44.8	25.2
	200		540	11.25	43.5	33.3
Annealed	400		599	12.88	38.5	54.0
	600		699	14.16	33.5	80.2
	800		649	14.33	23.9	115.2
	1 000		—	16.84	26.0	110.7
C 0.23 } En 14	RT	7.85	—	—	46.1	19.7
Mn 1.51 } 150M19	100		477	11.89	46.1	25.9
	200		511	12.68	44.8	33.3
	400		590	13.87	39.8	52.3
	600		741	14.72	34.3	78.6
	800		821	12.11	26.4	110.3
	1 000		—	13.67	27.2	117.4

Notes:

1. Where *specific heats* are quoted at temperatures above R.T., the values have been determined over a range of 50 °C up to the temperature quoted.
2. *Coefficients of expansion* are mean values from R.T. up to the temperature quoted.

Table A2 Some Data on the Magnetic Properties of Cast Steels and Cast Iron (Ref.58)

Material	*Condition*	*Flux density* T		*Rel. permeability*		*Max. flux density* T	*Remanence* T	*Coercive force* A/m
		H = 4kA/m	H = 8kA/m	Maximum	at H A/m	H = 20kA/m	H = 20kA/m	H = 20kA/m
Steels								
0.10% carbon steel,[1] Si, 0.33%; Mn, 0.67%	Annealed	1.62	1.74	2 420	216	1.92	0.80	136
	Normalised	1.64	1.76	1 950	248	1.96	0.85	168
	As-cast	1.61	1.74	2 100	208	1.95	0 66	128
0.19% carbon steel,[1] Si, 0.30%; Mn, 0.48%	Annealed	1.60	1.73	2 100	224	1.88	0.87	156
	Normalised	1.57	1.72	1 520	360	1.91	0.90	216
	As-cast	1.55	1.69	1 720	232	1.89	0.73	168
0.34% carbon steel,[1] Si, 0.44%; Mn, 0.55%	Annealed	1.53	1.66	1 200	400	1.85	1.05	296
	Normalised	1.50	1.67	970	575	1.87	1.05	440
	As-cast	1.45	1.65	840	480	1.87	0.85	440
Manganese steel[2] 0.19% C, 0.48% Si, 1.14% Mn	A 925 °C	1.51	1.66	1 300	400	1.86	—	—
0.29% C, 0.29% Si, 1.40% Mn	A 950 °C, N 880 °C, T 600 °C, A.C.	1.50	1.68	650	960	1.78	—	
0.31% C, 0.52% Si, 1.37% Mn	A 950 °C, OQ 860 °C, T 620 °C, A.C.	1.55	1.65	750	960	1.70	—	—
Chromium-molybdenum steel[2] 0.31% C, 0.69% Mn, 1.16% Cr, 0.39% Mo	A 925 °C, N 880 °C, T 700 °C, A.C.	1.45	1.59	—	—	1.76	—	—
	A 925 °C, OQ 860 °C, T 650 °C, A.C.	1.54	1.66	—	—	1.81	—	—
Cast-irons[3]						Hysteresis loss J/m³/cycle		
Grey iron T.C. 3.12%, Si 2.2%, Mn 0.67%, P 0.13% (low phosphorous)	As-cast	0.70	0.86	315	640	2 700	0.41	560
	Annealed	0.93	1.07	1 560	200	700	0.44	200
Grey iron T.C. 3.3%, Si 2.04%, Mn 0.52%, P 1.03% (high phosphorous)	As-cast	0.79	0.97	281	1 040	2 730	0.43	720
	Annealed	0.85	1.00	760	320	1 190	0.44	280

Sources of information: 1. 'Effect of Heat Treatment on the Magnetic Properties of Carbon Steel Castings', W. J. Jackson, *J. Iron Steel Inst.*, 1960, 194, 29.
2. Data submitted by British Steel Foundries.
3. Hillman, M. H. *BCIRA Journal of Research and Development*, 1954, 5, 188–248.

APPENDIX B

DESIGN CONSIDERATIONS

B.1 Saddle-tube System

B.1.1 Introduction

In designing a saddle-tube surface heating system two quantities need to be specified. These are:

1. the current to develop the required power for heat loss compensation
2. the tubes' radial dimensions to ensure that the field attenuates to zero at the external surface

The ability to choose these quantities leads to an economic design in terms of the kVA rating of the supply transformer and the cost of the steel tube and return copper conductor. The purpose of this Appendix is to develop an outline design procedure.

B.1.2 Design procedure based on semi-infinite slab solution

If the radius of a tube is much larger than the penetration depth, its curvature can be neglected and the tube can be replaced by a semi-infinite slab. Depending on the current and grade of steel, a tube having a diameter of the order of 4 cm and a wall thickness (depending on the diameter) in the region of 5 mm, may satisfy this condition (Chapter 6). This suggests the possibility of using the numerical solution applicable to the semi-infinite slab [9] for the saddle-tube system.

In Chapter 5, it was shown how the charts produced by Lim and Hammond [9] could be used to calculate the loss in a

large diameter bar. The possible application of these charts to the above case and to the saddle-tube system was not investigated by the authors and particularly the relevance of these charts to the saddle-tube arrangement is not obvious.

Fig. B.1 refers to the problem considered by Lim and Hammond.

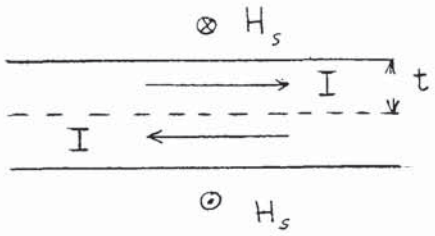

Fig.B.1 Induced current in a thick plate due to a magnetic field parallel to its surface.

If t in Fig. B.1 is sufficiently large so that the field reduces to zero at the interface, then there is no interaction of fields between the top and bottom half of the plate. Lim and Hammond show that this condition is satisfied if

$$\delta_F/t > 0.5$$

Consider now that in Fig. B.2 the value of d enables the cylindrical boundaries to be flattened and the value of t satisfies the limiting condition $\delta_F/t = 0.5$

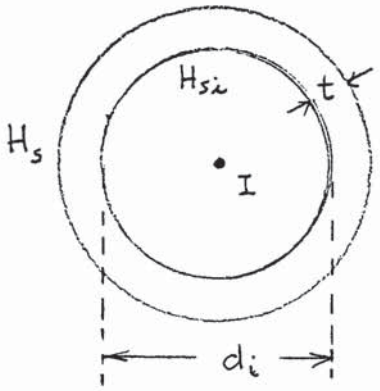

Fig. B.2 Establishment of surface magnetic fields in a saddle-tube system due to current I

Under these conditions, H_s in Fig. B.2 is zero and t specifies the wall thickness of the tube which can now be represented by half the plate of Fig. B.1 with H_s replaced by H_{si}. H_{si} is related to the current I and the internal diameter d_i by $H_{si} = I/\pi d_i$

For the concentric arrangement, the charts of reference 9 can be used as follows:

A given grade of steel specifices σ, B_s and ξ. For a chosen value of H_{si} and the known value of ξ, h_o is calculated. (If H_{si} is chosen too small, the diameter required is large or H_s is below the value corresponding to the "turning point")

From the normalised penetration curves, the value of η is determined from where the lines of constant h_o and $\delta_{F/t}$ = 0.5 intercept the constant characteristics. The wall thickness is obtained from

$$\eta = \sigma f t^2 B_s / \xi$$

knowing η and h_o, the value of the dimensionless loss P_n is read off from the charts.

For a required power P ($W\ m^{-1}$), the internal diameter is calculated from

$$P_n = P \sigma t / \pi d_i H_{si}^2$$

and the external diameter from

$$d_o = d_i + 2t$$

Finally, the required current to develop the power P is calculated from

$I = H_{si} \pi d_i$ (in the charts of ref. 9, $\hat{H}_{si}$ has been used)

B.1.3 Design procedures based on Chapters 6 and 7

Consider now that the tubes' dimensions do not permit the tube to be approximated to a thick plate as in the previous section. Under these conditions, the results of section 7.9.1 can be used and have been processed to produce Fig. B.3.

Three points referring to the tube d = 12 mm do not lie on the curve. Examination of the results in table 7.21 shows that agreement between calculated and measured loss values corresponding to these points is not as good as the remaining results. The dimensionless parameter $P\sigma / H_{si}^2 d_i$ has been obtained on the basis of the calculated loss values. If the measured values are used, the points will

be shifted upwards. It is rather surprising that all the points corresponding to the four tubes tested lie on the same curve considering that four wall thicknesses are involved.

In Fig. B.1, increasing t beyond the limiting value of $2\delta_F$ will not result in an increase in loss.

In Fig. B.2 however, the effective resistance increases with the wall thickness in a manner depending if d_i or d_o is increased to produce the increase in thickness (Fig. 4.6 and 4.10). Since for the case under consideration d is specified, for a given current the loss will not increase by increasing t; an observation consistent with Fig. 4.10 and a conclusion reached using the step-function theory (Sect. 7.9.1.)

The above suggests that Fig. B.3 is applicable to any diameter provided the wall thickness is sufficiently large to ensure that for a given current R_{ac} has reached its constant value (see Fig. 4.10). This wall thickness is much smaller than what is required for zero field at the surface of the tube.

The use of Fig. B.3 for design purposes is simple. For a selected H_{si} value, the corresponding parameter $P\sigma/H_{si}^2 d_i$ is determined from the curve of Fig. B.3. For a specified power, d_i is calculated from $P\sigma/H_{si}^2 d_i$ and the required current from $H_{si}\pi d_i$

The curve of Fig. B.3 is applicable to any steel of known values of σ and ξ if the H_{si} axis in Fig. B.3 is converted to h_o by dividing H_{si} by the value of ξ for

sample A material.

B.1.4 Discussion

The two methods of design are compared in table B.1. In order to calculate d from the curves of reference 9, the value of ξ for sample A needs to be known, since the curve of Fig. B.3 refers to this material. As ξ is unknown, the values of d_i in table B.1 have been calculated on the basis of four values of ξ within the expected range. The largest percentage difference in d_i between the two methods is 15% reducing to 3.5% as the diameter increases. The % difference is a function of diameter and also of H_{si}. For the same value of H_{si}, if the specified power is doubled, the required diameter must also be doubled. For example, if 200 (W m^{-1}) is required (see table B.1) with Hs = 5500 (A m^{-1}), the required diameter is 1.1 x 2 = 2.2 cm but the % difference in d is still 15%. For H_{si} = 2120 (A m^{-1}), 200 (W m^{-1}) will require a tube of 9 cm bore and the % difference between the two methods is as before 3.5. As the power specified is increased, larger values of H must be considered in order to keep d_i at a reasonable size (d_i must also be available as a standard bore) and the prediction based on Fig. B.3 becomes more accurate. Depending on the value of h_o, the accuracy of determining η and P_η and hence d_i and t varies with the degree of extrapolation required on the charts of reference 9. Whilst Fig. B.3 is independent of B_s, the calculation of d_i and t from the loss chart of reference 9 is influenced

by the value of B_s . A reduction in B_s leads to an increase in t and d_i . The value of 1.72 chosen for the comparison of results in table B.1 is a reasonable estimate.

The calculated values of d_i are insensitive to a wide variation in the value of ζ . For small values of ζ , the B/H curve approaches the step-function approximation and the thickness t calculated on this basis (equation 7.12) is therefore sensitive to the value of ζ. For a given H the field penetration increases with a decrease in diameter and therefore the small diameter tube will require the thicker wall for zero field at the surface. As the wall thickness must be commercially available, some readjustment (upwards) to the value calculated may be necessary and a precise calculation of t is not therefore a strict requirement.

The same power can be developed by tubes of different radial dimensions. The smaller diameter tube requires a smaller current and a smaller volume of steel. The smaller current however requires a higher voltage from the supply transformer to provide a given power. (the smaller tube will have a higher p.f.). For a given upper limit in transformer secondary voltage, the maximum length of pipeline which can be heated, will be smaller for the smaller diameter tube. For a given power an optimum design can be obtained on the basis of costs.

In the dimensionless loss parameter of Fig. B.3, σ can be corrected for temperature. The operating temperature of

the tube will be dictated by the power rating, the thermal resistance between the tube and pipe and the wall thickness.

The return conductor will contribute to the rate of heat generated and will equal $I^2 R_{dc}$, where R_{dc} is its dc resistance. This contribution can be taken as 10% of the power required or a more accurate estimate obtained from an iterative calculation. Alternatively, in calculating the tube rating, the contribution of the return conductor can be ignored and considered as a safety margin in meeting the specification. The presence of the air gap prevents this energy from being readily transferred to the tube, unless some heat transfer medium (better than air) is introduced in the space available.

B.2 Coaxial System

For the coaxial pipeline system, the dimensions of the outer pipe and its power loss (which does not contribute to the useful heat) can be determined in a similar manner to the saddle-tube. The power developed in the transport pipeline can be calculated from equation 4.45 by replacing μ_r by μ_{reff} or (if the wall thickness demands it) by the effective permeability method developed in chapter 6. If the required field strength is in the region of 1000 (Am^{-1}) or less, the step-function and effective permability methods will give inaccurate results.

Since in the case of the coaxial system, the diameter of the outer pipe is large, for

$$H_{si} < 1000 \ (A\ m^{-1})$$

the charts of reference 9 will give more accurate results since they extend (depending on the value of ξ) to H_s= 500 (Am^{-1}).

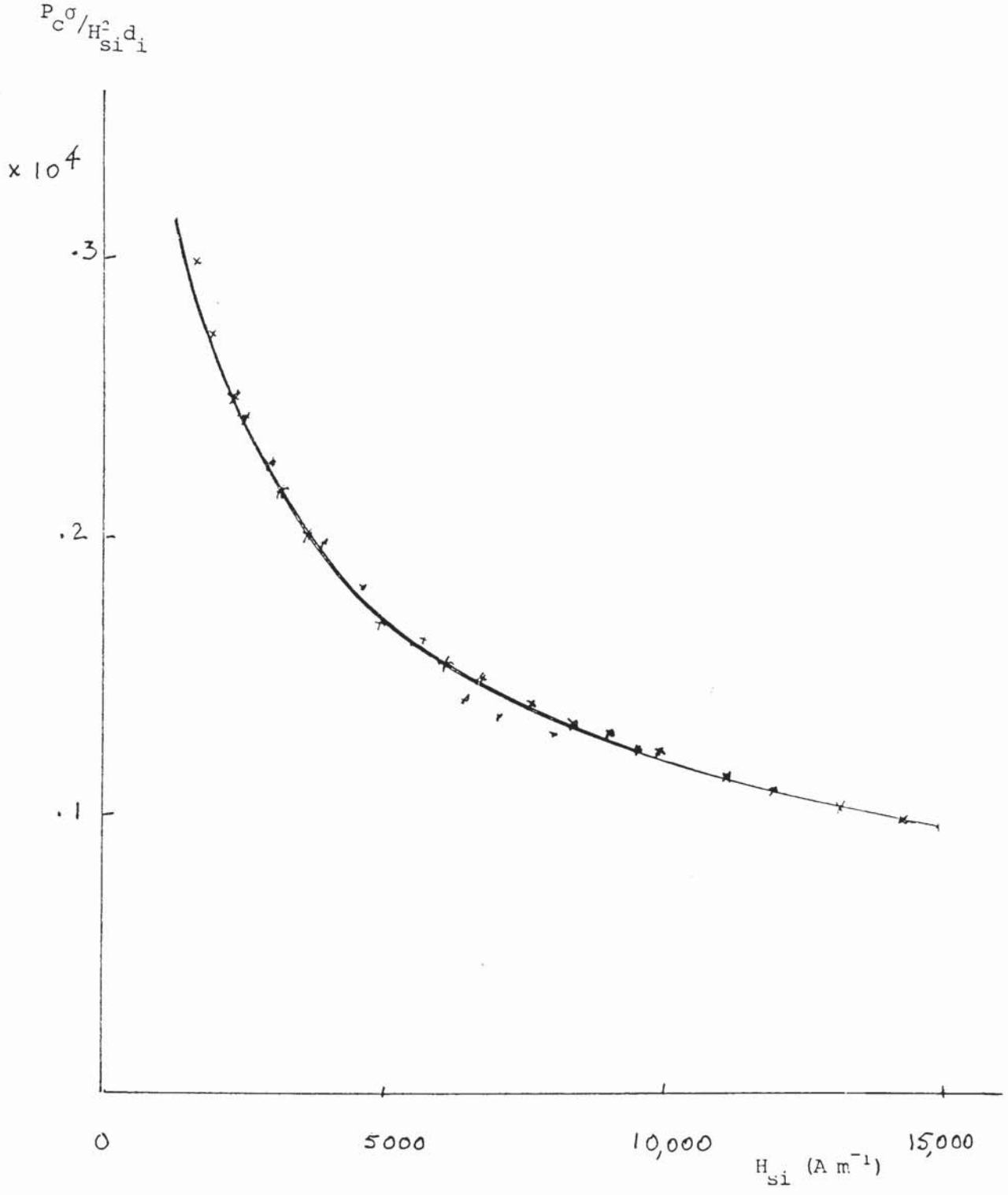

Fig. B3 Electrical performance characteristic of saddle-tube system

Table B.1 Comparison of Design Methods - Saddle tube system

P (Wm^{-1})	H_{si} (Am^{-1})	I (A)	Calculated d_i (cm) From Fig. B3	Calculated d_i (cm) From charts of ref. 9 ξ (Am^{-1})	450	500	600	750	Average	% difference in d_i Fig.B3 basis	Calculated t (mm) From step function method	Calculated t (mm) From charts of ref 9 ξ	450	500	600	750
100	5500	190	1.1		0.92	0.92	0.96	0.92	0.93	15.0	6.25		6.88	6.62	6.88	6.91
	3000	245	2.6		2.37	2.38	2.44	2.54	2.43	6.5	5		5.32	5.34	5.73	6
	2120	300	4.5		4.2	4.4	4.37	4.39	4.34	3.5	4.13		4.80	5.05	5.13	5.44

σ = 0.53×10^{7} (Sm^{-1})

B = 1.72 T

for step-function method $B_A = 0.75\ B_s$

REFERENCES

[1] SCHIFFARTH, J.: 'Heating billets and plate by the direct passage of current'. Brown Boveri Review, Oct/Nov, 1964, pp. 77-87

[2] OTHMER, D.F.: 'Pipe heating by a.c. steel'. Journal of Pipelines, No. 1, Jan 1981, pp. 113-125

[3] ANDO, M., and KAWAHARA, K.: 'How skin effect tracing works'. Hydrocarbon Processing, Dec 1976, pp. 90-92

[4] ANDO, M., and GOODAL, J.E. : ' Application of the SECT heating system to long distance pipe line'. AIM-CB.EE International Conference on Induction Heating and Melting. Liege, Oct 1978

[5] ANDO, M., and TAKAKI, H. : 'Application of the SECT electric heating system to long-distance pipelines'. U.I.E. 9th Int. Congress in Electroheat. Cannes, Oct 1980

[6] KOYANAGI, M., et al: 'The coaxial pipe electric heating system for pipelines', ASME Trans., J. of Energy, Vol. 105, Dec 1983, pp. 469-474

[7] GILLOTT, G.O., and CALVERT, J.F. : 'Eddy current losses in saturated solid magnetic plates, rods, and conductors'. IEEE Trans., 1965, MAG 1, pp. 126-137

[8] AGARWAL, P.D. : 'Eddy-current losses in solid and laminated iron'. IEEE Trans., 1969-1978, pp. 169-181

[9] LIM, K.K., and HAMMOND, P. : 'Universal loss Chart for the calculation of Eddy-current losses in thick steel plates'. Proc. IEE, 1970, 117, (4), pp. 857-864

[10] ZAKRZEWSKI, K., and PIETRAS, F. : 'Methods of calculating the electromagnetic field and power losses in ferromagnetic materials, taking into account magnetic hysteresis'. Proc. IEE, 1971, 118, (11), pp. 1679-1685

[11] BARTH, J.B. : 'Alternating electromagnetic fields, eddy currents and power loss in solid iron'. Proc. IEE, 1973, 120, (11), pp. 1454-1461

[12] GIERAS, J.F. : 'Analytical method of calculating the electromagnetic field and power losses in ferromagnetic halfspace, taking into account saturation and hysteresis'. Proc. IEE, 1977, (124), (11), pp. 1098-1104

[13] O'KELLY, D. : 'Flux penetration and losses in steel plate with sinusodial magnetisation'. IEE Proc. Vol. 127, Pt.B, No.5, Sept 1980, pp. 287-292

[14] BOWDEN, A.L., and DAVIES, E.J. : 'Analytic separation of the factors contributing to the eddy current loss in magnetically non linear steel'. Proc. IEE, 1983, 130, Pt.B, No.5, pp. 364-372

[15] BURKE, P.E., and LAVERS, J.D. : 'Resistance heating of a circular billet - two simple analytic models'. IEEE-I.A.S., Electric Process Heating Conf. Rec., 1977

[16] CREPAZ, G., and LUPI, S. : 'Influence of the installations electrical parameters on the transient temperature distrution in the direct resistance heating of ferromagnetic billets'. Electroheat for metals conference, BNCE, UIE, Cambridge, Sept 1982

[17] THORNTON, C.A.M. : 'Resistance heating of mild steel containers at power frequencies'. Proc. IEE, Pt. II, Vol. 99, No.68, 1952, pp. 85-93

[18] RAJAGOPALAN, P.K., and MURTY, D.V.S. : 'Internal impedance of solid ferromagnetic conductors'. Proc. IEE, 1965, 112, (7), 1965, pp. 1449-1461

[19] DAVIES, E.J., and SIMPSON, P.G. : 'Induction Heating Handbook. Mc Graw Hill, (UK), 1979

[20] DEELEY, E.M. : 'Flux penetration in two dimensions into saturating iron and the use of surface equations'. Proc. IEE, Vol. 120, No.2, Feb 1979, pp. 204-208

[21] WIDGER, G.F.T. : 'Represention of magnetisation curves over extensive range by rational-fraction approximations'. Proc. IEE, 1969, 116, (1), pp. 156-160

[22] KING, A.P. : 'The measurement of the relative magnetic permeability of steels'. Electricity Council reseach report., ECRC/M831, July 1975

[23] O'KELLY, D. : 'Hysteresis and eddy-current losses in steel plates with non-linear magnetisation characteristics', Proc. IEE, 1972, 119, (11), pp. 1675-1676

[24] KESAVAMURTHY, N., RAJAGOPALAN, P.K., and SUBBARAO, V. : 'Effects of saturation on the core loss of thin ferromagnetic plates subject to alternating flux'. Proc. IEE, 1963, 110, (2), pp. 459-473

[25] O'KELLY, D. : 'Flux penetration in a ferromagnetic material including hysteresis and eddy-current effects'. J.Phys., DS, 1972, pp. 203-213

[26] KESAVAMURTHY, N., and RAJAGONPALAN, P.K. : 'An analytic method taking account of saturation and hyteresis for evaluating the iron loss in solid-iron cores subjected to an alternating field'. Proc. IEE, 1962, 109C, pp. 237-243

[27] TOWNEND, R. : 'Direct resistance heating an interim report (currents up to 5000 A)'. Electricity Council research report., ECRC/N559, Nov 1972

[28] HARDING, R.M. : 'Rapid heating of methods for hot forming and heat treatment'. Electroheat for metals conference, paper 7.4, BNCE, UIE, Cambridge, Sept 1982

[29] ANGEL, F. : 'Electric trace heating for long pipe lines'. El.Rev., Vol. 204, No.11, March 1979, pp. 45-46

[30] Manufacturers Literature :- Chisso Eng. Co.
Isopad
Hotfoil
Raychem.

[31] BS 6351 : 1983 Parts 1, 2, 3

[32] DOBIE, W.C., et al. : 'The control and application of electric surface heating and design of equipment for flammable situations'. VIII th Congress of the UIE, Liege, 11-15, Oct 1976, Paper VII 5

[33] MATTINGLEY, J.M., and ADAMS, J.M. : 'Developments in electric surface heating'. Third Int. Conf. on Electric safety in Hazardous Environments'. IEE, Dec 1982

[34] OAKES, J.A., and SANDBERG, C.L. : 'Some aspects of self-limiting resistive electric heating elements'. IEEE Trans., Ind. Appl., Vol. I A-9, July/Aug 1973, pp. 462-466

[35] HAMMACK, T.J., and KUKLINCA, S.J. : 'Self-limiting electrical heat tracing : new solution to old problems'. IEEE Trans., Ind. Appl., Vol. I A-13, Pt.2, 1977, pp. 134-138

[36] Y.E.B. Internal report - Unpublished. 1971

[37] KENELLY, A.E., LAWS, F.A., and PIERCE, P.H. : 'Experimental reseaches on skin effect in conductors'. Proc. AIEEE, Aug 1915, Vol. 34, p. 1953

[38] ASTBURY, M.A. : 'Alternative-current properties of copper conductors clad in a magnetic sheath'. Proc. IEE, 1963, Vol. 110, No.11, Nov 1963, pp. 2055-2062

[39] McLACHLAN, N.W. : 'Bessel Functions for Engineers'. Oxford University Press, Oxford, 1934

[40] DWIGHT, H.B. : 'Reactance and skin effect of concentric tubular conductors'. Trans. AIEEE, 1942, Vol. 61, pp. 513-518

[41] ARNOLD, A.H.M. : 'The alternating-current resistance of tubular conductors'. JIEE, 1936, 78, pp. 580-593

[42] TEGOPOULOS, J.A., and KRIEZIS, E.E. : 'Eddy current distribution in cylindrical shells of infinite length due to axial currents Pt.II : Shells of finite thickness'. IEEE Trans., 1971, PAS-90, No.3, pp. 1287-1294

[43] COSTELLO, J.C. : 'Proximity effects. Single-phase and three-phase systems of parallel conductors'. The Electrician., Feb 22, 1935, pp. 240-241

[44] ARNOLD, A.H.M. : 'Proximity effect in solid and hollow round conductors'. JIEE, 1943, Vol. 88, Pt.II, pp. 349-359

[45] STOLL, R.L. : 'The analysis of eddy currents'. Clarendon Press. 1974

[46] DWIGHT, H.B. : 'Skin effect in tubular and flat conductors'. Trans. AIEEE, Vol. 37, 1918, pp. 1379-1403

[47] ARNOLD, A.H.M. : 'The alternating-current resistance of parallel conductors of circular cross-section'. JIEE, 1935, 77, pp. 49-58

[48] SILVESTER, P. : 'Modern electromagnetic fields'. Prentice Hall, 1968

[49] SILVESTER, P. : 'Dynamic resistance and inductance of slot-embedded conductors'. IEEE Trans., 1968, PAS-87, pp. 250-256

[50] SILVESTER, P. : 'The accurate calculation of skin effect in conductors of complicated shape'. IEEE Trans., 1968, PAS-87, No.3, pp. 735-741

[51] SILVESTER, P. : 'Skin effect in multiple and polyphase conductors'. IEEE Trans., 1969, PAS-88, No.3, pp. 231-238

[52] LIM, K.K., and HAMMOND, P. : 'Numerical method for determining the electromagnetic field in saturated steel plates'. Proc. IEE, 1972, 119, (11), pp. 1667-1674

[53] LAVERS, J.D. : 'An efficient method of calculating parameters for induction and resistance heating installations with magnetic loads'. IEEE Trans., on Ind. Appl., 1978, 1A-14, No.5, pp. 427-432

[54] ROSENBERG, E. : 'Eddy current in solid iron'. Elecktrotech. Maschboan, Vol. 41, 1923, pp. 317-25

[55] KENNELLY, A.E., ARCHARD, F.H., and DANA, A.S. : 'Experimental reseaches on the skin effect in steel rails'. Franklin Institute Journal, Vol. 182, No.2, Aug 1916

[56] DWIGHT, H.B. : 'Alternating current conductivity of iron pipe'. The Electric Jounal, 1926, Vol. 23, No.26, pp. 295-297

[57] DAVIES, E.J., and BOWDEN, A.L. : 'Direct resistance heating of ferromagnetic billets'. 7th Intelnational Congress on Electroheat, Warsaw, 1972, Paper N628

[58] SMITHELLS, C.J. : 'Metals reference book'. Butterworths, London, 1976

[59] KAYE, G.W.C., and LABY, T.B. : 'Tables of physical constants'. 14th Edition

[60] LOZINSKII, M.G. : 'Industrial applications of induction heating'. Pergamon Press, 1969

[61] LAMMERANER, J., and STAFL, M. : 'Eddy-currents'. Illiffe Books LH, 1966

[62] SALTER, E.H. : 'Problems in the measurements of a.c. resistance and reactance of large conductors'. Trans. AIEE, Vol. 67, 1948, pp. 1390-1397

[63] JACKSON, R.L. : 'Measurements of skin and proximity effects in circular conductors'. Proc. IEE, Vol. 117, No.7, July 1970, pp. 1435-1440

[64] FORBES, H.C., and GORMAN, L.J. : 'Skin effect in rectangular conductors. A method of measurement and experimental data'. Trans. AIEE, June 1933, pp. 516-520

[65] BALL, H.E., and MACSCHIO, G. : 'The a.c. resistance of segmental conductors as used in power cables'. IEEE Trans., 1968, PAS-87, (4), pp. 1143-1148

[66] EMANUEL, A., and DOEPKEN, H.C. : 'Calculation of losses in steel enclosures of three phase bus or cables'. IEEE Trans., 1974, PAS-93, No.6, pp. 1758-1767

[67] ELGAR, C.E., REHDER, R.H., and SWERDLON, N. : 'Measured losses in isolated-phase bus and comparison with calculated values'. IEEE Trans., 1968, PAS-87, No.8, pp. 1724-1729

[68] ELLETT, R.C. : 'Induction heating of mild steel vessels in a pulsating field'. M.phil thesis, University of Aston in Birmingham, Jan 1974

[69] BURKE, P.E., and ALDEN, R.T.H. : 'Current density probes'. Trans. IEEE, PAS-88, No.2, Feb 1969, pp. 181-185

[70] JEANS, J.H. : 'Electricity and magnetism'. Cambridge University Press, Third Edition, Chapter 15, p. 479

[71] HALE, J.W. and RICHARDSON, F.R. : 'Mathematical descriptions of core losses'. AIEE Trans., 1953, pp. 495-501

[72] McCONNELL, H.M. : 'Eddy-current phenomena in ferromagnetic materials'. AIEE Trans., 1954, 73, pp. 226-235

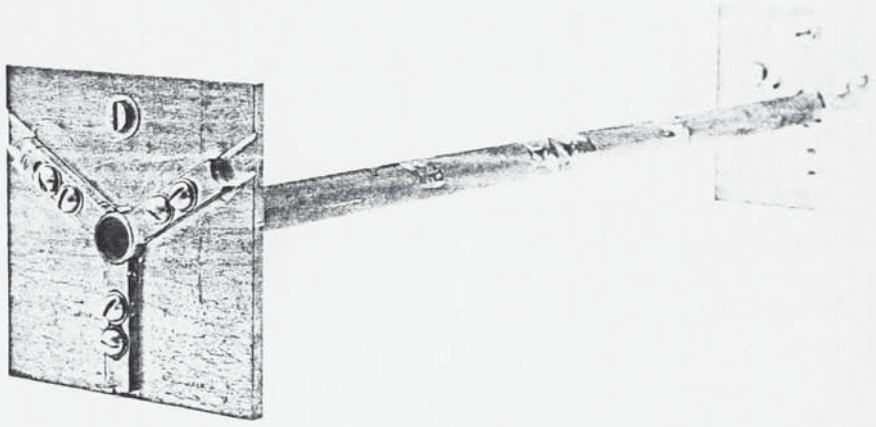

Plate 1 Arrangement for supplying electrical current to a tube under test